Dynamic Visual Servo Control of Robots: An Adaptive Image-Based Approach

Lee Elliot Weiss

CMU-RI-TR-84-16

Department of Electrical and Computer Engineering
The Robotics Institute
Carnegie-Mellon University
Pittsburgh, Pennsylvania 15213

April 1984

Copyright © 1984 Carnegie-Mellon University

Table of Contents

1. Introduction 3
- 1.1. Overview 3
- 1.2. Introduction to Visual Servo Control 3
- 1.3. Outline of Dissertation 13
  - 1.3.1. Dissertation Goals 13
  - 1.3.2. Design Approach 14
  - 1.3.3. Outline of Dissertation 14

2. Visual Servo Control 19
- 2.1. Overview 19
- 2.2. Robot Kinematics and Dynamics 20
  - 2.2.1. Kinematics 21
  - 2.2.2. Rigid Body Dynamics 22
- 2.3. Control 23
  - 2.3.1. Joint Level Control 24
    - 2.3.1.1. Feed-Forward Open-Loop Control 25
    - 2.3.1.2. Fixed Linear Servo Control 26
    - 2.3.1.3. Adaptive Feedback Control 28
  - 2.3.2. Kinematic Control 31
    - 2.3.2.1. Incremental Motion Control 33
- 2.4. Visual Servo Control Structures 34
  - 2.4.1. Computer Vision 36
  - 2.4.2. Position Based Visual Control Structures 37
    - 2.4.2.1. Static Position Based "Look and Move" 37
    - 2.4.2.2. Dynamic Position-Based "Look and Move" 39
    - 2.4.2.3. Position Based Visual Servoing 40
  - 2.4.3. Imaged Based Visual Control Structures 41
    - 2.4.3.1. Dynamic Image-Based "Look and Move" 42
    - 2.4.3.2. Image-Based Visual Servoing 44
- 2.5. Control Of Image-Based Systems 46
  - 2.5.1. Control Approach 47
  - 2.5.2. Feature Selection and Assignment 51
    - 2.5.2.1. Feature Assignment Using Diagonal Dominance 51
    - 2.5.2.2. Feature Selection 53
  - 2.5.3. Path Constraint 56
- 2.6. Summary 60

3. Model Reference Adaptive Control 63
- 3.1. Overview 63
- 3.2. MRAC for Systems Without Measurement Delay 63
- 3.3. MRAC Control With Measurement Delay 65

3.3.1. MRAC Controller with Delay 66
3.3.2. Control Penalty 68
3.3.3. Reference Model 68
3.4. Signal Biasing and Gravity Compensation 70
3.4.1. Signal Biasing 70
3.4.2. Gravity Compensation 71
3.5. Linear Control Interpretation 72
3.5.1. FP MRAC 73
3.5.2. SP MRAC 75
3.6. Parameter Specification 78
3.6.1. Model Time Constant Specification 78
3.6.2. Sampling Period Selection 79
3.6.2.1. Fundamental Upper Bound 80
3.6.2.2. Performance Margin 80
3.6.2.3. MRAC Identifier Requirements 81
3.6.3. Adaptive Gain Matrix Initialization and Limiting 81
3.6.4. Parameter Vector Initialization 82
3.6.5. Weighting Factor 83
3.6.6. Control Penalty 83
3.7. Summary 83
4. Task Modeling and Simulation 85
4.1. Overview 85
4.2. Task Configurations 86
4.2.1. Configuration 1: 2 DOF with linear kinematics and dynamics 86
4.2.2. Configuration 2: 2 DOF with nonlinear kinematics & dynamics 88
4.2.3. Configuration 3: 3 DOF with nonlinear kinematics, and linear and uncoupled dynamics 89
4.3. Plant Modeling for Translational and Rotational Stages 91
4.3.1. Rotational Stage 91
4.3.2. X-Y Stages 93
4.3.3. X-Y-Theta Stage Parameters 94
4.3.4. Computer Simulation Of Uncoupled Linear Models 96
4.4. Plant Modeling for 2 DOF Robot Arm 97
4.4.1. Kinematic Equations 99
4.4.2. Rigid Body Dynamics 100
4.4.3. Actuator Dynamics 101
4.4.4. Robot Arm Parameters 102
4.4.4.1. Motor 2 Selection 104
4.4.4.2. Motor 1 Selection 105
4.4.5. Computer Simulation of the Robot Arm 106
4.4.5.1. Linear Model 108
4.5. Modeling Picture Taking and Feature Measurement 110
4.5.1. Image Transformations 110
4.5.2. Feature Transformations 111
4.5.2.1. Two-Dimensional Line 111
4.5.2.2. Polyhedral Objects 115
4.5.2.3. Noise Signal Modeling 118
4.6. Summary 119

5. Evaluation: One DOF Systems 121
5.1. Overview 121
5.2. Baseline MRAC 122
5.2.1. MRAC Without Measurement Delay 123
5.2.2. MRAC With Measurement Delay 124
5.3. Linear IBVS 126
5.3.1. Noise Performance: Fixed vs. Adaptive Control 132
5.4. Nonlinear IBVS 135
5.4.1. Adaptive Control Vs. Fixed 144
5.5. Summary 147
6. Evaluation: Two DOF Systems 149
6.1. Overview 149
6.2. Linear Kinematics and Dynamics 150
6.2.1. Sensitivity Analysis 151
6.2.1.1. Predicted Path 153
6.2.1.2. Feature/Joint Assignment 156
6.2.1.3. Path Constraint 160
6.2.2. Control Evaluation 161
6.2.3. Independent Adaptive Control Problems 171
6.2.3.1. Sign-Sensitivity 171
6.2.3.2. Feature/Joint Reassignment 173
6.3. Nonlinear Kinematics and Dynamics 176
6.3.1. Control of Nonlinear Dynamics 176
6.3.1.1. Joint-Level Control Examples 178
6.3.2. Sensitivity Analysis 186
6.3.2.1. Feature/Joint Assignment 189
6.3.2.2. Path Constraint 192
6.3.3. IBVS Evaluation 192
6.3.3.1. Small Motion Trajectories 195
6.3.3.2. Large Motion Travel 199
6.3.3.3. Feature/Joint Reassignment 201
6.4. Summary 203
7. Evaluation: Three DOF 207
7.1. Overview 207
7.2. Candidate Control Features 208
7.2.1. Sensitivity Measurements 209
7.2.2. Feature/Joint Assignment 211
7.3. Small Signal Evaluation 213
7.4. Large Motion Evaluation 218
7.5. Summary 223
8. Conclusions 225
8.1. Overview 225
8.2. Conclusions 225
8.3. Suggestions for Future Research 229
8.3.1. MIMO vs. SISO Adaptive Control 229
8.3.1.1. On-Line Sensitivity Estimation 230
8.3.2. Implementation 231
8.3.2.1. Robot Mechanical Structure 231

8.3.2.2. Sensor Resolution 232
8.3.2.3. Extension to Higher DOF 232
8.3.2.4. Position vs. Image Based Control 233
Appendix A. MRAC Without Measurement Delay 235
A.1. Reference Model 236
A.2. Plant Model Structure 239
A.3. Controller 239
A.4. Adjustment Mechanism 241
A.5. Enhancements 242
Appendix B. Dynamic Equations for 2 DOF Arm 247
Appendix C. 2 DOF Controller Parameters 255
Appendix D. 3 DOF Controller Parameters 257

List of Figures

Figure 1-1: Robot Acquiring Object Using Computer Vision 4
Figure 1-2: Robot Assembling PC Boards Using Computer Vision 5
Figure 1-3: Basic Robot Positioning Control 6
Figure 1-4: Computer Vision 8
Figure 1-5: Static "Look and Move" Control 9
Figure 1-6: Dynamic Visual Servo Control 9
Figure 1-7: Features Change with Motion 11
Figure 2-1: Robot Block Diagram 20
Figure 2-2: Robot Control Block Diagram 25
Figure 2-3: Self-Tuning Regulator 29
Figure 2-4: Model Reference Adaptive Control 29
Figure 2-5: Open-Loop Kinematic Control 32
Figure 2-6: Incremental Robot System 34
Figure 2-7: Robotic Visual Servo Control 35
Figure 2-8: Computer Based Vision System 36
Figure 2-9: Static Position-Based "Look & Move" 38
Figure 2-10: Dynamic Position-Based "Look & Move" 39
Figure 2-11: Position-Based Visual Servoing 40
Figure 2-12: Dynamic Image-Based "Look & Move" 43
Figure 2-13: Image-Based Visual Servoing 45
Figure 2-14: Small-Signal Image-Based "Look and Move" 47
Figure 2-15: Small-Signal Image-Based Visual Servoing 48
Figure 2-16: MRAC Control of an IBVS System 50
Figure 2-17: Equivalent IBVS Control 51
Figure 2-18: Control Hierarchy 58
Figure 2-19: Hierarchical Control Example 59
Figure 2-20: Visual Based Control Structures 61
Figure 3-1: Analog Process Under MRAC Control 64
Figure 3-2: MRAC with Measurement Delay 66
Figure 3-3: Reference Model With Delays 69
Figure 3-4: Reference Model Root-Locus with One Delay 69
Figure 3-5: FP LMFC Control 73
Figure 3-6: FP Root Locus vs. π 75
Figure 3-7: SP LMFC Control 76
Figure 3-8: SP Root Locus vs. π 78
Figure 4-1: Configuration 1 87
Figure 4-2: Configuration 2. 88
Figure 4-3: Configuration 3 90
Figure 4-4: Rotational Stage Model 92

Figure 4-5: Translational Stage Model 93
Figure 4-6: Rotational Plant Block Diagram 96
Figure 4-7: Translational Plant Block Diagram 96
Figure 4-8: 2 DOF Robot Arm 98
Figure 4-9: Arm Coordinate Frames 99
Figure 4-10: Robot Actuator 102
Figure 4-11: Arm Simulation Block Diagram 109
Figure 4-12: Line-Image 113
Figure 4-13: Objects 115
Figure 4-14: Image Planes 117
Figure 4-15: Scaled Distribution 118
Figure 5-1: SP MRAC Without Measurement Delay 125
Figure 5-2: SP MRAC With Measurement Delay 127
Figure 5-3: Linear Time-Invariant Tasks 129
Figure 5-4: Linear Autonomous IBVS 130
Figure 5-5: IBVS with Control Signal Saturation 131
Figure 5-6: MRAC vs. LMFC Noise Performance (SNR = 44 db) 133
Figure 5-7: MRAC vs. LMFC Noise Performance (SNR = 30 db) 134
Figure 5-8: Error Index vs. SNR 134
Figure 5-9: 1 DOF Nonlinear Tasks 136
Figure 5-10: Task D Feature Characteristics 137
Figure 5-11: IBVS With Nonlinear Sensitivity 139
Figure 5-12: Sensitivity Change for TASK C 140
Figure 5-13: IBVS With Large Gain Changes 142
Figure 5-14: IBVS With Varying Sampling-to-Bandwidth Ratios 143
Figure 5-15: Fixed vs. Adaptive Performance (BW = 9.5 sec^{-1}) 145
Figure 5-16: Fixed vs. Adaptive Performance (BW = 4.4 sec^{-1}) 145
Figure 5-17: Fixed Feedback Control 146
Figure 5-18: Position Response of Fixed vs. Adaptive Control 147
Figure 6-1: Sensitivity Map 152
Figure 6-2: 2 DOF Linear Kinematic and Dynamic Tasks 154
Figure 6-3: Predicted Paths 155
Figure 6-4: Feature/Joint Assignment Map 158
Figure 6-5: Feature/Joint Assignment 159
Figure 6-6: Percentage Change In Feature Sensitivity 159
Figure 6-7: Hierarchy for 2 DOF Linear Kinematic System 161
Figure 6-8: Linear Kinematic Trajectories ($f_s/f_{BW} = 51$) 163
Figure 6-9: Linear Kinematic Trajectories (cont.) 164
Figure 6-10: Linear Kinematic Trajectories (cont.) 165
Figure 6-11: Adaptive Trajectories: First Trial 166
Figure 6-12: Sequential Adaptive Runs 167
Figure 6-13: Single Fixed Controller for Multiple Tasks 170
Figure 6-14: Sign-Sensitivity (T = 0.033 and $f_s/f_{BW} = 20$) 172
Figure 6-15: Sign Sensitivity (T = 0.013 and $f_s/f_{BW} = 51$) 172
Figure 6-16: Feature/Joint Reassignment (T = 0.033 and $f_s/f_{BW} = 20$) 174
Figure 6-17: Feature/Joint Reassignment (T = 0.013 sec and $f_s/f_{BW} = 51$) 175
Figure 6-18: Adaptive Control of a 2 DOF Robot Arm 177
Figure 6-19: Joint Level Nonlinear Dynamic Control 181
Figure 6-20: Torque Components for Second Trial 182

Figure 6-21: Torque Components for Third Trial 183
Figure 6-22: Fixed vs. Adaptive Control at Joint level 185
Figure 6-23: 2 DOF Nonlinear Kinematic Tasks 187
Figure 6-24: Nonlinear Kinematic Sensitivity and Assignment Map 188
Figure 6-25: Sensitivity With Diagonal Dominance Changes 191
Figure 6-26: Arm Jacobian Map 193
Figure 6-27: Hierarchy for 2 DOF Nonlinear Kinematic Configuration 194
Figure 6-28: Fixed vs. Adaptive: T = 0.033 sec and $f_s/f_{BW} = 20$ 195
Figure 6-29: Nonlinear Kinematic Trajectories (T = .003; $f_s/f_{BW} = 47$) 196
Figure 6-30: Nonlinear Kinematic Trajectories ($f_s/f_{BW} = 47$) (cont.) 197
Figure 6-31: Torque Components for TASK Q (MRAC) 198
Figure 6-32: Nonlinear Kinematics: Large Motion Travel ($f_s/f_{BW} = 415$) 201
Figure 6-33: Nonlinear Kinematic Feature/Joint Reassignment Task 202
Figure 6-34: Feature/Joint Reassignment (Nonlinear kinematics) 203
Figure 7-1: Cube Image 208
Figure 7-2: Cube on Edge 214
Figure 7-3: Sample Small Motion Task Trajectories 217
Figure 7-4: Coupling Index vs. Performance 217
Figure 7-5: Partial Coupling Index vs. Performance 218
Figure 7-6: Large Motion Task Images (Cases A, B, C, and D) 219
Figure 7-7: Large Motion Task Images (Cases E and F) 219
Figure 7-8: 3 DOF Trajectory (Case D) 221
Figure 7-9: 3 DOF Trajectory (Case F) 221
Figure 8-1: MIMO vs. SISO Computational Complexity 230
Figure A-1: FP Reference Model 237
Figure A-2: Discrete Reference Model 237
Figure B-1: Link # 2 251
Figure B-2: Link # 1 251
Figure D-1: Hierarchy for 3 DOF Configuration 258

List of Tables

Table 1-1:	Acronym Table	17
Table 4-1:	Electro-Craft E-508 DC MOTOR	94
Table 4-2:	Aerotech 416 Translational Stage	94
Table 4-3:	Aerotech 316 Rotational Stage	94
Table 4-4:	D. C. Motor E-660	105
Table 4-5:	D.C. Motor E-701	106
Table 4-6:	Configuration Summary	120
Table 5-1:	Identifier Parameter Initialization (1 DOF)	128
Table 6-1:	Maximum Path Deviations	168
Table 6-2:	identifier Initialization: Joint-Level Control	177
Table 6-3:	Nonlinear Dynamic Simulation Error	179
Table 6-4:	Joint Level Control: Maximum FP Errors	184
Table 6-5:	Nonlinear vs. Linear Kinematic Sensitivity Change	189
Table 7-1:	Small Motion Task Configuration	213
Table 7-2:	Small Motion Task Summary	215
Table 7-3:	Large Motion Task Performance Summary	220
Table C-1:	Identifier Parameter Initialization (2 DOF)	256
Table D-1:	3 DOF Parameter Initialization (T = 0.003 sec)	257

Abstract

The objective of this dissertation is to develop analytical tools for the design and evaluation of feedback compensators for *dynamic* vision-based robot control.

Sensory systems, such as computer vision, can be used to measure relative robot end-effector (or tool) positions to derive feedback signals for control of end-effector positioning. The role of vision as the feedback transducer affects closed-loop dynamics, and a visual feedback compensator is required. Vision-based robot control research has focused on vision processing issues (e.g., image filtering, structured lighting environments, and image feature interpretation), while control system design has been limited to ad-hoc strategies or linear single degree-of-freedom (DOF) systems. This dissertation formalizes an analytical approach to dynamic robot visual servo control systems by organizing and categorizing visual control strategies into *position-based* structures and *image-based* structures. The image-based structure represents a new approach to visual servo control, which uses image features (e.g., image areas, and centroids) as feedback control signals, thus eliminating a complex interpretation step (i.e., interpretation of image features to derive world-space coordinates). This approach also facilitates robot task training by a "teach-by-showing" strategy for specification of the control system reference signal commands. The dissertation includes an in-depth analysis, design, and evaluation of image-based control.

Image-based visual servo (IBVS) control presents formidable engineering problems for compensator design, including coupled and nonlinear dynamics, kinematics, and feedback gains, unknown parameters, and measurement noise and delays. To satisfy these requirements, a model reference adaptive control (MRAC) feedback system and a fixed linear model following controller (LMFC) are designed and evaluated using mainframe simulation models of two and three DOF systems, incorporating both nonlinear kinematics and dynamics. The MRAC is found to provide superior performance to the LMFC for large-signal trajectories of systems with unknown or nonlinear feature sensitivity gains. The issue of selecting features for image-based control is addressed by defining and evaluating an index of feature coupling. The dissertation focuses on compensator designs based on multiple uncoupled single-input single-output (SISO) controllers, for coupled systems, to simplify the design complexity and implementation.

Chapter 1
Introduction

1.1. Overview

The purpose of this chapter is to present an overview of the dissertation. In Section 1.2, the background and problems of *dynamic* visual servo control of robots are outlined, and a novel image-based approach to visual servo control is introduced. Section 1.3 includes a summary of the dissertation goals and design approach as well as a chapter-by-chapter outline. Detailed background and literature surveys are included in Chapter 2, in which the problem areas and design approaches are described in detail.

1.2. Introduction to Visual Servo Control

A conventional robot arm which is programmed to pick up an object from a table must be "taught" the position and orientation of that object before it can carry out the task. This process of teaching a robot positions and updating them for each new object or location is a routine part of current robot system development, and has become a major limitation in the adaptation of robots to unstructured tasks including many routine industrial applications. Flexible robotic systems would provide a capability to automatically modify positions and trajectories to accommodate changes in the task or task environment. Such flexibility is achievable only through the integration of sensors into robotic systems, and visual sensing, in particular, would appear to provide fundamental capabilities in the adaptation of robots to unstructured tasks. This dissertation will analyze and evaluate strategies which integrate visual sensing with robot movements, and will emphasize the design of such "visual servo control systems" in order to achieve stable and predictable system dynamics.

Figure 1-1 illustrates a visual servo control application for a robot. An object is placed on the table in a position which is unknown to the robot. The robot has not been preprogrammed with knowledge of the object position. In this sense, the task environment is said to be

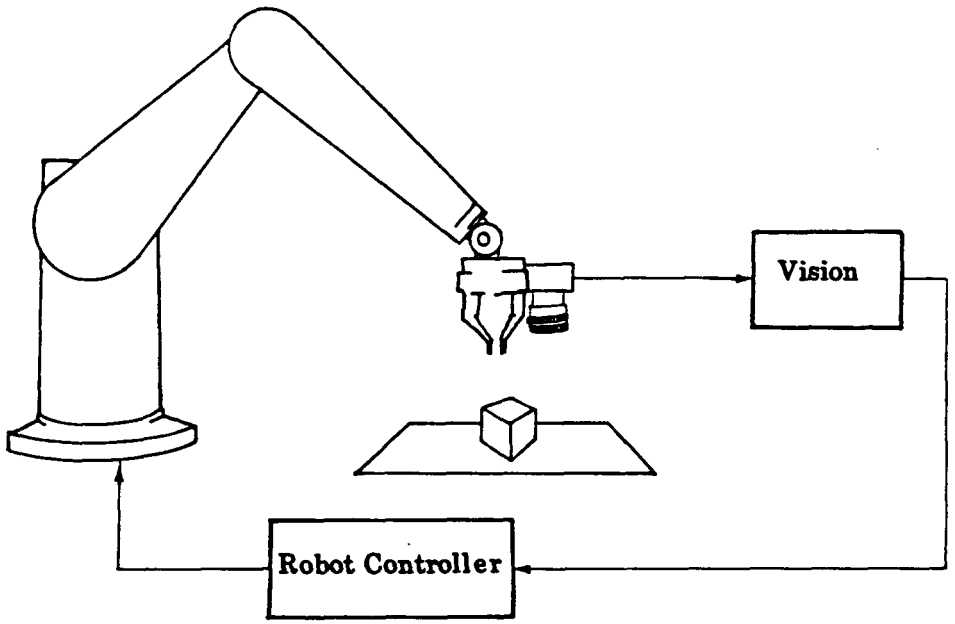

Figure 1-1: Robot Acquiring Object Using Computer Vision

"unstructured". A television camera is attached to the robot arm and provides visual sensing capability. The image acquired by the camera must be processed by a computer vision system in order to identify the object in the picture. The vision system extracts information from the image and may infer relationships between the spatial position of the object and camera position. Such relative position information may be used to guide the robot to acquire the object from the table.

Figure 1-2 shows a second typical application of visual servo control. In this case, a stationary camera is used to observe the lead tip of an electronic component which is held by the robot hand. The exact position of the lead tip relative to the robot hand is unknown due to the uncertainty in the forming of the component leads. The camera also observes the hole in the printed circuit board where the lead will be inserted. The vision system is used to resolve the uncertainty in lead position relative to the hole position. The robot controller then repositions the robot arm to correctly align the lead with the hole.

Several key issues arise in the design of visual servo control systems such as those described above. Processing and interpretation of image information to infer object position

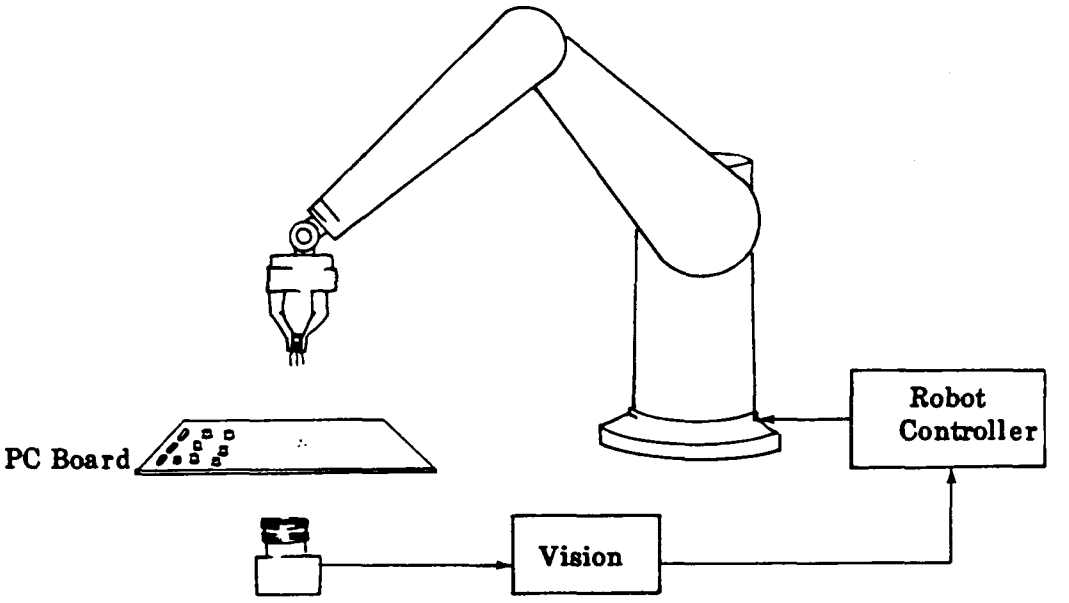

Figure 1-2: Robot Assembling PC Boards Using Computer Vision

and orientation are difficult and computationally complex tasks. The resulting estimates may be uncertain and require computational time delays. The robot controller, in turn, must compensate for these properties of the vision system as well as those of the robot. The resulting integrated system should have dynamic properties which are predictable and stable even in the face of unknown task conditions. In this dissertation, an adaptive controller is proposed to provide this consistent dynamic system response under unknown conditions.

The interpretation of image information to estimate object position normally requires the extraction of quantitative image features which are related to a stored object model. The resulting position estimates may be used to design a "position-based" visual servo control system. In this dissertation, an alternative strategy is explored. Image features which are monotonically related to spatial position may be used as a basis for control in place of position estimates. Such an "image-based" visual servo control strategy may offer advantages in terms of reduced delay and estimation noise, but require special attention to control strategies which accommodate position-to-feature relationships. The image-based visual servo control strategy is formalized for the first time in this dissertation and control strategies are examined in detail.

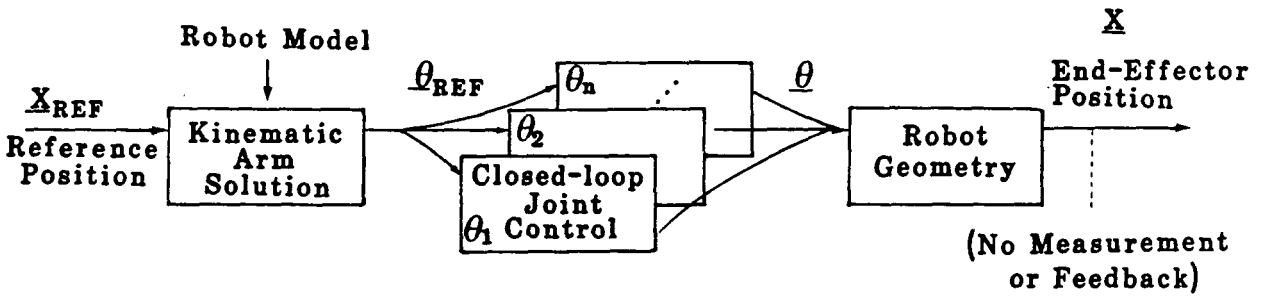

Figure 1-3: Basic Robot Positioning Control

In order to understand the relationship between conventional robot position control and visual servo control, it is useful to examine a robot positioning system in a bit more detail. Such a system may be described by the block diagram in Figure 1-3. The desired position of the robot hand or end-effector is specified by the reference position vector $\underline{X}_{REF}$. The robot moves by displacement of individual joint angles described by the vector $\underline{\theta}_{REF}$, and a model of the robot geometry, called the kinematic arm solution, must be used to find $\underline{\theta}_{REF}$ when $\underline{X}_{REF}$ is specified. An approximate kinematic arm solution is always available for a real robot though variations between individual robots may result in significant inaccuracies of final arm positioning.

The desired joint angles described by $\underline{\theta}_{REF}$ are expressed as input reference signals to individual joint angle control systems. Each joint controller uses position feedback to accurately position the joint motor to the desired angle. The resulting vector of joint angles $\underline{\theta}$ is therefore obtained by independent closed-loop control of the joints with respect to the desired $\underline{\theta}_{REF}$.

The position of the robot end-effector when the joints are set at angles $\underline{\theta}$ is determined by the robot geometry. In general, the robot geometry may be slightly different than the robot model, and therefore the actual end-effector position $\underline{X}$ may differ from the desired position $\underline{X}_{REF}$. In real systems, there is no way to determine this final positioning error since no measurement or feedback of final end-effector position is available. In this sense, the control

loop is never closed around the end-effector position itself leading to inherent limitations in the ability of such a system to compensate for inaccurate modeling of the arm or to derive positioning error signals relative to unstructured environments.

The addition of visual sensing as a measurement system for relative end-effector position provides a basis for overcoming some of these limitations. However, the use of computer vision to infer position and orientation of objects, or interpret general three-dimensional relationships in a scene, is in general a complex task requiring extensive computing resources. Techniques which may exploit simplier sensors or minimize processing for image interpretation offer major advantages for visual servo control implementations.

Figure 1-4 illustrates schematically some approaches to the interpretation of a two-dimensional image for inference of three-dimensional position and orientation. In the block diagram, a sensor, such as a TV camera, is used to acquire a two-dimensional array of brightness values from the three-dimensional scene. This image array may undergo various types of computer processing to enhance image properties and enable the extraction of both local and global image features These features typically include structural components of the image such as points, lines, and areas, as well as quantitative parameters attached to them. In reality there is a continuum of possible image features and their available transformations, and their choice depends on the purpose and requirements of their subsequent use or interpretation. The relationship between such structural components or image features is then used to interpret the observed scene. The resulting interpretation provides an estimate of the relative position $\hat{\underline{X}}$ which may be used for visual servo control. Such position estimates may contain object model inaccuracies as well as feature measurement inaccuracies and therefore may introduce measurement noise into a visual feedback control system.

Figure 1-5 shows a simple example of a visual servo control structure. This system is called a "static look and move" structure for visual servo control and is described in more detail in Chapter 2. The system operation consists of a sequence of independent steps:

1. Step 1: The vision system "looks" at the scene, or object, and estimates the end-effector position $\hat{\underline{X}}$;

2. Step 2: The position estimate is sent to a task computer. The task computer computes the difference, $\Delta\underline{X}$, between where the end-effector should be, $\underline{X}_{REF}$, and the current position estimate. The task computer then issues a command to the robot positioning system to "move" by the incremental distance $\Delta\underline{X}$; and

3. Step 3: The robot moves to the new position. Step 1 is not repeated until the robot completes the motion specified by the "move" command.

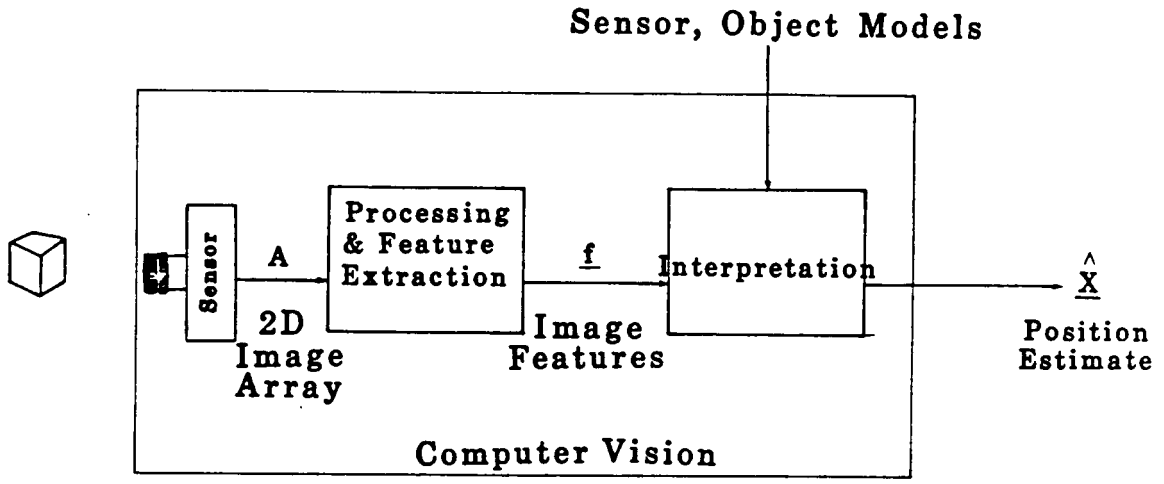

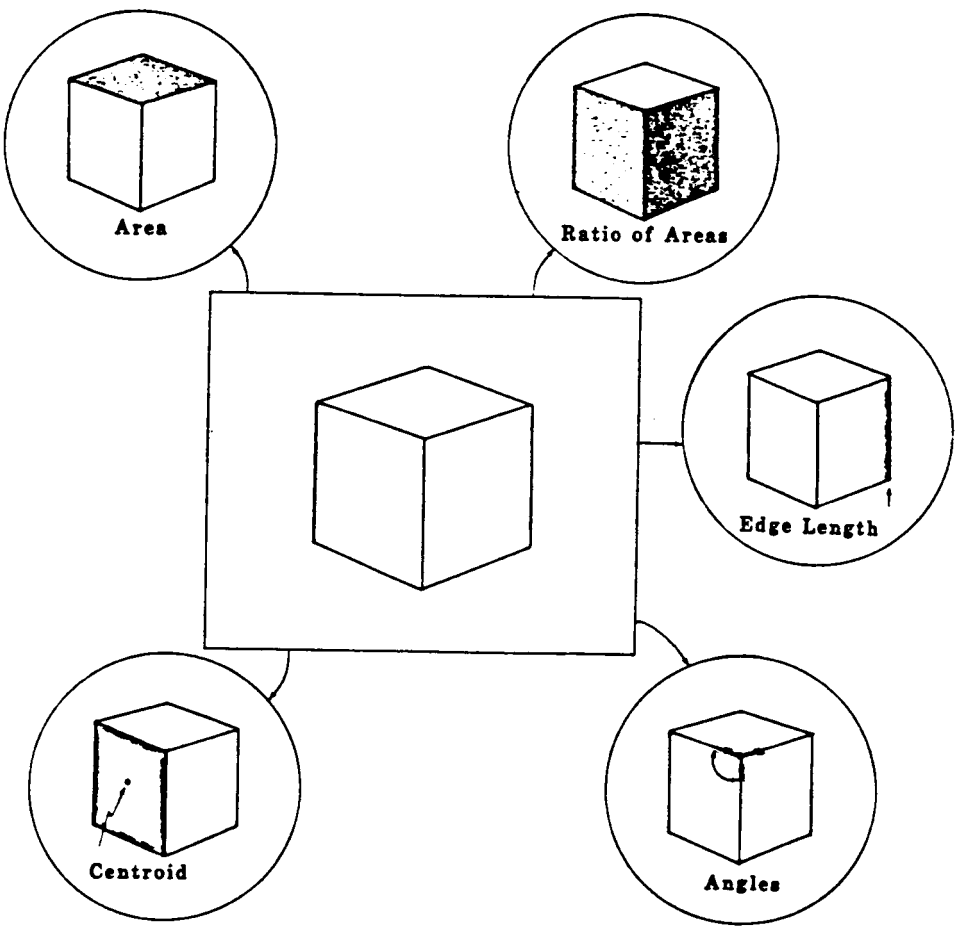

Figure 1-4: Computer Vision

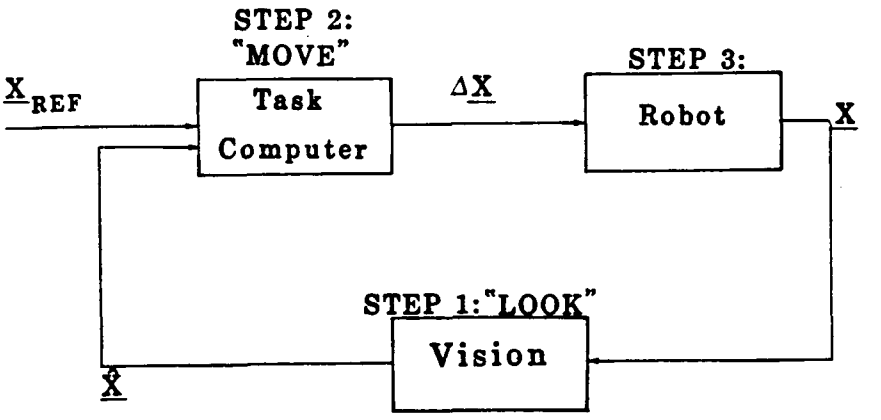

Figure 1-5: Static "Look and Move" Control

The sequence of operations is repeated until a specified accuracy is achieved, that is, $\Delta\underline{X}$ is reduced to some small quantity. The number of iterations will depend upon the particular task. The "static look and move" structure demonstrates the concept of interactive sensing for robot positioning, but is not a *dynamic* control system since each step is executed independently and in sequence.

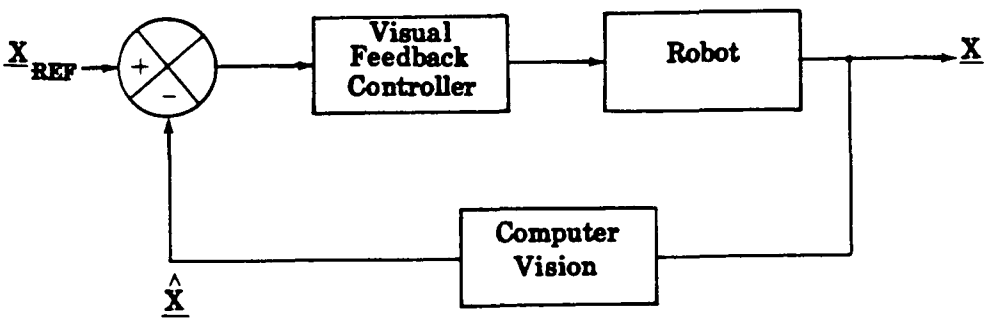

Figure 1-6: Dynamic Visual Servo Control

If the visual feedback system is structured so that the three steps outlined above are executed in parallel (i.e., positions estimates, $\hat{\underline{X}}$, and position errors, $\Delta\underline{X}$, are updated as fast

as they are measured, and position corrections are commanded to the robot while it is moving), then dynamic visual servo control systems such as that illustrated in Figure 1-6 can be synthesized. The role of computer vision as the feedback transducer now affects the over-all, or closed-loop, system dynamics, and a visual feedback controller is required for stability and acceptable transient response. While dynamic control has the potential to achieve faster responses than "static" systems, dynamic visual control presents a variety of difficult design problems which are not currently addressed in the literature. This dissertation focuses on two of these issues: the use of image features as feedback parameters in "image-based" visual servo control, and the implementation of adaptive control strategies for visual servo control.

In image-based visual servo (IBVS) control , the image features, as described in Figure 1-4, are used to control robot motion directly without inferring position in the spatial coordinate frame. This approach relies on the systematic variation of image features with relative object position. Such a relationship is illustrated in Figure 1-7. In this case, the task is specified by portraying the current camera image and the desired camera image. The image features corresponding to an image trajectory as the camera moves may be plotted as shown in the figure. Monotonic, although nonlinear, feature-to-position realtions are obtained in this case using area, relative area, and center-of-gravity as features.

In an IBVS system, the reference and feedback signals are defined in terms of these image feature values which correspond to current and desired robot positions. The feature error may be derived at every measurement time and used to drive the robot in a direction which decreases the error. The subsystem which converts the feature error to a robot control signal comprises the heart of the IBVS controller. This dissertation will address the analysis and design of such controllers for IBVS systems.

The IBVS approach to visual servo control presents a number of issues which require careful formulation and analysis. Selection of features is closely tied to the problem of image interpretation since features which are closely related to object position will be useful for both interpretation and servo control. Criteria for feature selection are developed in this dissertation based on feature sensitivity and feature coupling measures. The feature sensitivity (or slope of the feature-to-position curve) appears in the control structure as a small-signal gain term. The feature sensitivities are typically unknown a'priori and change nonlinearly with robot movements. These properties of the feature sensitivity lead to our use of adaptive control strategies in this study.

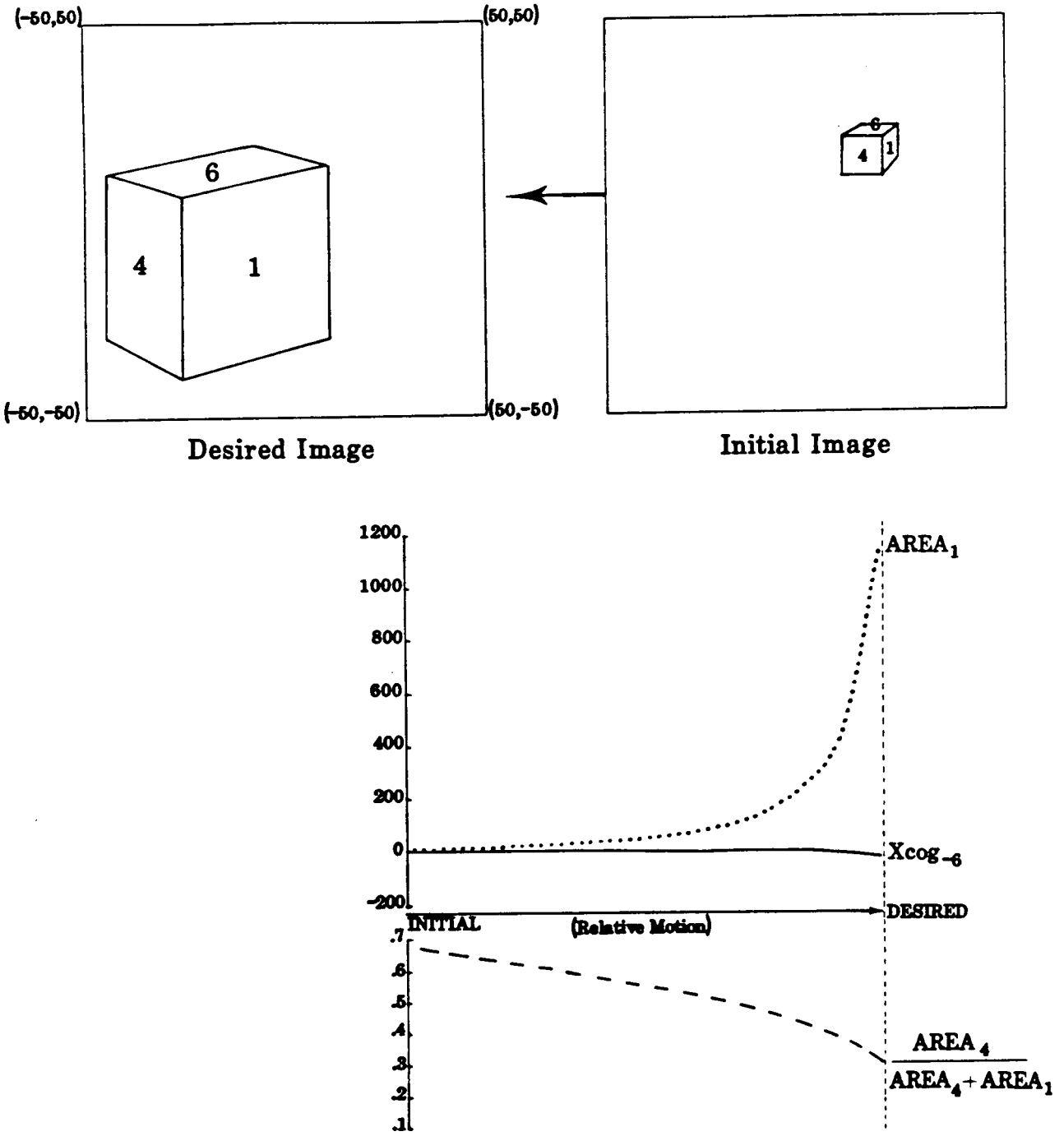

Figure 1-7: Features Change with Motion

Since an IBVS system controls image feature signals rather than position signals, it is difficult to design a system with precisely predictable position trajectories. The relationship between desired feature trajectory and resulting position trajectory is strongly dependent on the choice of features. An important result of the simulation studies carried out in this dissertation is the demonstration that position trajectories are typically well-behaved for smooth monotonic feature sensitivity relations.

Flexible robotic systems will most likely incorporate different modes of control for different tasks or subtasks. Visual servo control is one such mode of control which may be useful in sensor-based systems. Position-based and image-based visual servo controls, in turn, represent alternative but complementary strategies within this framework. As pointed out earlier, there is a continuum of features which may be derived by measurement and transformation from an image, and any combination of these may be useful as control parameters. In this sense, spatial position estimates are one set of transformed image features. They are particularly useful when available and reliable since an approximate model of robot geometry is typically known. The use of alternative features in the IBVS approach may have advantages in terms of speed and reliability when model-based information is not available.

In more general terms, IBVS represents a case study of robot control in unstructured environments where model-based information is either unavailable or unreliable. In this sense, the adaptive control strategy may be viewed as a "learning mode" in which interactive sensing of the environment defines an updated model of the world and provides a basis for consistent control strategies. A mobile robot, for example, consistently must predict and verify its motion using unreliable models of the world and robot itself. The identification phase of adaptive control provides a mechanism to test and update dynamic models, and the image-based approach can be used inversely to identify and confirm image features based on compatibility of predicted and observed dynamic changes.

Another example of adaptive robot control using sensors arises in relation to force and tactile sensing. Again, a consistent model relating robot control commands to desired force signals may exist, and performance may depend on identification of transformation matrices and on-line synthesis of an appropriate controller. Manipulation of structures with nonlinear compliant elements raises exactly these questions.

Visual servo control is a fundamental component of sensor-based robotic systems, and the

analysis and design of systems using image-based control demonstrates the feasibility of a new approach which may provide improved performance as one mode of an integrated system. Analysis of the IBVS problem and incorporation of adaptive control as a design solution have led us to derive principles with much broader applicability than to visual servo control. An increasing number of problems require multiple sensory modalities for robot control in unstructured environments, and adaptive modes of interactive sensing will become increasingly important. The research reported in this dissertation provides a basis for exploration of many such adaptive sensor-based strategies.

1.3. Outline of Dissertation

This section presents a brief summary of the goals and design approach of this dissertation as well as a chapter-by-chapter outline of the technical content. A table of acronyms used is included as Table 1-1 for reference.

1.3.1. Dissertation Goals

The goals of the dissertation are to address the problems of dynamic visual servo control of robots, and provide insight into visual servo control by:

1. Organizing and categorizing visual servo control systems into well-defined classical feedback control structures. Such an organization facilitates the analysis and design of a servo controller, by showing the role of computer vision as the feedback transducer, and by accounting for the static and dynamic properties of the robot and measurement systems, which must be compensated. The categorization can also serve as a framework for comparative evaluation of different control approaches.

2. Analyzing, designing, and evaluating the IBVS approach to visual servo control. The objectives are to show that IBVS can produce stable systems, with good transient responses, and suitable path performance; and to provide analytic tools to design real systems. In the dissertation, IBVS systems are evaluated using computer simulation models.

In the next section, a controller design approach for IBVS control is proposed.

1.3.2. Design Approach

Feedback controllers can be categorized as being either fixed or adaptive. It is a formidable engineering task to design effective fixed feedback controllers to compensate for nonlinear and unknown systems. The gains of an adaptive controller are adjustable and are dynamically changed during control from on-line parameter identification of the unknown system. The model reference adaptive control (MRAC) approach has been extensively studied for the control of unknown linear systems, and empirically evaluated for dynamic nonlinear systems. Based on these studies, MRAC appears to be well suited for IBVS control, and is the design approach developed in the dissertation. An enhanced MRAC (with series-parallel reference model and control penalty) is selected for IBVS control to suppress noise, and be less sensitive to control signal saturation. In the dissertation, the author modifies the MRAC to account for measurement delay, and identifies the requirement of a control penalty for use with nonlinear IBVS systems. The dissertation also includes a comparative evaluation of fixed versus adaptive control. The fixed controllers are synthesized by fixing the adjustable gains of the adaptive controller (i.e., linear model following control (LMFC)).

Feedback control of a multi-input multi-output (MIMO) system (with m inputs and m outputs) can be based on either m independent single-input single-output (SISO) controllers, or on a single MIMO controller design. MIMO control, of coupled systems, seems to have an inherently greater potential to achieve the desired control system performance criteria. SISO controllers are simplier to implement, since they are computationally less complex, and can be modularized. A modular system can easily be extended to increasing DOF, and distributed processing. In the dissertation, the author has selected to investigate an SISO approach, since it would be easier to implement (in future research) with current laboratory and factory computing environments. With increasingly powerful and less expensive processors, an MIMO approach may be more suitable for future research investigations.

1.3.3. Outline of Dissertation

In Chapter 2, visual servo control is discussed in detail. The chapter begins by reviewing robot kinematics, dynamics, and control. The formal categorization and organization of previously implemented and proposed visual servoing strategies, into classical feedback control structures, is then presented. The control requirements for IBVS are described, and the MRAC approach is proposed to meet these requirements.

In Chapter 3, the enhanced SISO MRAC algorithm is reviewed. The algorithm is modified for systems with measurement delay and coupling. The chapter concludes with guidelines for MRAC parameter selection.

The purpose of Chapter 4 is to specify the visual servoing tasks configurations (including 1, 2, and 3 DOF systems) which are evaluated, in simulations, using fixed and adaptive IBVS control. Mathematical models, required for the computer simulations and control evaluations, are developed, and incorporate robot kinematics and dynamics, camera picture taking, and feature transformations.

Chapters 5, 6 and 7 include the evaluation of LMFC and MRAC control of progressively more complex systems. The complexity relates to

- DOF: 1, 2, and 3 DOF (in Chapters 5, 6, and 7, respectively);
- Dynamics: linear uncoupled vs. nonlinear coupled;
- Kinematics: linear uncoupled vs. nonlinear coupled; and
- Features: minimal features (i.e., the number of features available for control equals the number of DOF to control) vs. excessive features (i.e., feature selection required when there are more features available than there are DOF to control).

The evaluation includes a sensitivity analysis of the feature transformation coupling; comparative study of fixed vs. adaptive control; isolation of problem areas associated with SISO control of coupled systems; evaluation of a path constraint strategy; and, evaluation of a feature selection strategy to discriminate among candidate features.

In Chapter 8, the results and contributions of the dissertation are summarized, and directions for future research are suggested. Preliminary investigations of MIMO control, issues of physical implementations, and simulated control of a 5 DOF IBVS system, are described.

The principal contributions of the dissertation are:

- Formalization of *dynamic* visual servo control of robots.
- Introduction of a novel "teach-by-showing" image-based control approach.
- In-depth analysis, design, and evaluation of fixed and adaptive control of IBVS systems.

- Extension of enhanced SP MRAC to control of systems with delay and nonlinear gains.

- Demonstration of enhanced SP MRAC for direct joint-level control of a simulated articulated robot arm.

- Identification of the applications and limitations of SISO adaptive control of coupled systems.

DOF	degree-of-freedom
FP	full-parallel
IBVS	image-based visual-servoing
LMFC	linear model following control
MIMO	multiple-input multiple-output
MRAC	model reference adaptive control
OFV	out-of-field of view
SISO	single-input single-output
SP	series-parallel
PBVS	position-based visual-servoing

Table 1-1: Acronym Table

Chapter 2
Visual Servo Control

2.1. Overview

The objective of this chapter is to formalize an analysis and design approach for dynamic robotic control using computer vision for sensory feedback information. Controller design will focus on an adaptive approach to compensate for nonlinear robot dynamics, and nonlinear and unknown gains introduced by the sensory feedback.

This chapter is organized as follows. Control system analysis and design requires kinematic and dynamic models of the robot under control. In Section 2.2, manipulator kinematics and dynamics are reviewed. Detailed model developments for specific cases are presented in Chapter 4. In Section 2.3, a review of control is presented, describing standard non-sensor based control at the joint and world levels when feedback measurements are limited to joint level space. The problem of controlling highly coupled, nonlinear, and possibly unknown dynamic systems is described. Control law approaches for these systems, including model reference adative control (MRAC), are discussed since similar problems arise in sensory based systems.

The remainder of the chapter summarizes the contributions of the dissertation. In Section 2.4, previously implemented and proposed visual servoing strategies are formally organized and categorized into classicial feedback control structures. Such organization has not previously appeared in the literature. While the scope of the dissertation is limited to a detailed design and evaluation for one of these structures, this formalization will provide a framework for future investigations. The control structures are based on feedback measurements which are extended to include world coordinate measurements. Previously implemented structures derive control laws based on relative world space position information. A novel structure is proposed, which uses image features for feedback. The image-based approach has potential advantages, including being able to teach a task by

visually "showing" the robot what to do. Design of the image-based visual feedback controller requires compensation of robot dynamics and kinematics, and of the feedback properties including delay, coupling, nonlinearity, noise and unknown parameters. In Section 2.5, an adaptive control law approach is proposed to meet these requirements. The remainder of the dissertation includes an analysis, design, and evaluation, in simulations, of image-based visual servoing.

2.2. Robot Kinematics and Dynamics

A robot consists of a sequence of links connected in series or parallel by revolute (i.e., rotational) or prismatic (i.e., translational) joints [Lee 82a]. Each joint is independently actuated by electrical, hydraulic, or pneumatic devices resulting in relative motion of the links. The first link is attached to a reference frame, which can be either fixed or mobile, while the end of the final link is equipped with an end-effector (e.g. mechanical hand or tool) to manipulate objects or perform assembly tasks. Each joint-link combination constitutes one degree-of-freedom (DOF). For general purpose tasks, six degrees-of-freedom are required; three for positioning and three for orienting. Fewer degrees-of-freedom may be used to accomplish specific tasks.

A block diagram of an N DOF robot is shown in Figure 2-1.

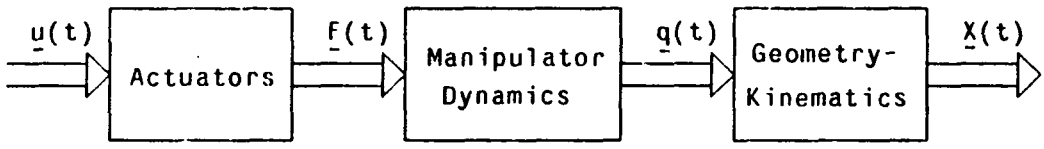

Figure 2-1: Robot Block Diagram

The control vector $\underline{u}(t) = \{u_1(t),...,u_n(t)\}^T$ represents the actuating or control signals. In response to $\underline{u}(t)$, the actuators develop forces or torques, $\underline{F}(t)$, which drive the manipulator links. The resultant joint positions, $\underline{q}(t)$, are called the generalized coordinates [Paul 81]. Each joint position, $q_i(t)$, is referenced to the coordinate system of the previous link in the chain. The position and orientation (or pose) of the end-effector, $\underline{X}(t) = \{X_1(t)...X_6(t)\}^T$, is referenced with respect to a world coordinate frame.

2.2.1. Kinematics

Robot kinematics deals with the static modeling of the spatial relationships of the links with respect to a world reference frame or coordinate system. Robot kinematics thus relates joint variable space, $\underline{q}$, to world space $\underline{X}$. World space can be defined in many possible coordinate systems including Cartesian, spherical, and cylindrical. While typical robotic tasks are defined in Cartesian space, particular robot geometries may lead to more natural definitions in other coordinate frames.

Kinematic modeling consists of two problems:

1. The direct kinematic problem: given $\underline{q}$, find $\underline{X}$, and

2. The inverse kinematic problem, or "arm-solution": given $\underline{X}$, find $\underline{q}$.

To solve these problems, kinematic modeling and analysis have been defined in terms of homogeneous transformation matrices [Paul 81]. A brief description of homogeneous transformations, for developing robot and visual servo control models, is presented here. Homogeneous transformation matrices, which define postions and orientation of coordinate systems, have the following important property. If matrix transformation $T_{i/k}$ describes the ith coordinate frame relative to the kth frame and $T_{j/i}$ describes the jth frame with respect to the ith frame, then

$$T_{j/k} = T_{j/i} T_{i/k}$$

and consequently,

$$T_{i/k} = T_{j/i}^{-1} T_{j/k}$$

For robotic manipulators, a Cartesian coordinate system is established for each link according to the systematic convention proposed by Denavit and Hartenberg [Denavit 55]. The homogeneous transformation matricies, or A matricies, describe the relative translation and rotation between successive link coordinate frames. Thus, A_1 describes the pose of the first link relative to the reference base, and A_i describes the pose of the ith link with respect to the $(i-1)^{th}$ link. For a six degree-of-freedom manipulator,

$$T_6 = A_1 A_2 A_3 A_4 A_5 A_6 \tag{2.1}$$

where T_6 describes the pose of the final link relative to the world reference frame. The direct kinematic problem is then to solve for $\underline{q}$ according to (2.1). The inverse "arm-solution" is more complex. Methods for finding $\underline{q}$ given T_6 are presented in [Paul 81].

And end-effector (or tool) can be fixed and referenced to the final link according to the transformation matrix T_{tool}. When $\underline{X}_{tool}$ is the tool pose relative to the reference frame, then

$$T_6\, T_{tool} = T_{tool/world} \doteq H[\underline{x}_{tool}]$$

where H[] maps a 6 DOF vector into the equivalent (4x4) homogeneous matrix transformation. Thus, the T_6 matrix, which must be evaluated by the "arm-solution", becomes

$$T_6 = T_{tool}^{-1}\, T_{tool/world} \tag{2.2}$$

In practice, the "arm-solution" produces only estimates of the joint positions, $\underline{q}$, which are required to produce a desired T_6. The following error sources can lead to inaccuracies:

- Inaccuracies in the geometric modeling of link or tool dimensions, or tool mounting dimensions;
- Unmodeled link compliance;
- Non-ideal joint coupling between links such as gearing backlash; and
- Computer quantization and round-off in the "arm-solution" evaluation.

While these error sources can be reduced by careful design and analysis, they can deteriorate task performance as the required accuracy increases.

2.2.2. Rigid Body Dynamics

Dynamic modeling of the robot arm is required for designing the control algorithm to achieve a desired system performance. Dynamic equations model the motion of the robot links in generalized coordinate space. This motion can then be related to world space by the kinematic equations. Several approaches are available for formulation of the arm dynamics [Hollerbach 80]. The Lagrangian method [Paul 81, Uicker 67], which is reviewed below and derived for a specific case in Appendix B, has the advantages that it is a systematic approach (utilizing the **A** matrices), and the equations have easily interpreted physical meaning which have significance when applied to control law design (Section 2.3).

The Lagrangian formulation for rigid body kinematic linkeages can be written as

$$D(q)\ddot{\underline{q}} + C(\underline{q},\dot{\underline{q}}) + G(\underline{q}) = F(t) \tag{2.3}$$

where $D(\underline{q})$ is the (n x n) inertial matrix, $C(\underline{q},\dot{\underline{q}})$ is the (n x 1) centrifugal and Coriolis vector, $G(\underline{q})$ is the gravitaional vector, and $\underline{F}(t)$ are the joint forces or torques. Equation (2.3) signifies that the robot dynamics are characterized by a system of of n second order, coupled, and nonlinear differential equations whose parameters are dependent on the robot's instantaneous configuration (generalized coordinate positions and velocities). The model

does not include frictional components, which may be significant for some robot designs. Viscous friction can often be modeled by additional linear terms of the form $F_{friction} = K_{friction}\dot{q}$. It is more difficult to derive simple models for Coulomb frictions. Whether or not they are included in the dynamic model, the control engineer must be aware of their effects.

Independent actuators develop the required force or torque to cause link motion. While the actuator can often be modeled by a linear system when operating in nominal regions, the control engineer must be aware of the nonlinearities and time-varying phenomena in the device. For example, DC motors have torque offset nonlinearities when operating in low torque regions. Power amplifiers exhibit current limiting saturation nonlinearities, and the gain drifts with time and temperature. While the control law design is based on the linear actuator model, the control engineer must choose a design which can still perform adequately in nonlinear regions and be relatively insensitive to parameter variations.

2.3. Control

Robot tasks (e.g., put the peg in the hole) must ultimately be defined in terms of a set of reference or command signal inputs to a control system. The control problem is to design a control law, based on dynamic models, so that the system is stable and the output tracks the reference signal according to a predefined performance specification.

With respect to robot positioning control, two levels of tasks can be identified:

1. Dynamic joint control, and

2. Kinematic (or end-effector positioning), path and trajectory control

While joint control deals directly with the issue of plant dynamics and control law design for reference signal tracking, kinematic control deals with generation of the reference signal required for end-effector positioning and motion along a specified path or trajectory. Depending on the approach to control law design, dynamic and kinematic control can be coupled or treated as independent problems.

In robotic control applications, the reference signal can be specified in terms of the generalized coordinate or world coordinate parameters, depending upon the required task. For example, when a robot is taught a desired position, or trajectory, through the "teach-mode" operation [Luh 83], joint positions are directly recorded and can be "played-back" as the desired reference signals. If the task requires that the end-effector move in a straight line

path to the end-point, then the reference signal must first be specified in Cartesian space. Without sensor-based control, with which the position of the end-effector can be measured directly, controller designs are constrained to use feedback measurements limited to the generalized coordinates (i.e., joint displacements). Thus, reference signals defined in Cartesian space must be mapped into estimated joint level reference signals by the inverse kinematic "arm-solution." This approach results in open-loop control of the end-effector.

This section includes a review of control at the joint and world levels when the feedback measurements are limited to the generalized coordinate space. In Section 2.4, visual servo control structures are described which extend the measurement space to include world coordinates.

2.3.1. Joint Level Control

Practical approaches to control law design for robotic manipulators include:

1. Feed-forward open-loop control [Lee 82b, Luh 80, Hollerbach 80, Raibert 78, Albus 75];

2. Linear servo control [Paul 81, Luh 83, Williams 83]; and

3. Adaptive servo control [Chung 82, Dubowsky 79, Horowitz 80, Koivo 80, Koivo 83, LeBorgne 81].

These controllers can be applied independently, or in combination, as each has certain advantages and disadvantages.

A block diagram of a robot under computer control is shown in Figure 2-2. The control system represents a sampled-data system in which $\underline{u}(k) \doteq \underline{u}(kT)$, where T is the constant sampling period. The control signals are applied through digital-to-analog converters (DAC) which can be modeled by the cascade of an ideal impulse sampler and a zero-order hold with saturation nonlinearity [Neuman 79a]. Over the interval $kT \leq t \leq (k+1)T$,

$$u_a(t) = \begin{cases} u_i(kT) & \text{for } |u_i(kt)| \leq V_{sat} \\ +V_{sat} & \text{for } u_i(kT) > V_{sat} \\ -V_{sat} & \text{for } u_i(kT) < -V_{sat} \end{cases} \tag{2.4}$$

where V_{sat} is the maximum DAC output signal. For simplicity, the block diagram in Figure 2-2 shows position feedback. The following discussions do not preclude the use of tachometers and observers to measure and estimate joint velocity and acceleration.

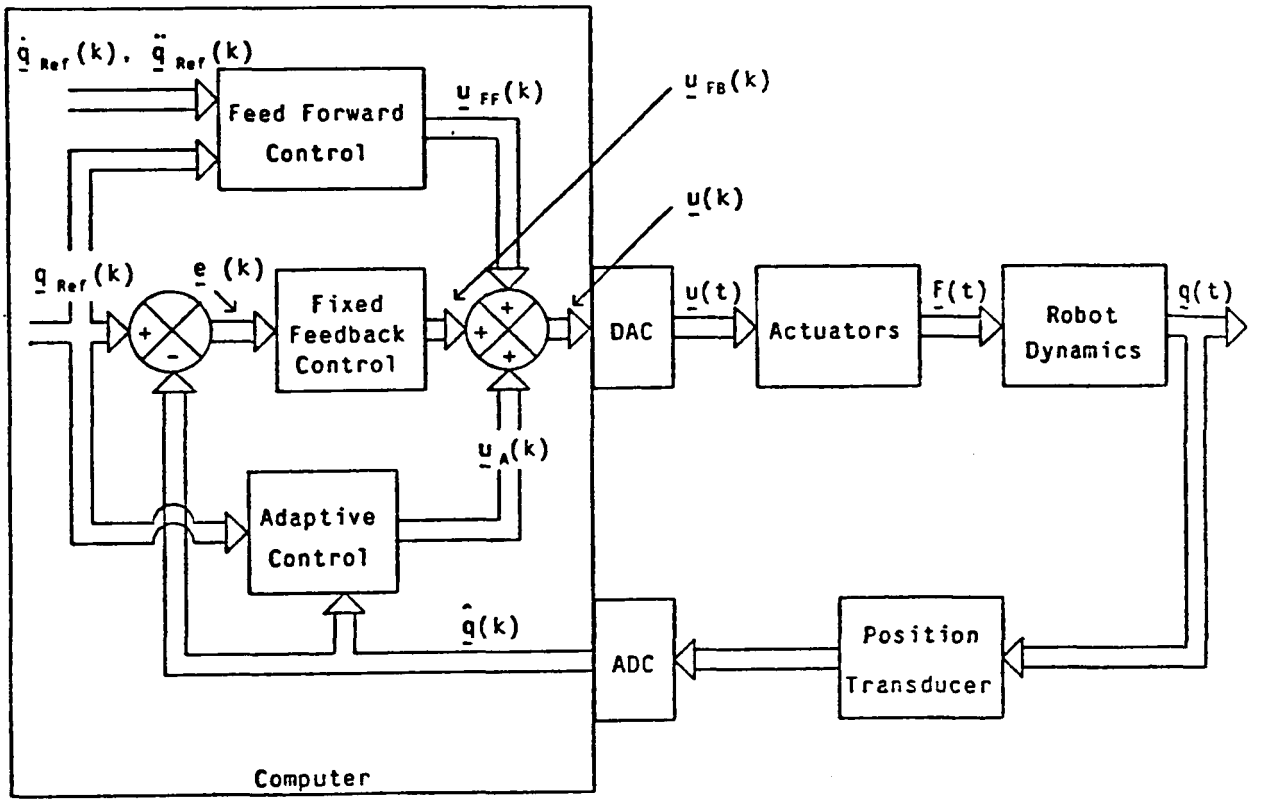

Figure 2-2: Robot Control Block Diagram

2.3.1.1. Feed-Forward Open-Loop Control

In feed-forward open-loop control, the reference signals are specified as a sequence of joint position, velocity and acceleration values $\{\underline{q}_{ref}(k), \dot{\underline{q}}_{ref}(k), \ddot{\underline{q}}_{ref}(k)\}$. Feed-forward open-loop controllers use the nonlinear dynamic equations of motion to compute the joint torques or forces, $\underline{F}(k)$, to track the reference signals. (In practice the dynamic equations include the actuator dynamics so that $\underline{u}(k)$ is computed). Since this method supplies a direct solution to these equations, it has the advantage of precision tracking of the reference commands. It has, however, three significant disadvantages. First, this open-loop controller is sensitive to parameter variations in the actuators, robot, and DAC converters, and to unmeasurable external torque or force disturbances. Second, this technique is computationally intensive. The on-line computational complexity can constrain the sampling interval, T, thus limiting the maximum allowed joint velocities. While the Lagrange-Euler approach is simple and systematic, it is inefficient for on-line computation and control. More efficient algorithms for on-line computation are available. These include recursive Newton-Euler formulations [Lee

82b, Luh 80], recursive Lagrangian formulations [Hollerbach 80], and table look-up methods [Raibert 78, Albus 75]. Finally the computed torques are only as accurate as the model in (2.3). Uncertainties in the model parameters, including the payload, and phenomena which are difficult to model, such as backlash, Coulomb friction, voltage offsets, and link-compliance, will introduce deviations from the reference signals. The relative mechanical simplicity of the CMU Direct-Drive Arm is an attempt to reduce such uncertainty [Asada 82].

To compensate for tracking errors due to imprecise models and controller sensitivity to parameter variation and uncertainty, these controllers can be augmented by conventional linear feedback controllers.

2.3.1.2. Fixed Linear Servo Control

Linear feedback or servo controllers compute control signals from the servo errors, including both position errors $\underline{e}(k)$ and velocity errors. In fixed control, the controller gains are constant.

In fixed controller design synthesis, it is assumed that the robot dynamics are time-invariant or can be linearized about a nominal operating point or trajectory. Upon examination of the dynamic equations (2.3), the robot can be assumed to have linear dynamics if the Coriolis-centrifugal terms are neglected, and if the interial matrix and gravitational torques are constant. When the Coriolis-centrifugal torque components are neglected, they can be viewed as external torque disturbances which must be rejected by the feedback control compensation. At low operating speeds, the magnitude of these apparent disturbances are often assumed to be small. However, the relative contribution of these terms may still be significant during typical movements at low velocities. If the actuators are coupled to the joints by gear-reducing mechanisms, then the Coriolis-centrifugal forces reflected back to the actuator are reduced by the gear ratio. In present industrial manipulators, gearing is used to optimize power transfer from the motor to the link, and minimize the required motor size. Gravitational forces reflected back to the motor are divided by the gear ratio and reflected link inertias are reduced by a factor of the gear ratio squared. Thus, apparent variations in the inertial and gravitational forces are reduced. Under the assumptions that Coriolis-centrifugal torques are neglected, and inertial and gravitational changes remain small, the control engineer designs a fixed controller using methods derived from classical and modern control engineering. Ideally, the fixed control design is insensitive to small parameter variations and small external torque disturbance sources. In practice, it is a formedable engineering task to design a robust fixed controller for such systems.

Feedback controller designs can either be uncoupled or coupled. Coupled, or multi-input multi-output (MIMO), control laws derive $u_i(k)$ as a linear combination of the entire reference and feedback vectors. Independent uncoupled, or single-input single-output (SISO), controllers produce $u_i(k)$ based only on the ith reference and feedback signals (i.e., $e_i(k)$). For an n DOF robot, n independent SISO controllers are used. There are no systematic rules for design of SISO controllers for coupled systems. MIMO control design is more straightforward, and can, in theory, achieve a larger degree of dynamic uncoupling than SISO control. However, SISO controllers facilitate implementation because they are:

1. Computationally less complex than a coupled controller;

2. Modular, and computation can be distributed; and

3. Simpler to tune than a coupled controller.

Commercially available industrial robots use SISO controllers. To the best of the authors knowledge, most use SISO control which is not augmented by feedforward control, because of gearing and their lower speed and tracking precision requirements.

A typical linear SISO controller is the Proportional + Summation + Difference (PSD) regulator derived as

$$u_i(k) = K_P e_i(k) + K_S \sum_{i=1}^{k} e_i(k) + K_D[e_i(k) - e_i(k-1)]$$

Fixed controller gains are selected using root-locus or frequency response techniques [Williams 83] (and ultimately manually tuned) to achieve an acceptable trade-off between transient speed of response and steady-state velocity errors to ramp inputs. The gain selection process is based be on a nominal robot configuration and neglecting inertial coupling. It has been suggested that improved performance results if a gain-scheduling approach is utilized, where the adjustable fixed gains are selected as a function of the robot configuration [Paul 81].

Relative to feedforward control, fixed linear controllers have the advantages of being simpler to implement in real-time and can be less sensitive to parameter variations and uncertainty. Fixed controllers cannot achieve adequate dynamic response at higher speeds, and over a broad range of arm configurations.

2.3.1.3. Adaptive Feedback Control

Recently researchers have sought a controller approach which can compensate for parameter uncertainty and variation over a wide range, while operating at high joint speeds. In addition, the controller should be compatible with microprocessor implementation to make it a feasible solution for common industrial application. To this end, initial research has been conducted, based on computer simulations, into the application of adaptive control to robotic manipulators [Chung 82, Dubowsky 79, Horowitz 80, Koivo 80, Koivo 83, LeBorgne 81]. While adaptive control theory has been in existence for twenty years, high speed digital computing has now made it a viable option for on-line robotic control applications. Adaptive controllers have adjustable gains which are automatically tuned, on-line, based on measurement of system performance and/or characteristics. Modern approaches to adaptive control [Goodwin 84] can be categorized as either

1. Self-Tuning Regulators (STR) [Astrom 77], or

2. Model Reference Adaptive Control (MRAC) [Landau 79].

Both approaches derive linear models of the manipulator, whose inadequacies are compensated by permanent parameter adaptation [LeBorgne 81]. While both STR and MRAC approaches lead to similar algorithms [Shah 80], the MRAC approach provides a simple and flexible means of specifying closed-loop system performance. STR and MRAC configuration block diagrams are shown in Figures 2-3 and 2-4. STR's derive a linear controller, whose gains are a function of identified robot parameters, under the assumption that the robot is linear and constant, but has unknown parameters. An on-line identifier estimates parameters of an equivalent input/output (I/O) linear model of the robot based on the I/O information vectors $\underline{u}(k)$ and $\underline{q}(k)$. An equivalent I/O model predicts the output $\underline{q}(k)$ from past and present I/O information independent of the physical model of the robot. The estimated parameter values are then used in the linear controller as though they where the actual parameters. Both SISO and MIMO equivalent model formulations can be used. Neuman and Stone [Neuman 83] have justified the latter modeling approach by demonstrating that individual joints of a coupled and nonlinear robot can be modeled by linear time-varying second-order SISO transfer functions. They show that the transfer function parameters vary smoothly in the work space as a function of the joint positions, velocities, and accelerations.

In MRAC control, the reference model output $\underline{q}^R(k)$ specifies a stable and realizable closed-loop dynamic response of the the output $\underline{q}(k)$ to the reference signal $\underline{q}_{Ref}(k)$. The difference between the reference model output and the process is called the full-parallel (FP) output error:

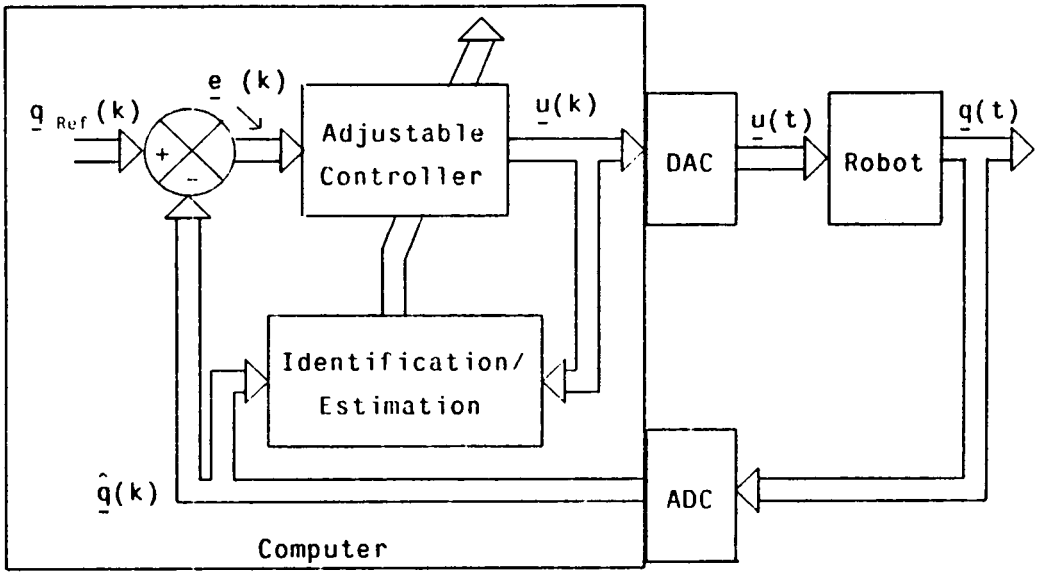

Figure 2-3: Self-Tuning Regulator

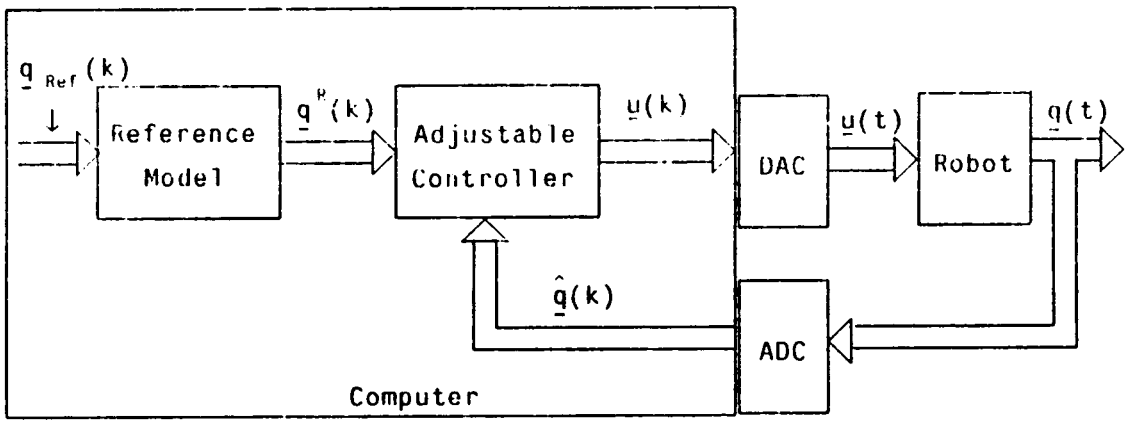

Figure 2-4: Model Reference Adaptive Control

$$\underline{e}_o^{FP}(k) = \underline{q}^R(k) - \underline{q}(k).$$

The adjustable controller utilizes I/O information to adjust the gains on-line to drive the FP error to zero, thus forcing the robot output to track the reference signal in accordance with the performance specified by the model. Within the framework of robot control, two methods have been applied [LeBorgne 81]:

1. Identification-error method, and

2. Output-error method

In the identification-error method (which is developed in detail in Chapter 4), an identifier predicts the robot joint outputs, $\underline{t}(k)$, based upon parameter estimates of an equivalent linear I/O model. The identification error

$$\underline{e}_{ID}(k) = \underline{q}(k) - \underline{t}(k)$$

drives the adjustment mechanism which updates the estimates of the equivalent parameters. These estimates are then used to adjust the gains of a linear controller which is driven by the model output. In the output-error method, the FP error drives an adjustment mechanism which directly adjusts the controller gains. From a physical implementation point-of-view, the identification error approach has the advantage that the adjustment mechanism need not be turned off during control signal saturation [Morris 79].

The adjustment mechanisms of STR or MRAC controllers can be designed from either parametric optimization or stability viewpoints. Parametric optimization techniques include recursive least squares (RLS) and gradient (or "steepest-descent") methods. The stability approaches derive adjustment mechanisms using stability theory to assure that the identification errors are asymptotically stable. Since the adjustment mechanisms are nonlinear, either Popov's hyperstabilty or Lyapunov's stability criteria have been used. Both the optimization and stability approaches make the assumption that the system under control is linear and time-invariant (or slowly time-varying).

For the optimization approach, stability analysis of the over-all closed-loop system is demonstrated through the theory of stochastic convergence of optimization mechanisms [Astrom 77]. When hyperstabilty or Lyapunov mechanisms are used, stability of the identification error is related directly to the FP error. Beacuse of the assumptions of linearity and time-invariance, stability of adaptive controllers applied to nonlinear and time-varying robot dynamics has not been proven, and it remains an open question as to whether it can. Control engineers rely on ad-hoc assumptions that fast adaptation speeds and the ability to model the robot as an equivalent time-varying linear system will lead to stable systems.

STRs and MRACs can be formulated as either SISO or MIMO controllers, depending whether the robot is modeled as an equivalent SISO or a MIMO system. The adaptive controllers can be used independently or augmented by feedforward control. When used independently, minimal a'priori knowledge of the dynamics is required.

STRs applied to multi-DOF manipulators have been reported to control arm simulations over a wide range of speeds and configurations [Chung 82, Koivo 80, Koivo 83, LeBorgne 81].

Koivo and Guo [Koivo 83] applied both coupled and uncoupled STRs (using RLS) to control a 6 DOF arm. They observed that the MIMO algorithm required a longer time to converge and, at least in the simulated trajectories, they showed no improvement in response relative to the SISO controllers. LeBorgne [LeBorgne 81] applied SISO STRs and output error MRACs (using a RLS adjustment mechanism) to control of a 3 DOF arm, and found that the STR was computationally less complex, but that the MRAC showed better overall performance. Chung and Lee [Chung 82] use feedforward control augmented by an RLS STR. In this approach the dynamic robot model is linearized about a nominal trajectory to obtain a small-signal perturbation model. The adaptive controller then identifies a small-signal model and drives the perturbations to zero.

Successful simulation results of MRAC control have also been reported [Dubowsky 79, Horowitz 80, LeBorgne 81]. Le Borgne [LeBorgne 81] applied SISO identification error and output error methods (using RLS adjustment mechanisms) and observed that the identification error approach displayed better overall performance. Neuman and Morris [Neuman 80, Neuman 79b] performed extensive analysis and evaluation of uncoupled MRAC applied to linear SISO plants, with emphasis on implementation and computational complexities. They suggest that these uncoupled algorithms can also be applied to robotic control [Morris 81]. Enhancements to the basic MRAC algorithm are included to reduce the effects of controller saturation and measurement noise. Added stability constraints limit the adjustable controller gains to assure a bounded and stable controller. They conclude that an enhanced identification-error MRAC, with a hyperstable adjustment mechanism, produce the best results with respect to convergence speeds, noise supression, recovery from control signal saturation, estimated parameter accuracy, and propagation delays [Morris 81].

2.3.2. Kinematic Control

Robotic positioning tasks require that the end-effector move between specified points in space, and along specified paths and trajectories. This kinematic control problem can be separated from the dynamic control problem if it can be assumed that the joint level controllers can assure reference signal tracking. Other approaches, including optimal and adaptive control, combined the kinematic and dynamic control problem. Kahn and Roth [Kahn 71] address the near-minimum-time optimal control problem for a nominal trajectory. This and other optimization techniques are still too complex to be practical. More recently, it as been suggested to extend joint level adaptive controllers to world-level

tracking [Koivo 83, Takegaki 81]. Measurement of the world level positions must still be predicted by the direct kinematic solution. Takegaki [Takegaki 81] has reported effective performnace of an output-error type controller in initial simulation studies. In practice, the kinematic problem is still considered to be independent of robot dynamics.

End-points and paths for the end-effector can be specified in three ways:

1. Teach-mode[1] (points defined at joint-level);

2. Pre-defined task (points generally defined in world space); and

3. On-line decisions (information supplied by external sensors, and points defined in world space).

Points defined in world space must first be mapped into joint space using the "arm-solution". Control of the world reference signal $\underline{X}_{ref}(k)$ is depicted in Figure 2-5, where the closed-loop block represents the joint-level control system depicted in Figure 2-2.

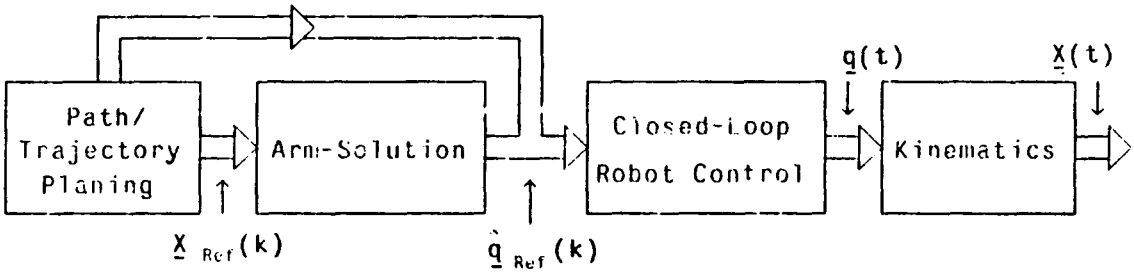

Figure 2-5: Open-Loop Kinematic Control

If the end-effector, or tool, is referenced to the final link by T_{tool}, then the arm-solution must evaluate T_6 according to

$$T_{6\text{-}ref}(k) = T_{tool}^{-1}\, H[\underline{X}_{ref}(k)]$$

The resultant joint level reference signal, $\hat{\underline{q}}_{ref}(k)$, is an estimate due to any of the aforementioned inaccuracies in the "arm-solution." In real systems, there is no way to determine the final positioning error since no measurement or feedback of final end-effector position is available. In this sense, the control loop is never closed around the end-effector postion itself leading to inherent limitations in the ability of such a system to compensate for

[1]The "teach-mode" operation, for programing industrial robots, includes manually guiding the manipulator to desired locations and recording the joint positions at each point. The stored points can then be used to derive the reference signals.

inaccurate modeling of the arm or to derive positioning error signals relative to unstructured environments.

The time-amplitude profile of the reference signal dictates end-effector path motion between task points. For example, when a well-defined path is required (e.g., to avoid obstacles), straight-line motion is specified. The points on a straight-line (including orientations) are mapped into joint level commands via the arm-solution. To compensate for speed limitations in computing the "arm-solution", linear interpolation of the resultant joint positions are used to supply intermediate points. When the task requires that the robot cannot stop between end-points of a path (e.g., welding), trajectory control deals with specification of smooth transitions between path segments. One approach is spline function fitting [Paul 81] to the endpoints of adjacent path segments.

2.3.2.1. Incremental Motion Control

Robotic tasks often require the end-effector to move by increments, $\Delta \underline{X}_{tool}$, rather than to absolute positions. If an absolute positioning control system is used, then the "arm-solution" must evaluate $T_{6\text{-}ref}$ according to

$$\hat{T}_{6\text{-}ref}(k) = \hat{T}_6(k)\, T_{tool}\, T_{inc}(k)\, T_{tool}^{-1}$$

where $T_6(k)$ is the estimated present position transformation based on the direct kinematic solution, and $T_{inc} \doteq H[\Delta X_{inc}]$.

A more efficient approach to incremental motion is resolved-rate-motion (RRM) control [Whitney 72]. In this approach the inverse arm Jacobian is used to find the incremental joint velocities which are required to achieve motion in the specified directions. If the direct kinematic solution, K, maps $\underline{q}$ into $\underline{X}$ according to $\underline{X} = K(\underline{q})$, where K can be derived from T_6, then the arm Jacobian, J_{arm}, is defined by

$$J_{arm} \doteq \frac{\partial K(\underline{q})}{\partial \underline{q}} \tag{2.5}$$

World increments are then related to joint increments according to

$$\delta \underline{X} = J_{arm}\, \delta \underline{q}$$

and the joint increments are

$$\delta \underline{q} = J_{arm}^{-1}\, \delta \underline{X}$$

These joint increments then drive closed-loop velocity servo mechanisms.

An incremental robot system, using either the direct "arm-solution" or the RPM approach, is

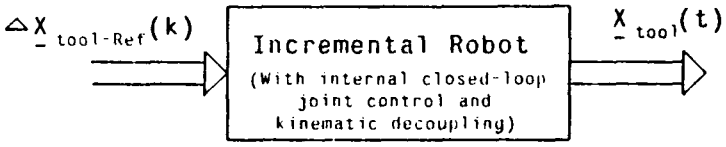

Figure 2-6: Incremental Robot System

represented by the block in Figure 2-6 for reference in Section 2.4. The system in Figure 2-6 includes internal joint level feedback and kinematic decoupling. Such a system is ideally linear uncoupled, without discrete time delays; i.e., each DOF can be represented by a transfer function of the form

$$\frac{\Delta X(s)_{tool\text{-}i}}{X(s)_{tool\text{-}Ref\text{-}i}} = \frac{K}{s(\tau s + 1)}$$

The next section extends dynamic robot control to closed-loop control of world-space coordinates.

2.4. Visual Servo Control Structures

Research in computerized vision for automation is directed toward fast systems which can interpret image features for

- Object recognition [Myers 80, Fu 82, Vuylsteke 81];
- Inspection [Jarvis 80, Porter 80]; and
- Measurement of object positions relative to the vision transducer, or relative positions between objects [Hall 82, Tani 77, Birk 79, Agin 79].

Such capabilities may be combined into more general modes of scene interpretation. Complete functional systems are not yet available. If such a system were used in conjunction with a robotic system, then direct world space measurements of relative end-effector positions could be achieved. For example, the vision transducer can be fixed to the end-effector and move with the manipulator as it observes an object's pose relative to itself [Agin 79]; or equivalently, it can be stationary while observing the relative pose between an end-effector and object [Ward 79]. Also, the transducer can be stationary while observing the relative pose between itself, or equivalently the world, and an object being manipulated or the end-effector itself [Birk 79]. These integrated systems have the potential for improving robot accuracy, and extend the robot's capability to operate in unstructured environments containing objects which can be in random poses or possibly moving.

When vision systems are integrated with robots, the measurement space is extended to include relative the end-effector pose. Positioning control systems, which directly utilize such measurements, can be synthesized using visual feedback [Sanderson 83a]. The resulting visual servo system is depicted in Figure 2-7, where $\underline{\mathcal{T}}_{ref}$ and $\underline{\mathcal{T}}$ represent the reference and feedback signals.

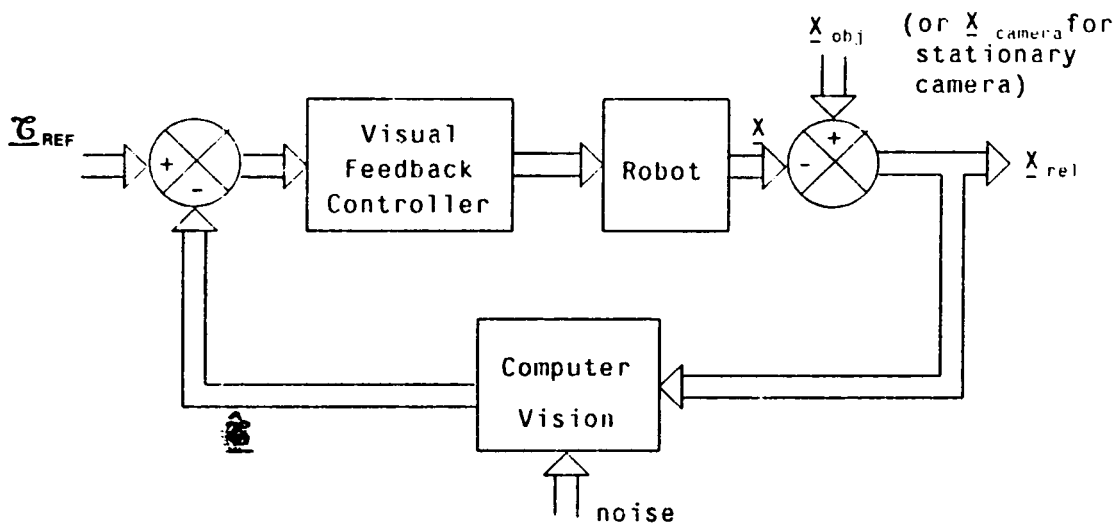

Figure 2-7: Robotic Visual Servo Control

The role of computer vision as the measurement process affects the overall system dynamics, and a visual feedback controller is required. The linearity, noise properties, coupling, and computational delays of this measurement process become essential considerations for controller design. Formal analysis and design of feedback controllers for visual servoing, in terms of well-defined control theory, has not appeared in literature except for a simple case [Coulon 83]. Visual servo controllers have been designed using ad-hoc strategies [Agin 79]. In this section, the dissertation contributes to the basic understanding of visual servo control by organizing previously implemented and proposed visual servo control strategies into clearly defined control structures. It is shown, in Sections 2.4.2 and 2.4.3, that the task reference signal, $\underline{\mathcal{T}}_{ref}$, and feedback signal, $\underline{\mathcal{T}}$, can be based on either image feature space or position space measurements. The robot under control can be either open-loop (i.e, without joint level feedback - Figure 2-1), or an incremental system (i.e., with internal joint level feedback, and kinematic decoupling - Figure 2-6). The formalization of visual servo control structures is based on these feedback signal and robot categorizations. The formalization clarifies the requirements placed on the visual servo controller, and facilitates the design process. In Section 2.5, a controller design for image-based structures is proposed. The

formalization also provides a framework for evaluating different visual servo control structures. It is beyond the scope of this dissertation to make such comparative evaulation.

The characteristics of a general vision system are reviewed in the next section. The objective of the dissertation does not include presention or proposal of a detailed design for such a system.

2.4.1. Computer Vision

A computer based vision system is represented in Figure 2-8.

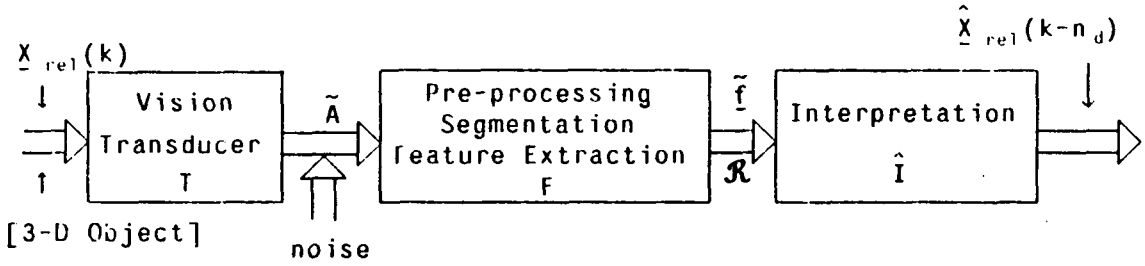

Figure 2-8: Computer Based Vision System

Vision transducers typically include vidicons, charge coupled devices (CCD), photosensitive diode arrays, and structured fiber optic sensors [Agrawal 83]. The transducer produces a 2-dimensional array, $\tilde{\mathbf{A}}$, of light intensities. The array can be distorted from an ideal image, **A**, due to:

- Transducer resolution;
- Transducer nonlinearities such as optical aberrations and out of being focus;
- Background lighting conditions; and
- Electronic noise and drift.

The transduction process can have time-dependent dynamics such as the persistence effects associated with CCD and vidicon devices. At slower sampling rates these effects can be neglected [Coulon 83].

The image is preprocessed by filtering operations to enhance image quality. The enhanced image is then segmented into connected regions. A one-dimensional feature vector, $\tilde{\underline{f}}$, or a relational feature description, $\mathfrak{R}$, which describe segmented regions of the image are then extracted. Features include areas, angles, center-of-gravity, and intensities. Feature

extractors are typically digital computer algorithms. High-speed optical processors can also be used for preprocessing, segmentation, and feature extraction [Merkle 83, Stermer 83].

Feature space representations must be interpreted (signified by $\hat{I}$ in Figure 2-8) to recognize both the object and its pose $\hat{\underline{X}}_{rel}(k-n_d)$. Interpretation is based on 3-dimensional models of the object and transduction process, and can include statistical modeling considerations. Transduction noise and modeling inaccuracies can degrade the estimate. The interpretation process can be facilitated by operating within structured lighting environments [Agin 79]. The measurement delay, n_dT, which is the total time required to acquire, process, extract, and interpret the image, can vary over wide ranges depending on the complexity of the image. High-speed feature extractors (33-100 msec) for simple structured images have been built or proposed [Bracho 82, Vuylsteke 81] and systems which can operate on more complex scenes can be envisioned using optical processors [Merkle 83]. Additionally, special purpose optical proximity sensors have been constructed which can measure positions and orientations of a plane in about 1 msec [Kanade 83].

Visual control structures, based on both image feature space and position space measurements, will now be described. Control structures can be categorized as either position-based or image-based. This formalization was first introduced by Sanderson and Weiss [Sanderson 82]. While individual structures are described as autonomous processes, the possibility of a complete system implementation which uses combinations and augmentations of these structures is a viable concept.

2.4.2. Position Based Visual Control Structures

Position-based control structures define task reference signals in world space position coordinates. The image interpretation step provides feedback by producing position estimates whose expectations are generally linearly related to actual positions.

2.4.2.1. Static Position Based "Look and Move"

The static position based "look and move" structure (Figure 2-9) is used most often in present industrial applications [Tani 77, Birk 79, Kashioka 77]. In the "look" stage, the vision system estimates the object pose. The control computer calculates the error, $\Delta\underline{X}$, between a reference and the measured pose. A "move" by the incremental error command is then issued to an incremental robot system. In this structure, the incremental robot system only accepts new commands after it has completed the previous commanded motion. This

characteristic is typical of commercially available robots where the programmer can only access higher level control functions. The control operation is sequential and asynchronous, and the sequence is repeated until $\Delta \underline{X}$ is within specified tolerance bounds.

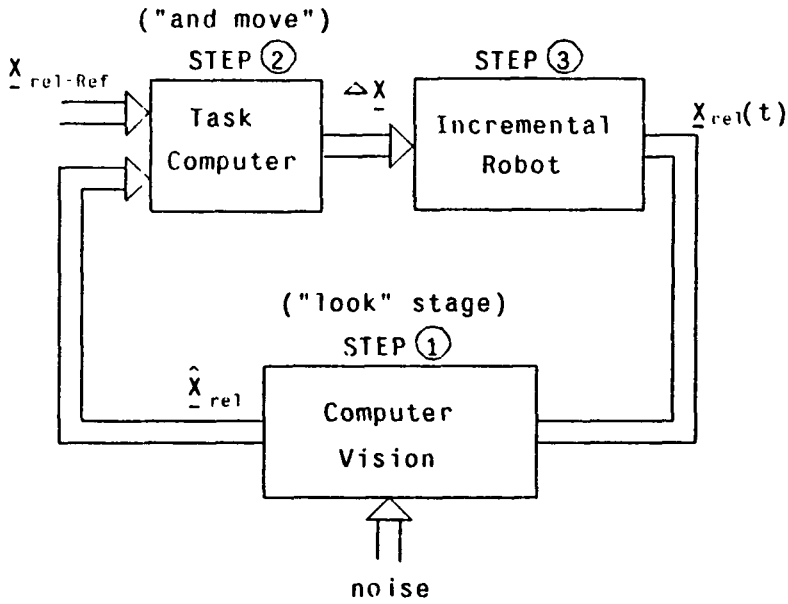

Figure 2-9: Static Position-Based "Look & Move"

When the camera is attached to the robot end-effector (according to the transformation T_{cam}), then $\underline{X}_{rel}$ becomes the relative position between the camera and object. In this case the tool transform is assigned according to:

$$T_{tool} \leftarrow T_{cam}$$

When the camera is stationary, T_{tool} can be either the position of the end-effector tool mounting or the object held by the manipulator.

The static "look and move" structure is not a dynamic closed-loop control system because each operation is performed sequentially and independently. Thus, the dynamics of each operation does not affect the overall system. No additional control law, except that used by the robot, is required. The resulting control system is slow, unable to track moving objects, and may require many iterations to achieve desired accuracy. Implementations of these structures have demonstrated the basic concept of interactive sensing.

2.4.2.2. Dynamic Position-Based "Look and Move"

In the static "look and move" structure, the reference signal to the robot can be updated only after the robot has reached a previously commanded goal. When the robot system is designed so that command inputs can be synchronously updated, independent of the robot's position and velocity (i.e., robot can be moving), then the "look and move" structure can be configured as a dynamic closed-loop sampled data system (Figure 2-10).

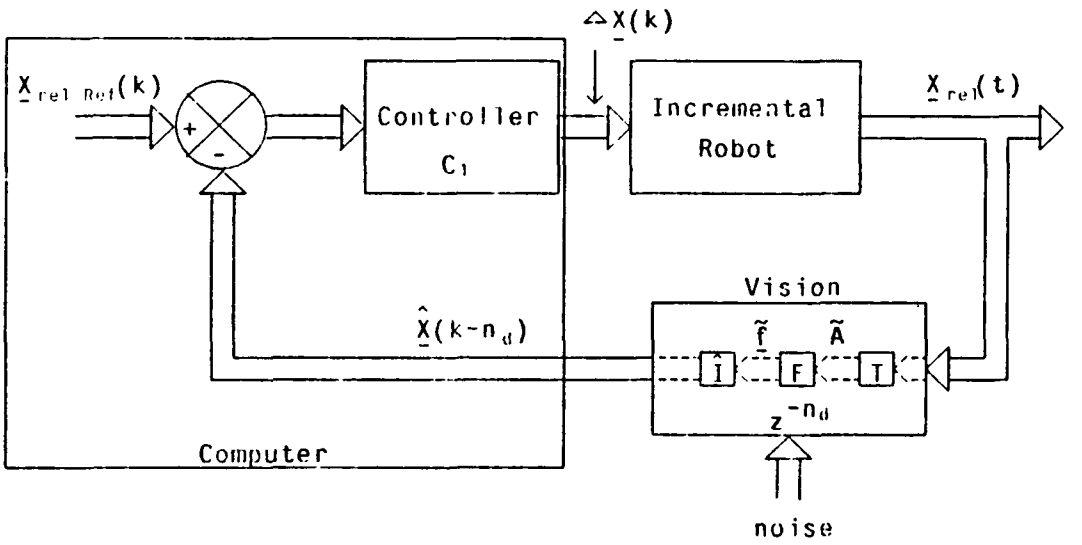

Figure 2-10: Dynamic Position-Based "Look & Move"

The closed-loop visual servo system requires a feedback controller, C_1, to compensate for system dynamics, with the added complexity presented by feedback delays and measurement noise. For applications requiring tracking of moving objects, prediction algorithms have been studied [Hunt 82] to improve system steady-state performance. When the vision system is viewed as a single process, then $n_d = 1$ (where n_d is the number of discrete feedback delays) and the sampling period is chosen to be the net time required by the individual vision processes. Alternatively, shorter intervals can be chosen by considering the vision system as a pipe-line of the individual processes. In this case, $n_d > 1$ and the time interval is determined by the maximum individual vision component processing time. From a control viewpoint, systems become more difficult to control with added delays, even if the sampling period is reduced. Sampling periods of 100 ms have been suggested as being sufficient for visual servo control; shorter sampling periods would be required for high-speed control.

Agin [Agin 79] was the first to implement dynamic visual control of a multi-DOF manipulator.

The camera was mounted to the end-effector and interpretation was facilitated by the use of structured light-striping techniques. Simple proportional controllers, sampling at between 150 to 500 msec, were manually tuned to achieve the desired response. Control system analysis did not accompany these experimnts. Geschke [Geschke 82], who has implemented similar multi-DOF visual servoing experiments, at 100 ms sampling periods, noted that the independent closed-loop joint-level robot servo controllers required high damping at these sampling periods, supposedly to avoid exciting structural resonances. Other examples of dynamic control are reported in [Albus 81] and [Ward 79]. To the best of the author's knowledge, the only reported research which uses control system analysis to design a dynamic visual servoing system is presented by Coulon [Coulon 83]. In this research, a fixed proportional + summation controller is designed for single-DOF linear system.

2.4.2.3. Position Based Visual Servoing

Since visual sensors provide direct world space information, and thus world space servo errors, it should be possible to control the open-loop robot dynamics and kinematics directly and eliminate the "arm-solution" or Jacobian required by the "move" commands to a closed-loop robot positioning system This configuration is termed Position-Based Visual Servoing (Figure 2-11).

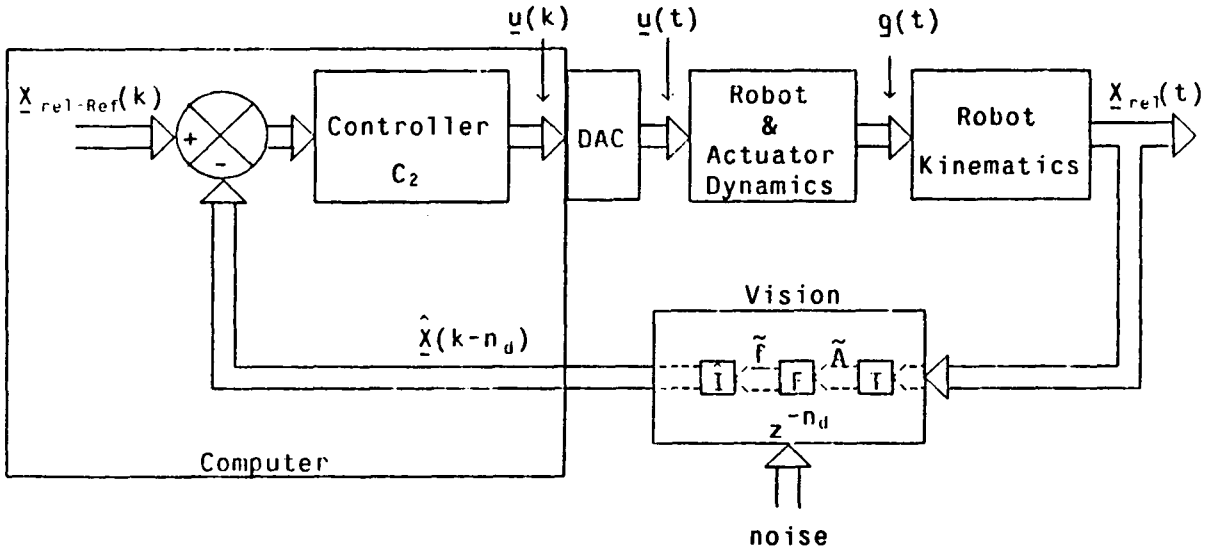

Figure 2-11: Position-Based Visual Servoing

This configuration may have potential advantages including:

1. Elimination of added computational delays, required by the "arm-solution" evaluation period, which detract from relative stability;

2. Elimination of "arm-solution" inaccuracies; and

3. Increased efficiency, since the "arm-solution" does not have to be evaluated, and independent joint controllers are not required. However, the sampling period dictated by the vision system may be too long to control the robot, depending upon the robot's dynamic and mechanical properties. In these cases, independent joint-level velocity feedback controllers, which operate at higher sampling rates, can be used. These cases are discussed in Chapters 3 and 8.

In addition to measurement delays and noise, the visual feedback controller, C_2, must compensate for possibly nonlinear and coupled robot dynamics and kinematics.

Implementions or simulations of this structure have not appeared in literature, in relationship to visual servo control. While Koivo [Koivo 81] and Takegaki [Takegaki 81] did not mention visual servoing , they did propose adaptive feedback controllers for combined dynamic and kinematic control. They assumed that the world coordinate position of the end-effector, as predicted by a direct kinematic solution, could be used as the feedback signals, but they did not consider measurement delays. Takegaki reported "effective" control with this approach in limited simulations of an output-error type controller using a Lyapunov adjustment mechanism.

2.4.3. Imaged Based Visual Control Structures

In the position-based approaches, the image interpretation step can be complex and affect control system design and performance by

1. Adding additional time delays, and

2. Introducing measurement noise resulting from inaccuracies of the object and transduction modeling.

As discussed in the remainder of this chapter, image features are often continuous functions of object position, and for fixed ranges of control, could provide sufficient information for robot control without carrying out the interpretation process. Thus, the continuity of feature representations of time-varying imagery can lead to potential simplifications of the control strategy including task training by a "teach-by-showing" operation.

2.4.3.1. Dynamic Image-Based "Look and Move"

The feedback path of the dynamic position-based "look and move" structure (i.e, the vision measurement system in Figure 2-8) can be decomposed into two nonlinear transformations. The transduction and feature extraction functions, or world-to-feature space transformation, can be viewed as the inverse of an ideal interpretation, in the absence of noise, according to:

$$\underline{f} = I^{-1}[\underline{X}_{rel}]$$

where I is "ideal" in the sense of being based on exact models. The feedback path is then mapped to world space by the interpretation transformation:

$$\hat{\underline{X}}_{rel} = \hat{I}[\underline{f}]$$

If the ideal interpretation has a unique inverse mapping, over the control region of interest, such that $\underline{X}_{rel}$ are single-valued functions of $\underline{f}$, then this suggests that the system can be controlled, to unique end-points, using $\underline{f}(k)$ directly as the feedback and reference signals, thus eliminating the interpretation step. This condition must also be satisfied for achieving unique solutions with the position-based approaches. The uniqueness condition is satisfied, for the control region of interest, when [Wylie 61]:

1. The first partial derivatives of $\underline{f}$ are continuous, and

2. If the Jacobian of the ideal inverse interpretation is nonsingular; i.e.,

$$\det \frac{\partial I^{-1}[\underline{X}_{rel}]}{\partial \underline{X}_{rel}} \doteq \det[J_{feat}] \neq 0 \tag{2.6}$$

where J_{feat} is defined as the feature sensitivity matrix.

In practice, J_{feat} could be measured on-line to test the condition in (2.6). This condition must be true for both position and image-based approaches. Since the dissertation does not directly address the imaging problem, features which are unique will be chosen. Further, since the determinant is only defined for square matrices, then the permitted number of degrees-of-freedom must equal the number of measured features.

The dynamic image-based "look and move" structure, shown in Figure 2-12, which uses feature feedback, was first proposed by Sanderson and Weiss [Sanderson 82]. In addition to compensating for robot dynamics, measurement noise, and feedback delays, the feedback controller, C_3 must also compensate for the nonlinear and coupled feature transformations.

Reference signals, $\underline{f}_{ref}(k)$, must now be defined in feature-space. The task could first be defined in world space, $\underline{X}_{rel\text{-}ref}$, and then mapped into $\underline{f}_{ref}$ according to an idealized inverse interpretation. Equivalently, if $J_{feat}(\underline{X}_{rel})$ is known, or can be measured, and the initial

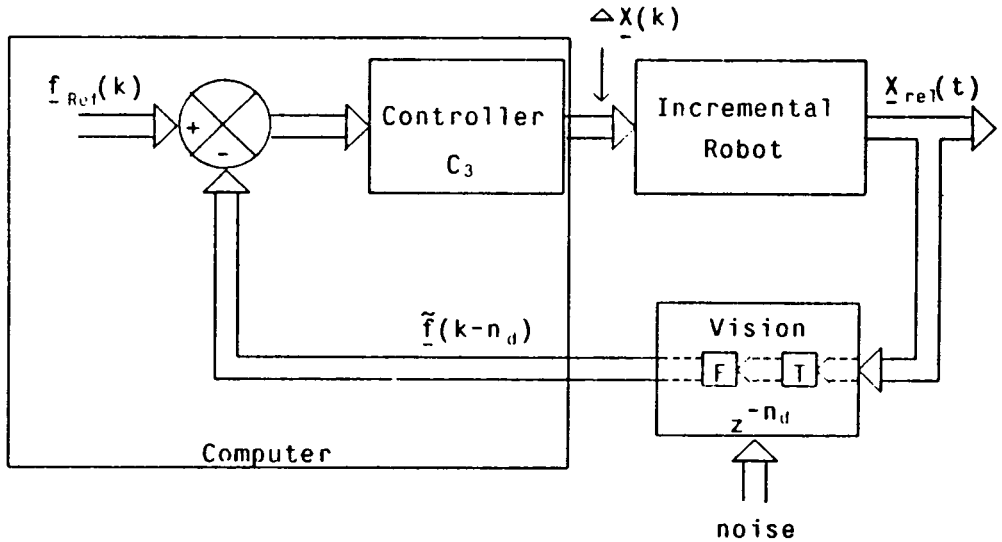

Figure 2-12: Dynamic Image-Based "Look & Move"

displacement $\underline{X}^{\circ}_{rel}$ is known, then the feature signal can be derived by evaluating the feature sensitivity matrix along $\underline{X}^{\circ}_{rel} + \delta\underline{X}_{rel\text{-}ref}$ according to

$$\delta\underline{f} = J_{feat}\delta\underline{X}_{rel}$$

Both approaches still require an interpretation step, but may have potential advantages by eliminating inaccuracies of the actual interpretation, in the feedback path, and by requiring smaller sampling periods as a result of the elimination of the feedback interpretation delay. Alternatively the reference signal could be defined directly in image feature space using a "teach-by showing" strategy whereby an image is transduced in the desired reference position and the corresponding extracted features represent the reference features. When the task is repetitive and the desired path or trajectory remains constant, the reference feature signals can be defined a'priori as a "moving" or time-varying image along the path. If the object is allowed to be in random poses, then only the final feature values can be defined a'priori. While the path cannot be directly specified, absolute positioning can still be achieved. The most useful applications of image-based systems might be for tasks requiring fast and accurate corrective motions, where exact path is not critical (e.g., for precision assembly including random part aquisition and parts alignment).

While path cannot be directly controlled with the IBVS "teach-by-showing" strategy, interesting relationships between predicted pathes (i.e., the path that would result if the control system achieved perfect tracking of the feature reference signals) and feature control are:

1. If the coupled feature sensitivity matrix J_{feat} is constant, and each feature is specified to have identical time responses, the predicted path is straight-line (Section 2.5.2.2).

2. For the 2 DOF system evaluated in Chapter 6, for which J_{feat} is coupled and varys dramatically over the trajectories, the predicted pathes are either straight-line, or approach straight-lines (Section 6.2.1.1).

3. For the 3 DOF system evaluated in Chapter 7, for which J_{feat} is also coupled and varys, the observed pathes are smooth (i.e., not tortuous), and approach straight-lines as features are selected which reduce system coupling. (The index of system coupling is described in Section 2.5.2.)

Such results are encouraging for future investigation of more general systems, and suggest that features may be found which can be used to achieve some degree of path control. As an alternative to path control, a path constraint strategy is proposed in Section 2.5, and evaluated in Chapters 6 and 7.

The "teach-by-showing" approach presents additional requirements for controller design. This approach assumes that the inverse transformation f^{-1} is unknown. Therefore, the controller C_3 must be based on a design approach which not only compensates for the nonlinear and coupled properties of f^{-1}, but also for unknown values. These control requirements are discussed in detail in Section 2.5, along with the issue of selection process. That is, how should a subset of n features be selected for control from a set of m extracted image features f_i (i = 1....n), where m>n?

In any of the visual based control structures, some a'priori knowledge of object geometry may be required for feature identification and a level of interpretation may be required for object recognition. In many industrial vision applications, identification and recognition is based on the "teach-by-showing" principle using statistical feature information generated by image training sets. Other approaches may only require qualitative and relational information for identification and recognition. Thus, detailed a'priori modeling would not be required at this level of vision processing.

2.4.3.2. Image-Based Visual Servoing

An image-based version of the position-based visual servoing structure can also be formulated by controlling the open-loop robot directly and eliminating the "arm-solution" [Sanderson 83a]. This approach is called image-based visual servoing (IBVS) (Figure 2-13). The physical variable under control, $\underline{q}(k)$, can be related to $\underline{f}(k)$ by

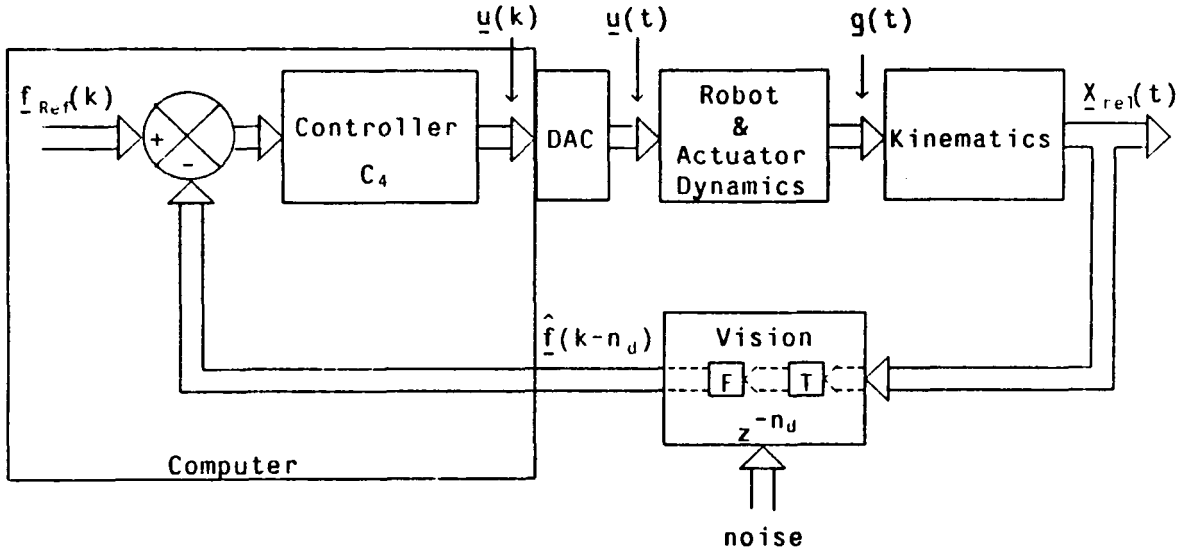

Figure 2-13: Image-Based Visual Servoing

$$\underline{f} = I^{-1}\left\{\underline{X}_{rel}\right\} = I^{-1}\left\{\underline{X}_{obj} - K(\underline{g})\right\} \doteq F(\underline{g}, \underline{X}_{obj}).$$

The feedback path is characterized by an overall small-signal sensitivity matrix J given by

$$J \doteq J_{feat}\, J_{arm} \tag{2.7}$$

where

$$J = \frac{\partial F}{\partial \underline{g}}$$

The IBVS approach is similar to the dynamic "look and move" structure except that the design of the feedback controller, C_4, is further complicated by having to compensate for any nonlinear and coupled robot dynamics and kinematics. In the "look and move" structures, the robot system is ideally linear and uncoupled, thus simplifying control system design.

The image-based structures are representative of sensor based control structures which include:

1. A measurement system which generates sensory information that is difficult to interpret;

2. A sensory feedback path which can be nonlinear, coupled, noisy, contain unknown parameters, and include delays; and

3. A robot under control which can be dynamically and kinematically nonlinear and coupled.

A control approach for image-based systems may then have potential for application to other

sensory modalities (e.g., touch and acoustic). Because of this potential and the novelty of this approach, the remainder of the dissertation is concerned with a detailed analysis, design and evaluation of "teach-by-showing" image-based systems. The "teach-by showing" approach is analogous to the basic robot control "teach-mode" operation. In the author's experience, the "teach-mode" strategy for robot task definition has greatly facilitated the incorporation of robots into the industrial environment by providing a simple means for task training. Similarly, the "teach-by showing" approach has the potential of simplifying applications of visual servoing.

2.5. Control Of Image-Based Systems

A control law approach for image-based control structures is presented in this section. Several characteristics of these structures, which are noted in Section 2.4, will present particular challenges for design of a suitable controller. These include:

1. Nonlinearities: dynamics (including actuator), kinematics, and feature-space transformations;

2. Unknown parameters: limited a'priori knowledge (e.g., in "teach-by-showing"). parameter variation and uncertainty,

3. Measurement delay;

4. Measurement noise;

5. Feature selection and assignment (the feature assignment process addresses issues in uncoupled control of coupled plants);

6. Path control: when tasks are specified directly in feature space; and

7. Tasks requiring tracking of moving objects.

The final aspect implies that, in designing the control system, a distinction is made between visual servoing applications where the object and camera are stationary versus moving in the steady-state. An example is the case of an object moving with velocity V which is tracked a by a system which does not include a prediction algorithm and has a unit feedback delay of T seconds. If the steady-state error between the reference and delayed feedback signals can be driven to zero, then an actual tracking error of VT remains. Steady-state servo errors can be made small with a sufficiently large bandwidth controller, but controller design trade-offs are usually made between transient response and steady-state errors. As T increases (due to vision processing constraints), the controller bandwidth is forced to be smaller. The steady-

state servo error and actual tracking error increase, and a prediction algorithm is required to reduce tracking errors. For tasks involving stationary objects, a controller can always be designed to reduce steady-state position errors to zero, irrespective of controller bandwidth or the use of prediction algorithms. For these applications, transient performance becomes the important design goal. As an initial step in understanding image-based control, prediction algorithms are not included in this dissertation and only tasks involving stationary steady-states are considered. Step input reference signals, defined by the "teach-by-showing" strategy, provide a suitable measure of system performance.

In this section, a control law approach is introduced, and the controller is designed in Chapter 3. The feature selection and assignment issues are addressed by defining a measure of feature transformation coupling. And, finally, methods for path constraint are suggested.

2.5.1. Control Approach

To design a controller, it is useful to consider small-signal models of the system. Small-signal models (about a nominal operating point or trajectory) of "look and move" and IBVS structures are represented in Figures 2-14 and 2-15, respectively.

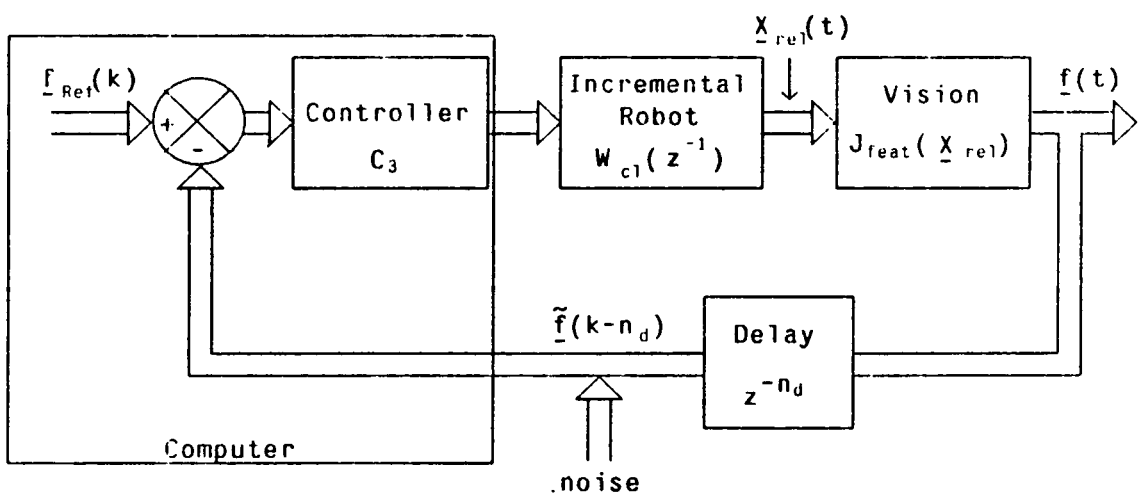

Figure 2-14: Small-Signal Image-Based "Look and Move"

In these figures, J_{feat} is defined in (2.6), and J_{arm} in (2.5). In Figure 2-15, J_{arm} is assigned a negative sign. Since

$$\underline{X}_{rel} = \underline{X}_{obj} - \underline{X}$$

then

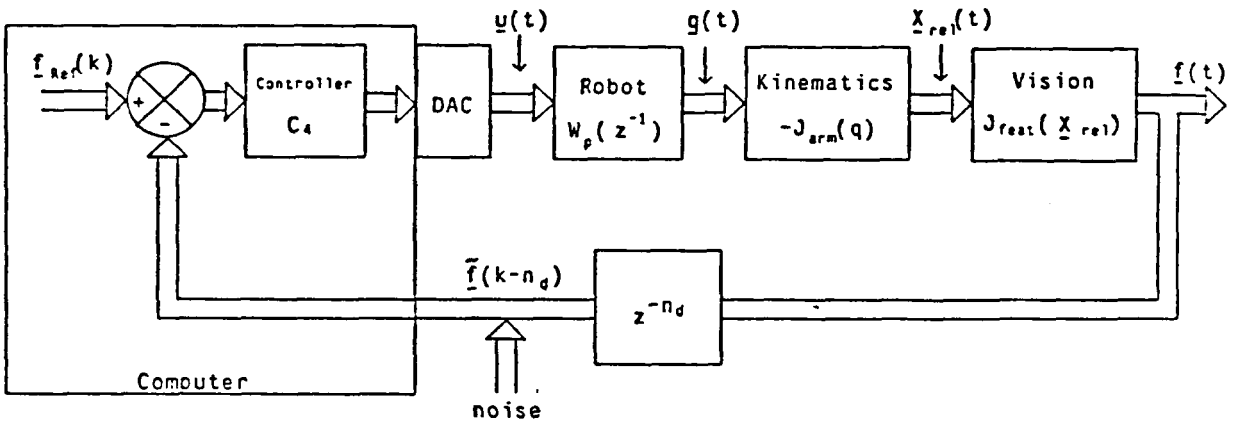

Figure 2-15: Small-Signal Image-Based Visual Servoing

$\delta \underline{X}_{rel} = -\delta \underline{X}$,

for a stationary object or camera. The system output is the undelayed feature, while the feedback path is modeled by discrete unit delays. The incremental robot system is $W_{CL}^{\cdot}(z^{-1})$ (Section 2.3.2.1). Linearized open-loop robot dynamics [Chung 82], or equivalent linear I/O modeles [Stone 84], are represented by $W_p(z^{-1})$. In addition to the control requirements of the robot dynamics, described in Sections 2.3 and 2.4, the design of the controller, C_3 or C_4, also depends on the "J" sensitivity matricies, feedback delays, and measurement noise. In Chapters 5, 6, and 7, the sensitivity matricies are shown to be nonlinear and coupled functions of $\underline{q}$ and $\underline{X}_{rel}$; thus, J varies as $\underline{q}$ varies, and feature-space transformations are manifested by time-varying open-loop gains. Predicted values of J can deviate from actual values due to inaccuracies in the modeling of the three dimensional object and transduction process, and from drift and variation in the transducer parameters. At the extreme, the values may be completely unknown a'priori when minimal knowledge of the inverse interpretation transformations I^{-1} are available, such as arises when task programing is limited to the "teach-by-showing" strategy.

Fixed feedback controller designs have limitations in the control of such nonlinear and unknown systems. Even if the nonlinearities are known, a fixed controller design for these systems is a formidable engineering problem. In contrast, the adaptive approach to controller design appears to be applicable for these requirements. The adaptive approach has already been suggested and studied in application to nonlinear dynamic and kinematic control of possibly unknown plants (Section 2.3.1.3). It would appear that this approach is also capable

of adapting to *nonlinear* and *unknown* feature gains (J_{feat} or J). The IBVS controller design developed in the dissertation will therefore emphasize the adaptive approach. Performance limitations and application of fixed controllers are also evaluated by fixing the adjustable gains of the adaptive controller (derived from initial adaptive learning trials) in the simulation experiments.

Adaptive and fixed controllers can be coupled or uncoupled. Coupled controllers have an inherently greater potential for being able to uncouple a coupled system. Uncoupling of a feature based input/output system, however, does not, in general, uncouple the world space variables. Coupled controllers have several potential disadvantages, including:

1. They are computationally complex relative to uncoupled controllers. For example, it is shown in Chapter 8. that the computational copmplexity of an m-input, m-output n^{th} order MIMO MRAC controller is order m^3n^2, versus mn^2 for m independent SISO controllers;

2. MIMO controllers do not lend themselves to modularity. A modular system can easily be extended to increasing degrees-of-freedom, and distributed processing; and

3. MIMO feedback controllers make available extra degrees-of freedom in the controller, such that non-unique combinations of controller gains can specify desired pole locations. Added controller degrees-of-freedom essentially complicate the manual tuning process, and parameter initializations.

Uncoupled adaptive controllers have already demonstrated the potential to control dynamically coupled robots. They are modular, and computationally simpler, and would thus be easier to implement (in future research) in current laboratory and factory computing environments. For these reasons, the approach developed in this dissertation will emphasize uncoupled control of coupled systems, using the concept of equivalent SISO plants (See section 2.3.1.3). For example, a 2 DOF IBVS system is controlled by independent MRAC controllers in Figure 2-16. The small-signal sensitivity matrix, J in (2.7), is included in the figure to clarify its role in system coupling. From the adaptive controller ($\mathcal{A}_1$ and $\mathcal{A}_2$) viewpoints, the system is equivalent to controlling two independent plants, depicted in Figure 2-17. In the figure, $\hat{W}_{1\text{-}eq.}(z^{-1})$ and $\hat{W}_{2\text{-}eq.}(z^{-1})$ are equivalent SISO linear prediction models with parameters that may be time-varying. That is, $\hat{W}_{i\text{-}eq}(z^{-1})$ predicts $f_i(k)$, from past and present values of $u_i(k)$ and $f_i(k)$, independent of actual physical plant models.

A coupled controller, which estimates coupled models, is outlined in Chapter 8 for computational complexity analysis and possible future implementation. Problem areas of

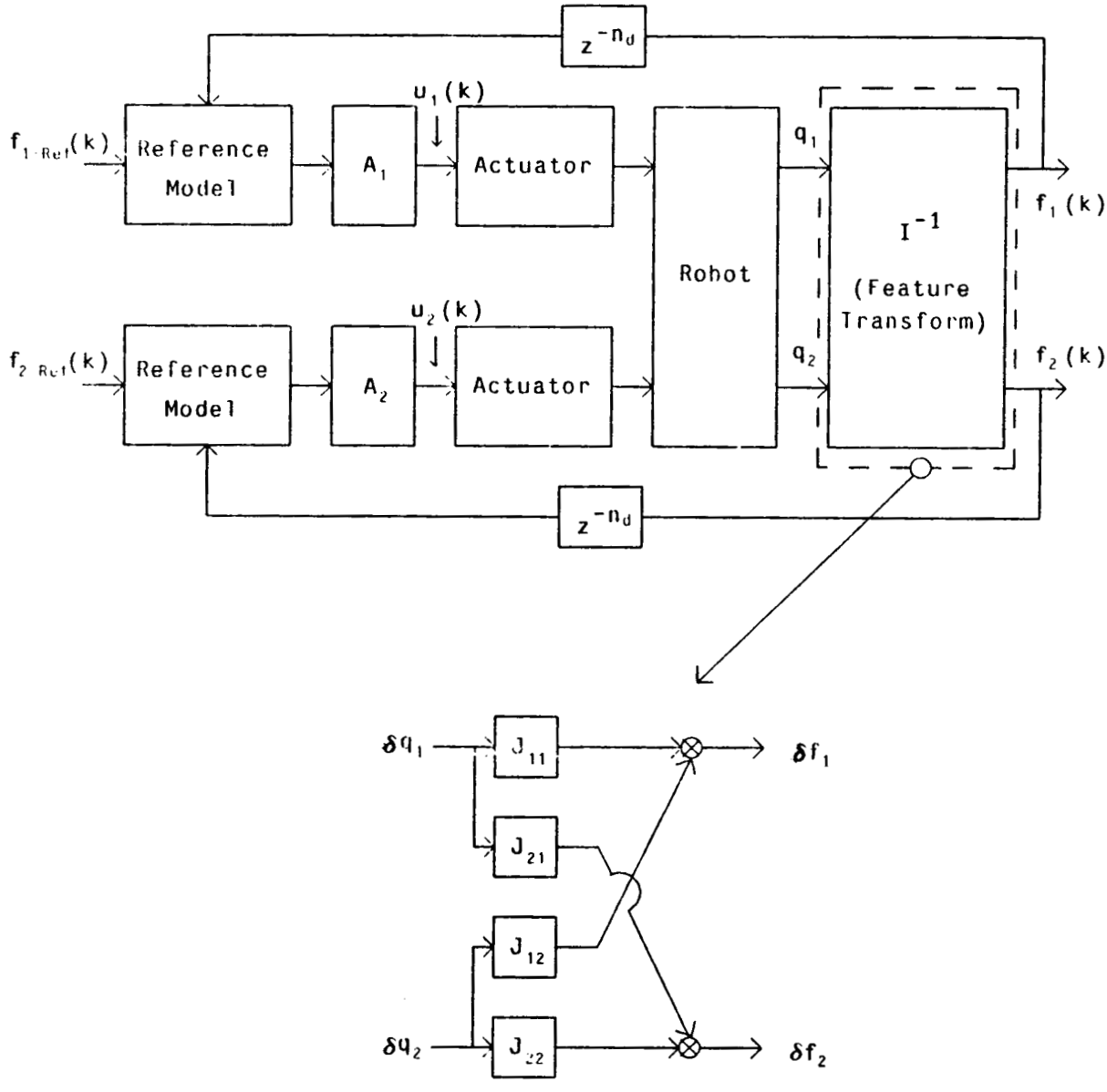

Figure 2-16: MRAC Control of an IBVS System

SISO control, which are isolated in Chapters 6 and 7, suggest the potential performance advantages gained by MIMO control.

The approach to adaptive control will follow the enhanced identification error MRAC developed by Morris and Neuman [Neuman 80]. While similar approaches have appeared in literature, their research focused on details of physical implementation including control signal saturation and controller stability, measurement noise, and computational complexity

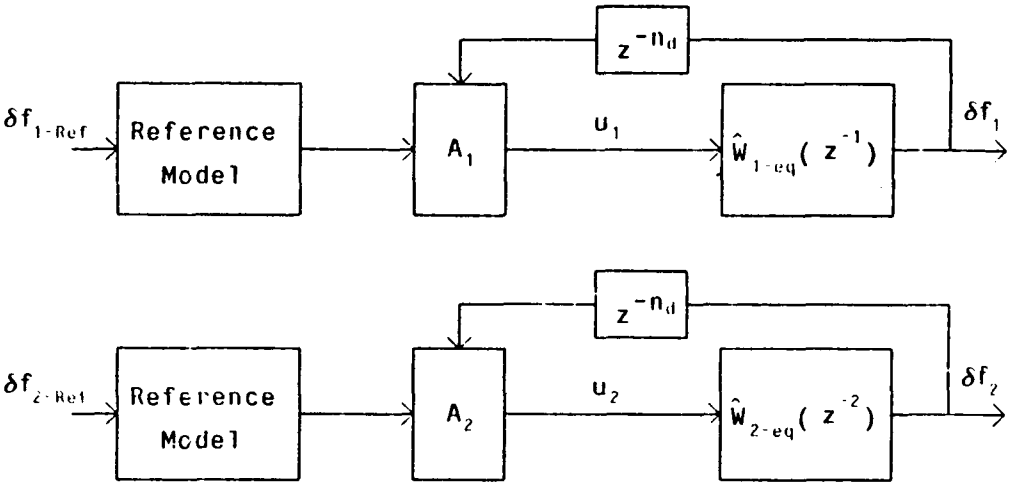

Figure 2-17: Equivalent IBVS Control

for microprocessor implementation. Since the algorithm does not include control of systems with discrete measurement delays, the algorithm is extended in Chapter 3 to include control of systems with delay. Additional modifications for applying uncoupled MRAC to the control of coupled nonlinear systems are also developed.

2.5.2. Feature Selection and Assignment

Feature transformation coupling (i.e., represented by the small-signal feature sensitivity matrix J) leads to related problems of feature selection and assignment. The feature selection process asks the question: How should a subset of n features be selected from a set of m possible control features f_i ($i = 1,\ldots,m$), where $m>n$? And, the feature assignment process asks: Since the uncoupled controllers are used to control coupled plants, which feature should be used to control each actuator? Both issues are related to the degree-of-coupling of the feature transformation. A measurement of coupling is proposed to help answer these questions.

2.5.2.1. Feature Assignment Using Diagonal Dominance

In applications, where uncoupled controllers are used to control coupled plants, there is always the problem of choosing which servo error will control which actuator; that is, for a set of n outputs y_i ($i = 1,\ldots,n$), which servo error, Δy_i, should be filtered and coupled to the jth actuator as u_j? The control engineer tackles this problem with insight into the physical nature of the system and formulates qualitative notions of the degree-of-coupling between the

independent actuators and the system output. For joint-level robot control, Δq_i should be used to derive u_i. For other systems, such as IBVS control, the assignment may not be straight forward. To formalize this procedure let the open-loop linear system be defined by

$$\underline{Y}(s) = H(s)\underline{u}(s)$$

where H(s) is an (n x n) transfer function matrix. When the system is uncoupled, H(s) can be transformed into a diagonal matrix by switching the jth and k^{th} columns of H(s), and therefore the jth and k^{th} rows of $\underline{u}(s)$, until all off diagonal elements of H(s) are zero. When H(s) is diagonal, the only choice for servo error/actuator assignment is $u_i \leftarrow \Delta y_i$. When the system is coupled, then H(s) cannot be transformed into a diagonal matrix. Servo error/actuator assignment selection can be accomplished by organizing H(s) in a "diagonally dominant" fashion [Rosenbrock 74], such that the diagonal elements dominate the off-diagonal elements. Diagonal dominance is defined as

$$|H_{ii}(s)| > \sum_{\substack{j=1 \\ j \neq i}}^{n} |H_{ij}(s)| \quad \text{for } i = 1,\ldots n; \text{ and all s on a desired contour.} \tag{2.8}$$

When H(s) can be organized according to this definition of dominance, then limited stability properties of both coupled and uncoupled fixed control of the system can be formulated [Rosenbrock 74]. When applied to image-based systems, with $|JW_p| \leftarrow H(s)$, it will be shown in Chapter 6, that for limited degrees-of-freedom, the sensitivity matrices cannot in general satisfy this definition of dominance.

An alternative approach is to organize JW_p to maximize the inequality (2.8) over all possible column arrangements. This criterion reduces to defining the dimensionless measure of diagonal dominance as

$$D(k) = \log \sum_{\substack{i=1 \\ j \neq i}}^{n} \sum_{j=1}^{n} \frac{|JW_{p\text{-}ij}(k)|}{|JW_{p\text{-}ii}(k)|} \quad \text{(dimensionless)} \tag{2.9}$$

and then minimizing $D(JW_p)$ over all n! possible column arrangements. The logarithm of the dominance is used since the ratios change by orders of magnitude. The suitability of minimizing $D(JW_p)$ to predict a suitable feature/joint assignment[2] will be evaluated in Chapters 6 and 7. In these evaluations, it is assumed that the open-loop plant time constants

[2] The nomenclature "feature/joint assignment", throughout the dissetation, is used to mean the feature to actuator servo error assignment issue.

are much smaller than the closed-loop system time constants. The plant W_p will be approximated by its low frequency gains for calculation of dominance. This corresponds to the DC gains for Type 0 plants. For Type I plants, the low-frequency gain of the open-loop integrator is used.

Since J, and possibly W_p, are time-varying, the assignment might require on-line reassignment during control. This would require J and W_p to be known a'priori or estimated on-line. In the 2 DOF evaluations (in Chapter 6), J and W_p are derived analytically for specification of feature assignment over the trajectory. In the 3 DOF evaluations (in Chapter 7), $|JW_p|$ it is measured at the start of the control task by sequentially moving each degree-of-freedom by small increments, and measuring the change in features. The resulting feature joint assignment is then fixed over the entire control trajectory. Evaluation of limited degree-of-freedom systems suggests, for a set of features, the feature/joint assignment remains constant over large regions of control for uncoupled kinematic configurations (e.g., Cartesian robot and "look and move" structures). For coupled kinematic configurations (e.g., an articulated arm), a feature/joint reassignment is predicted when controlling over large distances in space. Thus, measurement of JW_p at the start of the control task may only be suitable for feature/joint assignment applications requiring small corrective motions. A general image based system would require on-line estimation of JW_p to determine suitable assignments. A method for accomplishing this task is proposed in Chapter 8.

2.5.2.2. Feature Selection

The image of a typical scene generally contains more features than there are degrees-of-freedom to control. The number of features must equal the number of degrees-of-freedom in an image based system since the feature sensitivity matrix is constrained to be square. The feature selection question is then: How should a subset of n features be selected, for an n-DOF robot, from a set of m features, where $m \geq n$? The possible number of candidate subsets is

$$\binom{m}{n} = \frac{m!}{n!(m-n)!}$$

If a coupled control law is used, then the ordering of the feature subset is not an issue. The process of feature selection becomes more complex when an independent control law strategy is used. The feature/joint assignment issue increases the total number of ordered candidate subsets to

$$p(m,n) = \frac{m!}{(m-n)!}$$

How can a subset be chosen from p(m,n) potential candidates? To arrive at a strategy, it is useful to first describe the idealized attributes for a feature subset. While such attributes may not be expected in practice, they can serve as guidelines.

To arrive at a criterion for feature selection, two aspects of feature-based control are analyzed:

1. Ability to specify world space path using feature based trajectories (assuming that the control system can achieve a specified feature space performance), and

2. The control effort required to achieve the specified feature space dynamic performance.

It is shown below that the attributes of the feature sensitivity matrix, J_{feat}, relate to path performance, while the attributes of JW_p relate to the control effort aspects.

With respect to world space path, it is desireable to be able to control independently each world level DOF. To achieve this goal, an ideal subset of features should yield a feature sensitivity J_{feat} which is diagonal and constant. Then,

$$\Delta X_i = \frac{\Delta f_i}{J_{feat\text{-}i,i}}$$

where, ΔX_i is the path error for the ith DOF, Δf_i is the ith feature error, and $J_{feat\text{-}i,i}$ is the $(i,i)^{th}$ element of J_{feat}. If straight-line motion is desireable, and all of the features exhibit the same dynamic response, then straight-line motion would be achieved. For example, assume that the ith feature response is specified by the critically damped response

$$f_i^{\circ}(t) \doteq f_i(t) - f_i(0) = \Delta f_i(1 - e^{-t/\tau})$$

and all feature responses have the same time constant τ. The response of the ith DOF is

$$X_i^{\circ}(t) \doteq X_i(t) - X(0) = J^{-1}_{feat\text{-}i,i}\, f_i^{\circ}(t)$$

The relationship between any two Cartesian degrees-of-freedom becomes

$$\frac{X_i^{\circ}}{X_j^{\circ}} = \frac{J^{-1}_{feat\text{-}i}\,\Delta f_i}{J^{-1}_{feat\text{-}j}\,\Delta f_j}\,\frac{1-e^{-t/\tau}}{1-e^{-t/\tau}} = \text{Constant}$$

which is constant and specifies the equation of a straight-line in Cartesian coordinates. It thus becomes straightforward to specify straight-line motion!

If an ideal feature sensitivity matrix could be synthesized, then it still remains to control dynamically the system to achieve the desired feature response. Attributes of the overall sensitivity, JW_p, can be used to describe the control effort required to achieve the desired response. Similar to the feature sensitivity attributes, the idealized overall sensitivity matrix should be diagonal and constant. Diagonalization permits the unqualified use of independent controllers. And, constant elements would permit the use of fixed controllers, or using an adaptive approach, would require lower sampling-to-bandwidth ratios (Section 3.6.2).

The evaluations, in Chapters 6 and 7, demonstrate that the idealized sensitivity attributes cannot be expected in practice. The matricies are coupled (i.e., not diagonal) and typically are time-varying. Feature sensitivity changes are minimized for small motion tasks, and for configurations with large magnifications. If the feature sensitivity were constant, but coupled, the predicted path would still be straight-line motion! Since

$$\underline{X}^{\circ} = J_{feat}^{-1}\,\underline{f}$$

then

$$X_i^{\circ} = (J_{feat\text{-}i,1}^{-1}\Delta f_1 + \ldots + J_{feat\text{-}i,n}^{1}\Delta f_n)(1-e^{-t/\tau})$$
$$= K_i(1-e^{-t/\tau})$$

where K_i is a constant. The constant relationship between any two Cartesian DOF becomes

$$X_i^{\circ}/X_j^{\circ} = K_i/K_j$$

From the dynamic control viewpoint, it will be shown that SISO independent controllers can be used to control these feature coupled systems, with limitations. An MIMO control law might produce superior performance, but with added computational complexities.

Since we may not expect to find feature subsets which yield idealized sentitivity attributes, a feature selection strategy could seek a subset which best approximates these ideals; i.e., select features which minimize the coupling and senitivity changes along a trajectory. The dissertation will limit its scope by focusing on feature coupling issues for feature selection. The question which again arises is how to quantify degree-of-coupling. In the dissertation, the diagonal dominace measure, $D(JW_p)$, in (2.9), will be used to quantify system coupling. The feature selection strategy then becomes minimizing $D(JW_p)$ and $D(J_{feat})$ over the set of candidate features. By minimzing $D(JW_p)$, improved dynamic response is expected with SISO

controllers. And, by minimizing $D(J_{feat})$, closer to monotonic path performance would be expected. Each strategy may not produce mutually exclusive decisions, and arbitration between them would be based on the relative importance of each attribute. For example, a system could be feature uncoupled in the joint space of an articulated robot arm, but not uncoupled in Cartesian space. Since the degree-of-coupling plays such an important role in the independent control approach, the dissertation will limit the evaluations to feature selection based on minimization of $D(\mathbf{J}\mathbf{W}_p)$.

Finally, when designing an image-based "look and move" system, the feature selection process can equivalently be viewed as a world coordinate system selection process. That is, the "arm-solution" could be based on Cartesian, cylindrical, or spherical reference frames. For a subset of features, J_{feat} may be less coupled in one world frame than in others. While this approach is not evaluated in this dissertation, this is an important topic for future research.

2.5.3. Path Constraint

In this section, the issue of path constraint is addressed, when the task is specified directly in feature space and objects can be in random poses so that only the end-points of the reference commands are known a'priori. In this case the exact path cannot be specified. For example, for a "look and move" structure, with J_{feat} uncoupled (i.e., $D = -\infty$), a monotonic path can be predicted. When J_{feat} is coupled, the path which produces asymptotic feature errors need not be monotonic. When this occurs, task performance can be affected as follows:

1. An object image can be driven out of the field-of-view, and the feature control must be stopped;

2. A potential for collisions with other objects in the surrounding environment can arise;

3. Longer distances to travel increase the response time; and

4. Overshoot can occur, resulting in physically bumping into the object.

The alternative to path control becomes path constraint. In this approach, independent robot degrees-of-freedom (i.e., joint level in IBVS and world level in "look and move") are constrained by dynamic braking (by position servoing), disabling (by mechanical braking), or by forcing direction reversal along that degree-of-freedom. Constraint is based on on-line

measurements of path performance. For example, path performance can be specified in robot world space by requiring that either boundaries and/or directions of travel are constrained to limits defined by a'priori task knowledge. Directional constraints may arise naturally from the task requirement (e.g., the object is always in front of or to the right of the initial robot position). Work cell boundaries can also be specified. During control, $\underline{q}$ is measured and robot world coordinate positions are predicted using the direct kinematic solution. Deviations from specified directions or across boundaries signal the requirement to constrain motion along the responsible degrees-of-freedom. In the "look and move" structures, it is straightforward to command independent world coordinates. In the IBVS structure, the problem becomes more difficult without the internal compensation for nonlinear kinematics, and only the generalized (or joint) degrees-of-freedom which "dominate" the specified world coordinates can be constrained. Generalized coordinate domination is then predicted based upon the diagonal dominance minimization of J_{arm} (i.e., q_i dominates X_j when J_{arm} is organized to minimize $D(J_{arm})$. Directional constraints might also be evaluated by using feature space measurements and on-line estimates of J_{feat} according to

$$\delta \underline{X}_{rel} = J^{-1}_{feat}\, \delta \underline{f}$$

If a'priori task constraints are not specified, can feature measurements alone be used to constrain motion, and if so how? While a general approach for feature based path constraint has not been developed, a potential strategy has evolved, and is evaluated in the dissertation. In this approach, a hierarchy of control is established (Figure 2-18). At the top level of control, limited degrees-of-freedom are under feature control, while the remaining are constrained. In proceeding from top to bottom, additional degrees-of-freedom become available for feature control. At the bottom level, all degrees-of-freedom are under feature control. At each sampling instant, decisions are made to determine the operating level. These decisions are based on feature performance indices, PI (defined below), compared with a threshold ε. By not forcing all degrees-of-freedom to be turned-on initially, this strategy may minimize non-monotonic path deviations. It remains to specify how to select the degrees-of-freedom which comprise each level, and performance measures which dictate which level is operational.

The object pose, $\underline{X}_{rel}$, is defined in Cartesian space and is divided into three movement modes according to:

1. position: X_{rel}, Z_{rel}

2. orientation: $\varphi, \varepsilon, \psi$

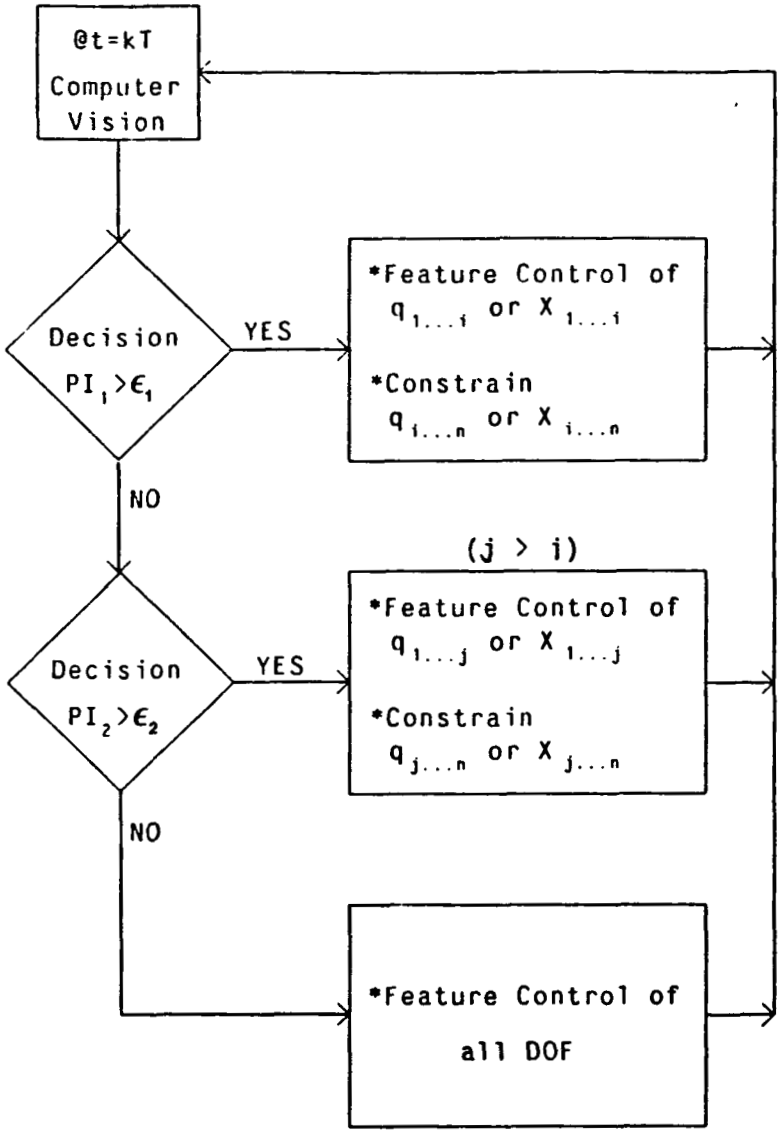

Figure 2-18: Control Hierarchy

3. depth: Y_{rel}

It appears logical to control first the position degrees-of-freedom which grossly align the perceived object image with the desired view. Depth control would be operational at the lowest level of the hierarchy, only after gross positioning and orientation have been achieved. Individual feature measurements are assigned to each degree-of-freedom according to the diagonal dominance organization of J_{feat}, and movement in each mode is evaluated according to the corresponding percentage feature error used as the PI:

$$PI \doteq \frac{\Delta f}{\Delta f_{max}} \times 100\%$$

This measure attempts to normalize the feature error relative to the image boundaries. In IBVS structures, generalized coordinates which dominate movement in the world modes are selected according to the diagonal dominance of J_{arm} (i.e., minimization of $D(J_{arm})$). The resulting hierarchy is represented in Figure 2-19.

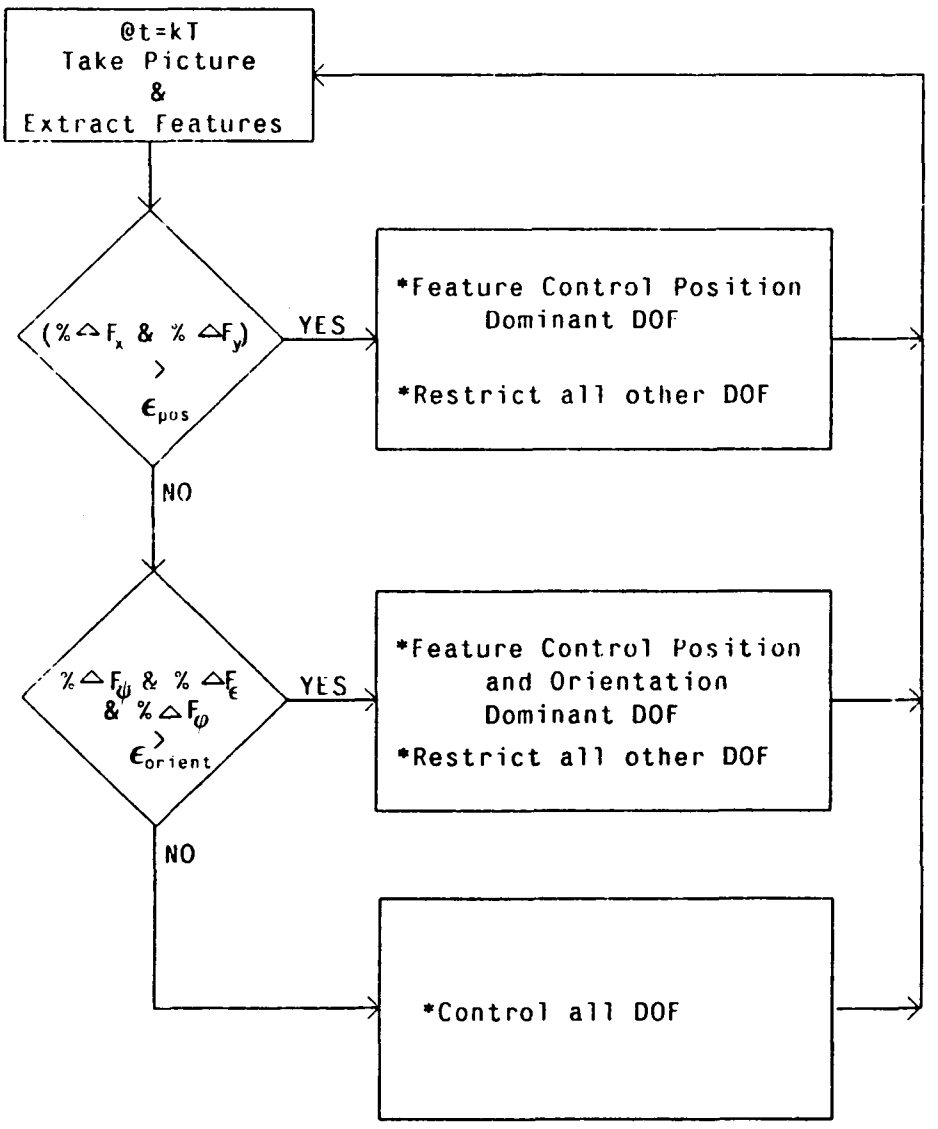

Figure 2-19: Hierarchical Control Example

In the experimental simulations, joints are assumed to be constrained by mechanical breaking, and the threshold levels are determined experimentally.

2.6. Summary

The central theme of this chapter is the dynamic control of robot end-effectors. Non-sensor based robotic systems are limited to control systems which use generalized coordinate measurements for feedback, while end-effector position is then predicted using kinematic models. The control issues involve compensation of nonlinear, coupled, and possibly unknown robot dynamics. Feedforward control leads to precise tracking, but is computationally intensive and relies on accurate robot models. Fixed linear feedback controllers are simple to implement, but their dynamic performance can degrade with increasing joint speeds, and over broad ranges of arm configurations. Application of adaptive controllers has only recently be evaluated, but initial simulation studies suggest that they are suitable for robot control over a wide range of speeds and configurations, and can be implemented using currently available microprocessor technology.

Computer vision extends the feedback measurement space to include relative end-effector position. This capability permits the synthesis of control systems which utilize such measurements for control of end-effector positioning. These integrated visual servo systems have the potential for improving robot accuracy and extending their capabilities for operating in unknown environments (e.g., objects to be aquired, or worked on, are in random positions). Control structures for visual servoing are formally organized, and summarized in Figure 2-20. The image-based approaches are novel structures and facilitate robot task training by using a "teach-by-showing" strategy. They may also exhibit superior accuracy, relative to the position-based approaches, since they do not require explicit interpretation, of image features, to measure world coordinates.

For each control structure (with the exception of "static" position-based), a visual feedback controller is required since the role of computer vision as a measurement process affects the closed-loop system dynamics. In addition to robot dynamics and kinematics, the linearity, noise properties, coupling, unknown parameters, and computational delays of the measurement process must be considered in the design of the control system. To meet the requirements for image-based control, an adaptive SISO MRAC approach for control system design is proposed. Issues of feature selection and assignment are addressed by defining an image feature transformation coupling measure based on "diagonal dominance" of the transformation Jacobian. While the analysis (in this chapter and Chapters 6 and 7) shows that the predicted position trajectories, for image-based control, can be straight-lines or approach

Robot Under Control

Measurement Space ↓	Incremental System (Fig 2-6)	Open-loop (Fig 2-1)
Position	Static "Look & Move" (Fig 2-9) Dynamic PB "Look & Move" (Fig 2-10)	PBVS (Fig 2-11)
Image Feature	Dynamic IB "Look & Move" (Fig 2-12)	IBVS (Fig 2-13)

Figure 2-20: Visual Based Control Structures

straight-lines (for the systems evaluated in the dissertation), the end-effector path cannot be directly specified. Path control reduces to a problem of path constraint. A hierarchical control strategy, using feature based performance measurements, is proposed to minimize deviations from a non-monotonic path.

The model-reference adaptive controller is developed in Chapter 3. In Chapter 4, simulation models are presented for the visual servoing tasks to be evaluated (in Chapters 5, 6, and 7) using the IBVS approach.

Chapter 3
Model Reference Adaptive Control

3.1. Overview

The purpose of this chapter is to review the uncoupled MRAC control algorithm, and modify it for systems with measurement delay. Additional modifications for applying uncoupled MRAC to control of coupled systems are presented. Interpretation of MRAC control of a constant linear plant, and selection of MRAC parameters are also discussed. The controller described here is based on the algorithm developed at Carnegie-Mellon University by Neuman and Morris [Neuman 80, Morris 81]. Their research concentrates on microprocessor adaptive control of linear SISO processes with slowly time-varying parameters. Similar algorithms have been applied in the literature [Dubowsky 79, Horowitz 80, LeBorgne 81] to control simulations of nonlinear and coupled robot dynamics, but have not utilized the enhancements, stability viewpoints, and attention to implementation presented in this dissertation.

The SISO MRAC controller, developed at CMU, is reviewed in Section 3.2. A contribution of this dissertation is the extension (in Section 3.3) of this controller to control systems with measurement delay. In Section 3.5, steady-state analysis of this system predicts a minimum requirement for a control penalty enhancement to insure relative stabilty. Additional modifications for applying uncoupled MRAC to control of coupled systems, including signal biasing and gravity compensation, are presented in Section 3.4. Finally, Section 3.6 includes guidelines for selection of MRAC parameters.

3.2. MRAC for Systems Without Measurement Delay

The purpose of this section is to review the SISO MRAC controller developed by Neuman and Morris [Neuman 80]. A detailed derivation and discussion of this controller is included in Appendix A.

A block diagram for a SISO plant under discrete computer MRAC control is shown in Figure 3-1 [Neuman 80]

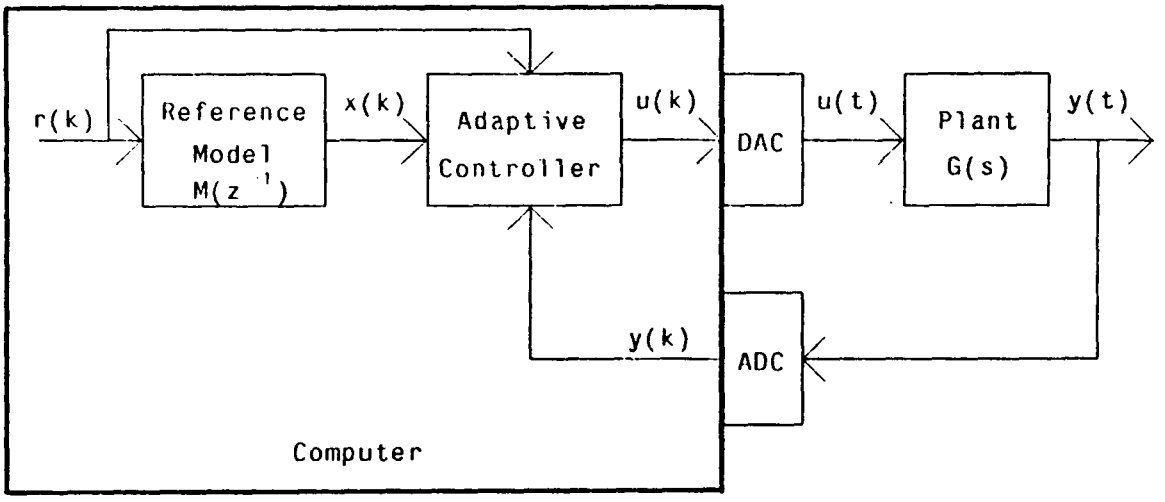

Figure 3-1: Analog Process Under MRAC Control

The MRAC system comprises three basic components:

1. Analog plant under control;

2. Full-parallel reference model; and

3. Adaptive controller

The reference model transfer function $M(z^{-1})$ specifies the desired closed-loop response of the sampled plant output, y(k), to a reference signal r(k). The adaptive controller is a digital feedback controller. The controller gains are adjusted to drive the closed-loop response of the system to that of the reference model. The controller uses both plant and model input and output information to generate the control signal u(k).

At the heart of the MRAC is the controller adjustment mechanism. If the full-parallel (FP) output error is defined as

$$e_o^{FP}(k) = x(k) - y(k), \tag{3.1}$$

the adjustment mechanism must be designed so that

1. $e_o^{FP}(k)$ asymptotically approaches zero, and

2. The closed-loop system is stable.

Adjustable controller design is based on the identification-error [Neuman 80]. The plant input-output information generates estimates of the plant parameters and are used by an identifier to predict the plant output. The identification error is

$$e_{ID}(k) = y(k) - t(k) \tag{3.2}$$

where the identifier output t(k) is the predicted plant output. This error drives the adjustment mechanism which updates the estimates of the plant parameters. In turn, these estimates are used to adjust the controller gains. The adjustment mechanism is designed so that $e_{ID}(k)$ is globally asymptotically stable for a SISO linear system. The controller is then designed to guarantee the asymptotic stability of the full-parallel error.

The mathematical structure of the MRAC, without measurement delay, is described in Appendix A.

3.3. MRAC Control With Measurement Delay

The adaptive control algorithm, reviewed in Section 3.2, assumes instantaneous transduction of the feedback signal. Control systems, such as IBVS, have time delays in the feedback path. These delays, which increase the order of the system under control (by adding discrete open-loop poles at $z = 1$), make the system more difficult to control and reduce the margins of relative stability.

One approach to the adaptive control of systems with delay might be to apply the algorithm reviewed in Section 3.2, with higher-order estimators. Preliminary simulation evaluation with this approach resulted in unstable systems.

Another approach is to make the order of the system equal to that of the plant by using a predictive algorithm to estimate the undelayed process output. For example, Bahill [Bahill 83] suggests the use of a Smith predictor control scheme which includes an adaptive controller. This approach adds another level of complexity to the control law design and evaluation. The approach followed in this dissertation is to use the delayed output directly as the feedback signal by extending the basic MRAC algorithm to include known time delays in the control law. Extension of the MRAC algorithm to include measurement delays follows.

3.3.1. MRAC Controller with Delay

The functional arrangement for a system, with n_d unit time delays in the feedback path, under MRAC control is shown in Figure 3-2.

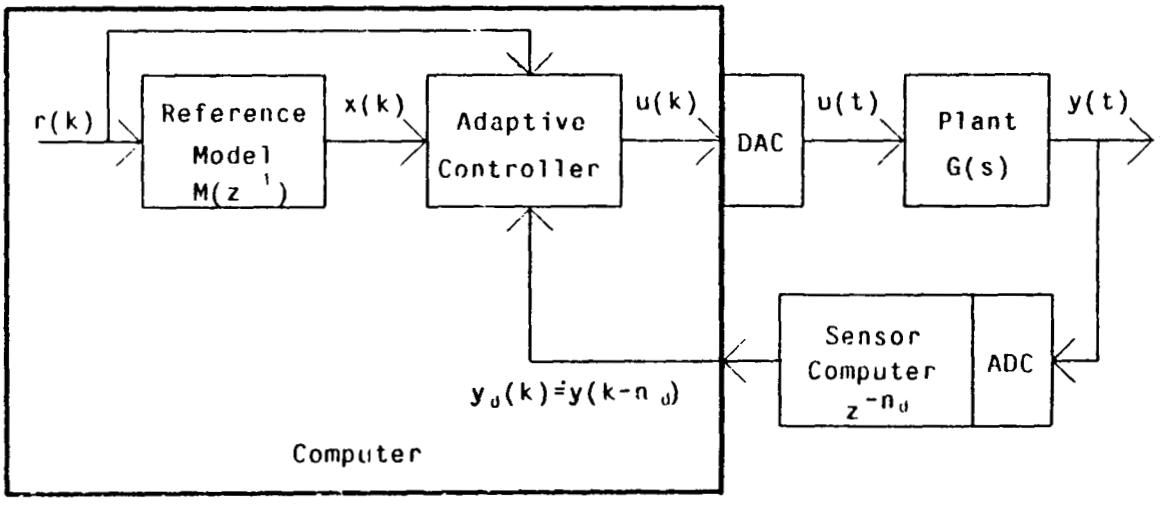

Figure 3-2: MRAC with Measurement Delay

To modify the control algorithm, the measurable signal at $t = kT$, $y_d(k)$, is assumed to be the variable under control. The actual process output, delayed by n_d sampling periods, is $y_d(k)$. If $y_d(k)$ is stable, then $y(k)$ must be stable since $y_d(k)$ is related to $y(k)$ by the stable polynomial z^{-n_d}.

The process under control becomes G(s) in cascade with n_d time delays. The discrete process transfer function $W_d(z^{-1})$ is

$$W_d(z^{-1}) = \frac{Y_d(z^{-1})}{U(z^{-1})} = z^{-n_d} W(z^{-1})$$

where $W(z^{-1})$ is specified in (A.8). Thus,

$$W_d(z^{-1}) = \frac{b_1 z^{-(1+n_d)} + \ldots + b_n z^{-(n+n_d)}}{1 - a_1 z^{-1} - \ldots - a_n z^{-n}}.$$

The input-output difference equation of the process under control becomes

$$y_d(k) = \left[\sum_{i=1}^{n} b_i q^{-(i+n_d)}\right] u(k) + \left[\sum_{i=1}^{n} a_i q^{-i}\right] y_d(k) \tag{3.3}$$

or

$$y_d(k) = \underline{\beta}^T \underline{\Phi}(k-1)$$

where

$\underline{\Phi}_d(k-1) \doteq [u(k-1-n_d)...u(k-n-n_d)\ y_d(k-1)...y_d(k-n_d)]^T$ is the (2n X 1) information vector modified to reflect the measurement delay. The adjustment mechanism in (A.15), (A.16), and (A.17) becomes

$$\hat{\underline{\beta}}(k-n_d) = \hat{\underline{\beta}}(k-1-n_d) + \frac{1}{\lambda} P(k-1)\underline{\Phi}_d(k-1)s(k) \tag{3.4}$$

$$s(k) = \frac{e_{ID}(k)}{1 + (1/\lambda)\underline{\Phi}^T{}_d(k-1)P(k-1)\underline{\Phi}_d(k-1)} \tag{3.5}$$

$$P(k) = \frac{1}{\lambda}P(k-1) - \frac{1}{\lambda^2}\left[\frac{s(k)}{e_{ID}(k)}\right] P(k-1)\underline{\Phi}_d(k-1)\underline{\Phi}^T{}_d(k-1)P(k-1) \tag{3.6}$$

The identifier is chosen to represent an input-output model of the process with delay, and (A.11) becomes

$$t_d(k) = \left[\sum_{i=1}^{n} \hat{b}_i(k-1-n_d)q^{-(i+n_d)}\right]u(k) + \left[\sum_{i=1}^{n} \hat{a}_i(k-1-n_d)q^{-i}\right]y_d(k) \tag{3.7}$$

where $t_d(k)$ is the estimated process output delayed by n_d sampling instants.

The identification error becomes

$$e_{ID}(k) = y_d(k) - t_d(k) = \left[\underline{\beta}^T - \hat{\underline{\beta}}^T(k-1-n_d)\right]\underline{\Phi}_d(k-1) \tag{3.8}$$

The identifier in (3.7) is inverted to derive the control law. From (3.7),

$$t_d(k) = \hat{b}_1(k-1-n_d)u(k-1-n_d) + \left[\sum_{i=2}^{n} \hat{b}_i(k-1-n_d)q^{-(i+n_d)}\right]u(k) + \left[\sum_{i=1}^{n} \hat{a}_i(k-1-n_d)q^{-i}\right]y_d(k).$$

Solving for the control signal $u(k-n_d)$ that would have been required to force the one-step ahead identifier output $t_d(k+1)$ to follow the reference model signal leads to

$$u(k-n_d) = \frac{1}{\hat{b}_1(k-n_d)}\left\{X^R(k) - \left[\sum_{i=2}^{n} \hat{b}_i(k-1-n_d)q^{-(i-1+n_d)}\right]u(k) - \left[\sum_{i=1}^{n} \hat{a}_i(k-1-n_d)q^{-(i-1)}\right]y_d(k)\right\} \tag{3.9}$$

This approach specifies what the control signal should have been n_d sampling instants in the past. The actual control signal is formulated according to (3.9), with the left-hand side of the equation replaced by u(k):

$$u(k) = \frac{1}{\hat{b}_1(k-n_d)}\left\{X^R(k) - \left[\sum_{i=2}^{n} \hat{b}_i(k-n_d)q^{-(i-1+n_d)}\right]u(k) - \left[\sum_{i=1}^{n} \hat{a}_i(k-n_d)q^{-i-1}\right]y_d(k)\right\} \quad (3.10)$$

3.3.2. Control Penalty

The control penalty is reformulated to account for control delays. The Z-transform of (3.10), with the control penalty included, is

$$U(z^{-1}) = \frac{\dfrac{\pi(k)}{\hat{b}_1(k-n_d)}\left\{X^R(k) - \left[\sum_{i=1}^{n} \hat{a}_i(k-n_d)z^{-(i-1)}\right]Y_d(z^{-1})\right\}}{1 + \dfrac{\pi(k)}{\hat{b}_1(k-n_d)}\left[\sum_{i=2}^{n} \hat{b}_i(k-n_d)z^{-(i-1+n_d)}\right]}$$

and the controller characteristic equation is

$$F_d(z^{-1}) = 1 + \frac{\pi(k)}{\hat{b}_1(k-n_d)}\left[\sum_{i=2}^{n} \hat{b}_i(k-n_d)z^{-(i-1+n_d)}\right] \quad (3.11)$$

The Jury conditions are applied to (3.11) for the case of $n = 2$ and $n_d = 1$. Upon applying the transformation $z = \gamma z^*$,

$$F_d(z^*) = z^{*2} + \pi(k)\frac{\hat{b}_2(k-1)}{\hat{b}_1(k-1)}.$$

For this quadratic equation, the Jury conditions lead to

$$|\pi(k)\hat{b}_2(k)/\hat{b}_1(k)| < \gamma^2.$$

The control penalty is computed as

$$\pi(k) = \begin{cases} 1 & \text{for} \quad |\hat{b}_2/\hat{b}_1| < \gamma^2 \\ [\hat{b}_1(k)/\hat{b}_2(k)]\gamma^2 & \text{for } |\hat{b}_2/\hat{b}_1| > \gamma^2 \end{cases} \quad (3.12)$$

3.3.3. Reference Model

The reference model in Figure A-1 is modified in Figure 3-3 to include n_d unit delays in the output. In Figure 3-3, $W_{model}(z^{-1})$ is specified in (A.7), and the root-locus as a function of the gain (for $n_d = 1$) is shown in Figure 3-4. There are two dominant right-half z-plane poles and a fast pole on the negative real axis. The gain is tuned to achieve critical damping of the two dominant poles. The critical gain is found as follows. The characteristic equation is

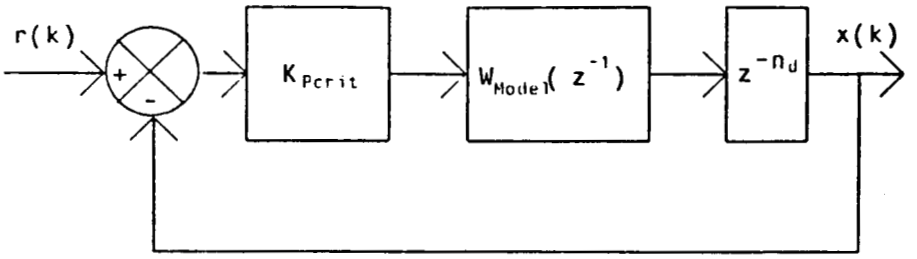

Figure 3-3: Reference Model With Delays

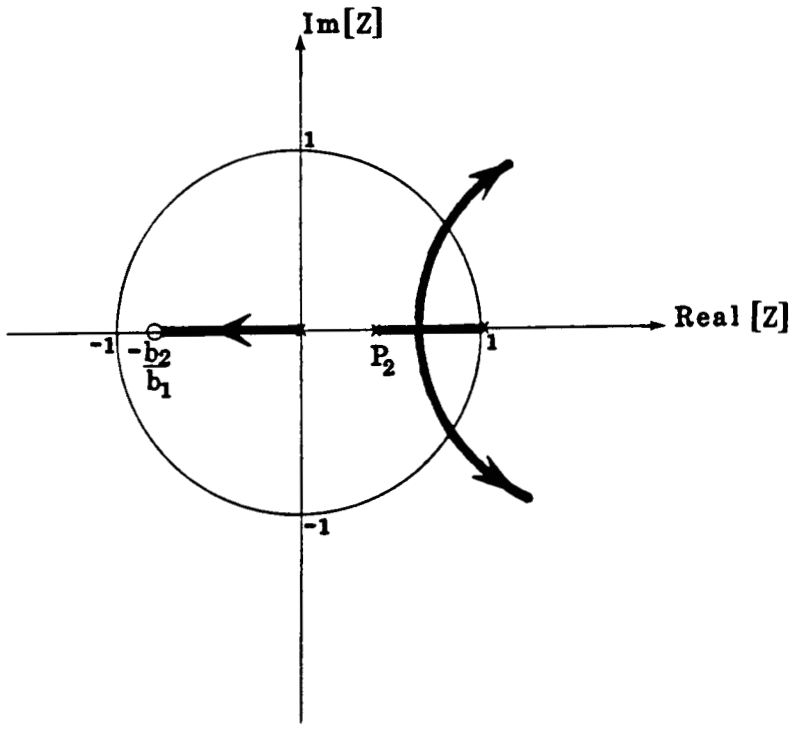

Figure 3-4: Reference Model Root-Locus with One Delay

$$1 + K_p \frac{b_1 z + b_2}{z(z^2 - a_1 z - a_2)} = 0 \tag{3.13}$$

Differentiating (3.13) with respect to the gain, K_p results in the third order polynomial

$$2b_1 z^3 + (3b_2 - a_1 b_1) z^2 - 2a_1 b_2 z - a_2 b_2 = 0$$

The roots are found with the Fortran IMSL [IMSL 82] library routine ZPOLR, and the root lying between 1 and $-a_2$ corresponds to z_{break}. The critical gain is determined by evaluating (3.13) at $z = z_{break}$:

$$K_{Pcrit} = \frac{-z_{break}(z^2_{break} - a_1 z_{break} - a_2)}{b_1 z_{break} + b_2}$$

The closed-loop transfer function becomes

$$M_d(z^{-1}) = K_p \bullet \frac{b_1 z^{-1} + b_2 z^{-2}}{1 - a_1 z^{-1} + (K_p b_1 - a_2) z^{-2} + K_p b_2 z^{-3}}$$

and the model parameters of (A.13) are

$$b_1^\circ = b_1 K_{Pcrit}$$

$$b_2^\circ = b_2 K_{Pcrit}$$

$$b_3^\circ = 0$$

$$a_1^\circ = a_1$$

$$a_2^\circ = a_2 - b_1 K_{Pcrit}$$

$$a_3^\circ = -b_2 K_{Pcrit}$$

$$m = 3$$

3.4. Signal Biasing and Gravity Compensation

To apply the uncoupled MRAC controller to a coupled nonlinear system, two modifications are required:

1. Biasing of the reference and output measurement signals so that the operating point is numerically zero, and

2. Addition of gravity compensation if the plant under control is type zero.

3.4.1. Signal Biasing

To assure that the FP steady-state errors go to zero, the control operating points must be referenced to zero. To demonstrate this requirement, a step input, $r(k) = R$, is applied to the controller and the steady-state FP error is calculated. In steady-state, it is assumed that the reference, output, and control signals have the following constant values:

$$X^R(k) = R$$
$$y(k) = Y_{ss}$$
$$u(k) = U_{ss}.$$

In addition the estimated parameter vector is assumed to be in steady-state:

$$\hat{\beta} = \beta_{ss}$$

If $\pi = 1$, the controller in (A.12) or (3.10) reduces to:

$$U_{ss} = \frac{R - Y_{ss}\sum_{i=1}^{n} \hat{a}_i}{\sum_{i=1}^{n} \hat{b}_i} \tag{3.14}$$

Upon solving (3.14) for R, the steady-state FP error, $e_{FP\text{-}ss} = R\text{-}Y_{ss}$, is

$$e_{FP\text{-}ss} = \left[U_{ss}\cdot Y_{ss}/\hat{W}(1)\right]\cdot\sum_{i=1}^{n} \hat{b}_i \tag{3.15}$$

where $\hat{W}(1)$, the estimated DC gain of the equivalent SISO system, is

$$\hat{W}(1) = \frac{\sum_{i=1}^{n} \hat{b}_{ss\text{-}i}}{1\text{-}\sum_{i=1}^{n} \hat{a}_{ss\text{-}i}}$$

If the open-loop plants are type I (ie: there is an open-loop pole at z = 1), then U_{ss} must be zero for the system to be at rest. For $e_{ss} = 0$, then $Y_{ss}/\hat{W}(1)$ must be zero. Thus, either Y_{ss} or $1/\hat{W}(1)$ must be zero. Type I systems have infinite open-loop gains. However, simulations using type I plants with nonlinear gains (Section 5.4) produce steady-state equivalent SISO model estimates which can be type 0. Type 0 processes have finite open-loop gains. Thus, the operating point, Y_{ss}, must be forced to be zero. To accomplish this, the reference signal is forced to zero, and the output signal is biased by the reference:

1. $X^R(k) \doteq 0$;
2. $y(k) \leftarrow [y(k)\text{-}X^R(k)]$; and
3. Initial model conditions: $x(0) \leftarrow [y(0)\text{-}x(0)]$.

3.4.2. Gravity Compensation

Let a type 0 SISO process be under MRAC control. When the gravity component is zero, no actuating force is required and $U_{ss} = 0$. From (3.15), the measured output signal must then be referenced such that $Y_{ss} = 0$ when $U_{ss} = 0$. In contrast, each type 0 process in a coupled system (such as an articulated robot arm) has an equilibrium point which is configuration dependent. The zero reference point cannot be assigned in advance. To overcome this problem, the identifier in (3.7) is modified to include the bias a_o as follows:

$$t_d(k) = \left[\sum_{i=1}^{n} \hat{b}_i(k\text{-}1\text{-}n_d)q^{-(i+n_d)}\right]u(k) + \left[\sum_{i=1}^{n} \hat{a}_i(k\text{-}1\text{-}n_d)q^{-i}\right]y_d(k) + \hat{a}_o(k\text{-}1\text{-}n_d) \tag{3.16}$$

The information and parameter vectors, respectively, are redefined to be

$$\underline{\Phi}_d(k-1) \doteq [u(k-1-n_d)...u(k-n-n_d)\ 1\ y_d(k-1)...y_d(k-n_d)]^T \ ([2n+1] \times 1) \text{ inform. vector,}$$

$$\underline{\beta}^T \doteq (b_1...b_n a_o a_1...a_n) \quad ([2n+1) \times 1) \text{ parameter vector}$$

and the dimension of adjustable gain matrix becomes ([2n + 1] X [2n + 1]). This identification structure has been used successfully by Koivo [Koivo 81], for optimal least-squares estimation, to estimate an equivalent SISO model for a robot joint. With this identifier, the controller in (3.10) becomes

$$u(k) = \frac{\pi(k)}{\hat{b}_1(k-n_d)} \left\{ X^R(k) - \left[\sum_{i=2}^{n} \hat{b}_i(k-n_d) q^{-(i+n_d)} \right] u(k) - \left[\sum_{i=1}^{n} \hat{a}_i(k-n_d) q^{-i} \right] y_d(k) \right\} + \frac{\hat{a}_o(k-n_d)}{\hat{b}_1(k-n_d)} \tag{3.17}$$

For control of type 0 processes, a steady-state error can occur when a control penalty and $U_{ss} \neq 0$, according to (A.13). Neuman and Morris suggest that auxillary fixed PSD control can be used to drive these errors to zero. Alternatively, the adaptive bias term proposed in (3.16) can also drive steady-state errors to zero. This approach requires that the control penalty not be applied to the bias term in (3.17). Also, when ramp inputs are applied to type I processes (e.g., moving targets), steady-state errors could also be reduced to zero with this approach.

3.5. Linear Control Interpretation

When a SISO linear process, under adaptive control, remains constant and the adjustment mechanism converges, the closed-loop MRAC becomes a linear time-invariant feedback system. This is called linear model following control (LMFC) [Landau 79]. When the actual plant is time-varying, the MRAC attempts to perform as if the true linear parameters were being utilized, since the nonlinear and time-varying adjustment mechanism attempts to drive the identification error to zero. The characteristics of the LMFC approximate those of the MRAC even when the nonlinear and time-varying adjustment mechanism is active. Linear analysis of a SISO linear autonomous process under LMFC control (with reference model and control penalty enhancements included) can thus provide insight into MRAC control. Neuman and Morris have performed extensive linear analysis to systems without measurement delay. This section extends the linear root-locus analysis to systems with delay.

This analysis shows that with measurement delays, the control penalty enhancement is a requirement for relative stability, and the stability margin of the SP MRAC system exceeds that of the FP MRAC.

In the following analysis, the plant under control is assumed to be linear (described by (A.8)), and the adjustable parameters have converged to their true values, that is $\hat{\beta} = \beta$.

3.5.1. FP MRAC

The closed-loop transfer function of the FP MRAC is derived. The Z-transform of the controller (3.10), with control penalty included, is

$$U(z^{-1}) = \frac{K}{1-z^{-n_d}K^u} X^R(z^{-1}) + \frac{K^y}{1-z^{-n_d}K^u} Y_d(z^{-1}) \tag{3.18}$$

where the controller gains are

$$K^u(z^{-1}) \doteq K^u \doteq -\frac{\pi(k)}{b_1}\sum_{i=2}^{n} b_i z^{-(i-1)}$$

$$K \doteq \frac{\pi(k)}{b_1}$$

$$K^y(z^{-1}) \doteq K^y \doteq -\frac{\pi(k)}{b_1}\sum_{i=2}^{n} a_i z^{-(i-1)}$$

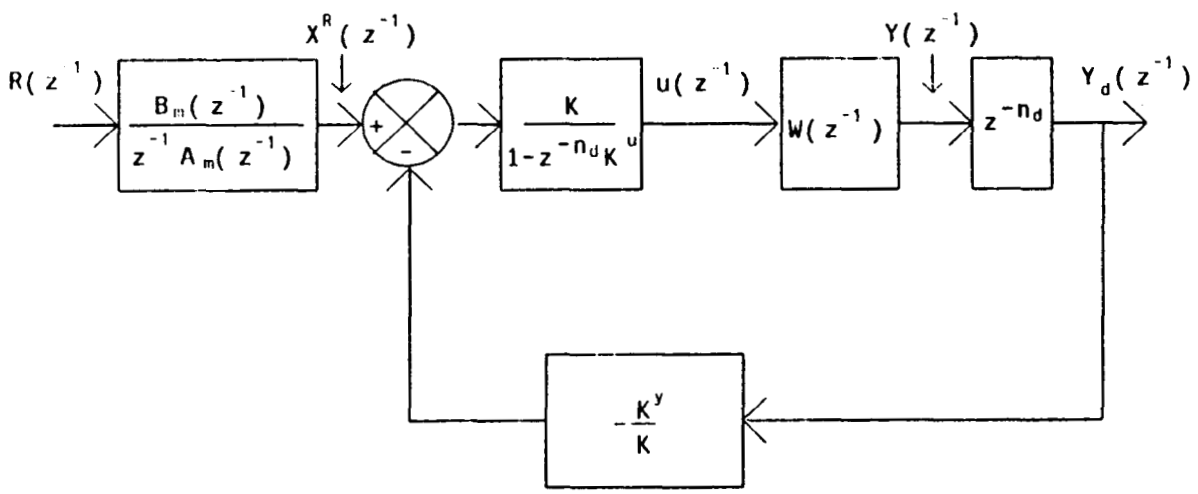

Figure 3-5: FP LMFC Control

From the block-diagram, in Figure 3-5, the closed-loop transfer function is

$$\frac{Y_d(z^{-1})}{R(z^{-1})} = \frac{B_m(z^{-1})}{z^{-1}A_m(z^{-1})} \cdot \frac{Kz^{-n_d}W(z^{-1})}{(1-z^{-n_d}K^u)-K^yW(z^{-1})z^{-n_d}} \tag{3.19}$$

Upon substituting the controller gains into (3.19), the closed-loop transfer function becomes

$$\frac{Y_d(z^{-1})}{R(z^{-1})} = \frac{B_m(z^{-1})}{A_m(z^{-1})} \cdot \frac{\frac{\pi(k)}{b_1} W(z^{-1}) \frac{z^{-n_d}}{z^{-1}}}{[1-\pi(k)z^{-n_d}] + \frac{\pi(k)}{b_1} W(z^{-1}) \frac{z^{-n_d}}{z^{-1}}} \tag{3.20}$$

When $n_d = 0$ and $\pi(k) = 1$, (3.20) reduces to

$$\frac{Y_d(z^{-1})}{R(z^{-1})} = \frac{B_m(z^{-1})}{A_m(z^{-1})} = M(z^{-1})$$

and the closed-loop transfer function reduces to the model in (A.3). If $n_d \neq 0$ and $\pi(k) = 1$, (3.20) becomes

$$\frac{Y_d(z^{-1})}{R(z^{-1})} = M(z^{-1}) \cdot \frac{\frac{1}{b_1} W(z^{-1}) \frac{z^{-n_d}}{z^{-1}}}{[1-z^{-n_d}] + \frac{1}{b_1} W(z^{-1}) \frac{z^{-n_d}}{z^{-1}}}$$

and the closed-loop response is a filtered model response. Without a control penalty, this filter can be unstable as demonstrated by the following root-locus analysis.

The characteristicf equation of (3.20) is

$$1-\pi(k)z^{-n_d} + \frac{\pi(k)}{b_1} W(z^{-1}) \frac{z^{-n_d}}{z^{-1}} = 0 \tag{3.21}$$

Let the process under control be described by (A.6), and let there be a single delay. This structure is simulated, in Chapter 5, to verify the root-locus analysis, with the parameters

$\tau_{model} = 0.072$ sec
$K_{model} = 26.58$
$T = 0.033$ sec

and a reference model with two closed-loop poles at $z = 0.730$, and one at $z = -0.015$. The roots of the characteristic equation, in (3.21), as a function of the control penalty π (as π varies from 0 to 1) are shown in Figure 3-6. When $\pi = 0$, there are two open-loop poles which originate at the open-loop process poles

$$z_1 = e^{-T/\tau_m} = .632\ ; \text{ and } z_2 = 1$$

and a pole at the origin. As the control penalty decreases (and π approaches 1), the dominant poles originating from the process poles break away from the real axis (when $\pi \simeq 0.015$), become oscillatory and eventually cross the unit circle and become unstable. A relatively large control penalty is thus required to achieve a smooth response, at the expense of slower tracking of the reference model.

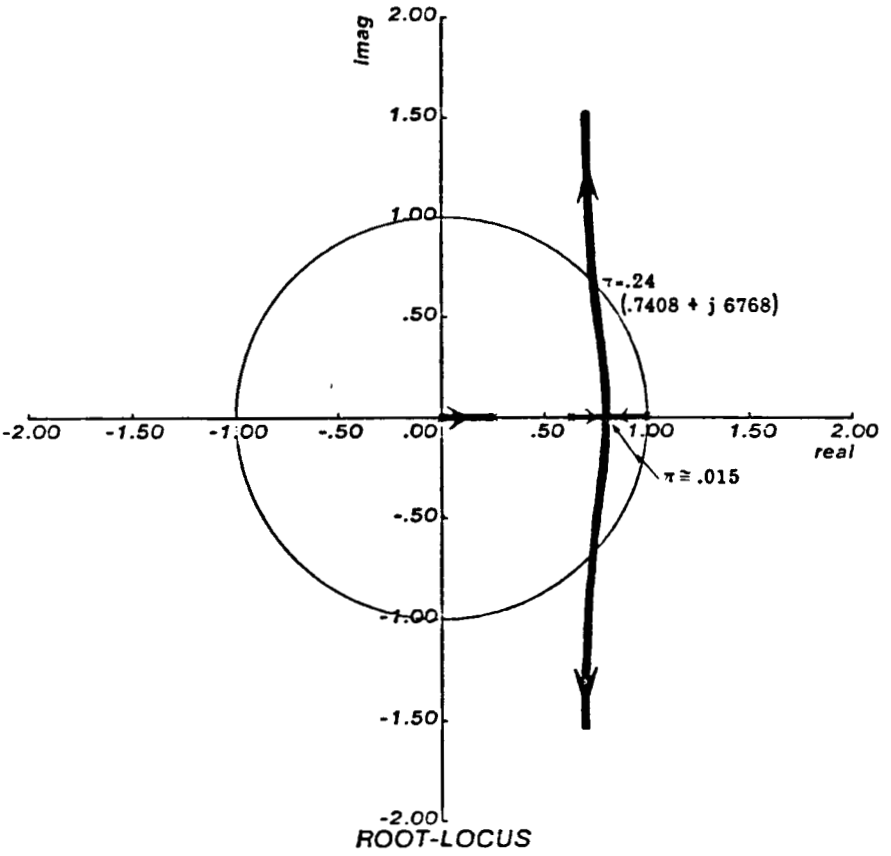

Figure 3-6: FP Root Locus vs. π

3.5.2. SP MRAC

The Z-transform of the SP reference model is

$$X_{sp}{}^{R}(z^{-1}) = \frac{B_m(z^{-1})}{z^{-1}} R(z^{-1}) + \frac{A^{o}(z^{-1})}{z^{-1}} Y_d(z^{-1}). \tag{3.22}$$

Upon substituting (3.22) into (3.18), the Z-transform of the SP controller is

$$U(z^{-1}) = \frac{1}{1-z^{-n_d}K^{u}} \left\{ \left[\frac{KB_m(z^{-1})}{z^{-1}} \right] R(z^{-1}) + \left[K^{y} + \frac{KA^{o}(z^{-1})}{z^{-1}} \right] Y_d(z^{-1}) \right\}.$$

From the block diagram in Figure 3-7, the closed-loop transfer function is

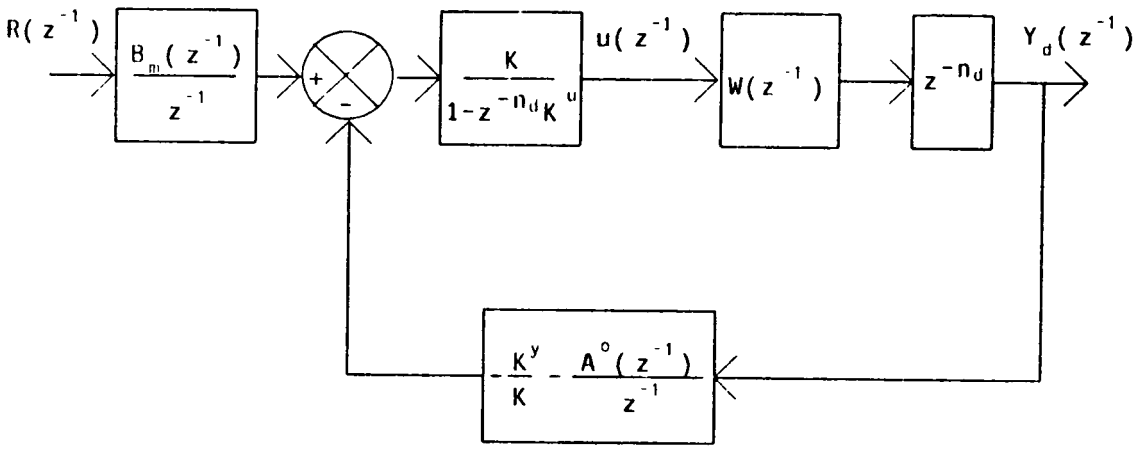

Figure 3-7: SP LMFC Control

$$\frac{Y_d(z^{-1})}{R(z^{-1})} = B_m(z^{-1}) \cdot \frac{\frac{1}{b_1}\frac{\pi z^{-n_d}}{1-\pi z^{-n_d}}\frac{W(z^{-1})}{z^{-1}}}{1 + A_m(z^{-1})\frac{1}{b_1}\frac{\pi z^{-n_d}}{1-\pi z^{-n_d}}\frac{W(z^{-1})}{z^{-1}}} \tag{3.23}$$

When $n_d = 0$ and $\pi(k) = 1$, (3.23) reduces to

$$\frac{Y_d(z^{-1})}{R(z^{-1})} = \frac{B_m(z^{-1})}{A_m(z^{-1})} = M(z^{-1})$$

and the closed-loop model reduces to the model, as predicted. If $n_d \neq 0$ and $\pi(k) = 1$, (3.23) reduces to

$$\frac{Y_d(z^{-1})}{R(z^{-1})} = B_m(z^{-1}) \cdot \frac{\frac{1}{b_1}\frac{z^{-n_d}}{1-z^{-n_d}}\frac{W(z^{-1})}{z^{-1}}}{1 + A_m\frac{1}{b_1}\frac{z^{-n_d}}{1-z^{-n_d}}\frac{W(z^{-1})}{z^{-1}}} \tag{3.24}$$

which does not reduce to the model. To understand the characteristics of (3.24), the root-locus is examined. The characteristic equation of (3.24) is

$$1 + A_m\frac{1}{b_1}\frac{\pi z^{-n_d}}{1-\pi z^{-n_d}}\frac{W(z^{-1})}{z^{-1}} = 0. \tag{3.25}$$

For the process paramaters in Section 3.5.1, the roots of the characteristic equation, in (3.25), as a function of the control penalty (π varies from 0 to 1) are shown in Figure 3-8. When $\pi = 0$, two open-loop poles originate at the process poles, and there are three poles at the origin. As the control penalty decreases, the process poles migrate toward the two dominant critically damped model poles and eventually break away with a relatively small overshoot. One of the poles at the origin migrates toward the fast model pole on the negative real axis. Even though the system characteristics tend toward the model, two additional poles at the origin break away from the real axis causing significant oscillation as π decreases.

Comparison of the SP and FP root-loci, in Figures 3-8, and 3-6 shows that the SP MRAC system has a significantly larger margin of stability when operating with the same control penalty. Since it is desirable to minimize the control penalty (to keep the closed-loop bandwidth large), the SP MRAC is recommended for control of systems with delay.

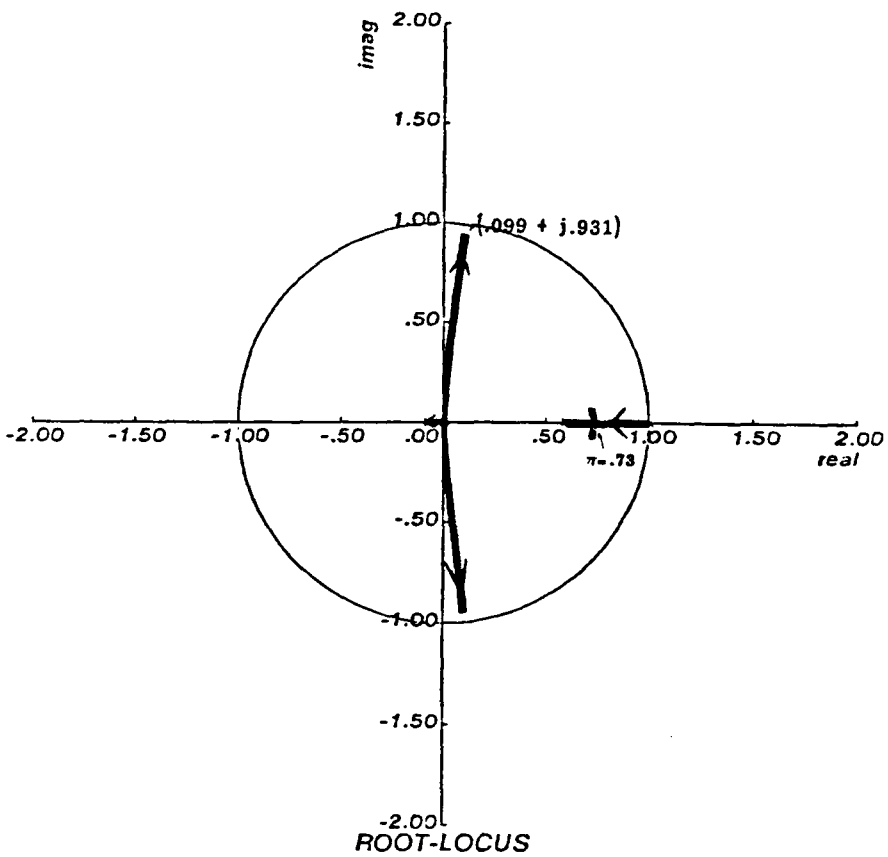

Figure 3-8: SP Root Locus vs. π

3.6. Parameter Specification

Selection of MRAC controller parameters involves compromises among several factors. In this section, guidelines and tools are presented to aid the control engineer in making suitable choices. Optimal selections result from the tuning of the parameters over specific regimes of system operation. Parameters are selected in Chapters 5 through 7 to achieve acceptable operation over a wide range of control tasks, as opposed to optimizations over local regions.

3.6.1. Model Time Constant Specification

The reference model specifies the desired closed-loop system performance. Control performance can be defined by time or frequency domain specifications, performance index optimization, or pole-zero location. For step-inputs, a convenient performance measure is rise-time, t_r, defined as the time it takes the output to go from 0 to 99% of it's final value. The

rise-time criterion is specified by s-plane pole requirements which are then mapped into the z-plane according to $z = e^{st}$. The model time constant, τ_{model} in (A.6), is then selected to place z_{break} at the desired location according to the methods outlined in Appendix A, for $n_d = 0$, or in Section (3.3.3), for $n_d = 1$.

An s-plane model of a system, with a pair of critically damped poles at ω_n, is

$$\frac{X(s)}{R_{ef}(s)} = \frac{\omega_n^2}{(s + \omega_n)^2}$$

where ω_n specifies the system bandwidth. The unit step response is

$$x(t) = 1 - e^{-\omega_n t}(1 - \omega_n t)$$

The bandwidth vs. rise-time is found by solving

$$0.01 = e^{-\omega_n t_r}(1 - \omega_n t_r) \tag{3.26}$$

Once the desired rise-time is selected, (3.26) is solved numerically for ω_n. This bandwidth then specifies the closed-loop reference model pole at

$$z_{break} = e^{-\omega_n T}$$

Many constraints must be considered in specifying t_r. Selecting too large or too small a rise-time can result in the following problems:

1. The sampling period (in Section 3.6.2) places constraints on ω_n and thus t_r. A lower bound on t_r results from lower bound constraints on T.

2. As t_r decreases, ω_n increases and z_{break} decreases. As z_{break} becomes smaller, and the system speeds-up, the the controller gain increases, thus amplifying noise and degrading system performance. As the controller gain increases, the system tends to saturate more which in turn reduces relative stability. As t_{rise} increases and z_{break} approaches the unit circle, the full-parallel error e_{FP} (A.23) increases, relative to any identification error since $A_m(z^{-1})$ increases.

3.6.2. Sampling Period Selection

While there are guidelines for the selection of the sampling period T, the choice can be forced upon the designer by hardware, software, or cost constraints. When this occurs, control performance criteria must be evaluated in light of these constraints.

The following guidelines are used in to specify the sampling period and control performance specifications.

3.6.2.1. Fundamental Upper Bound

When the closed-loop system bandwidth is specified to be ω_n, the Nyquist sampling theorem sets the upper bound on the sampling period according to

$$T_{UB} \leq \frac{\pi}{\omega_n}. \tag{3.27}$$

If hardware, software, or cost constraints limit the sample period to $T_{constraint}$, where

$$T_{constraint} > T_{U.B.},$$

the closed-loop system bandwidth must be constrained by

$$\omega_n \leq \frac{\pi}{T_{constraint}}.$$

It is important to note that there is a distinction between the closed-loop bandwidth and the highest frequency components of the open-loop process dynamics, since these two frequencies can be quite different. Thus, potentially slow visual sampling rates can be used to control fast open-loop processes, if the closed-loop bandwidth is reduced proportionally.

3.6.2.2. Performance Margin

For reasons outlined below, T_{UB} is judged to be insufficient. A performance margin (PM) can be specified to decrease the sample period according to

$$T = \frac{T_{UB}}{PM} \quad \text{where} \quad PM > 1$$

and therefore,

$$T \leq \frac{\pi}{PM \cdot \omega_n}.$$

For control of constant systems, typical values for PM are $2 \leq PM \leq 10$, depending upon the particular application. Adaptive control of nonlinear systems require larger margins (Section 3.6.2.3). In terms of a sampling rate to closed-loop bandwidth ratio, this requirement is

$$\frac{f_s}{f_{BW}} = \frac{1/T}{\omega_n/2\pi} = 2 \cdot PM. \tag{3.28}$$

The performance margin is specified to:

1. Reduce any delay between a reference signal command change and system response to that change;

2. Smooth the system response to the control inputs which are applied to the process through a DAC;

3. Minimize aliasing effects, since the actual system may have attenuated signal components above ω_n; and

4. Increase relative stability for MRAC with discrete delays by minimizing the difference between the estimated control signal and the required control signal.

From (3.28), the constraint on the closed-loop system bandwidth becomes

$$\omega_n < \frac{\pi}{PM \cdot T_{constraint}} \tag{3.29}$$

3.6.2.3. MRAC Identifier Requirements

The discrete time-identifier used by MRAC places additional requirements on the sampling period.

1. If the open-loop plant to be identified is constant and linear with no complex poles, then no additional requirement is placed on T (assuming the computer has sufficient precision to measure smaller input-output signal changes, as T increases and t_r decreases). The plant dynamics can be identified independently of T. If the plant has complex poles at $\alpha \pm j\omega_{max}$, then the sampling theorem requires that

   $$T_{ID} \leq \frac{\pi}{\omega_{max}}$$

   If sampling period constraints cannot satisfy this requirement, then an independent velocity feedback (which samples at a higher rate than the main control loop) can be incorporated.

2. If the plant is time-varying or nonlinear, then the sampling period must be chosen to be short enough to track parameter variations. In evaluations in Chapters 5, 6, and 7, performance margins of $10 \leq PM \leq 25$ are demonstrated to be suitable for tracking the nonlinear plant gains for IBVS tasks which require small corrective motions. Motions over large distances, and thus larger gain changes, require even higher margins. These requirements are discussed in Chapters 5 and 6.

3.6.3. Adaptive Gain Matrix Initialization and Limiting

The adaptive gain matrix **P**(k) in (3.6) is initialized to a non-zero value prior to the start of control. Subsequent control tasks can then use previously learned values. To the best of the author's knowledge, guidelines for the initialization are not presented in literature and the approach seems to be empirical. This topic is an area requiring future research since initialization of **P**(k) will affect the identifier's rate of convergence and thus the controller's relative stability. The following tools and guidelines have been developed to facilitate the experimentation.

1. When the estimated process gain $\hat{b}_1$ is small it becomes difficult to find an initialization which is not too sensitive. Thus, the reference and output signals are multiplied by a scale factor (SF) to increase the apparent process gain. The scale factor is increased until $\hat{b}_1$ execceds 0.001 .

2. Since the operating points vary widely from one control task to the next, it becomes difficult to find an initialization that is suitable over a wide range of control tasks. Signal biasing (Section 3.4.1) makes it much easier to find values which can be used over a wide range of tasks.

3. In accordance with Neuman and Morris' work [Neuman 79b], P(0) is initialized to be a diagonal matrix.

4. When the sampling interval is decreased, P(0) is also decreased.

5. Values of P(0) found to be suitable for control of uncoupled SISO systems appeared to be suitable for control of the coupled systems.

6. When P(0) is initialized with unsuitably small values, the controller would exhibit poor stability. In these cases, if the the signs of the steady-state estimated gain terms were opposite (e.g., $\hat{\beta}_1>0$. and $\hat{\beta}_2<0$), then larger gain matrix initializations, resulted in improved stabilty and consistent signs (Appendix D).

Equally important is gain matrix limiting. If the system reaches steady-state ($\underline{\Phi} = 0$), the gain matrix adjustment mechanism reduces to

$$P(k) = (1/\lambda)P(k-1),$$

and the gain matrix thus becomes unbounded when $\lambda<1$. This presented implemention problems for Neuman and Morris due to arithmetic overflow in the μ-processor. To overcome this, Neuman and Morris simply reset P(k) = P(0) when the diagonal element $P_{nn}(k)$ exceeded a threshold P_{tresh}. In this dissertation, simulations are implemented on a large mainframe where overflow is not an immediate problem. However, as P(k) becomes large, the adjustment mechanism becomes too sensitive to adaptation to changes in the plant parameters, and decreases system relative stability. To overcome this problem, P(k) is reset to P(0) whenever

$$P_{1,1}(k) \text{ or } P_{2n,2n}(k) > P_{thresh},$$

where the threshold is selected experimentally. Similar to the initialization of P(k), the threshold should decrease as the the sampling period decreases.

3.6.4. Parameter Vector Initialization

While hyperstability does not put any constraints on the initialization of $\hat{\underline{\beta}}(0)$, better initialization leads to faster convergence of the identifier. If the initialization of b_1 is too large, the rate of convergence and system response are unacceptably slow. This is observed to be more pronounced as the reference model bandwidth decreases. If $b_1(0)$ is too small, then the system accelerates rapidly, decreasing relative stability.

Any a'priori knowledge of the system should be used to guide the initialization. For instance, as the sampling period becomes smaller, the gains $\{b_i\}$ become smaller, and the poles approach unity. Initializations which are satisfactory for control of SISO uncoupled plants appear to be acceptable for the coupled plant initializations.

3.6.5. Weighting Factor

The least-squares weighting factor λ is chosen as a compromise between sensitivity to adaptation to process changes and over reaction to noise measurement. For the experimentation presented in this dissertation, and for Neuman and Morris' research, $\lambda = 0.85$ provided satisfactory response.

3.6.6. Control Penalty

The controller pole bound, γ, which indirectly sets the control penalty, is tuned to minimize ringing in the output. Faster model responses cause increased saturation tending to ring the controller more. When this occurs, the control penalty is increased by reducing γ.

Physical implementation, by Neuman and Morris [Morris 81], of MRAC position control of a DC motor required smaller values of γ than for simulation trials. This resulted from the computational delay required to actually compute u(k). The LMFC analysis, in Section 3.5, explains why systems with delay require increased control penalties. Since the computational delay is only a fraction of the sampling interval, Neuman and Morris set γ in the vicinity of 0.9 . When unit delays are present, as with IBVS, larger control penalties are needed.

3.7. Summary

In this chapter, the independent MRAC controller is extended to include measurement delays. Analysis of this controller, for control of a constant linear plant, predicts the requirement for a control penalty to achieve relative stability. Chapter 5 includes simulation examples which verify the algorithm for control of SISO plants. Analysis of independent control of a coupled nonlinear plant shows an additional requirement for signal biasing and gravity compensation to assure zero steady-state errors. Guidelines for the practical selection of controller parameters are emphasized and will be used in the following chapters where actual values are selected.

Chapter 4
Task Modeling and Simulation

4.1. Overview

The purpose of this chapter is to specify the visual servoing task configurations which are evaluated under fixed and MRAC control in this dissertation. Mathematical models of robot kinematics and dynamics, camera picture taking, and feature transformations (which are required for implementation of the task simulations)[3] are developed. The task configurations are selected so that the delay, nonlinear, and coupling aspects of IBVS can be studied and evaluated independently as applied to control progressively complex dynamic and kinematic systems consisting of:

- 1 DOF linear dynamic and kinematic robot, with either constant or nonlinear feature sensitivity;
- 2 DOF linear, uncoupled dynamic and kinematic robot, with nonlinear and coupled feature sensitivity;
- 2 DOF nonlinear, coupled dynamic and kinematic robot, with nonlinear and coupled feature sensitivity; and
- 3 DOF linear, uncoupled system dynamics, with a combination of linear and nonlinear kinematics, and nonlinear and coupled feature sensitivity.

The 1 DOF configuration simulations are summarized in Chapter 5 to verify the basic MRAC algorithm (with and without delay), and provides an initial evaluation of a system for which the control variable is nonlinearly related to the physical plant variable. The 2 DOF systems, which include coupled feature transformations, are evaluated in Chapter 6. For these configurations, the basic MRAC algorithms will be augmented by a hierarchical control strategy, and feature/joint assignment is based on the concept of diagonal dominance. One of the 2 DOF configurations represents an ideal "look and move" structure since the robot is

---

[3] All simulations are implemented on a DEC-20 processor.

dynamically and kinematically linear and uncoupled. The other configuration specifies an articulated robot arm in order to investigate the relative contributions of nonlinear and coupled robot dynamics and kinematics. The 3 DOF simulation represents a visual servoing configuration, with planar Cartesian and rotational degrees-of-freedom, presently implemented in the CMU Flexible Assembly Laboratory [Sanderson 83b] using a static position-based "look and move" control structure. Simulations of this configuration, with linear and uncoupled dynamics, emphasizes the feature selection process. It is natural to implement IBVS for this system in future research.

This chapter is organized as follows. In Section 4.2, the task configurations, including transducer mounting (the transducer is assumed to be a camera), robot type, and object in the scene are described. In Section 4.3, the dynamic modeling and simulation of the linear and uncoupled robots is presented. The dynamic and kinematic modeling and simulation of a 2 DOF robot arm is described in Section 4.4. Modeling of picture taking and feature measurement is described in Section 4.5.

4.2. Task Configurations

This section describes the visual servoing task configurations (i.e., transducer mounting, robot type, and object in scene). The first configuration describes a 2 DOF system. This system is then used to simulate 1 DOF systems by restricting relative motion to one of the degrees-of-freedom.

4.2.1. Configuration 1: 2 DOF with linear kinematics and dynamics

The camera is mounted on a 2 DOF linear kinematic system such as a Cartesian robot, a set of translational stages, or possibly a mobile robot. The camera is servoed relative to a fixed line in space to control the relative position between the robot and a line (Figure 4-1) . A line in space problem is selected because the corresponding sensitivity functions can be easily analyzed. It is complex enough to be both interesting and useful. The line is assumed to be fixed in spaced so that

1. The line lies entirely in the plane defined by $[\vec{X}_o, \vec{Y}_o]$; and

2. $Z_{rel} = 0$

The camera is mounted to the robot so that:

1. $[\vec{Y}_{cam}]$ is parallel to $[\vec{Y}_o]$; and

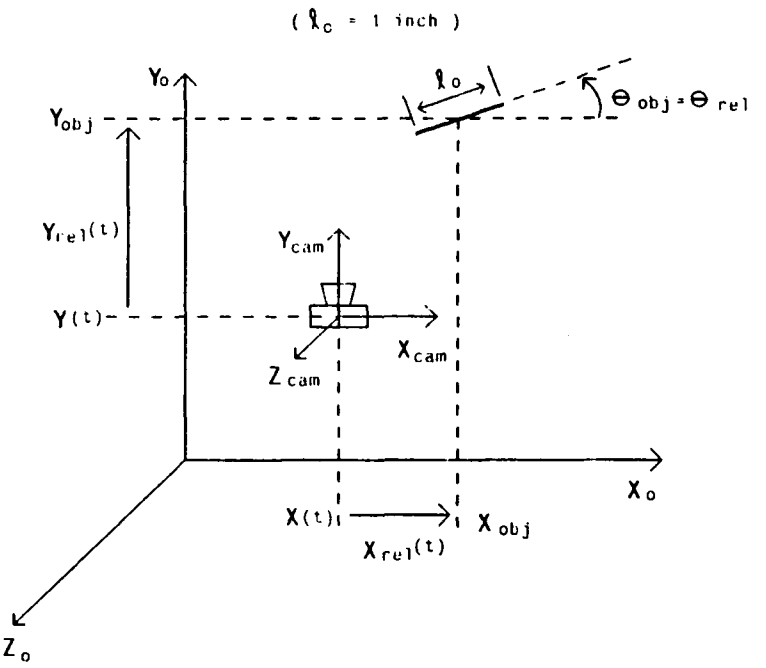

$[X_o, Y_o, Z_o]$	World Coordinate Frame
$[X_{cam}, Y_{cam}, Z_{cam}]$	Camera Coordinate Frame
l	3 dimensional length of line
θ_{obj}	Angle of line relative to $\vec{X}_o$
$X(t), Y(t)$	Position of line relative to world
X_{obj}, Y_{obj}	Position of center of line relative to world
$X_{rel}(t), Y_{rel}(t)$	Position of line relative to camera

Figure 4-1: Configuration 1

2. $[\vec{Z}_{cam}]$ is parallel to $[\vec{Z}_o]$

The robot is modeled as X-Y translational stages with the Y-stage mounted on top of and orthogonal to the X-stage. The camera is fixed to the Y-stage. The X-stage controls only x(t) and the Y-stage controls only y(t). The actuators are armature controlled DC motors with negligible armature inductance. When the translational stages are orthogonal, the axes are decoupled. In addition, it is assumed that gravity acts in the Z-axis direction so that gravitational effects are abscent. Thus, the robot is modeled an uncoupled linear system.

It is shown, in Chapter 5, that when motion is constrained to the X-axis, and the center-of-gravity of the line image is chosen as the control feature, this configuration becomes a 1 DOF

autonomous linear system. When motion is constrained to the Y-axis, and the line image length is the control feature, then the configuration becomes a nonlinear system. When both degrees-of-freedom are free, the robot represents an idealized incremental robot system (Section 2.3.2.1), since the dynamics and kinematics are uncoupled and linear. Thus, the resulting control structure represents a dynamic "look and move" structure.

4.2.2. Configuration 2: 2 DOF with nonlinear kinematics & dynamics

In the second configuration, the camera is mounted to a 2 DOF nonlinear kinematic articulated robot arm (Figure 4-2).

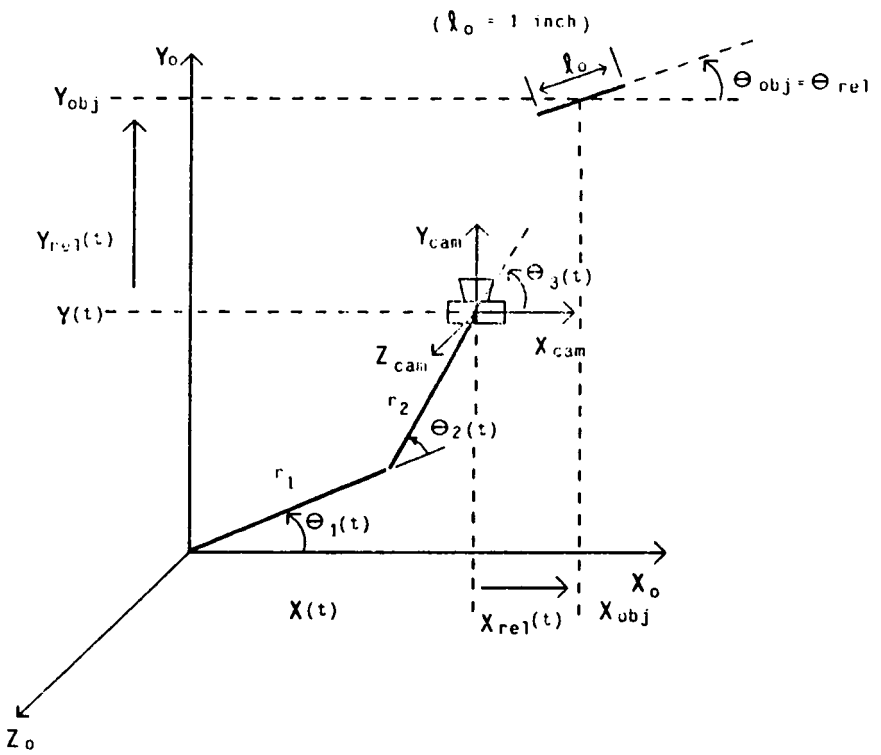

r_1, r_2 Length of robot links
$\theta_1(t), \theta_2(t)$ Link angles
$\theta_3(t)$ Angle of $\vec{X}_{cam}$ relative to the second link

Figure 4-2: Configuration 2.

The line is fixed in space so that:

1. The line lies entirely in the plane defined by $[\vec{X}_o, \vec{Y}_o]$; and

2. $Z_{rel} = 0$

The camera is mounted so that

1. $\theta_3(t)$ is automatically rotated to $-[\theta_1(t) + \theta_2(t)]$ so that $[\vec{Y}_{cam}]$ is always parallel with $[\vec{Y}_o]$;

2. $[\vec{Z}_{cam}]$ is parallel to $[\vec{Z}_o]$; and

3. The end of link 2 is coincident with the origin of $[\vec{X}_{cam}, \vec{Y}_{cam}, \vec{Z}_{cam}]$

The robot is modeled as a two linkage arm, with nonlinear and coupled dynamics. The actuators are armature controlled DC motors with negligible aramature inductance. It is assumed that gravity acts in the Z direction so that gravitational effects are abscent.

4.2.3. Configuration 3: 3 DOF with nonlinear kinematics, and linear and uncoupled dynamics

This visual servoing task consists of servoing a three-dimensional object (described in Section 4.5.2.2) relative to a stationary camera. The object is placed on a 3 DOF linear kinematic manipulator consisting of the set of X-Y translational stages, described in Configuration 1, and an additional rotational stage mounted on top (Figure 4-3).

The camera is mounted relative to the X-Y-θ stages so that:

1. $[\vec{X}_{cam}]$ is parallel to $[\vec{X}_o]$;

2. The plane defined by $[\vec{Z}_{cam}, \vec{Y}_{cam}]$ is coplanar with the plane defined by $[\vec{Z}_o, \vec{Y}_o]$; and

3. The plane defined by $[\vec{X}_{turn}, \vec{Y}_{turn}]$ is coplanar with the plane defined by $[\vec{X}_o, \vec{Y}_o]$.

The dynamics of this system are simplified by assuming that the inertial coupling and centrifugal forces caused by the load are negligible This assumption is justified when the load does not shift the center-of-mass away from the center of the turntable. The center-of-mass will remain in the vicinity of the turntable center when the load is centered on the turntable or has a weight much smaller than that of the turntable platter. The manipulator is then modeled as a dynamically linear and uncoupled system.

The evaluation of this configuration, in Chapter 7, focuses on the feature selection process, by evaluating system performance as a function of the coupling index $D(JW_p)$ for various candidate feature subsets. Since $D(JW_p)$ is the measure of overall system coupling, system performance is evaluated at the joint level (i.e., performance of the X-Y-θ axes). The 3 DOF

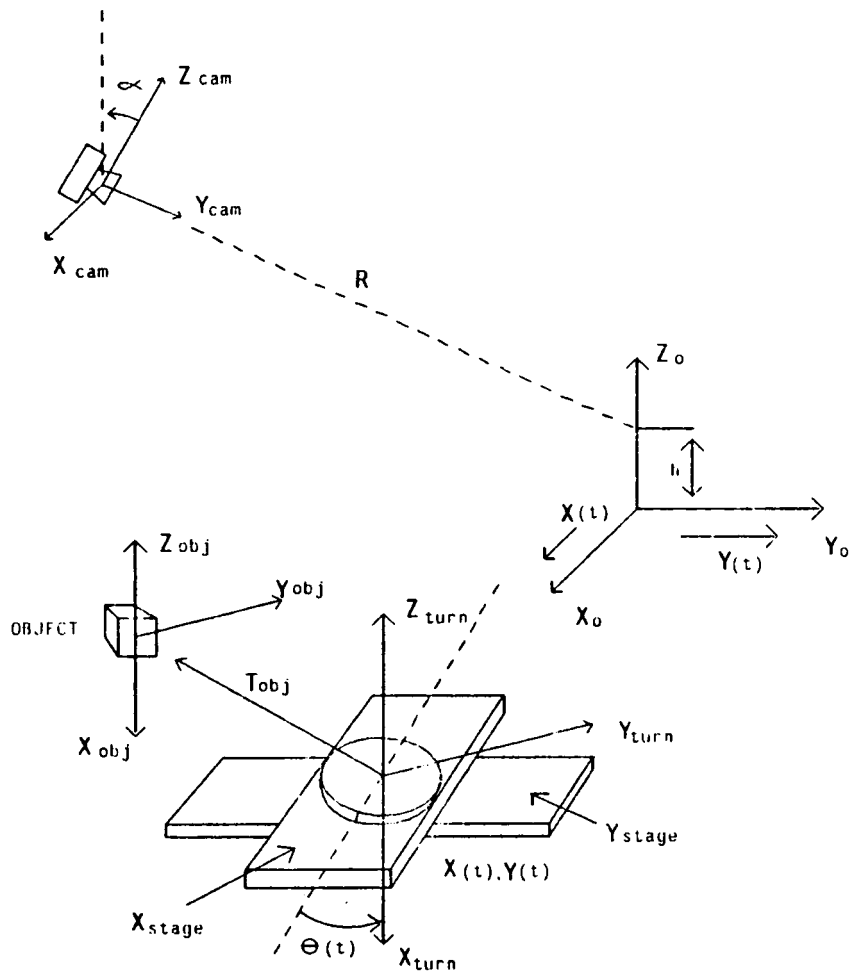

$[X_o, Y_o, Z_o]$	World Coordinate Frame
$[X_{cam}, Y_{cam}, Z_{cam}]$	Camera Coordinate Frame
α	camera tilt (angle between $[\vec{Z}_{cam}]$ & $[\vec{Z}_o]$)
R	distance along $[\vec{Y}_{cam}]$ to $[\vec{Z}_o]$
h	intersection of $[Y_{cam}]$ with $[\vec{Z}_o]$
$[X_{turn}, Y_{turn}, Z_{turn}]$	turntable Coordinate Frame
$[X_{obj}, Y_{obj}, Z_{obj}]$	Object Coordinate Frame
$(X(t), Y(t))$	turntable position relative to world
$\theta(t)$	angle of turntable relative to world
T_{obj}	Transform relating object to turntable

Figure 4-3: Configuration 3

configuration can be viewed as a Cartesian robot with the turntable, or θ-stage, acting as the final link (or gripper). The object, which sits on the turntable, is viewed as a tool held by the gripper. The camera is stationary relative to a world reference frame. The motion of the object is not uncoupled relative to the world, because radial points on the θ-stage, upon which the objects rests, are coupled to both X and Y world coordinates. Therefore, $J \neq J_{feat}$, and this is not a "look and move" system with respect to the object's frame.[4] While the final position and orientation of the object relative to the world can be controlled, the object path may not correspond to the X-Y table trajectory, unless the object is centered on the θ-stage. It is of practical importance to be able to control the X-Y-θ stage trajectories since their motion must ultimately be constrained within the boundaries of a physical workcell environment.

4.3. Plant Modeling for Translational and Rotational Stages

The X-Y-θ stage dynamics are modeled in this section. By neglecting dynamic interactions, each stage can be modeled independently. Newton's Second Law leads directly to the dynamic equations of motion.

4.3.1. Rotational Stage

The rotational stage (in Configuration 3) consists of a turntable platter driven through a gear-box by a DC motor with negligible aramture inductance. An equivalent diagram is shown in Figure 4-4.

The following assumptions are made to develop the mathematical model:

1. Ideal gearing (i.e., negligible backlash, friction, and inertia);
2. Negligible turntable bearing friction;
3. No motor voltage off-sets; and
4. Amplifier (amp) bandwidth (BW) is large in comparison with the motor/turntable mecahanical BW; thus, the amplifier dynamics can be neglected in the modeling.

The transfer function $G_m(s)$, from the applied voltage $e_a(t)$ to the motor shaft displacement $\theta_m(t)$ is [Kuo 82]

---

[4] This configuration would represent a "look and move" system if the task were configured such that the camera was mounted and centered on the θ-stage, while observing a stationary object.

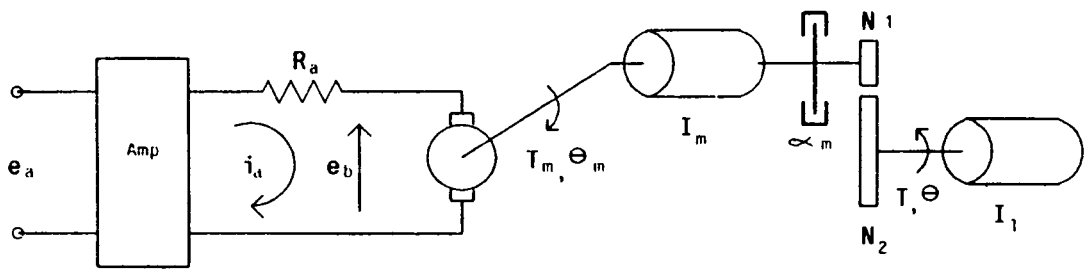

$e_a(t)$	applied control signal voltage	(volts)
amp.	unity gain, high B.W., high impedance amplifier	(volts/volt)
R_a	armature-winding resistance	(ohms)
$i_a(t)$	armature current	(amps)
$e_b(t)$	back E.M.F.	(volts)
$\theta_m(t)$	angular displacement of motor shaft	(radians)
T_m	motor torque	(oz-in)
I_m	armature moment of inertia	(oz-in-sec^2)
α_m	motor viscous-friction coefficient	(oz-in/rad/sec)
η	gear ratio N_2/N_1	(motor/turntable)
$\theta(t)$	angular displacement of turntable	(radians)
T	turntable torque	(oz-in)
I_L	moment of inertia of turntable + load	(oz-in-sec^2)
K_b	back emf constant	(volts/rad/sec)
K_t	motor torque constant	(oz-in/amp)

Figure 4-4: Rotational Stage Model

$$G_m(s) = \frac{K_m}{s(\tau_m s + 1)} \tag{4.1}$$

where the equivalent motor gain constant K_m is

$$K_m \doteq \frac{K_t}{R_a \alpha_m + K_t K_b} \tag{4.2}$$

and the equivalent motor time constant τ_m is

$$\tau_m \doteq \frac{R_a I_{eq}}{R_a \alpha_m + K_t K_b} \tag{4.3}$$

and the equivalent inertia, I_{eq}, referenced to the motor shaft is

$$I_{eq} = I_m + I_L/\eta^2$$

4.3.2. X-Y Stages

A translational stage (in Configurations 1 and 3) translates the load through a lead-screw mechanism. An equivalent diagram is shown in Figure 4-5.

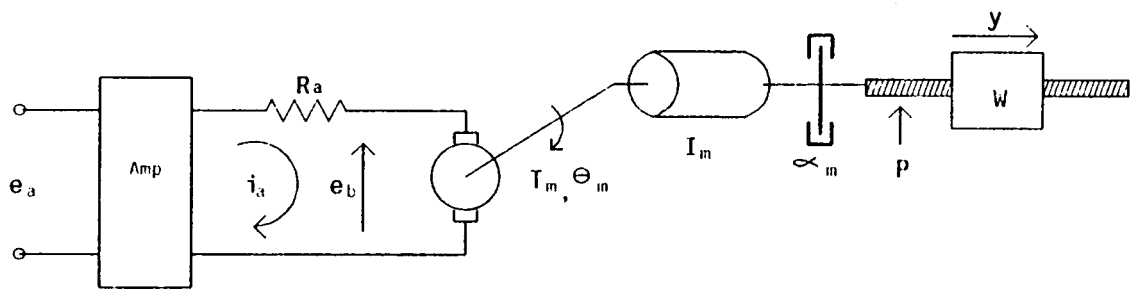

$e_a(t)$	applied control signal voltage	(volts)
amp.	unity gain, high BW amplifier	
R_a	armature-winding resistance	(ohms)
$i_a(t)$	armature current	(amps)
$e_b(t)$	back E.M.F.	(volts)
$\theta_m(t)$	angular displacement of motor shaft	(radians)
I_m	armature moment of inertia	(oz-in-sec^2)
I_{LS}	Lead-screw moment of inertia	(oz-in-sec^2)
α_m	motor-viscous friction coefficient	(oz-in/rad/sec)
p	lead-screw pitch	(threads/in)
y	linear displacement	(in)
W	net load weight	(lbs)

Figure 4-5: Translational Stage Model

The following additional assumptions are made to develop the model:

1. The lead-screw mechanism has zero backlash and negligible friction; and

2. Stage bearing friction is negligible.

The inertial equivalent, I_W, of the load referenced to the motor is [Electro-Craft 80]

$$I_W = \frac{W(\text{lbs})}{p^2} \times .0010417 \ (\text{oz-in-sec}^2)$$

When the equivalent inertia, $I_{eq} = I_m + I_{LS} + I_W$ is substituted into (4.3), the transfer function model structures for the translational stages are equivalent to the rotational stage model. The transfer functions $G_{m\text{-}x}(s)$ and $G_{m\text{-}y}(s)$, from the applied aramature voltages $e_a(t)$ to the X and Y axes motor shaft displacements, respectively, are

$$G_{m\text{-}x}(s) = \frac{K_m}{s(\tau_{m\text{-}x}s + 1)} \tag{4.4}$$

and

$$G_{m\text{-}y}(s) = \frac{K_m}{s(\tau_{m\text{-}y}s + 1)} \tag{4.5}$$

4.3.3. X-Y-Theta Stage Parameters

The X-Y-θ stage model parameter values are based on commercially available products such as the AEROTECH stages used in the Robotics Institute Flexible Assembly Lab [Sanderson 83b]. The system includes a model 316 rotational (Table 4-3), and two model 416 translational stages (Table 4-2). Each stage is driven by a motor which is equivalent to an ELECTRO-CRAFT E-508 (62 oz in) DC motor (Table 4-1).

$I_m = 0.0015$ oz-in-sec^2

$\alpha_m = 0.00095$ oz-in/rad/sec

$R_a = 3.36\ \Omega$

$K_b = 0.037$ volts/rad/sec

$K_t = 5.20$ oz-in/amp

Volts(max) = 40

Table 4-1: Electro-Craft E-508 DC MOTOR

Net-weight = 50 lbs

Platter weight = 10 lbs

Lead-screw type = Steel Ball-screw

Lead-screw pitch = 7 threads/in

Lead-screw dimension = 16 x .55 in

Table 4-2: Aerotech 416 Translational Stage

Net-weight = 29 lbs

Platter weight = 10 lbs

platter diameter = 10 in

gear ratio (η) = 108:1

Table 4-3: Aerotech 316 Rotational Stage

It remains to calculate the equivalent inertial values for each stage. It is assumed that the load inertia equals the turntable platter's inertia. This assumption is not critical because of the linear and uncoupled assumption and the large gear ratio ($\eta = 108$).

The equivalent inertia for the θ-stage is

$$I_{eq\text{-}\theta} = I_m + \frac{I_{turntable\text{-}platter} + I_{load}}{\eta^2}$$

The platter is modeled as a thin disc so that

$$I_{turntable\text{-}platter} = \frac{W(lbs)r^2(in)}{48} \ (oz\text{-}in\text{-}sec^2)$$

$$= \frac{10x(5)^2}{48} = 5.208 \ (oz\text{-}in\text{-}sec^2)$$

Since $I_{load} = I_{turntable\text{-}platter}$,

$$I_{eq\text{-}\theta} = 0.0015 + (1/108)^2(2x5.208) = 0.0024 \ oz\text{-}in\text{-}sec^2 \tag{4.6}$$

The equivalent inertia for the Y-stage is calculated according to

$$I_{eq\text{-}Y} = I_m + I_{LS} + I_W$$

The lead-screw inertia is

$$I_{LS} = D^4(in)xlength(in)x(0.0011667)$$
$$= (.55)x16x(0.0011667) = 0.0017 \ oz\text{-}in\text{-}sec^2$$

For a 10 lb. load, the net load on the Y-stage is 49 pounds [i.e., θ-stage(29) + Y-platter(10) + load(10)]. Thus,

$$I_W = 49x\frac{1}{7^2}x0.0010417$$

$$= 0.001 \ oz\text{-}in\text{-}sec^2$$

Therefore,

$$I_{eq\text{-}Y} = 0.0015 + 0.0017 + 0.001 = 0.0042 \ \ oz\text{-}in \ sec^2 \tag{4.7}$$

The net load on the X-stage is 99 pounds [i.e., θ-stage(29) + Y-stage(50) + X-platter(10) + load(10)]. Thus, the equivalent inertia of the X-stage is,

$$I_W = 99x\frac{1}{7^2}x0.0010417$$

$$= 0.0021 \ \ oz\text{-}in \ sec^2$$

Hence,

$$I_{eq\text{-}X} = 0.0015 + 0.0017 + 0.0021 = 0.0053 \ \ oz\text{-}in\text{-}sec^2 \tag{4.8}$$

Upon substituting (4.6), (4.7), and (4.8) into (4.3), the equivalent model parameters become

$$\tau_{m\text{-}\theta} = 0.041 \ sec$$
$$\tau_{m\text{-}y} = 0.072 \ sec$$
$$\tau_{m\text{-}x} = 0.091 \ sec$$

and $K_m = 26.586$ rad/sec/volt, for all stages.

4.3.4. Computer Simulation Of Uncoupled Linear Models

In this section, the computer simulation model of the linear uncoupled robots under digital computer control are derived. The discrete control signal u(kT) is fed to the motor by a digital-to-analog converter (DAC). Thus, the motor input is held constant over each sampling period T (Figures 4-6 and 4-7).

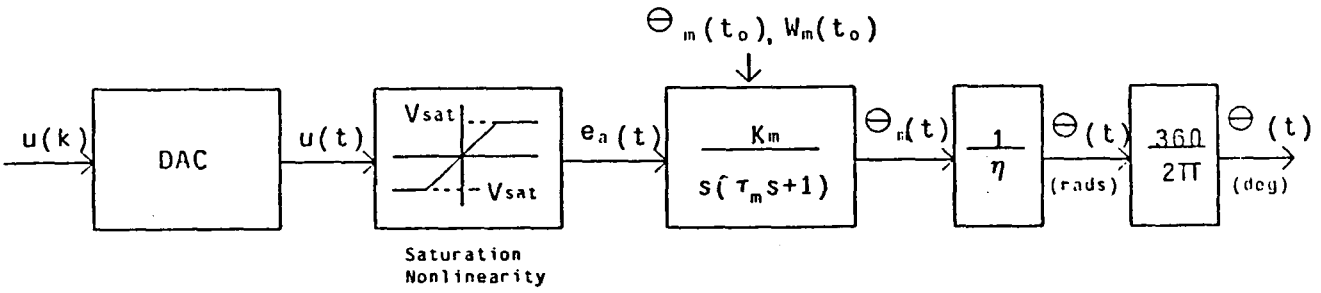

Figure 4-6: Rotational Plant Block Diagram

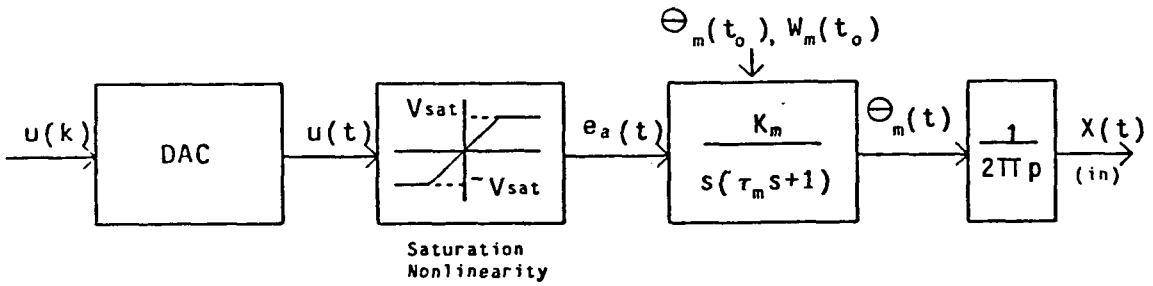

Figure 4-7: Translational Plant Block Diagram

Saturation in the DAC (and equivalently current limiting to the motor amplifier) is included in the simulation. Over the interval [$kT \leq t < (k+1)T$], the motor voltage is

$$e_a(t)=\begin{cases} u(kT) & \text{for } |u(kt)| \leq V_{sat} \\ +V_{sat} & \text{for } u(kT) > V_{sat} \\ -V_{sat} & \text{for } u(kT) < -V_{sat} \end{cases} \tag{4.9}$$

In the model, V_{sat} is set at the maximum motor driving voltage (40 Volts).

A discrete model of the analog process, which specifies the output at the sampling instants, is appropriate for the computer simulation. However, it is important to be able to examine the output between sampling intervals. Thus, the analog output, $\theta_m(t)$, over the interval

$[t_o \leq t \leq t_o + T]$, to a constant step input of magnitude V (volts) applied at t_o, with initial conditions $\theta_m(t_o)$ and $\omega_m(t_o)$, is derived. The motor speed, $\omega_m(t)$, is also derived so that the initial speed can be determined at the start of each sampling period.

The transfer function in (4.1) represents the differential equation

$$\tau_m \ddot{\theta}_m + \dot{\theta}_m = K_m e_a(t)$$

which can be written as two scaler state-space equations:

$$\dot{\theta}_m = \omega_m \tag{4.10}$$

$$\dot{\omega}_m = (-1/\tau_m)\omega_m + (K_m/\tau_m)e_a(t) \tag{4.11}$$

where the input $e_a(t) = V$ for $t_o \leq t < t_o + T$. The solution to the system in (4.10) and (4.11) is

$$\theta_m(t) = \theta_m(t_o) + \tau_m[\omega(t_o) - K_m V]\left(1 - e^{-(t-t_o)/\tau_m}\right) + K_m V(t-t_o) \qquad \text{for } t_o \leq t \leq t + T$$

and

$$\omega_m(t) = \omega_m(t_o)e^{(t-t_o)/\tau_m} + K_m V\left(1 - e^{-(t-t_o)/\tau_m}\right)$$

If the motor displacements for the turntable, X-stage, and Y-stage are $\theta_{m\text{-}\theta}$, $\theta_{m\text{-}x}$, and $\theta_{m\text{-}y}$, respectively, then

$$X(t) = \frac{1}{2\pi p}\theta_{m\text{-}x}(t) \quad \text{inches}$$

$$Y(t) = \frac{1}{2\pi p}\theta_{m\text{-}y}(t) \quad \text{inches}$$

$$\theta(t) = \frac{360.0}{2\pi\eta}\theta_{m\text{-}\theta}(t) \quad \text{degrees}$$

4.4. Plant Modeling for 2 DOF Robot Arm

A 2 DOF articulated robot arm is modeled in this section. The arm is actuated by DC servo motors which are mechanically coupled to the link joints by gearing mechanisms. (Figure 4-8) The motor for link 2 is mounted at the rear of link 1 to act as a counterweight. The motor for link 1 is mounted in the stationary base.

The following assumptions are made to derive the dynamic model:

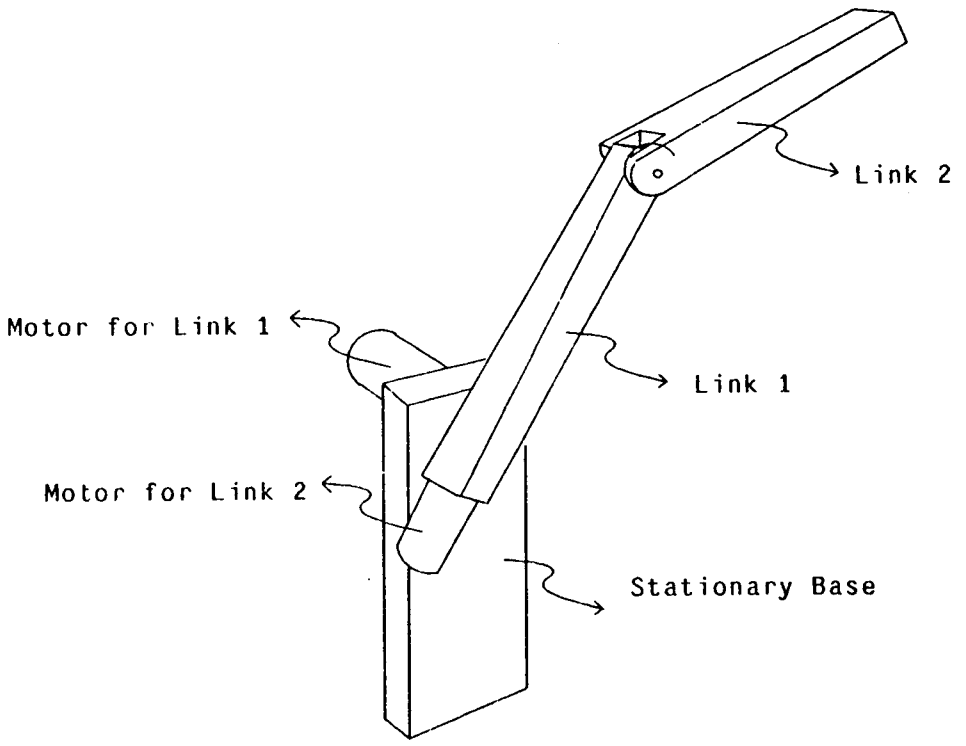

Figure 4-8: 2 DOF Robot Arm

1. Links 1 and 2 are modeled as thin rigid rods of lengths r_1 and r_2, and mass m_{r1} and m_{r2}, respectively;

2. Any payload (including a camera) is modeled as a point mass, m_{p2}, at the end of link 2;

3. The gear box coupling for link 2 is modeled as a point mass, m_{p1}, at the end of link 1;

4. The counter-weight (motor) is modeled as a thin rigid rod, of length r_1/k[5] and mass m_c, at the rear of link 1;

5. There are no off-sets between links;

6. All gearing is ideal; and

7. All bearing friction is negligible

This simplified geometric arm model facilitates development of the mathematical model. The

---

[5]The counter-weight length is defined as a fraction (1/k) of the link length to facilitate derivation of the dynamic equations in Appendix B.

model results in a nonlinear dynamic system which exhibits the Coriolis, centrifugal, gravitational, and inertial coupling torque components present in a real arm.

4.4.1. Kinematic Equations

The arm kinematic equations describe the motion of the arm in Cartesian space. These equations are required to derive the arm dynamics and image transforms.

A coordinate frame diagram of the arm is shown in Figure 4-9.

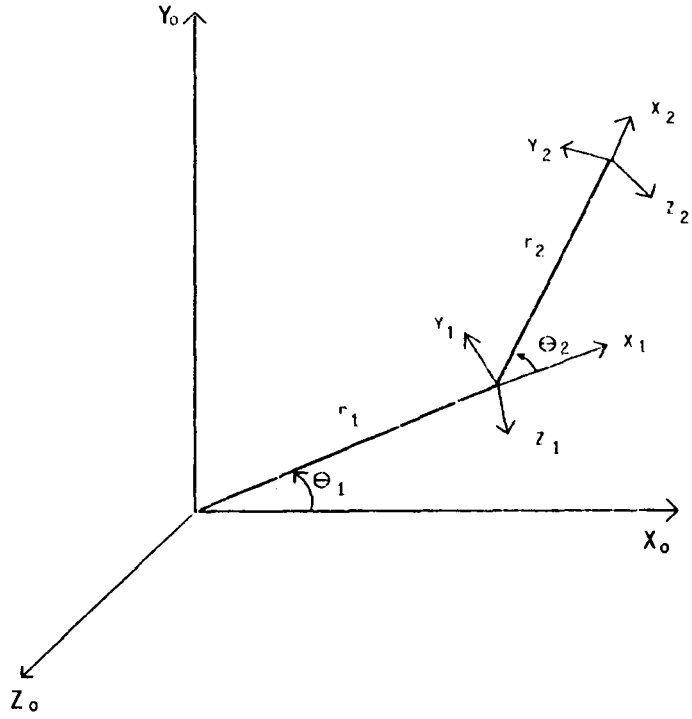

Figure 4-9: Arm Coordinate Frames

Each link, including the base, is assigned a Cartesian coordinate frame in accordance with the Denavit-Hartenberg convention [Denavit 55]. The coordinate frame associated with the reference base, $[\vec{X}_o, \vec{Y}_o, \vec{Z}_o]$, serves as the world coordinate frame. The frames associated with links 1 and 2 are $[\vec{X}_1, \vec{Y}_1, \vec{Z}_1]$ and $[\vec{X}_2, \vec{Y}_2, \vec{Z}_2]$.

The position of the end of link 2 with respect to the world frame is derived. Let

T_j = homogeneous transformation describing the position

of link j relative to the world frame, and

A_i = homogeneous transform describing the position of link i relative to link i-1 (where link 0 corresponds to the reference base).

Thus,

$$T_j = A_1 A_2 \cdots A_j$$

For the two DOF arm,

$$A_1 = \begin{bmatrix} C_1 & S_1 & 0 & r_1C_1 \\ -S_1 & C_1 & 0 & r_1S_1 \\ 0 & 0 & 1 & 0 \\ 0 & 0 & 0 & 1 \end{bmatrix} \quad ; \quad A_2 = \begin{bmatrix} C_2 & -S_2 & 0 & r_2C_2 \\ S_2 & C_2 & 0 & r_2S_2 \\ 0 & 0 & 1 & 0 \\ 0 & 0 & 0 & 1 \end{bmatrix}$$

where

$C_i \doteq \cos(\theta_i)$
$S_i \doteq \sin(\theta_i)$

Thus,

$$T_1 = A_1$$

$$T_2 = A_1 A_2 = \begin{bmatrix} C_{12} & -S_{12} & 0 & r_2C_{12} + r_1C_1 \\ S_{12} & C_{12} & 0 & r_2S_{12} + r_1S_1 \\ 0 & 0 & 1 & 0 \\ 0 & 0 & 0 & 1 \end{bmatrix} \tag{4.12}$$

where

$C_{ij} \doteq \cos(\theta_i + \theta_j)$
$S_{ij} \doteq \sin(\theta_i + \theta_j)$

From (4.12), the rrobot positions are

$$X(t) = r_2\cos\left(\theta_1(t) + \theta_2(t)\right) + r_1\cos\theta_1(t)$$

$$Y(t) = r_2\sin\left(\theta_1(t) + \theta_2(t)\right) + r_1\sin\theta_1(t) \tag{4.13}$$

4.4.2. Rigid Body Dynamics

The dynamic equations for the manipulator are developed, in Appendix B, using the Lagrangian formulation. The dynamic models for the two revolute joint angles θ are:

$$F_1 = D_{11}\ddot{\theta}_1 + D_{12}\ddot{\theta}_2 + D_{112}\dot{\theta}_1\dot{\theta}_2 + D_{122}\dot{\theta}_2^{\,2} + D_1 \tag{4.14}$$

$$F_2 = D_{12}\ddot{\theta}_1 + D_{22}\ddot{\theta}_2 + D_{211}\dot{\theta}_1^{\,2} \qquad + D_2 \tag{4.15}$$

where

$$D_{11} = \left[\frac{m_{r1}}{3} + \frac{m_c}{3k^2} + m_{p1} + m_{r2} + m_{p2}\right] r_1^2 + 2r_1 r_2 C_2 \left[\frac{m_{r2}}{2} + m_{p2}\right] + \left[\frac{m_{r2}}{3} + m_{p2}\right] r_2^2$$

$$D_{12} = \left[m_{p2} + \frac{m_{r2}}{3}\right] r_2^2 + r_1 r_2 C_2 \left[\frac{m_{r2}}{2} + m_{p2}\right]$$

$$D_{112} = -2r_1 r_2 S_2 \left[\frac{m_{r2}}{2} + m_{p2}\right]$$

$$D_{122} = -r_1 r_2 S_2 \left[\frac{m_{r2}}{2} + m_{p2}\right]$$

$$D_1 = g\left\{\left[\frac{m_{r1}}{2} + m_{p1} - \frac{m_c}{2k}\right] r_1 S_1 + \left[\frac{r_2}{2} S_{12} + r_1 S_1\right] m_{r2} + \left[r_2 S_{12} + r_1 S_1\right] m_{p2}\right\}$$

$$D_{22} = \left[m_{p2} + \frac{m_{r2}}{3}\right] r_2^2$$

$$D_{211} = r_1 r_2 S_2 \left[\frac{m_{r2}}{2} + m_{p2}\right]$$

$$D_2 = g r_2 S_{12} \left[m_{p2} + \frac{m_{r2}}{2}\right]$$

In the simulations, the gravity torques, D_1 and D_2, are set equal to zero.

4.4.3. Actuator Dynamics

The link torques F_1 and F_2 are related to the actuator dynamics. The DC motor actuator for the ith link is modeled Figure 4-10.

The motor torque F_{mi} driving link i is

$$F_{mi} = K_{ti}(e_{a1} - K_{bi}\dot{\theta}_{mi})/R_{ai} = I_{mi}\ddot{\theta}_{mi} + \alpha_{mi}\dot{\theta}_{mi} + F_i/\eta_i$$

so that the link torque F_i is

$$F_i = \frac{K_{ti}\eta_i}{R_{ai}}(e_{ai} - K_{bi}\dot{\theta}_{mi}) - I_{mi}\eta_i\ddot{\theta}_{mi} - \alpha_{mi}\eta_{mi}\dot{\theta}_{mi}$$

In terms of the link displacement, $\theta_i = \theta_{mi}/\eta_i$, the link torques are

$$F_1 = \frac{K_{t1}}{R_{a1}}(e_{a1}\eta_1 - K_{b1}\eta_1^2\dot{\theta}_1) - \alpha_1\eta_1^2\dot{\theta}_1 - I_{m1}\eta_1^2\ddot{\theta}_1 \tag{4.16}$$

and

$$F_2 = \frac{K_{t2}}{R_{a2}}(e_{a2}\eta_2 - K_{b1}\eta_2^2\dot{\theta}_2) - \alpha_2\eta_2^2\dot{\theta}_2 - I_{m2}\eta_2^2\ddot{\theta}_2 \tag{4.17}$$

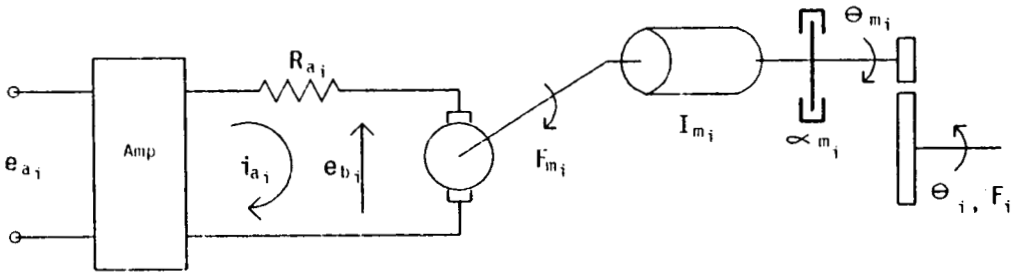

$e_{ai}(t)$	applied control signal voltage	(volts)
amp.	unity gain, high B.W., high impedance amplifier	
R_{ai}	armature-winding resistance	(ohms)
$i_{ai}(t)$	armature current	(amps)
$e_{bi}(t)$	back E.M.F.	(volts)
$\theta_{mi}(t)$	angular displacement of motor shaft	(radians)
F_{mi}	motor torque	(oz-in)
I_{mi}	armature moment of inertia	(oz-in-sec^2)
α_{mi}	motor viscous-friction coefficient	(oz-in/rad/sec)
η_i	gear ratio N_2/N_1	(rev. motor/rev. turntable)
$\theta_i(t)$	angular displacement of link	(radians)
F_i	link torque	(oz-in)
K_{bi}	back emf constant	(volts/rad/sec)
K_{ti}	motor torque constant	(oz-in/amp)

Figure 4-10: Robot Actuator

4.4.4. Robot Arm Parameters

In this section a manipulator is designed for the model structure assumptions specified at the outset of this section. The mechanical structure is assumed to have the following dimensions and weights;

- Maximum payload = 5 lbs. (1 pound of which is the camera)
- Link lengths $r_1 = r_2 = 17$ in.
- Weight of link 1 = 7 lbs
- Weight of link 2 = 5 lbs
- Weight of gear-box = 1 lb

The motors and gearing are selected according to the design criteria:

1. Maximum individual link speed = 180 deg/sec = π rad/sec

2. Maximum individual link acceleration = 1800 deg/sec^2 = 10π rad/sec^2

3. Minimize motor energy dissipation while keeping the gear ratio η small enough to reduce gearing backlash and friction.

The design steps are outlined below, and are performed for each individual link, under the assumption of negligible dynamic coupling:

STEP 1: Find the torque ($T_{max\text{-}acc}$) required to achieve the maximum specified acceleration for the maximum payload at the maximum link inertia.

STEP 2: Find the maximum torque ($T_{max\text{-}g}$) required to hold the maximum payload against gravity.

STEP 3: Specify motor torque requirements:

1. The peak motor torque, $T_{peak} = (T_{max\text{-}acc} + T_{max\text{-}g})/\eta$

2. The continuous motor stall torque, $T_{stall} = T_{max\text{-}g}/\eta$

3. The peak motor speed as $180 \bullet \eta$ deg/sec = $30 \bullet \eta$ RPM

STEP 4: To select the gearing, choose a motor (which is anticipated to satisfy the torque requirements in Step 3) and set

$$\eta_i = (D_{ii\text{-}nominal}/I_m)^{1/2}$$

where $D_{ii\text{-}nominal}$ is chosen as a nominal value of the link inertia. This selection for η minimizes the energy dissipation in the motor and maximizes the power transfer to the link. For this design, choose $D_{ii\text{-}nominal}$ as the average of D_{ii} evaluated at the maximum five pound load and no load operating points. To evaluate D_{11}, it is assumed that $\theta_2 = 45$(deg). If η_i is too large (e.g.,η>35)), then it can be reduced by a third with only a 17% increase in motor dissipation [Electro Craft 80]. Finally, check if this motor/gear combination satisfy the motor torque requirements in Step 3.

While ther are numerous motor/gear combinations which will satisfy the stated requirements, the following additional guidelines are used:

1. Maintain η<35 to minimize backlash, friction, weight, and cost: and

2. If possible, allow for a safety margin in the peak and stall torque ratings.

Before proceeding, the weights are converted to mass according to

$$m = W/g$$

The units for g and W are selected so that the torques are specified in units of oz-in. Thus,

$$m = \frac{W(lbs)16(oz/lb)}{32(ft/sec^2)12(in/ft)}$$

$$= \frac{W(lbs)}{24} \quad (oz/in/sec^2)$$

and

$m_{r1} = 0.29167$
$m_{r2} = 0.20833$
$m_{p1} = 0.04167$
$m_{p2} = 0.20833$ (with 5 lb. load)
$m_{p2} = 0.04167$ (with 1 lb. load)
$m_c =$ (to be determined in motor selection process)

The motor selection process proceeds backward from the last link.

4.4.4.1. Motor 2 Selection

Step 1:

$$D_{22} = (m_{r2}/3 + m_{p2})r_2^2$$

$$D_{22\text{-}max} = 80.27 \text{ oz-in-sec}^2$$

and

$$T_{max\text{-}acc} = D_{22\text{-}max}\ddot{\theta}_{max}$$

$$= 2522 \text{ oz-in}$$

Step 2:

$$T_g = D_2 = gr_2S_{12}(m_{p2} + m_{r2}/2)$$

$$T_{max\text{-}g} = 2040 \text{ oz-in (with a 5 Lb. load)}$$

Step 3:

$$T_{peak}/\eta_2 = (2522 + 2040)/\eta_2 = 4562/\eta_2 \text{ oz-in}$$

$$T_{stall}/\eta_2 = 2040/\eta_2 \text{ oz-in}$$

$$\eta \text{ X peak motor speed} = \eta_2 \bullet 30 \text{ RPM}$$

Step 4: Before calculating the gear ratio, it is noted that the effective inertia of motor 2 includes the armature inertia and the non-negligible inertia of the motor-to-gear shaft

coupling. This shaft is modeled as a 17x3/8 in round steel shaft. Assuming the density of steel is .28 lb/in^3, the shaft weighs .52 lbs (which is assumed to be included in the net weight of link 2). Thus,

$$I_{shaft} = .5 m_{shaft} r^2_{shaft}$$

$$= 0.00038 \text{ oz-in-sec}^2$$

To meet these requirements, ELECTRO-CRAFT 660-E motor is selected (Table 4-4).

$I_m = 0.032$ oz-in-sec^2

$\alpha_m = 0.0065$ oz-in/rad/sec

$R_a = 2.15\ \Omega$

$K_b = 0.24$ volts/rad/sec

$K_t = 34.19$ oz-in/amp

Volts(max) = 43

Weight = 6 lb. 2 oz. ($m_c = 0.2552$ oz/in/sec^2)

length = 5.5

Table 4-4: D. C. Motor E-660

This motor is over-rated for the peak and stall torque requirements, but a smaller motor would require a significantly larger gear ratio. This motor is chosen to achieve a reasonable gear ratio, while its added weight serves as a counter-weight.

The link inertia with no load is

$$D_{22} = 20.07 \text{ oz-in-sec}^2$$

and, the nominal link inertia is

$$(80.27 + 20.07)/2 = 50.17 \text{ oz-in-sec}^2$$

The nominal gear-ratio is

$$\eta_2 = (50.17/.03238)^{1/2} = 39.36$$

and, reduced by 33% is

$$\eta_2 = 26$$

4.4.4.2. Motor 1 Selection

Step 1:

$$D_{11} = \left[\frac{m_{r1}}{3} + \frac{m_c}{3k^2} + m_{p1} + m_{r2} + m_{p2}\right] r_1^2 + 2r_1 r_2 C_2 \left[\frac{m_{r2}}{2} + m_{p2}\right] + \left[\frac{m_{r2}}{3} + m_{p2}\right] r_2^2$$

$$D_{11\text{-}max} = 424 \text{ oz-in-sec}^2$$

and

$$T_{max\text{-}acc} = D_{11\text{-}max}\ddot{\theta}_{max} = 13322 \text{ oz-in}$$

Step 2:

$$T_{g\text{-}max} = D_1 = g\left\{\left[\frac{m_{r1}}{2} + m_{p1}\cdot\frac{m_c}{2k}\right]r_1S_1 + \left[\frac{r_2}{2}S_{12} + r_1S_1\right]m_{r2} + \left[r_2S_{12} + r_1S_1\right]m_{p2}\right\}$$

$$= 2723 \quad \text{oz-in}$$

Step 3:

$$T_{peak} = (13322 + 2723)/\eta_1 = 16045/\eta_1$$
$$T_{stall} = 2723/\eta_1$$

Step 4:

$$D_{11\text{-}full\text{-}load} = 371 \text{ oz-in sec}^2 \text{ (at } \theta = 45 \text{ deg)}$$
$$D_{11\text{-}no\text{-}load} = 166 \text{ oz-in sec}^2 \text{ (at } \theta = 45 \text{ deg)}$$

thus

$$D_{nominal} = (371 + 166)/2 = 269 \text{ oz-in-sec}^2$$

To satisfy these requirements, Electro-Craft motor E-701 is selected (Table 4-5).

$K_t = 40.77$ oz-in/amp
$K_b = .288$ v/rad/sec
$R_a = 2.6\ \Omega$
$I_m = 0.1$ oz-in-sec^2
$\alpha_m = 0.048$ oz-in/rad/sec
Volts(max) = 46.8

Table 4-5: D.C. Motor E-701

The nominal gear ratio is

$$\eta_1 = (269/0.1)^{1/2} = 51.86$$

and reducing by 33%

$$\eta_1 = 35$$

4.4.5. Computer Simulation of the Robot Arm

The differential equations (4.14),(4.15),(4.16), and (4.17) define a fourth order coupled nonlinear dynamic system. The simulation uses the IMSL [IMSL 82] Fortran library routine "DVERK" to numerically solve these equations. The routine is a sixth order Runge-Kutta algorithm with an automatic variable integration step size.

To implement the algorithm, the dynamic equations are represented as the system of first-order differential equations $\dot{\underline{X}} = F(\underline{X})$, where $\underline{X}^T = [X_1, X_2, X_3, X_4]$ are the state-variables. DVERK

produces estimates of $X_i(t_o + T_{inc})$ from $X(t_o)$. In the simulation, T_{inc} is set to T/n_k (n_k = integer) to exhibit the output between sampling instants. (The integration step-size is typically much smaller than T_{inc} and is automatically adjusted in DVERK to minimize the estimation error.)

The system is represented in state-variable form according to the following assignments:

$$X_1 = \theta_1$$
$$X_2 = \dot{\theta}_1$$
$$X_3 = \theta_2$$
$$X_4 = \dot{\theta}_2$$

Thus,

$$\dot{X}_1 = X_2$$
$$\dot{X}_3 = X_4$$

From (4.14),(4.15),(4.16), and (4.17)

$$F_1 = D_{11}\dot{X}_2 + D_{12}\dot{X}_4 + D_{112}X_2X_4 + D_{122}X_4^2 + D_1 \tag{4.18}$$

$$F_2 = D_{12}\dot{X}_2 + D_{22}\dot{X}_4 + D_{211}X_2^2 + D_2 \tag{4.19}$$

$$F_1 = \frac{K_{t1}}{R_{a1}}(e_{a1}\eta_1 - K_{b1}\eta_1^2X_2) - \alpha_1\eta_1^2X_2 - I_{m1}\eta_1^2\dot{X}_2 \tag{4.20}$$

$$F_2 = \frac{K_{t2}}{R_{a2}}(e_{a2}\eta_2 - K_{b2}\eta_2^2X_4) - \alpha_2\eta_2^2X_4 - I_{m2}\eta_2^2\dot{X}_4 \tag{4.21}$$

To simplify the notation let

$$Q \doteq \frac{K_{t1}}{R_{a1}}(e_{a1}\eta_1 - K_{b1}\eta_1^2X_2) - \alpha_1\eta_1^2X_2$$

and

$$Z \doteq \frac{K_{t2}}{R_{a2}}(e_{a2}\eta_2 - K_{b2}\eta_2^2X_4) - \alpha_2\eta_2^2X_4$$

where e_a is defined in (4.9). Equations (4.18),(4.19),(4.20), and (4.21) become

$$Q = (D_{11} + I_{m1}\eta_1^2)\dot{X}_2 + D_{12}\dot{X}_4 + D_{112}X_2X_4 + D_{122}X_4^2 + D_1 \tag{4.22}$$

$$Z = (D_{22} + I_{m2}\eta_2^2)\dot{X}_4 + D_{12}\dot{X}_2 + D_{211}X_2^2 + D_2 \tag{4.23}$$

Upon solving (4.22) and (4.23) for $\dot{X}_2$ and $\dot{X}_4$, the state model is:

$$\dot{X}_1 = X_2 \tag{4.24}$$

$$\dot{X}_2 = \frac{D_{2e}}{D_{1e}D_{2e} - D_{12}^2}\left\{Q - \frac{D_{12}}{D_{2e}}\left[Z - D_{211}X_2^2 - D_2\right] - D_{112}X_2X_4 - D_{122}X_4^2 - D_1\right\} \tag{4.25}$$

$$\dot{X}_3 = X_4 \tag{4.26}$$

$$\dot{X}_4 = \frac{D_{1e}}{D_{1e}D_{2e} - D_{12}^2}\left\{Z - \frac{D_{12}}{D_{1e}}\left[Q - D_{122}X_4^2 - D_{112}X_2X_4 - D_1\right] - D_{211}X_2^2 - D_2\right\} \tag{4.27}$$

where

$$D_{1e} = D_{11} + I_{m1}\eta_1^2$$
$$D_{2e} = D_{22} + I_{m2}\eta_2^2$$

During hierarchical control either links 1 or 2 can be braked. These cases are simulated as follows:

Case 1: link 1 - free and link 2 - braked

Equations (4.18) and (4.20) reduce to

$$F_1 = D_{11} + D_1$$

and

$$F_1 = Q - I_{m1}\eta_1^2 X_2$$

so that

$$\dot{X}_1 = X_2$$
$$\dot{X}_2 = \frac{Q - D_1}{D_{1e}}$$
$$\dot{X}_3 = 0$$
$$\dot{X}_4 = 0$$

Case 2: link 1 - braked and link 2-free

The state-space model becomes

$$\dot{X}_1 = 0$$
$$\dot{X}_2 = 0$$
$$\dot{x}_3 = X_4$$
$$\dot{X}_4 = \frac{Z - D_2}{D_{2e}}$$

The computer simulation of the robot arm is depicted in Figure 4-11.

4.4.5.1. Linear Model

During initial analysis of IBVS, it is useful to model the arm dynamics as an uncoupled linear system. The MRAC controller's ability to adjust to the nonlinear feature gains can then be evaluated independent of the nonlinear dynamics. An uncoupled linear model is obtained by assuming that all the coupling terms in (4.14) and (4.15) are zero, while D_{ii} is evaluated at the operating point. (D_i is set to zero since gravity is not modeled in these simulations.)

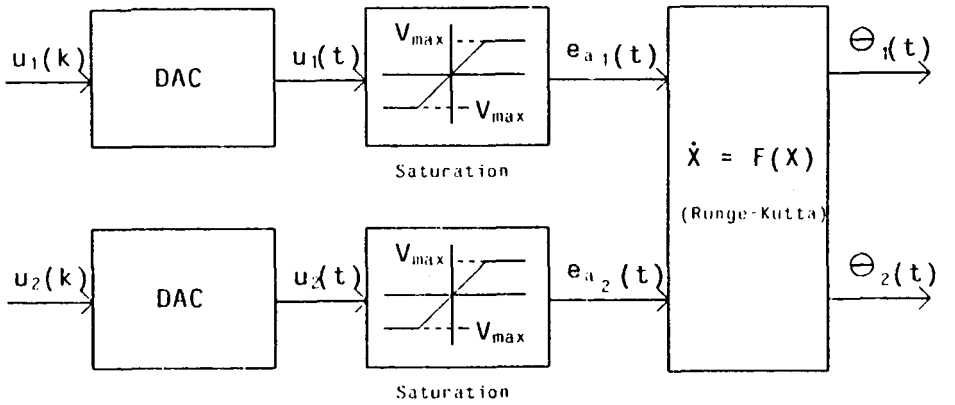

Figure 4-11: Arm Simulation Block Diagram

Equations (4.14),(4.15),(4.16), and (4.17) reduce to

$$\frac{K_i}{R_{ai}}(e_{ai}\eta_i - K_{bi}\eta_i^2\dot{\theta}_i) - \alpha_{mi}\eta_i^2\dot{\theta}_i - I_{mi}\eta_i^2\ddot{\theta}_i = D_{ii}\ddot{\theta}_i$$

To apply the linear model routines developed in Section 4.3, the displacement of the ith link, θ_i, is converted to a motor displacement according to, and $\theta_i = \theta_{mi}/\eta_i$

$$\frac{K_i}{R_{ai}}(e_{ai}\eta_i - K_{bi}\eta_i\dot{\theta}_{mi}) - \alpha_{mi}\eta_i\dot{\theta}_{mi} - I_{mi}\eta_i\ddot{\theta}_{mi} = D_{ii}\ddot{\theta}_{mi}/\eta_i$$

The corresponding transfer function $G_{mi}(s)$, from the applied voltage to the motor shaft, is

$$G_{mi}(s) = \frac{K_{mi}}{s(\tau_{mi}s + 1)}$$

where

$$K_{mi} = \frac{K_{ti}}{R_{ai}\alpha_{mi} + K_{ti}K_{bi}}$$

$$\tau_{mi} = \frac{D_{ii\text{-}eq}R_{ai}}{R_{ai}\alpha_{mi} + K_{ti}K_{bi}}$$

and

$$D_{ii\text{-}eq} = I_{mi} + D_{ii}/\eta_i^2$$

4.5. Modeling Picture Taking and Feature Measurement

In this section, a model for the vision system described in Chapter 2 is developed. The transduction process (or camera and image) are modeled by defining image transformations which map 3-dimensional object coordinates into 2-dimensional image points. The image intensities are assumed to be binary, and image point coordinates are considered to be analog. Image feature measurements are then derived from the image point coordinates. The dynamics of the transduction-to-feature extraction process are modeled by a unit delay (i.e., $n_d = 1$ Section 3.3). Various time delay durations, and thus sampling periods T, are simulated to evaluate the effect of different sampling-to-bandwidth ratios. A measurement noise model (which can represent transducer quantization, thresholding effects, and lighting noise) is also included.

4.5.1. Image Transformations

The camera is modeled by defining a transformation which maps 3-dimensional object coordinates into 2-dimensional image coordinates. To perform this transformation, the camera is modeled as a pinhole lens, with an image plane lying at a distance F behind the lens [Duda 73]. To produce a non-inverted image, a frontal image plane, defined by $[\vec{X}_{cam}, \vec{Z}_{cam}]$ is assumed to lie at a distance F in front of the lens. Thus, $[\vec{Y}_{cam}]$ defines the optical axis. This camera model defines the perspective transformation,

$$T_p = \begin{bmatrix} 1 & 0 & 0 & 0 \\ 0 & 1 & 0 & 0 \\ 0 & 0 & 1 & 0 \\ 0 & 1/F & 0 & 1 \end{bmatrix}$$

For a three-dimensional object point $(X_{rel}, Y_{rel}, Z_{rel})$ measured in the camera coordinate frame, the corresponding two-dimensional image or picture coordinate (X_{pic}, Y_{pic}) is specified by the homogeneous perspective transformation

$$\begin{bmatrix} 1 & 0 & 0 & 0 \\ 0 & 1 & 0 & 0 \\ 0 & 0 & 1 & 0 \\ 0 & 1/F & 0 & 1 \end{bmatrix} \begin{bmatrix} X_{rel} \\ Y_{rel} \\ Z_{rel} \\ 1 \end{bmatrix} = \begin{bmatrix} X_{rel} \\ Y_{rel} \\ Z_{rel} \\ 1 + Y_{rel}/F \end{bmatrix}$$

Thus,

$$X_{pic} = \frac{X_{rel}}{1 + Y_{rel}/F}$$

and

$$Z_{pic} = \frac{Z_{rel}}{1 + Y_{rel}/F} \tag{4.28}$$

The picture points are normalized to the dimensions of the image plane so that the features (derived in Section 4.5.2.1) are dimensionless. If it is assumed that the image plane (e.g., film, or ccd chip) is a square with sides of length equal to 'ret'[6], then (4.28) becomes

$$X_{pic} \leftarrow X_{pic}/ret$$

$$Z_{pic} \leftarrow Z_{pic}/ret$$

The focal length, F, is adjusted so that the largest object dimension occupies approximately 25 to 33 percent of the image in the desired view. This allows for a margin of motion of the object within the image during control.

4.5.2. Feature Transformations

Image features are derived from the idealized non-distorted two-dimensional image points (X_{pic},Z_{pic}). Image distortions, which can arise from the numerous factors noted in Chapter 2, are difficult to model and vary widely with lighting conditions, transducer resolution and linearity. These distortions are manifested as measurement noise and limit the system accuracy, dynamic performance, and relative stability. To evaluate characteristics of IBVS control under noisy conditions, simulations are performed in Chapter 5 using additive measurement noise. Noise modeling is included in Section 4.5.2.3.

4.5.2.1. Two-Dimensional Line

Two features are derived for the line in space simulations (for Configurations 1 and 2). According to the configuration specification, the perceived angle of the line's image remains constant, and only two features can be obtained from such a binary image:

1. length of line - l_{ength}; and

2. X center-of-gravity of line - X_{cog}

These features are derived as follows. The position of the center of the line (Figure 4-1) relative to the image plane is (X_{rel},Y_{rel}). The end-points of the line (Figure 4-12), measured in the camera coordinate system, are

---

[6] In the simulations, ret = 0.25 inches (e.g., approximating the dimension of a typical CCD device such as the Fairchild CCD211).

$$(X_1,Y_1) = \left([X_{rel} + .5\, l_o\cos\theta_{rel}],[Y_{rel} + .5\, l_o\sin\theta_{rel}]\right)$$
$$(X_2,Y_2) = \left([X_{rel} - .5\, l_o\cos\theta_{rel}],[Y_{rel} - .5\, l_o\sin\theta_{rel}]\right) \tag{4.29}$$

From (4.28) and (4.29), the perceived line length is

$$l_{ength} = X_{pic\text{-}1} - X_{pic\text{-}2}$$
$$= \frac{4Fl_o}{ret} \bullet \frac{(F + Y_{rel})\cos\theta_{rel} - X_{rel}\sin\theta_{rel}}{4(F + Y_{rel})^2 - (l_o\sin\theta_{rel})^2} \quad \text{(dimensionless)} \tag{4.30}$$

and, the perceived center-of-gravity is

$$X_{cog} = \frac{X_{pic\text{-}1} + X_{pic\text{-}2}}{2}$$
$$= \frac{F}{ret} \bullet \frac{4X_{rel}(F + Y_{rel}) - l_o^2\sin\theta_{rel}\cos\theta_{rel}}{4(F + Y_{rel})^2 - (l_o\sin\theta_{rel})^2} \quad \text{(dimensionless)} \tag{4.31}$$

It remains to calculate X_{rel}, Y_{rel}, and θ_{rel} as a function of the object and robot positions. For the Cartesian system (Figure 4-1):

$$X_{rel}(t) = X_{obj} - X(t)$$
$$Y_{rel}(t) = Y_{obj} - Y(t)$$
$$\theta_{rel} = \theta_{obj} \tag{4.32}$$

For the articulated arm (Figure 4-2), coordinate transformations are used. The basic transformation is

$$T_2 T_{cam} T_{rel} = T_{obj} \tag{4.33}$$

where

T_2 = end of arm relative to world
T_{cam} = image plane relative to end of arm
T_{rel} = line relative to image plane
T_{obj} = line relative to world

From (4.33)

$$T_{rel} = T_{cam}^{-1}\, T_2^{-1} T_{obj} \tag{4.34}$$

T_{cam} is specified by the assumptions of Section 4.2.2 to be a rotation about the **Z** axis of the arm. Thus,

$$T_{cam} = \begin{bmatrix} C_{12} & S_{12} & 0 & 0 \\ -S_{12} & C_{12} & 0 & 0 \\ 0 & 0 & 1 & 0 \\ 0 & 0 & 0 & 1 \end{bmatrix} \tag{4.35}$$

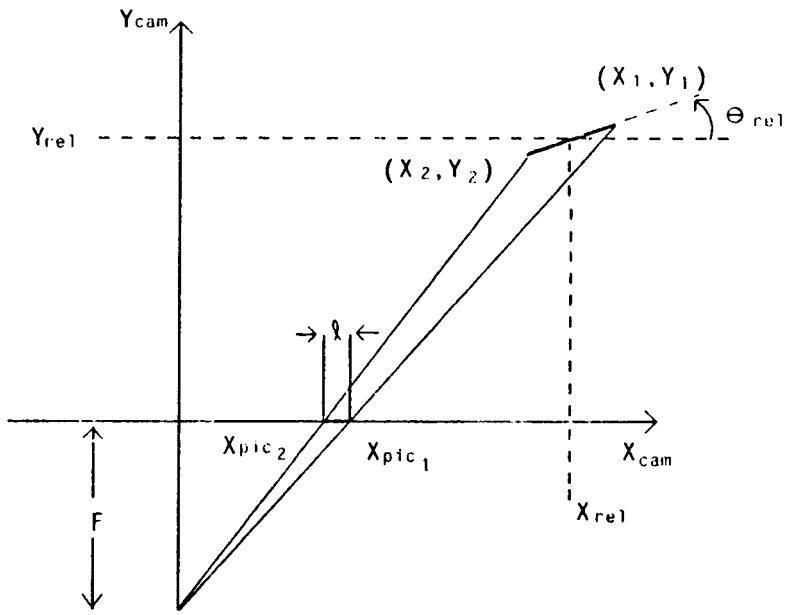

Figure 4-12: Line-Image

and

$$T_{cam}^{-1} = \begin{bmatrix} C_{12} & -S_{12} & 0 & 0 \\ S_{12} & C_{12} & 0 & 0 \\ 0 & 0 & 1 & 0 \\ 0 & 0 & 0 & 1 \end{bmatrix}$$

Since T_2 is defined in (4.12),

$$T_2^{-1} = \begin{bmatrix} C_{12} & -S_{12} & 0 & -(r_1C_2 + r_2) \\ S_{12} & C_{12} & 0 & r_1S_2 \\ 0 & 0 & 1 & 0 \\ 0 & 0 & 0 & 1 \end{bmatrix}$$

Since

$$T_{obj} = \begin{bmatrix} C\theta_{obj} & -S\theta_{obj} & 0 & X_{obj} \\ S\theta_{obj} & C\theta_{obj} & 0 & Y_{obj} \\ 0 & 0 & 1 & 0 \\ 0 & 0 & 0 & 1 \end{bmatrix}$$

then according to (4.34)

$$T_{rel} = \begin{bmatrix} C\theta_{obj} & -S\theta_{obj} & 0 & X_{obj}-(r_2C_{12} + r_1C_1) \\ S\theta_{obj} & C\theta_{obj} & 0 & Y_{obj}-(r_2S_{12} + r_1S_1) \\ 0 & 0 & 1 & 0 \\ 0 & 0 & 0 & 1 \end{bmatrix}$$

Hence

$$X_{rel}(t) = X_{obj} - \left[r_2\cos\left(\theta_1(t) + \theta_2(t)\right) + r_1\cos\theta_1(t) \right]$$

$$Y_{rel}(t) = Y_{obj} - \left[r_2\sin\left(\theta_1(t) + \theta_2(t)\right) + r_1\sin\theta_1(t) \right]$$

$$\theta_{rel} = \theta_{obj} \tag{4.36}$$

During the simulation experiments, three conditions are evaluated to assure that the derived features are valid. The conditions determine if the line is:

1. In front of the camera (or image plane);

2. In the field of view; and

3. Not hidden (it is assumed that only one side of the line is visible)

If any of these conditions are violated, then the experiment is terminated. The conditions are evaluated as follows:

Condition 1: true if (Y_1 or Y_2) > 0; else false

Condition 2: true if $|X_{pic\text{-}1}|$ or $|X_{pic\text{-}2}| < ret/2$; else false

Condition 3: true if $\theta_{rel} < \arctan(Y_{rel}, X_{rel})$; else false. (4.37)

4.5.2.2. Polyhedral Objects

The third configuration uses convex polyhedral objects for the control tasks. Each object is defined by:

1. Labeling it's constituent vertices and identifying their coordinates in the object coordinate system; and

2. Defining the object planes by assigning to each an ordered listing of the bounding vertices.

Three objects (a cube, pyramid, and wedge) are shown in Figure 4-13.

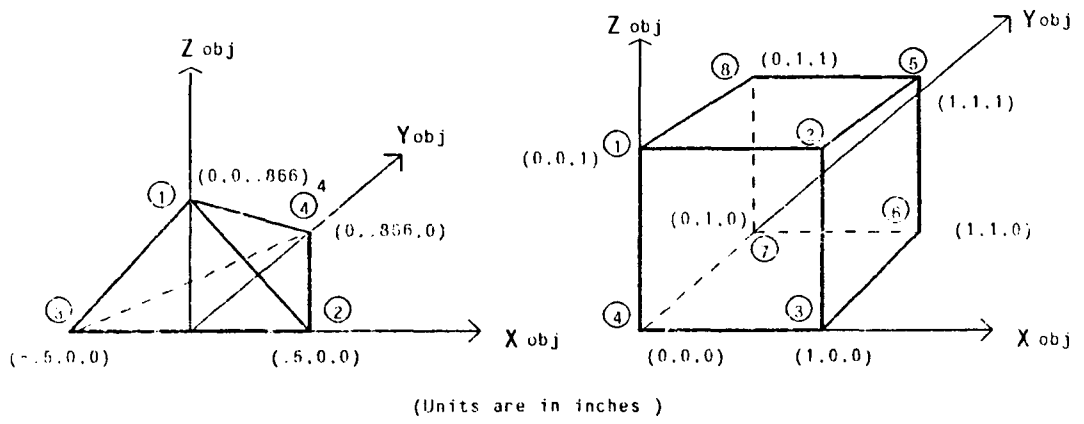

Figure 4-13: Objects

For each visible object plane, two features are obtained:

1. Perceived area of the i_{th} plane - $A_{rea\text{-}i}$; and

2. Perceived X center-of-gravity (or centroid) of the i_{th} plane - $X_{cog\text{-}i}$

These features are typical of those extracted from binary images, in commercially available systems, following image segmentation. It has been suggested that such features, which are based on integral or summation operations, are preferable for visual servoing applications, since these operations attenuate signal noise [Hasegawa 77]. Feature selections, which can include both linear and nonlinear combinations of the extracted features, are presented in Chapter 7.

Each object vertex is transformed into the image plane as follows: A point defined in the object coordinate system is defined by

$$\vec{V}_{obj} = (X_{obj}, Y_{obj}, Z_{obj}, 1)^T$$

And it's position relative to the frontal image plane is

$$\vec{V}_{rel} = (X_{rel}, Y_{rel}, Z_{rel}, 1)^T \tag{4.38}$$

Then,

$$\vec{V}_{rel} = T_t \bullet T_{obj} \bullet \vec{V}_{obj}$$

where the homogeneous transformation T_t defines the position of the turntable coordinate system $[X_{turn}, Y_{turn}, Z_{turn}]$, relative to the camera's coordinate system $[\vec{X}_{cam}, \vec{Y}_{cam}, \vec{Z}_{cam}]$. The position of the object coordinate system, relative to the turntable coordinate system, is defined by T_{obj}. Then, T_t is found by the following transformation:

$$T_t = \mathrm{TRANS}[Y,R] \bullet \mathrm{ROT}[X,\alpha] \bullet \mathrm{TRANS}\begin{matrix} X,x(t) \\ X,y(t) \\ Z,-h \end{matrix} \bullet \mathrm{ROT}[Z,\theta(t)]$$

$$= \begin{bmatrix} C\theta(t) & -S\theta(t) & 0 & x(t) \\ S\theta(t)C\alpha & C\theta(t) & -S\alpha & y(t)C\alpha + hS\alpha + R \\ S\theta(t)S\alpha & C\theta(t)S\theta & C\alpha & y(t)S\alpha - hC\alpha \\ 0 & 0 & 0 & 1 \end{bmatrix}$$

If the object frame is referenced to the turntable by translations in the X-Y-Z directions corresponding to (P_x, P_y, P_z) and oriented according to the Euler convention by $(\varphi, \varepsilon, \psi)$ [Paul 81], then

$$T_{obj} = \begin{bmatrix} C\varphi C\varepsilon C\psi - S\varphi S\psi & -C\varphi C\varepsilon S\psi - S\varphi C\psi & C\varphi S\varepsilon & P_x \\ S\varphi C\varepsilon C\psi + C\varphi S\psi & -S\varphi C\varepsilon S\psi + C\varphi C\psi & S\varphi S\varepsilon & P_y \\ -S\varepsilon C\varphi & S\varepsilon S\varphi & C\varepsilon & P_z \\ 0 & 0 & 0 & 1 \end{bmatrix}$$

Finally, $\vec{V}_{rel}$ is mapped into homogeneous image points $\vec{V}$ via the perspective transformation, T_p, according to

$$\vec{V} = T_p \bullet T_t \bullet T_{obj} \bullet \vec{V}_{obj} \doteq (V_x, V_y, V_z, S)^T$$

Hence,

$$X_{pic} = V_x / S$$

$$Z_{pic} = V_z / S$$

In addition, the image points are normalized to the image plane size ('ret') according to

$$X_{pic} \leftarrow X_{pic} / ret$$
$$Z_{pic} \leftarrow Z_{pic} / ret$$

Once the object planes are mapped into object image planes (by finding the perceived vertices), the features are calculated. The image plane is either a quadrilateral or triangle (Figure 4-14). The area and centroid of the triangle are [Kindle 50]

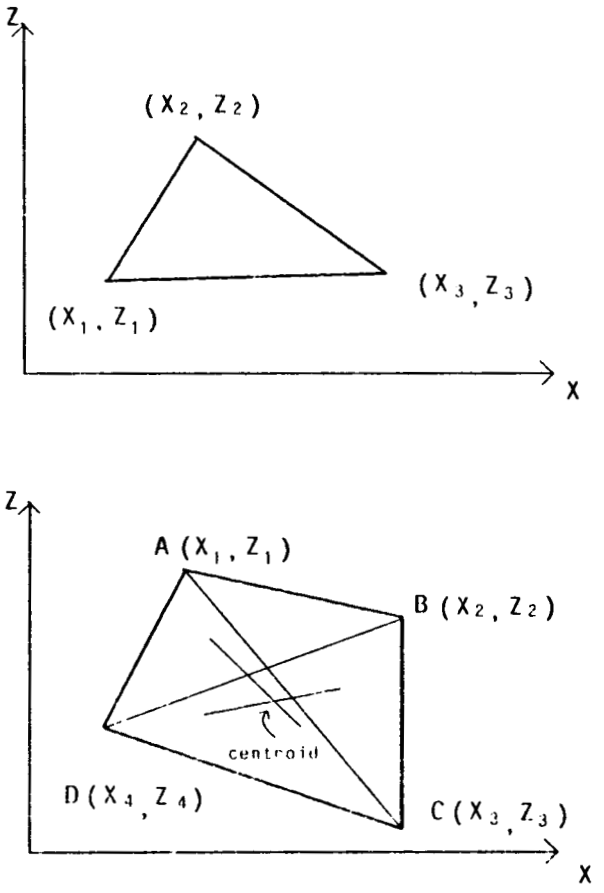

Figure 4-14: Image Planes

$$A_{rea} = -0.5(X_1Z_2 + X_2Z_3 + X_3Z_1 - X_1Z_3 - X_3Z_2 - X_2Z_1)$$

and

$$X_{cog} = \frac{X_1 + X_2 + X_3}{3}$$

The area of the quadrilateral is given by

$$A_{rea} = -0.5(X_1Z_2 + X_2Z_3 + X_3Z_4 + X_4Z_1 - X_1Z_4 - X_4Z_3 - X_3Z_2 - X_2Z_1)$$

The centroid of the quadrilateral can be determined by the following algorithm [Marks 78]:

The quadrilateral is divided into two sets of triangles by means of the diagonals (Figure 4-14). Find the centroid of the four triangles belonging to the same set. The intersection of these lines will be the centroid of area. Thus, in the figure, O, O_1, O_2, and O_3 are, respectively, the centroids of the triangles ABD, ABC, BDC, and ACD. The intersection of O_1O_3 with OO_2 give the centroid.

In accordance with the line example, the three conditions in (4.37) are evaluated for each plane, during the simulations. to assure that the features are valid. If the ith plane image features are sought, the conditions are:

Condition 1: true if Y_{rel} (for all vertices comprising the ith plane) > 0 ; else false

Condition 2: true if $|X_{pic}|$ and $|Y_{pic}|$ (for all vertices comprising the ith plane) < ret/2 ; else false

Condition 3: Each object plane is defined by assigning to it an ordered listing of the bounding vertices. Specifically, the vertex labels are specified in a clockwise ordering. In 3-dimensional space, when two connected edge vectors of a plane, whose head and tails are defined in a clockwise fashion, are cross multiplied then the magnitude of the resultant vector has a positive sense according to the "right-hand" rule. If the plane containing these edge vectors are rotated or translated out of the field of view, then the perceived sense of the original defining vertices would be counter-clockwise and the vector cross-product of the perceived edge- vectors would have a negative sense.

4.5.2.3. Noise Signal Modeling

Single DOF simulation studies (in Chapter 5) include additive feature measurement noise. The noise signal is modeled as zero-mean white-noise having a uniform random distribution (Figure 4-15), which is scaled by the factor α to produce a specified signal-to-noise ratio (SNR).

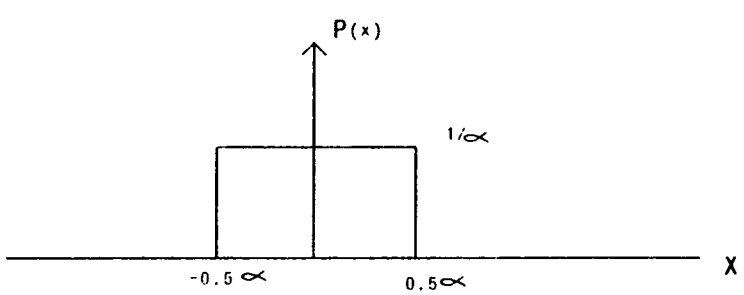

Figure 4-15: Scaled Distribution

The noise signal, n(k), is generated according to

$$n(k) = \alpha[RAN(k)-.5]$$

where RAN(k) is the TOPS-20 Fortran library routine which generates independent samples

from the uniform random distribution. To determine α, the SNR is specified with respect to the average power of a step function signal:

$$s^2 = (\text{reference signal} - \text{initial value})^2$$

Thus,

$$\text{SNR} = 10 \log \frac{s^2}{\sigma_x^2} \tag{4.39}$$

where σ_x^2 is the variance of the noise, and for a uniform distribution

$$\sigma_x^2 = \alpha^2/12$$

Hence, for a specified SNR, the scale-factor is

$$\alpha^2 = 12 * 10^{\{\log s^2 - \text{snr}/10\}}$$

4.6. Summary

In this chapter, visual servoing tasks are defined for evaluation in subsequent chapters. Mathematical models of robot kinematics and dynamics, picture taking, and feature transformation, which are required for task simulations, are also developed. The tasks vary from control of 1 DOF to 3 DOF systems, and are summarized in Table 4-6. The task configurations are selected to facilitate the IBVS evaulation of progressively complex dynamics, kinematics, and image feature transformations, and will help to understand the relative contributions of each to the control issues. While these configurations have limited degrees-of-freedom, which may be useful for some practical tasks, their models may be considered representative of more general configurations. It is believed that the results obtained with these examples may then be applied to more general cases.

Name	Robot Type/Task	Model Derivation
Configuration 1 (Figrue 4-1)	•2 DOF with linear uncoupled dynamics and kinematics (evaluated in Chapter 6), or 1 DOF by constraining motion to one axis (evaluated in Chapter 5) •Control position of a mobile camera (fixed to robot end-effector) relative to a fixed line in space	Configuration Definition: Section 4.2.1 Robot Model: Section 4.3.2 Feature Measurement: Sections 4.5.1, 4.5.2, and 4.5.2.1
Configuration 2 (Figrue 4-2)	•2 DOF with nonlinear coupled dynamics and kinematics (evaluated in Chapter 6) •Control position of a mobile camera (fixed to robot end-effector) relative to a fixed line in space	Configuration Definition: Section 4.2.2 Robot Model: Section 4.4 Feature Measurement: Sections 4.5.1, 4.5.2, and 4.5.2.1
Configuration 3 (Figrue 4-3)	•3 DOF with linear uncoupled dynamics, and a combination of 2 planar Cartesian with 1 rotational DOF •Control position of a mobile polyhedral object (fixed to robot) relative to a stationary camera	Configuration Definition: Section 4.2.3 Robot Model: Section 4.3 Feature Measurement: Sections 4.5.1, 4.5.2, and 4.5.2.2

Table 4-6: Configuration Summary

Chapter 5
Evaluation: One DOF Systems

5.1. Overview

The purpose of this chapter is to evaluate SP MRAC adaptive control of one DOF linear and nonlinear systems. The evaluation analyzes examples which are relevant to the two and three DOF visual servoing tasks evaluated in Chapters 6 and 7. While single DOF IBVS systems may be useful for specific robotic applications, these results serve to help understand MRAC control of nonlinear IBVS systems, and as a guideline for implementing and evaluating higher degree-of-freedom systems required for visual servo control.

The chapter is organized as follows. In Section 5.2, MRAC is introduced for the control of a simple motor positioning system. These examples are then used for:

- Verification of the basic FP and SP MRAC algorithms developed by Morris and Neuman [Neuman 80] for constant linear systems, and
- Verification of the algorithms which include a measurement delay (Section 3.3)

In Section 5.3, IBVS feature feedback is introduced, and

- Extends SP MRAC control, with delay, to include a constant feature sensitivity gain, and
- Demonstrates the superior noise filtering performance of the fixed LMFC controller relative to MRAC control.

In Section 5.4, control is extended to include a nonlinear feature sensitivity gain, and

- Demonstrates the stability of SP MRAC control for this nonlinear system,
- Evaluates position response when the controlled signal is nonlinearly related to position, and
- Includes a performance comparison of MRAC vs. Fixed LMFC control, which demonstrates superiority of the adaptive approach at smaller system bandwidth's and the superiority of the fixed approach at smaller sampling-to-bandwidth ratios.

5.2. Baseline MRAC

The purpose of this section is to verify the SP and FP MRAC algorithms (derived in Chapter 3), for systems with and without measurement delay, by simulating a simple motor positioning control task. The position of the Y-translational stage (Figure 4-7), which is measured directly, is the variable under control. The examples included in this section focus on the SP MRAC, since this controller is used for <u>all</u> subsequent IBVS control. While the FP MRAC exhibits faster tracking of the reference signal (without a delay), the SP MRAC is selected for IBVS control for the following reasons:

1. Relative to the FP reference model, a SP reference model reduces the high frequency gain of the feedback path, reducing the noise amplification.

2. In contrast to the FP MRAC's deadbeat response characteristic to recovery from control signal saturation, the SP MRAC is not susceptible to deadbeat.

3. While the relative stability of the FP MRAC is susceptible to control signal saturation, the SP MRAC is not as sensitive.

4. The SP MRAC requires a smaller control penalty with measurement delay.

The Y-translational stage dynamics represent a constant linear SISO system. For this type of system, the MRAC algorithms are verified by showing that the identifier (3.4), (3.5), and (3.6) can perfectly identify the plant parameters, and by showing that:

1. For FP MRAC, without measurement delay, there is perfect modeling following, when $e_{ID}(k) = 0$, according to (A.14). It is also verified that relative stability with this type of control is susceptible to control signal saturation.

2. For SP MRAC, without measurement delay, the FP error is a filtered identification error according to (A.23). Slower tracking of the reference model occurs when identification errors exist. The SP MRAC, however, is not as sensitive to saturation.

3. For FP MRAC, with measurement delay, a control penalty is required for absolute stability according to the root-locus analysis in Figure 3-6.

4. For SP MRAC (with measurement delay), a control penalty is required for relative stability according to the root-locus analysis shown in Figure 3-8.

The discrete open-loop plant model is calculated below for comparison with the parameters estimated by the identifier. The open-loop system gain (in Figure 4-7) is

$$K = K_m \cdot \frac{1}{2\pi p} \cdot SF = K = (26.58)\left(\frac{1}{2\pi 7}\right)(100) = 60.43$$

when the scale factor SF (Section 3.6.3) is set equal to 100. The analog model (4.5) of the process under control becomes

$$G(s) = \frac{60.43}{s(.072s + 1)}$$

and the corresponding discrete model of is

$$W_p(z^{-1}) = \frac{b_1 z^{-1} + b_2 z^{-2}}{1 - a_1 z^{-1} - a_2 z^{-2}}$$

where

$$a_1 = 1 + e^{-T/\tau} \quad ; \quad \tau = .072$$
$$a_2 = -e^{-T/\tau}$$
$$b_1 = -(K\tau^2)(1 - T/\tau - e^{-T/\tau}) \quad ; K = 60.43$$
$$b_2 = (K\tau^2)(1 - e^{-T/\tau} - T/\tau\, e^{-T/\tau})$$

Since the plant dynamics has real poles (i.e., at $z = 1$ and $z = .632$), there is no upper-bound constraint on the sampling period selection. The sample period is selected as $T = 0.033$ (sec) to correspond to the period used in initial IBVS simulations. For this sampling period, the actual parameter vector (A.10) becomes

$$\underline{\beta} = [.3945 \;\; .3387 \;\; 1.63235 \;\; -.63235]^T$$

5.2.1. MRAC Without Measurement Delay

In the first set of experiments, the MRAC algorithm for systems without delay (i.e., $n_d = 0$) is verified. The controller parameters, listed below, are empirically selected (according to the guidelines in Section 3.6) and the controller algorithm is implemented according to:

1. Control signal (A.12) .

2. The identifier, (A.15),(A.16), and (A.17), uses second order-estimators (i.e., for a second-order plant) with a weighting factor $\lambda = 0.85$. In the first trial of each experiment, the estimated parameter vector is initialized to

   $$\hat{\underline{\beta}}(0) = [10 \;\; 10 \;\; 1.1 \;\; -.1]^T$$

   which represents large gains and fast poles so that the system is not forced to start out too fast, causing overshoot. The adaptive gain matrix is initialized to

   $$P(0) = \mathrm{DIAG}[10 \;\; 10 \;\; 80 \;\; 80]$$

   and reset with a threshold of

   $$P_{thresh} = 2500$$

   Each experiment is repeated, for a second trial, with $\hat{\underline{\beta}}(0)$ and $P(0)$ initialized to the steady-state values of $\hat{\underline{\beta}}$ and P learned in the first trial.

3. SP reference model (A.22). The reference model bandwidth, or the closed-loop system bandwidth, is specified by (3.29). With a performance margin PM = 10 (Section 3.6.2.2), the bandwidth is

$$\omega_n = \frac{\pi}{10T} = 9.52 \text{ sec}^{-1}$$

This bandwidth corresponds to a rise-time $t_r = .7$ (sec) according to (3.26), and a sampling-to-bandwidth ratio of $f_s/f_{BW} = 20$ according to (3.28). The open-loop reference model time constant, $\tau_{model} = 0.048$, is chosen to achieve this bandwidth according to the methods outlined in Section 3.6.1. Discrete model parameters are then generated according to the method outlined in Appendix A.

The unit-step response of the SP MRAC is displayed in Figure 5-1. In the first trial, the identification error goes to zero in .4 sec. Unlike an FP MRAC, the FP error does not immediately go to zero due to the model filtering effect predicted by (A.23). In the second trial, $e_{id}(k) \simeq 0$ for all k, which results in perfect model following. The estimated parameter vector, at the end of the first trial, does not correspond to the actual vector. This can be expected since the control signal may not be sufficiently rich in frequency content [Yuan 77] to identify a physical model. However, by at the end of the second trial there is perfect parameter identification. While saturation does not occur in this experiment, the examples in subsequent sections, which exhibit saturation, do not display the deadbeat response associated with an FP MRAC.

The simulations verify the the baseline MRAC algorithms. The next section includes an evaluation of these algorithms extended to include a measurement delay.

5.2.2. MRAC With Measurement Delay

In this section, a measurement delay is included by setting $n_d = 1$. The controller is implemented according to:

1. Control signal (3.10).

2. The identifier, (3.4),(3.5), and (3.6), is initialized as in Section 5.2.1.

3. SP reference models (A.22). The reference model bandwidth remains at $\omega_n = 9.52$ sec^{-1}. The open-loop reference model time constant becomes $\tau_{model} = 0.036$ according to the methods outlined in Section 3.6.1. And, the discrete model parameters are generated according to the methods outlined in Section 3.3.3.

4. Control penalty (3.12). (The controller pole bound, γ, will be specified for each experiment).

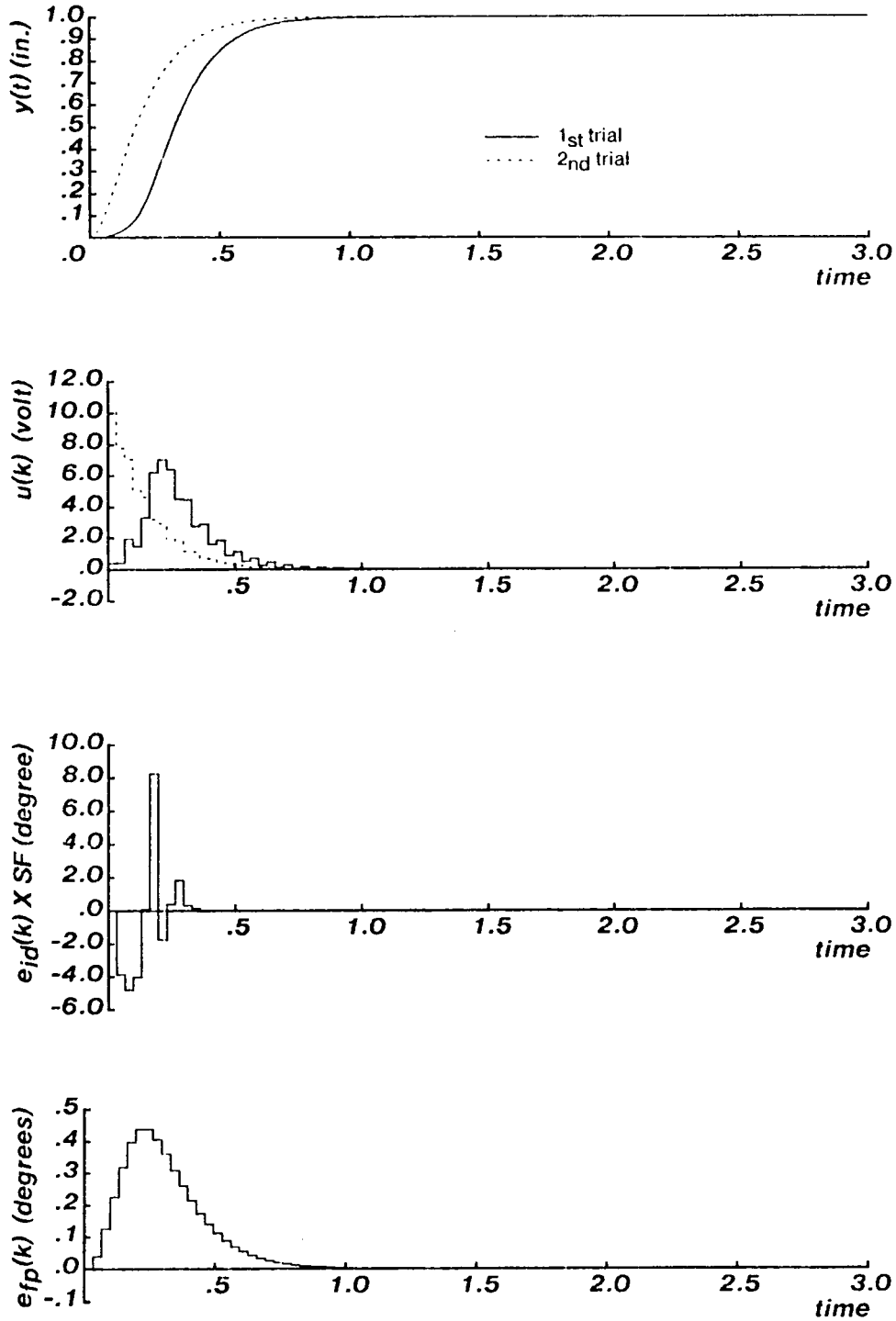

DC MOTOR CONTROL

Figure 5-1: SP MRAC Without Measurement Delay

The root-locus in Figure 3-8 predicts that the SP MRAC should be stable for all $\pi(k)$. In the simulation displayed in Figure 5-2, the controller pole bound is initially set to $\gamma = 1$. After the initial learning trial, the system responds with a rise-time .7 (sec), with a decaying small amplitude oscillation superimposed. By the end of this trial there is perfect identification. Since $|\hat{b}_2/\hat{b}_1| < \gamma^2$, then $\pi(k) = 1$, and the dominant closed-loop poles at (.099±.931j) predict the observed asymptotic oscillation frequency. Since the angle between the poles and the real axis is

$$\theta = \omega_d T$$

then these poles correspond to a frequency of

$$f = \frac{\tan^{-1}(.931/.099)}{2\pi T} = 7 \text{ Hz.}$$

The magnitude of oscillation can be attenuated by decreasing the pole bound to $\gamma = 0.8$, thus increasing the control penalty. The oscillation is suppressed at the expense of a larger rise-time, $t_r \simeq 0.8$ (sec). While increasing control penalty improves stability, it produces results equivalent to reducing the system bandwidth, and leads to larger tracking errors.

These experiments summarized here verify the basic SP and FP MRAC algorithms by demonstrating adaptive control of a simple positioning system. While fixed controllers can be designed for this system, based on a'priori knowledge of the plant, the adaptive controller required minimal a'priori information. Next, the SP MRAC is extended to control a linear image-based system. The SP MRAC is selected for IBVS control since it is less susceptible to saturation and noise, and requires smaller control penalties required for measurement delays.

5.3. Linear IBVS

One DOF IBVS systems are simulated using Configuration 1 (Figure 4-1), and restricting relative motion to either the X or Y directions. When motion is in the X direction, either the length (4.30) or center-of-gravity (4.31) features can be used for control. For each case, the feature sensitivity scaler, J_{feat}, becomes either

$$\frac{\partial X_{cog}}{\partial X_{rel}} = \frac{F}{ret} \cdot \frac{4X_{rel}(F + Y_{rel})}{4(F + Y_{rel})^2 - (l_o \sin\theta_{rel})^2} \tag{5.1}$$

or

$$\frac{\partial l_{ength}}{\partial X_{rel}} = \frac{-4Fl_o}{ret} \cdot \frac{\sin\theta_{rel}}{4(F + Y_{rel})^2 - (l_o \sin\theta_{rel})^2} \tag{5.2}$$

If $\theta_{rel} = 0$ or π radians, then $\partial l_{ength}/\partial X_{rel} = 0$ and (5.2) degenerates to zero. The center-of-

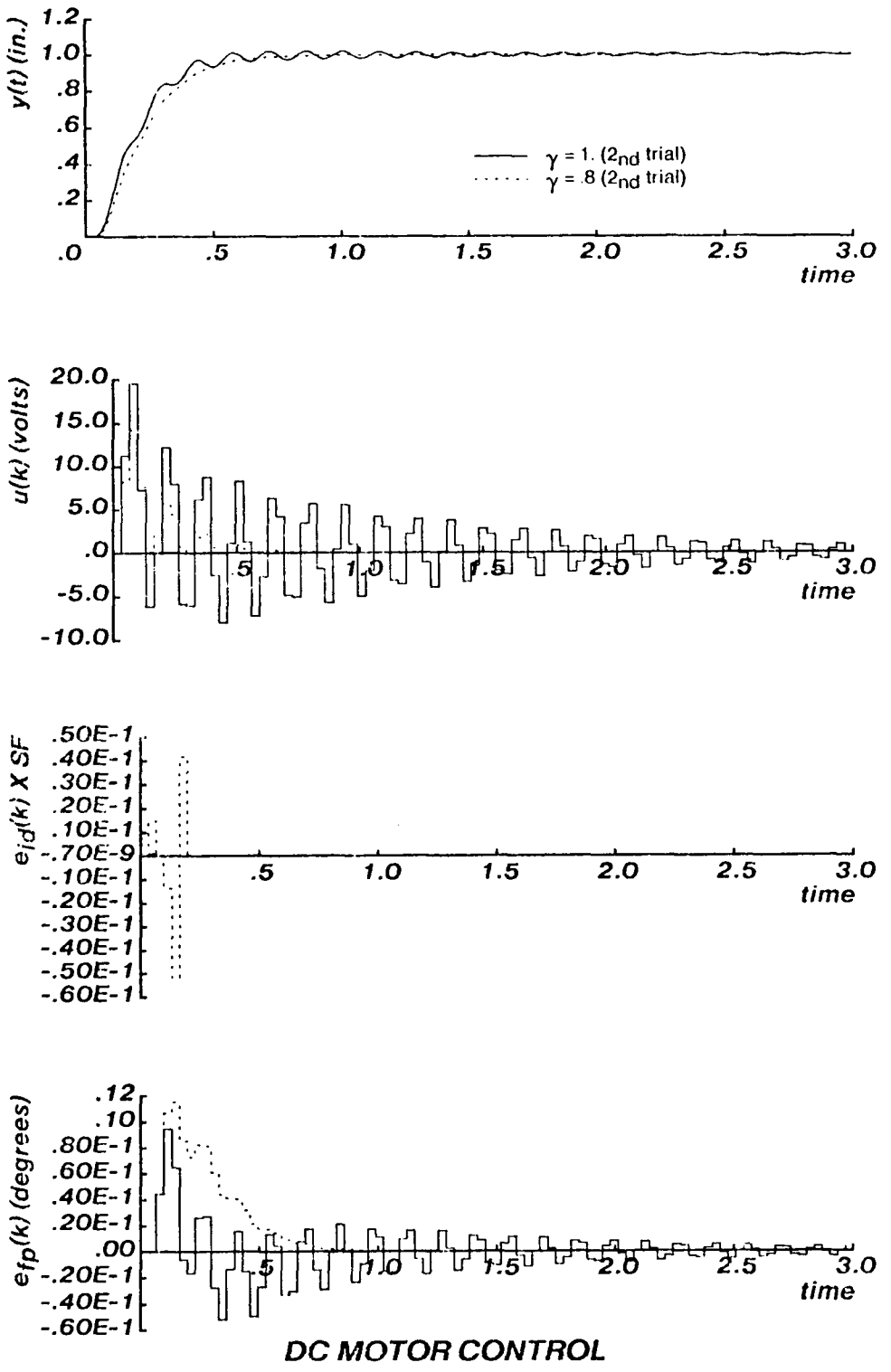

Figure 5-2: SP MRAC With Measurement Delay

gravity feature is thus selected for one DOF control of the X-axis. Since this system has linear kinematics and the camera is mounted with the image plane's axis parallel to the translational stage axis, the arm jacobian scaler is $J_{arm} = 1$. The sensitivity (2.7) becomes

$$J = -J_{arm} J_{feat} = -J_{feat}$$

Since J_{feat} is independent of X_{rel}, the system under control is linear. The discrete open-loop model parameters are obtained from Section 5.2 by including the feature sensitivity J in the gain K:

$$K = J K_m \frac{1}{2\pi p} SF$$

The value selected for SF depends upon the sampling-period and the feature sensitivity magnitudes (since the discrete gains decrease with sampling-period and sensitivity). For all IBVS examples in Chapters 5 and 6, the scale factors are empirically determined to be:

$$\begin{aligned} SF_{T=.033} &= 2500 \\ SF_{T=.013} &= 5000 \\ SF_{T=.003} &= 10000 \end{aligned} \tag{5.3}$$

The SP MRAC control parameters are initialized according to Table 5-1.

T(sec)	P(0)	P_{Thresh}	$\hat{\beta}(0)$
0.033	Diag [10 10 80 80]	2500	$[\pm 10 \ \pm 10 \ 1.1 \ -0.1]^T$
0.013	Diag [1 1 1 1]	100	$[\pm 1 \ \pm 1 \ 1.5 \ -0.5]^T$
0.003	Diag [.1 .1 .01 .01]	10	$[\pm 1 \ \pm 1 \ 1.5 \ -0.5]^T$

Table 5-1: Identifier Parameter Initialization (1 DOF)

In Table 5-1, the initial estimated parameter vectors, $\hat{\beta}(0)$, represent large gains and fast poles so that the system is not forced to start out too fast. In practice, more accurate initial guesses can be made to achieve faster convergence of the identifier. As T decreases, the gain terms $\{b_i\}$ decrease, and open-loop poles move closer to the unit circle. The initial estimated parameter vector is varied with T to reflect these changes. In the initial experiments, the the estimated gain terms $\{\hat{b}_1(0), \hat{b}_2(0)\}$, are initialized to the incorrect sign to demonstrate MRAC sign sensitivity. This sensitivity becomes an important aspect of independent MRAC control of coupled systems, and is discussed in Chapter 6. When $\gamma = 0.85$, the linear IBVS systems still exhibit a decaying very low amplitude and frequency

oscillation. By further reducing the controller pole bound to $\gamma = 0.65$, a smoother response is obtained.

In the simulations presented in this section, the sampling period is set to T = 0.033 (sec), and the specified close-loop bandwidth remains $\omega_n = 9.53$ sec^{-1}, so that the sampling-to-bandwidth ratio is $f_s/f_{BW} = 20$. Two control tasks, labeled Tasks A and B in Figure 5-3, represent time invariant linear IBVS systems.

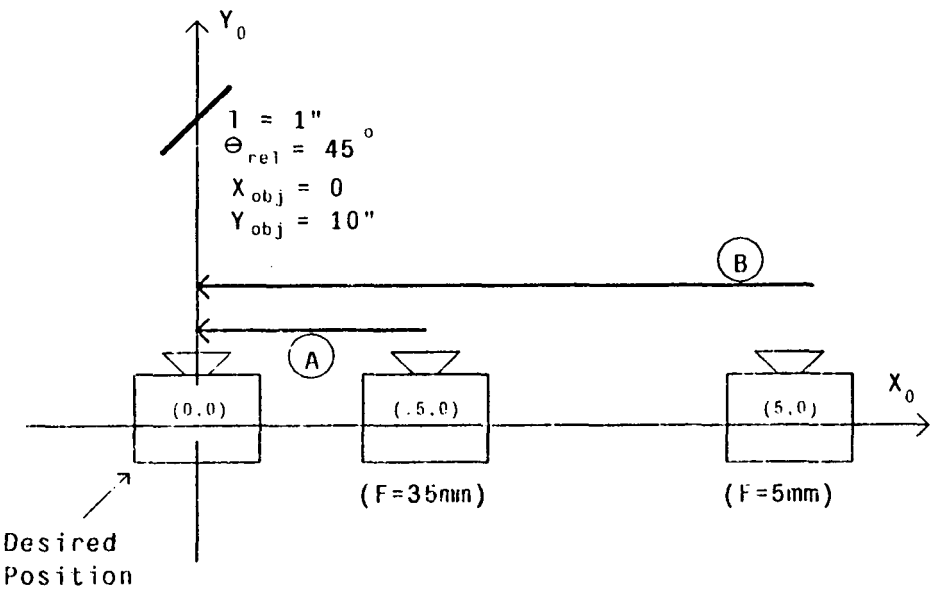

Figure 5-3: Linear Time-Invariant Tasks

For each task, a picture is taken when the camera is in the desired position and the extracted X_{cog} feature value is used as the reference step-input. The simulation of Task A is displayed in Figure 5-4. The FP output and identification errors are expressed in terms of the scaled feature. For this configuration, the actual parameter vector is

$$\underline{\beta} = [-3.8984\ -3.4550\ 1.6958\ -.6958]$$

when T = 0.033, $\tau_x = 0.091$, and $J_{eq} = -0.4849$. In the initial trial, $\hat{b}_1(0) = \hat{b}_2(0) = +10$, and the system starts off in the wrong direction due to the incorrect sign of the initial estimated gain terms. As the system learns, the estimated gain becomes negative and the table reverses direction. After this learning trial, the system starts out in the correct direction in the second trial. By the end of the second trial, the estimated parameter vector equals the actual parameter vector. The system rise-time has increased to $t_r = .9$ (sec), and there is a larger FP output error due to the increased control penalty. The sensitivity of the MRAC controller to

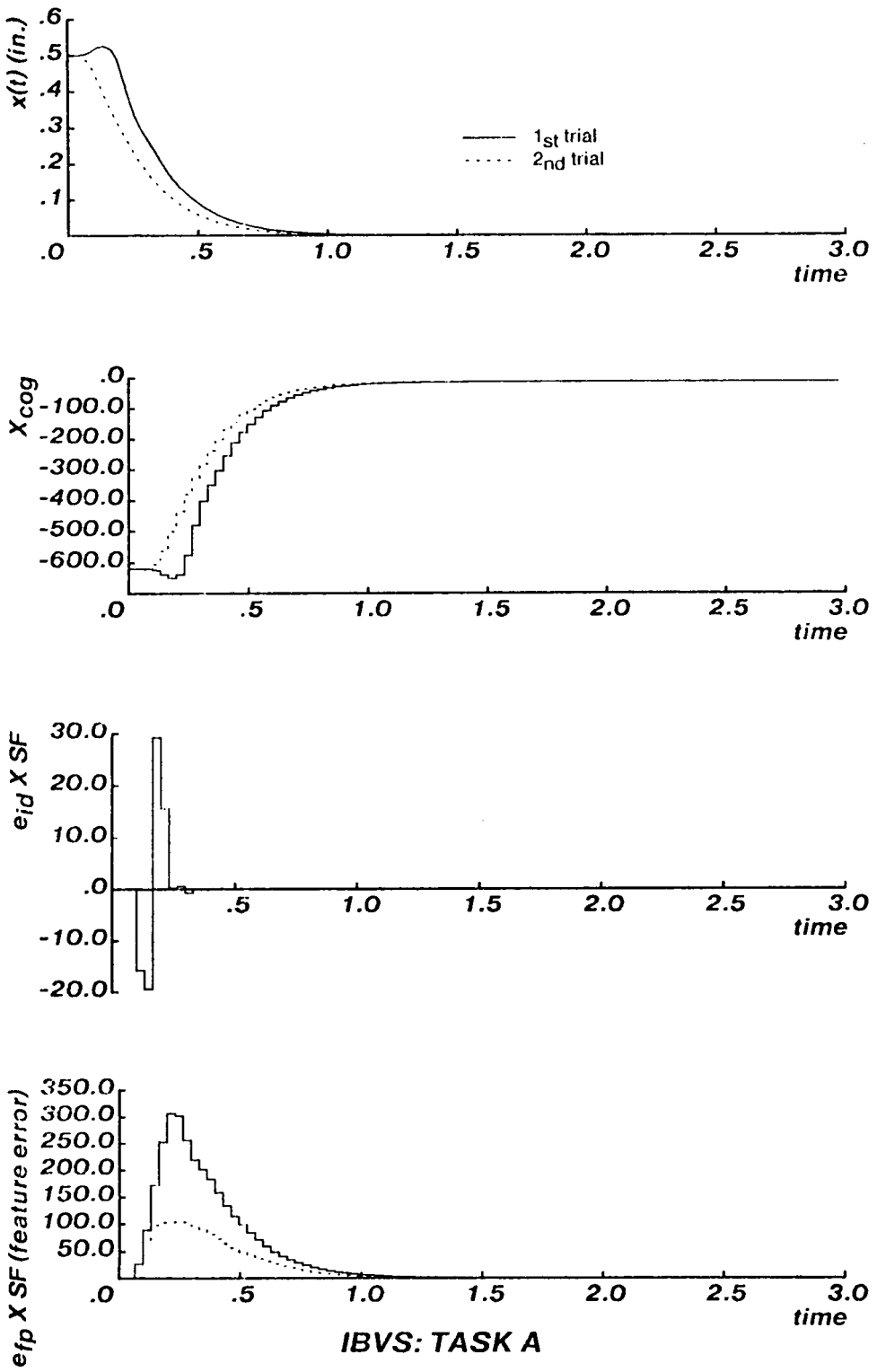

Figure 5-4: Linear Autonomous IBVS

the sign of the gain term is an important aspect of adaptive control. For SISO control of multi-DOF systems, it is shown in Chapter 6 that sign sensitivity can degrade path trajectory response.

Task B is specified to force control signal saturation resulting from the longer distance that must be traveled. The position response and control signals are displayed in Figure 5-5.

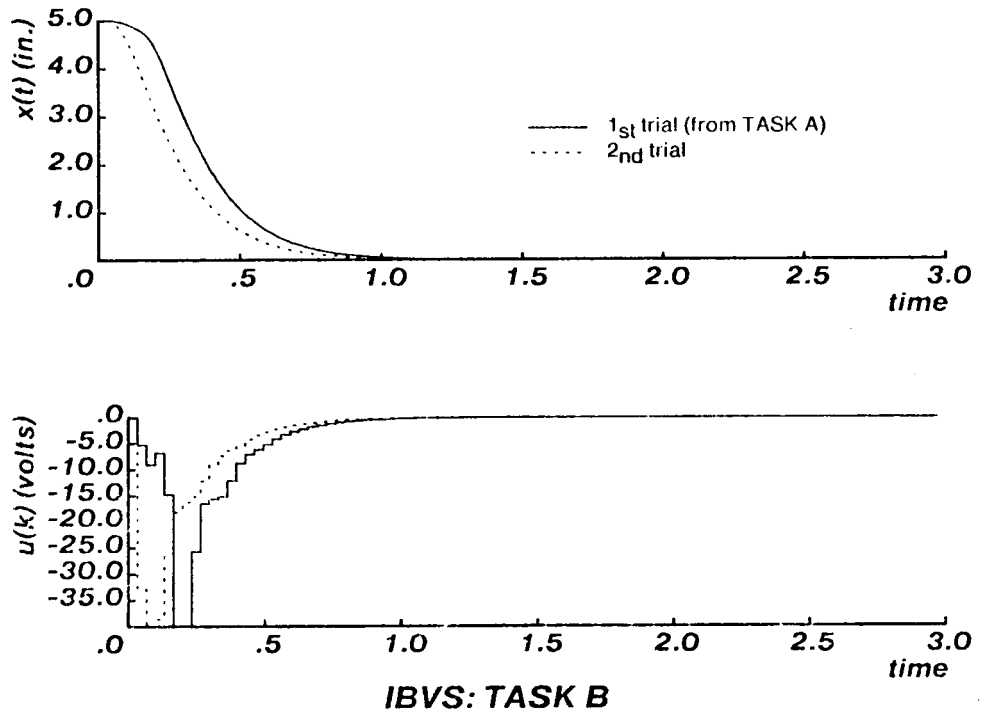

Figure 5-5: IBVS with Control Signal Saturation

The camera focal length, F, is reduced so that the line does not go out of field of view (OFV). Therefore, the feature sensitivity is reduced to $\partial X_{cog}/\partial X_{rel} = -0.0773$, thus decreasing the plant gain. The first trial uses parameter and adaptive gain values initialized to the values learned from the Task A simulation. While there is control signal saturation, no deadbeat response results. This experiment demonstrates the ability for the same adaptive controller to operate equally well with different plant sensitivities.

5.3.1. Noise Performance: Fixed vs. Adaptive Control

A potential drawback of any identification and feedback control strategy is susceptibility to measurement noise. The control algorithm and measurement system must be designed to reduce noise. Fixed controllers are inherently less susceptible since they do not include on-line identification. In computerized vision measurement systems, image pre-processing becomes the primary mechanism for noise reduction. Post-processing, or filtering, of the estimated positions or features may be required for further noise reduction. The MRAC algorithm provides inherent means for minimizing noise effects. Morris [Morris 79] has demonstrated that:

- The SP reference model has superior noise performance, relative to the FP reference model.
- The control penalty enhancement attenuates the gain of the feedback path, and thus noise amplification.
- The gain of the feedback path can be further attenuated by reducing the closed-loop system bandwidth (i.e., by specifying a slower reference model).
- The least-squares weighting factor λ provides a noise filtering effect for the estimation process.

In the next series of experiments, the relative noise performance of the LMFC and MRAC are compared for two values of λ. Fixed controllers are implemented by fixing the gains of the MRAC controller, and turning-off the adjustment mechanism. Fixed gain values are derived by fixing the estimated parameter vector to the actual parameter values.

Task A (Figure 5-3) is simulated with added measurement noise. The focal length has been reduced, to F = 25 (mm), to keep the line in the field of view when smaller SNRs are used. Noise performance is evaluated at five noise levels, including infinity (i.e., no noise), 80, 60, 44, and 30 dB. For example, the SNR = 44 dB corresponds to quantization noise due to pixel resolution for a 512 X 512 CCD array without further pre-processing. For each SNR, an experiment consists of five trials. The first two correspond to successive adaptive trials with $\lambda = 0.85$, the next two correspond to $\lambda = 1$, and the final trial corresponds to a fixed LMFC with the estimated parameter vector set equal to the actual parameters:

$$\hat{\underline{\beta}}(k) \leftarrow \underline{\beta} = [-2.88453\ -2.55645\ 1.69584\ -.69584]^T$$

Each trial uses the same noise sequence. The simulation results are shown in Figures 5-6 and

5-7 for noise levels of 44 and 30 db, respectively. The X-stage starts off in the wrong direction, for SNR = 30 db and $\lambda = 0.85$, since the estimated gain $\hat{b}_1$ term is positive at the end of the first trial. At 20 dB, the line would not stay in the field of view.

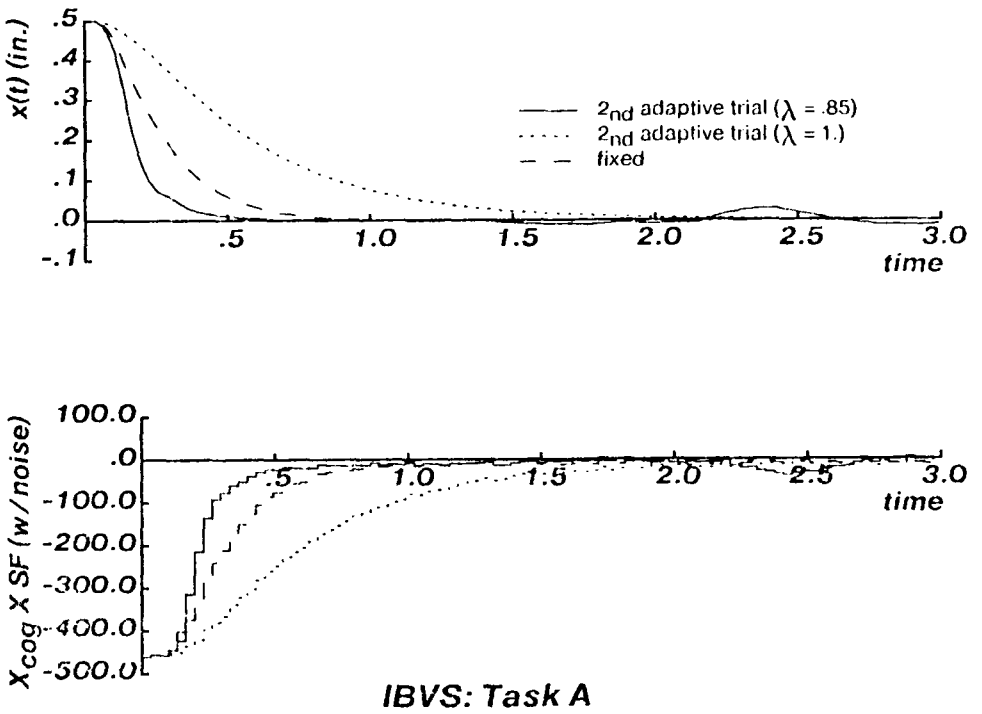

Figure 5-6: MRAC vs. LMFC Noise Performance (SNR = 44 db)

The relative noise performance is evaluated by defining the error index (E) according to

$$E = \log\left[\sum e^2_{FP}(k)\right] \quad \text{for } kT \geq 2 \text{ sec}$$

which is a measure of steady-state error[7]. The error-index vs. SNR is plotted in Figure 5-8 for the second learning trial at each λ. The fixed controller, which exhibits a performance which is linearly related to the noise level, performs better than the MRAC controller when $\lambda = 0.85$. When $\lambda = 1$, the LMFC and MRAC have similar performance. However, λ is set to less than one when controlling the nonlinear systems described in the following sections. While other approaches have been noted for noise reduction, such as larger control penalties and smaller bandwidths, it appears that independent noise filters, operating on the measurement signals, would be required to achieve suitable responses, at lower SNRs.

---

[7]Without noise, the full-parallel error is essentially zero after 2 seconds. The error index, E, is thus calculated for $kT > 2$ sec., so that that E, calculated without noise, approaches minus infinity, and is the reference level

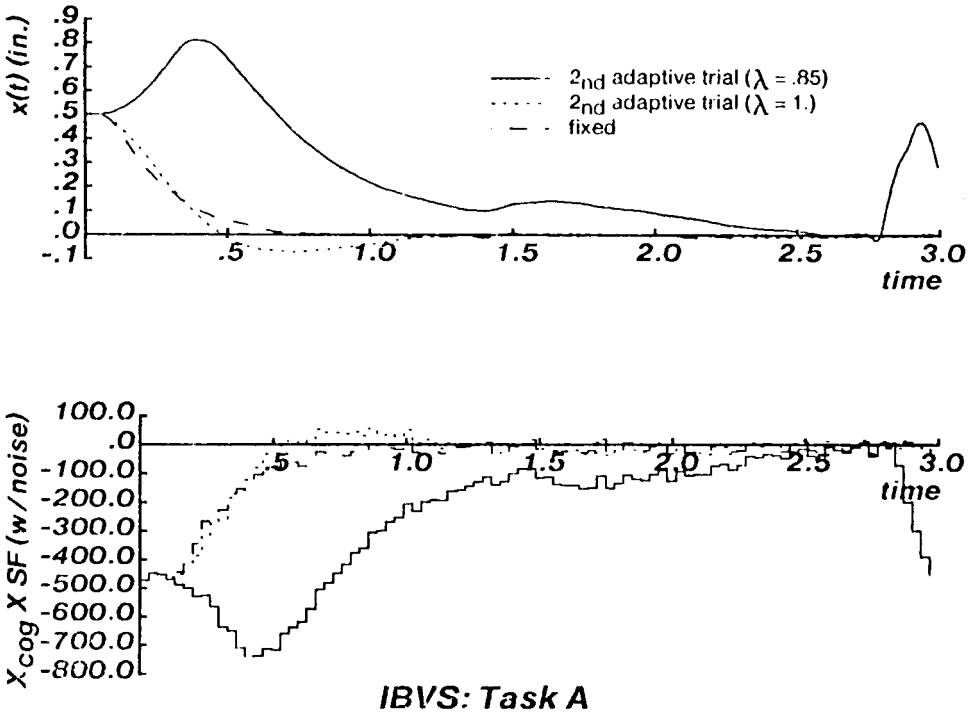

Figure 5-7: MRAC vs. LMFC Noise Performance (SNR = 30 db)

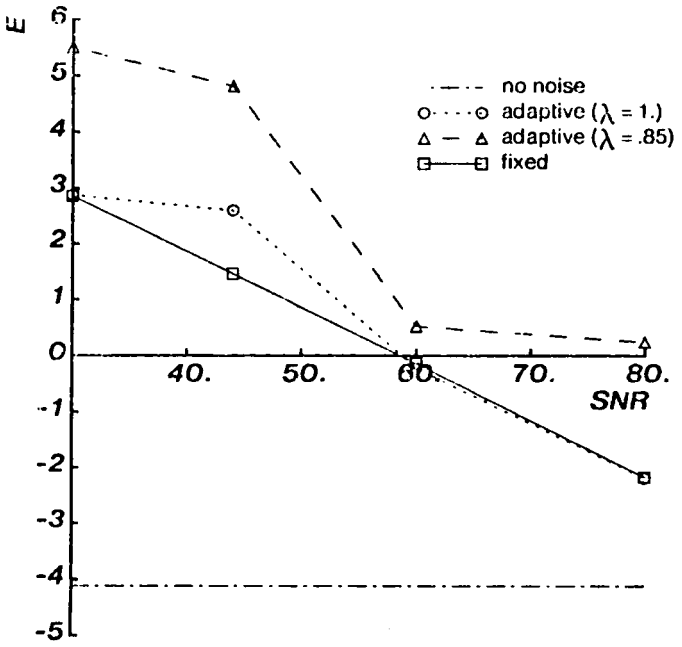

Figure 5-8: Error Index vs. SNR

5.4. Nonlinear IBVS

When motion is restricted to the Y direction, the sensitivity J_{feat} become

$$\frac{\partial l_{ength}}{\partial Y_{rel}} = \frac{4Fl_o}{ret} \cdot \frac{-4\cos\theta_{rel}(F + Y_{rel})^2 + 8X_{rel}\sin\theta_{rel}(F + Y_{rel}) \cdot \cos\theta_{rel}(l_o\sin\theta_{rel})^2}{\left[4(F + Y_{rel})^2 \cdot (l_o\sin\theta_{rel})^2\right]^2} \tag{5.4}$$

and

$$\frac{\partial X_{cog}}{\partial Y_{rel}} = \frac{4F}{ret} \cdot \frac{-4X_{rel}(F + Y_{rel})^2 + 8l_o^2(F + Y_{rel})\sin\theta_{rel}\cos\theta_{rel} \cdot X_{rel}(l_o\sin\theta_{rel})^2}{\left[4(F + Y_{rel})^2 \cdot (l_o\sin\theta_{rel})^2\right]^2} \tag{5.5}$$

When $X_{rel} = 0$ and $\theta_{rel} = 0$, then $\partial X_{cog}/\partial Y_{rel} = 0$ and (5.4) is degenerate. Therefore, l_{ength} is chosen as the feature for depth control. Since J_{feat} is a function of Y_{rel}, the system under control has linear dynamics and nonlinear gains. For example, in Figure 5-9, the camera moves along a trajectory specified by Task The corresponding feature transformation, (5.4), and the corresponding feature sensitivity, ($\partial l_{ength}/\partial Y$), are plotted in Figure 5-10 for various values of line angle (θ_{obj}). These plots demonstrate that the gains can change rapidly and dramatically, especially as the camera approaches the object. For these systems, stable adaptive performance is expected (if the identifier is fast enough to track the gain changes), with responses similar to the linear cases, with the following exceptions:

- Since the variable under control, feature length, is nonlinearly related to the plant variable, Y, the time response of Y does not match the time response of the feature.

- Since the process under control is nonlinear, there is no reason to expect that the estimated plant parameters will converge to the to the physical parameters.

- Larger values of sampling-to-bandwidth ratios and smaller values of λ will be required to track time-varying gain terms.

To study the behavior of these systems, the simulations of Tasks C and D (Figure 5-9) are repeated for various values of θ_{obj}. Tasks are simulated in both the approach direction (i.e., camera approaches the line as indicated by the arrow in Figure 5-9), and in the backing away trajectory. Task C represents a relatively small motion task, with a sensitivity that changes by a factor of 2.2 over the trajectory. Task D represents a large motion trajectory, with sensitivity that changes by a factor of 90. With respect to the identifier requirements, both cases can be considered as extreme examples because the gains change very rapidly as the camera comes

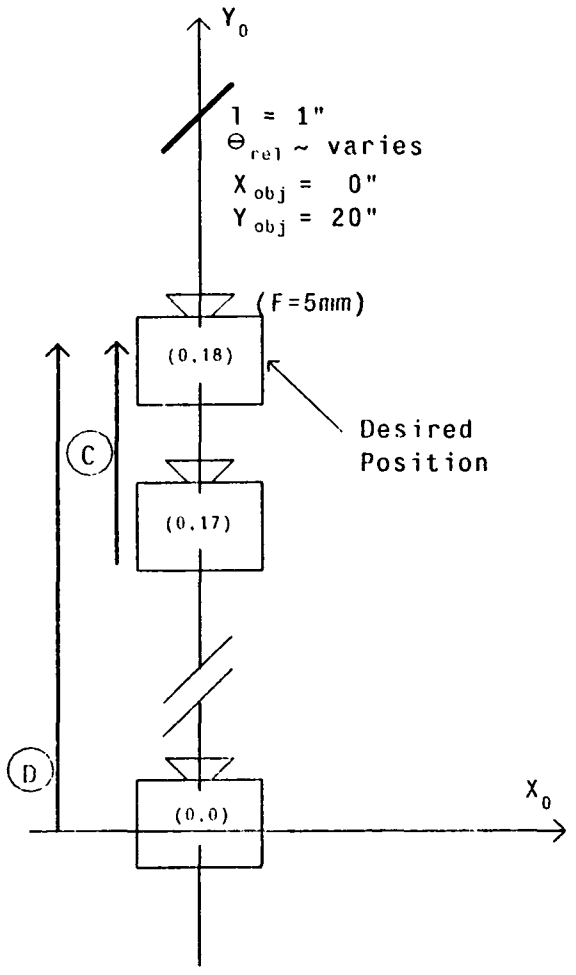

Figure 5-9: 1 DOF Nonlinear Tasks

in close proximity with the line. If the tasks had been specified so that the camera were further away from the line, but with a larger focal length (F) to increase the magnification, the sensitivity changes would not be as large. The relationship between the sensitivity and the focal length and relative distance (Y_{rel}) is given by (5.4). For example, with $\theta_{rel} = 0$, (5.4) is

$$\frac{\partial l_{cngth}}{\partial Y_{rel}} = -\frac{l_o}{ret} \frac{F}{(F + Y_{rel})^2} \tag{5.6}$$

As F and Y_{rel} increase, the sensitivity decreases.

For the initial studies, the SP MRAC is implemented according to the aforementioned linear examples (Section 5.2.2), with $\lambda = 0.85$, $\omega_n = 9.5$ sec^{-1}, and $T = 0.033$. The following observations emerge from specific simulation studies. In all simulations, the performance is

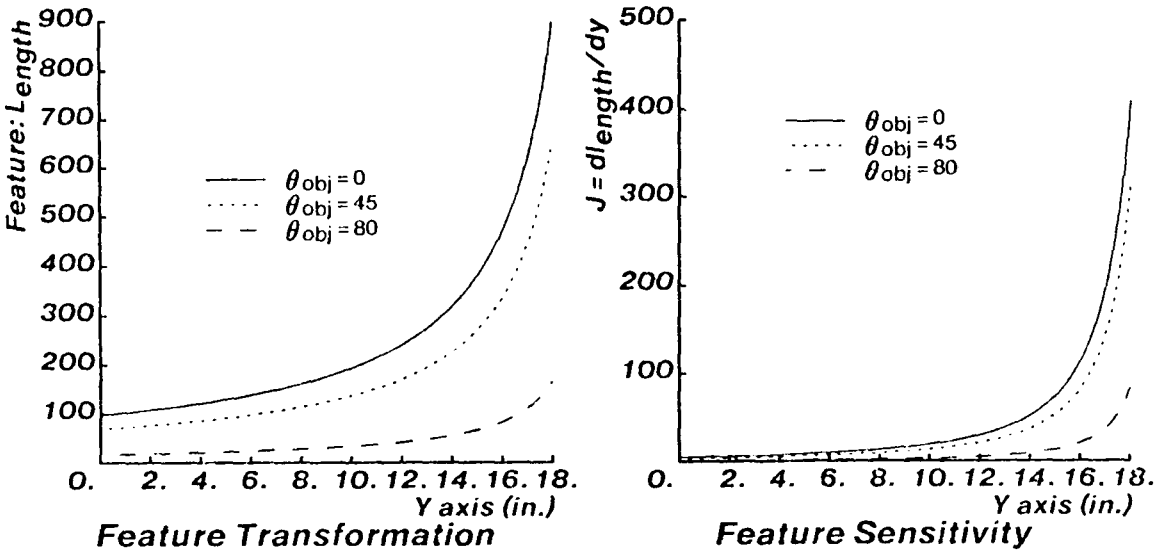

Figure 5-10: Task D Feature Characteristics

stable and the steady-state identification error goes to zero. Transient identification errors always remain. Both type 0 and type I estimated plants result. Since type 0 plants may be estimated, a signal bias (Section 3.4.1) must be used to the reduce steady-state errors to zero. When type I plants are estimated, the estimated poles do not match the actual poles. In many cases, non-minimum phase zeros are estimated. Thus, a control penalty is required, irrespective of the penalty required for feedback delay.

As the least squares weighting factor λ is reduced, the controller becomes too sensitive to tracking rapidly changing gains, especially for tasks where the camera approaches the object over large distances. The controller tries to decelerate too quickly as it estimates rapidly increasing gains. This can cause temporary reversal of table direction. Conversely, as λ increases, smoother responses result, but with possibly small underdamped target overshoots and longer settling times. The author has found that the value $\lambda = .85$ provides an acceptable tradeoff. In applications where small overshoots can be tolerated, larger values can be used. However, the most effective way to track rapidly changing parameters is to increase the sampling-to-bandwidth ratio.

When the feature signal is nonlinearly related to position (e.g., Tasks C or D), the feature and position time responses will be different. Since control of position is the goal, it is important to understand the relationship between position and feature time-domain

responses. To investigate this relationship, the the time response of forward and reverse trajectories are analyzed below, since the observed responses exhibit the following interesting relationships:

1. When approaching the object, feature rise-times are smaller than feature rise-times when backing away from the object.

2. When approaching the object, position rise-times are less than the corresponding feature rise-times.

3. When backing away from the object, position rise-times are greater than the corresponding feature rise-times.

4. Consequently the position rise-times associated with approach trajectories are smaller than the backing away position rise-times.

The explanation for these observations are discussed in conjunction with the specific examples which follow.

First, Task C is simulated with θ_{obj} = 45 degrees. The response, which is displayed in Figure 5-11, includes the initial and subsequent trials in the forward direction. The third trial, which is in the opposite direction, uses the estimated parameter vector and adaptive gain matrix initialized to values learned from the second trial. The rise times for this example are

Approach Feature Rise-Time: t_r = 0.9 sec (2nd trial)
Backaway Feature Rise-Time: t_r = 1.5 sec
Approach Position Rise-Time: t_r = 0.83 sec (2nd trial)
Backaway Position Rise-Time: t_r = 1.55 sec

Since the feature signal is controlled directly, it is expected that the approach and backing away feature rise-times would be identical. In the approach trajectory, the feature rise-time matches that of the linear IBVS example Task A, however in backing away, the rise-time is much larger. The explanation for these results requires evaluation of the gain change with time. The gain change, dJ/dt, which must be tracked by the identifier, is evaluated according to

$$\frac{dJ}{dt} = \frac{\partial J}{\partial Y} \cdot \frac{dY}{dt} \tag{5.7}$$

where $\partial J/\partial Y$ is the second derivative of the feature transformation (5.4). The gain change (5.7) for Task C is plotted in Figure 5-12 for both approach and reverse trajectories. The maximum rate of gain change is larger when backing away since the camera starts in a region where $\partial J/\partial Y$ is large, and during the initial part of the critically damped feature response dY/dt is large. Upon approaching the line, the initial $\partial J/\partial Y$ is smaller, and during the final

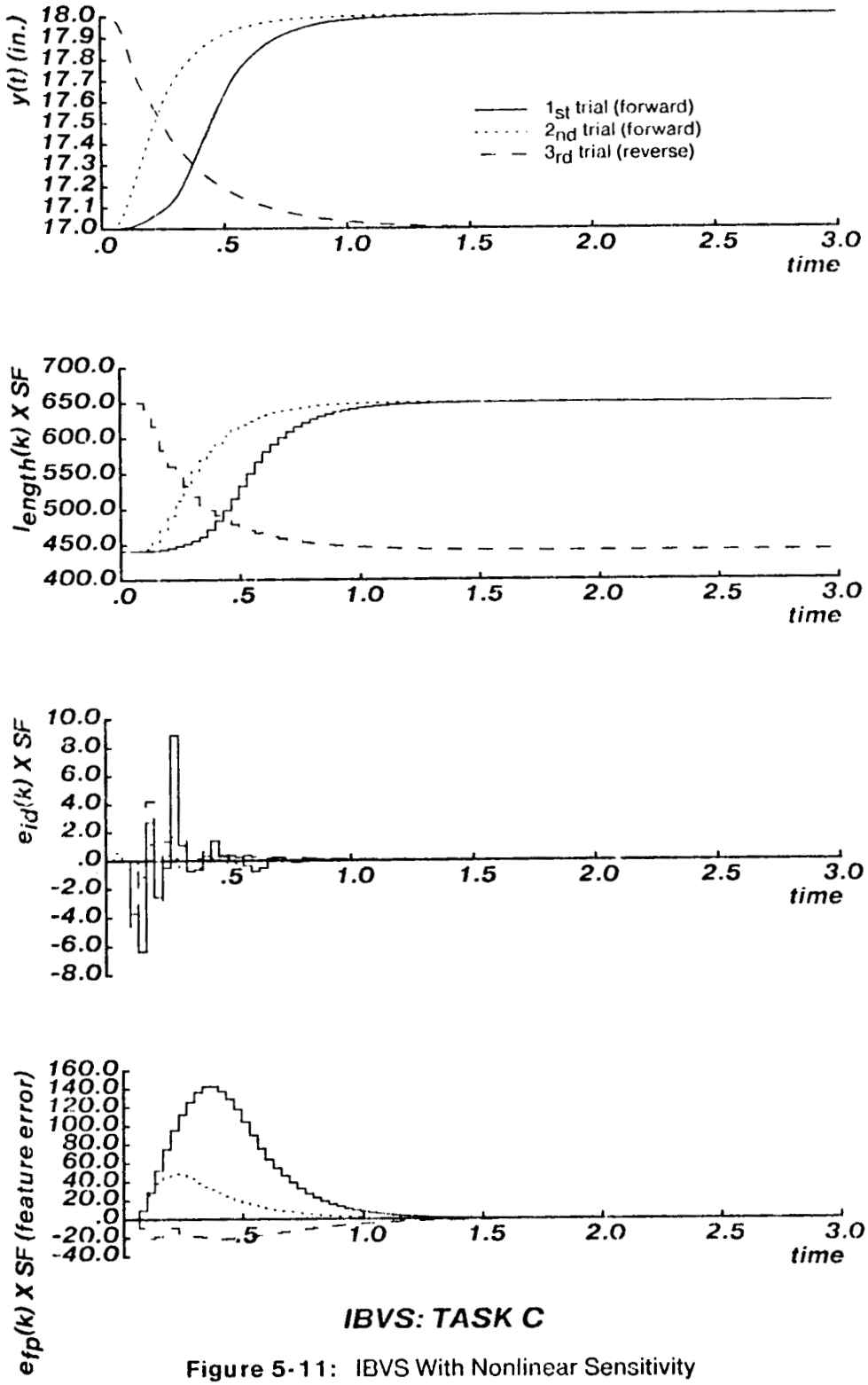

IBVS: TASK C

Figure 5-11: IBVS With Nonlinear Sensitivity

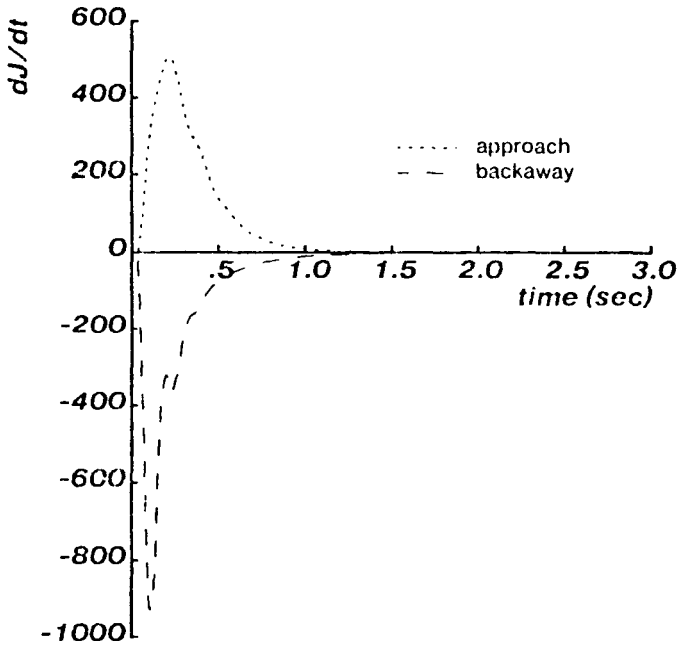

Figure 5-12: Sensitivity Change for TASK C

part of the trajectory dY/dt decreases. Since dJ/dt is larger for backing away, the transient identification error is larger during the time when most of the motion occurs. A longer time is required to recover from identification tracking errors, and the rise time increases.

Analysis of the relationship between feature and position response follow. It is shown below that the predicted position approach times (i.e., the response that would occur for perfect model following, or $e_{FP}(k) = 0.0$ for all k) are smaller than in a reverse trajectory, irrespective of tracking errors due to sensitivity changes. While this analysis provides insight into IBVS, it may have potential implications for task planning to minimize cycle times. To derive the position signal as a function of the feature signal, the expression for the length feature (4.30) is solved for Y_{rel}, with $X_{rel} = 0$:

$$(4\ \mathrm{ret}\ l_{ength})[Y_{rel} + F]^2 - (4\ F\ SF \cos\theta_{rel})[Y_{rel} + F] - (\mathrm{ret}\ l_{ength} \sin\theta_{rel}) = 0 \qquad (5.8)$$

For each sampling period, (5.8) is solved for $Y_{rel}(k)$ as a function of the length feature reference model signal $l_{ength\text{-}ref}(k)$. This analysis is used to predict the position response if perfect model following were achieved. (Actual response will lag behind the predicted response due to control penalties, transient identification errors, and possibly control signal saturation). From (5.8) for Task C, the predicted position rise-time in a forward trajectory is 0.69 seconds, and 0.79 seconds in the reverse direction. While the position excursion is the

same, the sensitivity change differences account for the position time response differences. These predicted results are explained as follows. The position approach rise-time is smaller than the corresponding feature rise-time since $\partial Y/\partial l_{ength}$ decreases as the camera approaches the line. Thus, Y can be close to it's final value, while the length feature can change by larger amounts to reach to it's final value. Upon backing away from the object, $\partial Y/\partial l_{ength}$ increases, and larger changes in Y are required for the same changes in the length feature.

The effect of the sampling-to-bandwidth ratio f_s/f_{BW} on system performance is evaluated below. Task C is simulated for θ_{obj} varying between 0 and 80 degrees, using a sampling-to-bandwidth ratio of $f_s/f_{BW} = 20$ (which is the same value used for the linear IBVS control in Section 5.3). The simulations all exhibit good stability, and the approach position rise-times remain essentially constant ($t_r = .83$ sec), while the feature rise-times increase with increasing θ_{obj}. Motions over larger distances, and thus larger gain change, require larger sampling-to-bandwidth ratios to achieve equivalent performance. Performance with movement over a distance of 18 inches, represented by Task D (Figure 5-9), is displayed in Figure 5-13. Rise-times become larger because of control signal saturation. The oscillation in position is due to larger identification errors, as a result of larger gain changes (Figure 5-10). It was noted, at the outset of this section, that decreasing λ to reduce e_{iD} makes the system too sensitive to the rapidly changing gains. An effective means to smooth this response is to increase the sampling-to-bandwidth ratio. For example, Figure 5-14 compares the response for three ratios, which are varied by fixing the bandwidth at $\omega_n = 9.5$ sec^{-1}, and changing the sampling period according to

1. $T = 0.033$ ($f_s/f_{BW} = 20$)
2. $T = 0.013$ ($f_s/f_{BW} = 50$)
3. $T = 0.003$ ($f_s/f_{BW} = 220$)

Overall time responses are comparable, but become smoother as the sampling-to-bandwidth ratio increases. At the highest ratio, the identification error becomes negligible. In the next section, it is shown that an advantage of fixed control is that it can exhibit superior stability at the lower ratios.

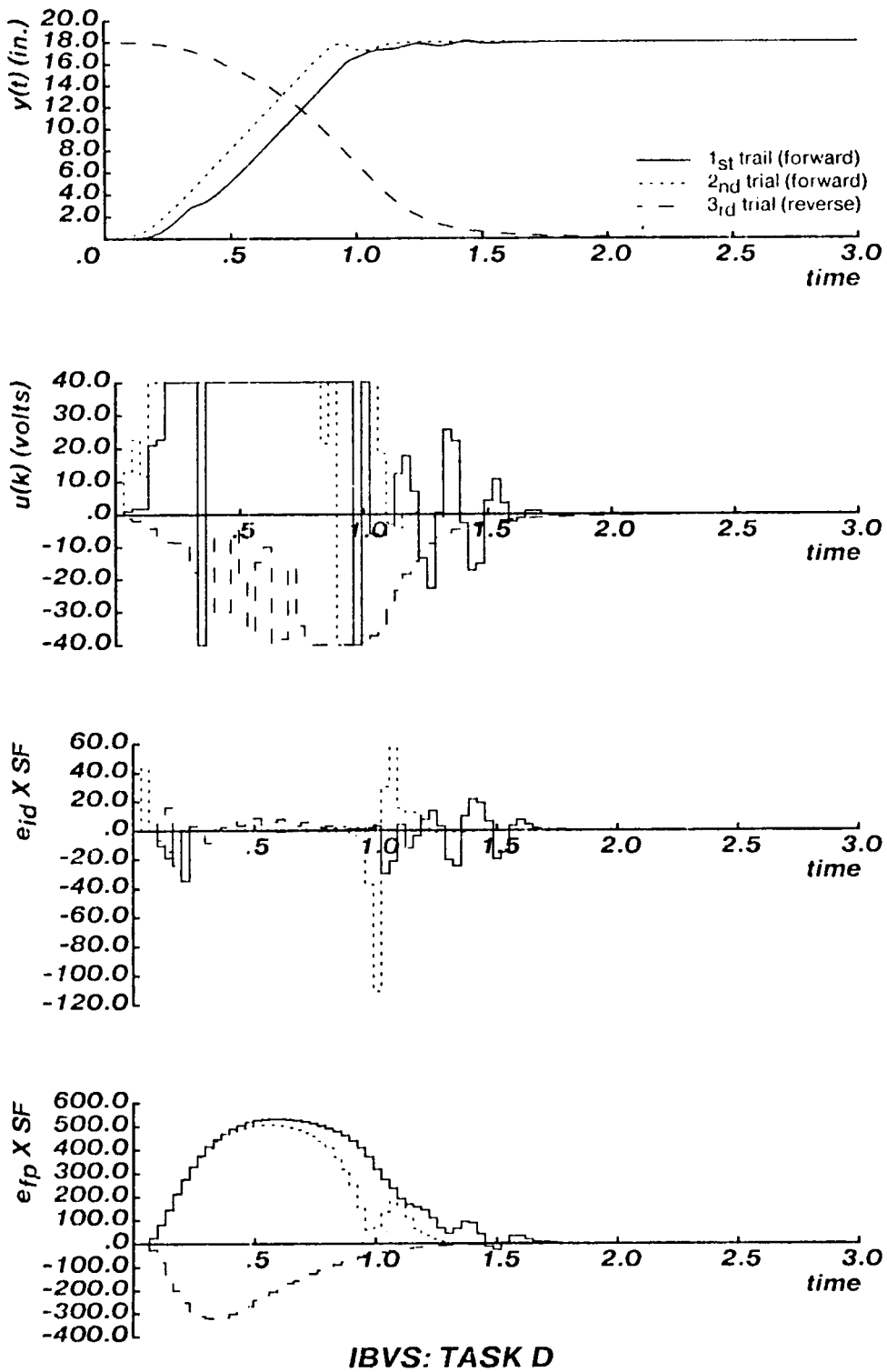

Figure 5-13: IBVS With Large Gain Changes

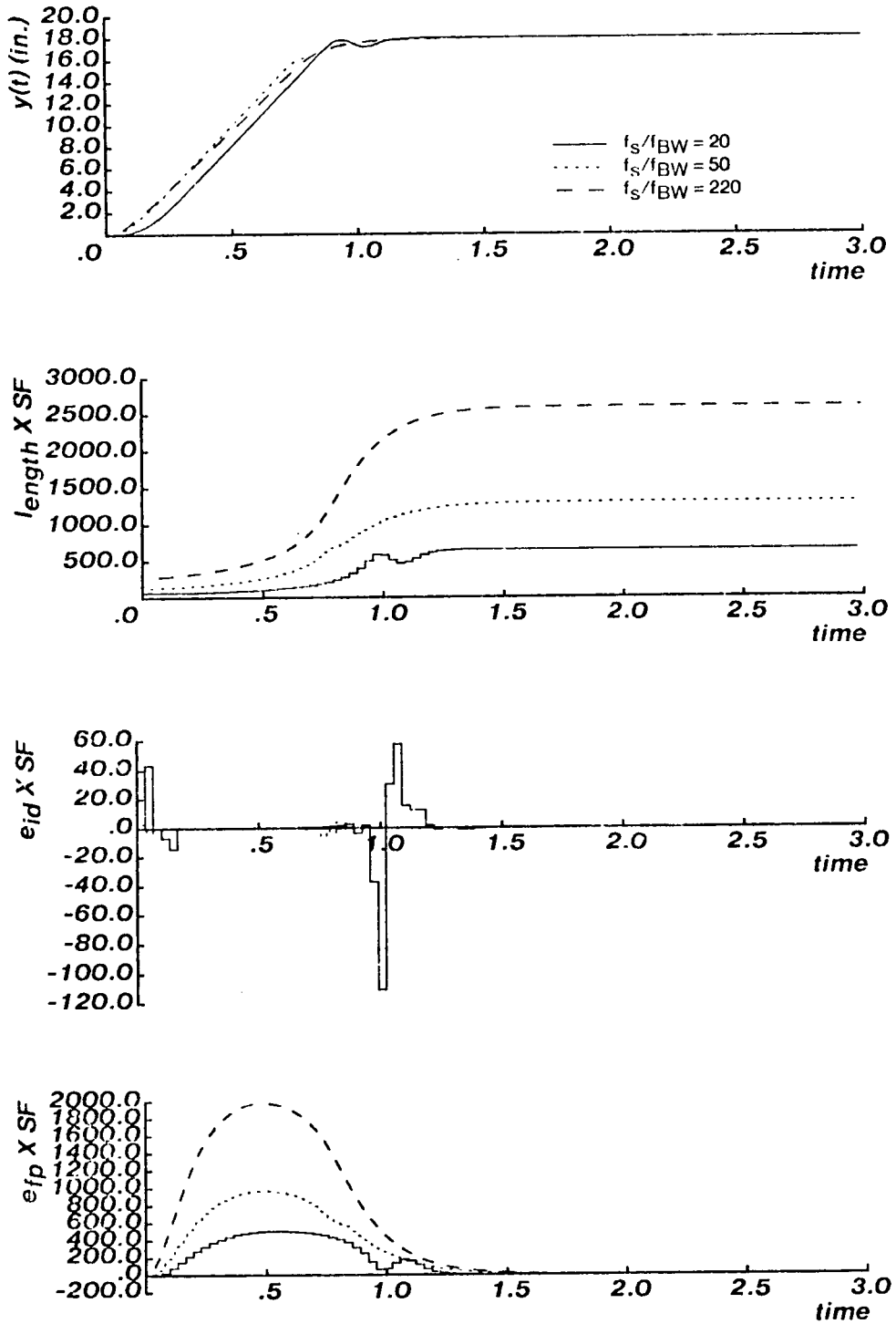

IBVS: TASK D

Figure 5-14: IBVS With Varying Sampling-to-Bandwidth Ratios

5.4.1. Adaptive Control Vs. Fixed

A performance comparison of adaptive versus fixed control, for the nonlinear IBVS system, is presented here. Fixed controllers are implemented by fixing the gains of the MRAC controller. Fixed gain values are derived from the estimated parameter values $\hat{\beta}$ which are identified from initial adaptive learning trials. The studies include the effects of varying the range of motion (and thus the change in feature gain), bandwidth, sampling-to-bandwidth ratio, and the strategy for initial model parameter estimation. The results of these experiments suggests the following:

- For a specific task, and at a sufficiently large bandwidth, a fixed controller can be tuned to achieve a time response comparable to the adaptive controller. As the bandwidth decreases, fixed control performance becomes sluggish relative to the adaptive response.

- A fixed controller tuned for a specific task cannot perform as well for another task. Adaptive controllers can perform well over a wide range of tasks.

- Fixed control performance is smoother than adaptive performance (i.e., improved stability) at lower sampling-to-bandwidth ratios.

Each task in Figure 5-9, including tasks at intermediate distances, are simulated at two reference model bandwidths; $\omega_n = 9.5$ sec^{-1} and $\omega_n = 4.4$ sec^{-1}. In both cases, the sampling period is set to $T = 0.033$ (sec). For each task, at each bandwidth, three control modes are evaluated:

1. Adaptive;

2. Fixed Control; where $\hat{\underline{\beta}}$ is fixed to the values learned in the initial adaptive run; and

3. Fixed Control; where $\hat{\underline{\beta}}$ is fixed to the values learned from adaptive control of Task C.

Task performance, which is summarized in Figures 5-15 and 5-16, is evaluated by the measured position rise-times. At the higher bandwidth, the adaptive controller and the fixed controller (with $\hat{\underline{\beta}}$ learned over the entire trajectory) have comparable performance. When the fixed system is tuned for a high gain region (i.e., Task C), it performs sluggishly when required to track gain changes in lower gain regions. Other initial learning strategies are possible. However, if learning is biased to the low gain region, the fixed controller becomes underdamped, and possibly unstable, as it approaches the target. At the lower bandwidth, fixed control performance degrades, relative to adaptive control, as ΔJ increases. One of the

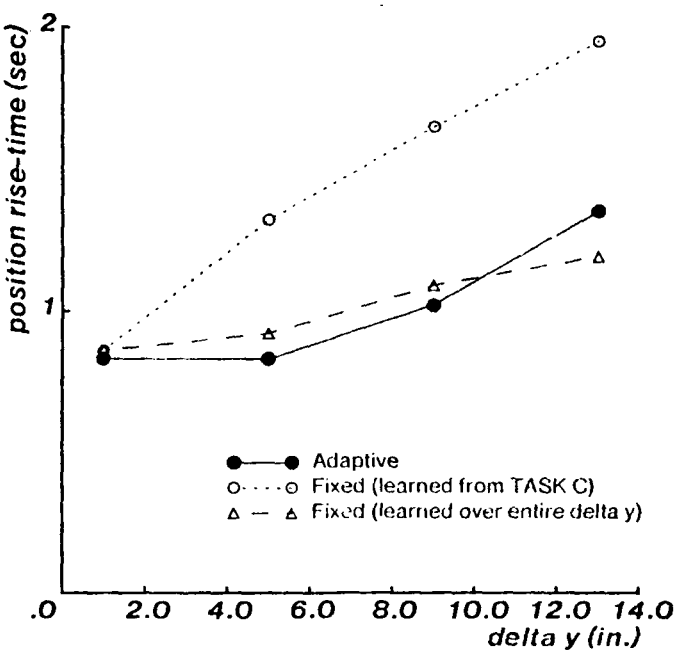

Figure 5-15: Fixed vs. Adaptive Performance (BW = 9.5 sec^{-1})

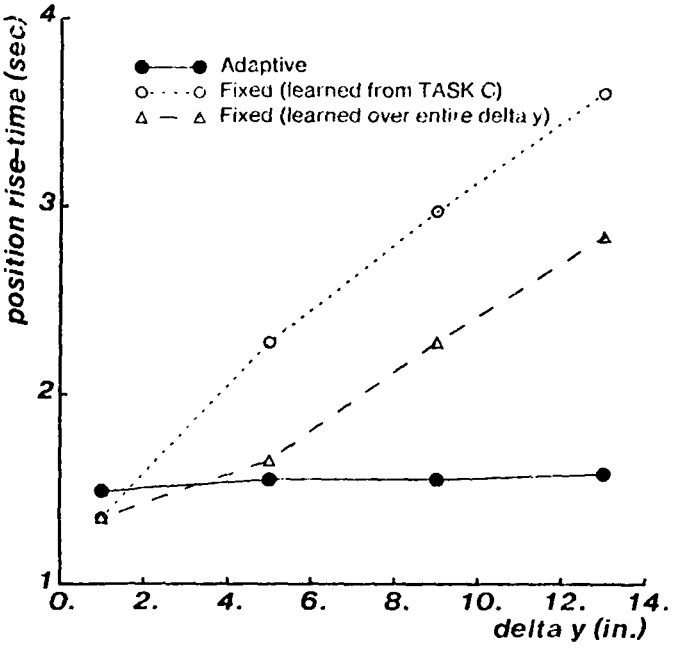

Figure 5-16: Fixed vs. Adaptive Performance (BW = 4.4 sec^{-1})

primary purposes for using feedback control is to reduce the sensitivity of a closed-loop system to open-loop parameter variations. This sensitivity, to the closed-loop bandwidth, is

explained as follows. A plant $KW(z^{-1})$ is controlled with a fixed feedback controller (Figure 5-17), where the gain term, K, varies with time. The feedback compensators are $C(z^{-1})$ and $H(z^{-1})$.

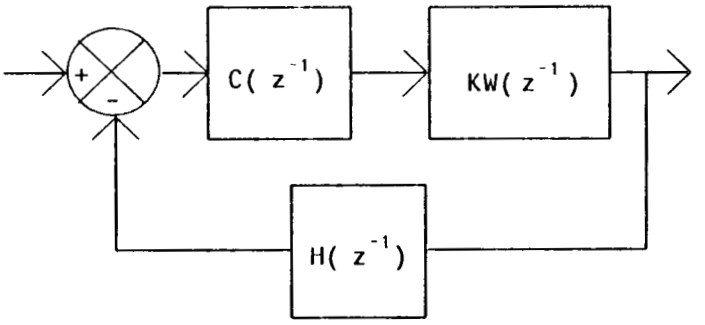

Figure 5-17: Fixed Feedback Control

The closed-loop transfer function, $M(z^{-1})$,

$$M(z^{-1}) = \frac{C(z^{-1})KW(z^{-1})}{1 + C(z^{-1})H(z^{-1})KW(z^{-1})} \tag{5.9}$$

is the same form as the LMFC represented in Figure 3-7. Over the frequency range of interest, the transfer function (5.9) approaches

$$M(z^{-1}) \rightarrow \frac{1}{H(z^{-1})} \tag{5.10}$$

independent of the plant gain. Therefore, as the closed-loop bandwidth increases, the system becomes less sensitive to gain variations [Kuo 82].

At the higher bandwidth (Figure 5-15), the adaptive response degrades as ΔJ and the distance traveled increase, as a result of control signal saturation and larger transient identification errors. At the lower bandwidth (Figure 5-16), the adaptive performance remains essentially constant because the sampling-to-bandwidth ratio has increased, thus reducing $e_{ID}(k)$, and because saturation is reduced for the smaller required velocities.

At the outset of this section, it is noted that, for small excursions and relatively small changes in J, the adaptive response is smooth. As the distance traveled increases, and ΔJ increases, small oscillations result unless f_s/f_{BW} is increased. Fixed control results in a smooth response even at the lower f_s/f_{BW} ratios. For example, Figure 5-18 compares the adaptive versus fixed responses for Task D, with $T = 0.033$ sec. and $\omega_n = 9.5$ sec^{-1}. An

advantage of fixed control is that it exhibits superior stability at lower sampling-to-bandwidth ratios. This becomes an important consideration when the hardware used in an actual implementation constrains the sampling period.

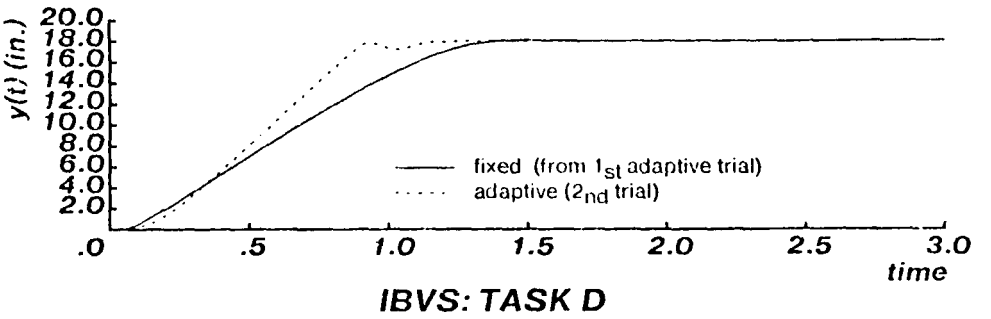

Figure 5-18: Position Response of Fixed vs. Adaptive Control

5.5. Summary

The experiments included in this chapter verify the simulation of the MRAC adaptive controllers (Chapter 3), for SISO systems. The SP MRAC is selected for IBVS control since it less sensitive to control signal saturation, has improved relative stability with measurement delays, and has superior noise performance.

The analysis shows that for IBVS control, the system under control exhibits nonlinear open-loop gains (or sensitivities) which can change dramatically over the task trajectory. A contribution of this dissertation is that MRAC control of such nonlinear systems (with measurement delay) produce dynamically stable closed-loop systems, in simulation, without directly interpreting actual positions. Achievement of acceptable stability then requires attention to the following details:

1. A least squares weighting factor of $\lambda = 0.85$ provides a suitable trade-off between tracking feature sensitivity changes and over-reaction to those changes. Larger values may be used to improve noise response.

2. The sampling-to-bandwidth, f_s/f_{BW} ratio must be selected in terms of the magnitude and slope of feature sensitivity change. For example, as the required distance of travel increases, larger sensitivity changes result, which require larger ratios. While $f_s/f_{BW} = 20$ is suitable for a small motion task (e.g., with a 1 inch travel, where the sensitivity changes by a factor of 2.2), the ratio must be increased to $f_s/f_{BW} = 50$ for an 18 inch excursion task, in which the sensitivity changes by a factor of 90. The specific sampling-to-bandwidth ratios also depend on the features used for control and relative object orientations.

3. A controller pole bound of $\gamma = 0.65$ is suitable for damping out oscillations due to measurement delays. The control penalty is also required for stability since the identifier can estimate non-minimum phase zeros arising from the nonlinear gain terms.

It is straightforward to design a fixed control law for a linear system when the control engineer has detailed knowledge of the open-loop system. The adaptive controller is implemented with minimal a'priori knowledge. When the plant is nonlinear, or has unknown parameters (e.g., for the 'teach-by-showing' strategy), it is a formedable engineering task to design a suitable fixed control law. A contribution of this dissertation is to evaluate an approach for implementing fixed controllers for such nonlinear system. The steady-state estimated plant parameters, derived by MRAC control, are used to specify a fixed LMFC controller. Comparison of the adaptive and fixed control approaches suggests the following:

1. While the stabity of an adaptive controller is highly susceptible to measurement noise, especially as λ decreases, a fixed controller exhibits superior noise performance.

2. A fixed controller exhibits a better transient response than the MRAC as the sampling-to-bandwidth ratio decreases. An adaptive approach has superior time responses at lower closed-loop bandwidths.

3. A fixed controller tuned for one task may not be suitable for another task. A single adaptive controller can be suitable for many tasks.

The following chapter extends the evaluation of adaptive MRAC and fixed LMFC to the independent control of multiple DOF coupled systems.

Chapter 6
Evaluation: Two DOF Systems

6.1. Overview

This chapter includes an evaluation for IBVS control of both linear and nonlinear kinematic two DOF configurations. The linear kinematic configuration (Section 4.2.1) is modeled with uncoupled linear robot dynamics. The kinematic structure of this configuration is uncoupled in a Cartesian frame, permiting the camera to be mounted so that the robot's degrees-of-freedom coincide with the camera's reference frame (i.e., the translational X and Y axes are parallel to the image plane's frame of reference). The articulated arm configuration (Section 4.2) displays nonlinear and coupled kinematics and dynamics. In this configuration, the articulated degrees-of-freedom (i.e., θ_1 and θ_2) are nonlinearly related to the camera's frame. Because of the kinematic and dynamic distinctions, these configurations are evaluated separately. While the evaluations focus on image-based control, enhanced SP MRAC joint-level control of the nonlinear dynamic robot is also evaluated.

The chapter is divided into two parts. The first part (Section 6.2) includes the evaluation of the linear kinematic configuration. In the second part (Section 6.4), the nonlinear and coupled kinematic and dynamic configuration is evaluated, along with the enhanced SP MRAC joint-level controller. (The controller parameters are summarized in Appendix C.) The evaluations include an analysis of the sensitivity matricies, and compare the control system performance of both uncoupled adaptive and fixed controllers. Potential performance advantages of a coupled controller are suggested by isolating specific problems associated with independent control.

The chapter includes detailed explainations and interpretations of the responses observed in the simulations. The predominant observations are:

- Adaptive IBVS control achieves dynamically stable systems for both configurations. The system performance exhibits good transient response, and zero steady-state errors. This performance is achieved without explicit a'priori knowledge of object positions or robot dynamics.

- For these two degree-of-freedom systems, predicted paths (i.e., those paths which would result if perfect feature reference model following were achieved) are nearly straight line trajectories. It is encouraging, for future implementations of more general systems, that these paths do not exhibit tortuous trajectories.

- The "teach-by-showing" strategy provides a convenient means for specifying visual servoing tasks when stringent path control is not required. For example, it may be used for small motion precision positioning (e.g., in precision assembly, for parts aquistion and mating alignment), and for gross positioning when smooth motion is acceptable and the work area is free of obstacles.

- Independent controllers produce deviations from the predicted path. Typical deviations are relatively small, with the exception of large motion nonlinear kinematic tasks. In these cases, large deviations increase the risk of obstacle collisions, and make it difficult to keep the observed object in the field-of-view. Thus, independent controllers may not be suitable for such tasks.

- Another limitation of the independent control strategy is accentuated by the kinematic coupling of the nonlinear kinematic configuration. In this configuration, there is a requirement for a feature/joint reassignment strategy. In contrast, a fixed feature/joint assignment is suitable for the linear kinematic configuration.

- The enhanced SP MRAC controller, with delay, yields stable systems, with good transient response, when used as a joint-level controller. To the best of the author's knowledge, this is the first simulation demonstration of an enhanced MRAC (i.e., SP MRAC, with control penalty and measurement delay) for robot control.

- An MRAC can be used to derive a fixed LMFC control law. ThE fixed controllers have better relative stability at lower sampling-to-bandwidth ratios, and tend to exhibit faster rise-times. Relative to the MRAC, however, they produce larger path deviations, and are only suitable for small motion tasks which have smaller sensitivity changes. A single fixed controller cannot achieve uniform performance over a broad range of tasks.

6.2. Linear Kinematics and Dynamics

This section includes an evaluation for the linear kinematic and dynamic system represented by Configuration 1 (Figure 4-1). The adaptive control approach is demonstrated to exhibit dynamically stable responses, and zero steady-state feature and position errors. Predicted position trajectories (i.e., the predicted pathes if perfect reference modeling were achieved) are smooth and approximate straight-line trajectories. Actual position trajectories deviate from the predicted response, however, typical deviations are relatively small. The MRAC time response lags the specified reference model rise-times. The fixed LMFC, which does not include an on-line identifier, produces larger path deviations, and faster rise-times.

Larger path deviations limits the LMFC to tasks requiring small motions. Potential performance advantages gained from a coupled controller are suggested by isolating specific problems associated with the independent adaptive controllers.

6.2.1. Sensitivity Analysis

The sensitivity matrix, $J(\underline{X})$, is

$$J(\underline{X}) = -J_{feat}(\underline{X}_{rel}) = \begin{bmatrix} -\frac{\partial X_{cog}}{\partial X_{rel}}(5.1) & -\frac{\partial X_{cog}}{\partial Y_{rel}}(5.5) \\ -\frac{\partial l_{ength}}{\partial X_{rel}}(5.2) & -\frac{\partial l_{ength}}{\partial Y_{rel}}(5.4) \end{bmatrix} \tag{6.1}$$

and the transfer function matrix, for the robot, is

$$W_p(s) = \begin{bmatrix} \frac{K_m}{s(\tau_{m\text{-}x}s+1)}\frac{1}{2\pi p} & 0 \\ 0 & \frac{K_m}{s(\tau_{m\text{-}y}s+1)}\frac{1}{2\pi p} \end{bmatrix} \tag{6.2}$$

The sensitivity matricies are evaluated to address the following questions:

1. Are the elements in (6.1) continuous and non-degenerate according to condition (2.6)?

2. If the controller could achieve perfect model following of the reference features (i.e., $e_{FP}(k) = 0$ for all k), what would be the predicted Cartesian path?

3. What is the diagonal dominance organization of JW_p, which determines the feature/joint coupling, and over what boundaries does this organization remained fixed?

To answer these questions, numerical maps of J were made for three line angles ($\theta_{obj} = 0$, 45, 75 degrees) and over the range of relative positions

$$-4 \leq X_{rel} \leq 4 \text{ (in.)} \quad \text{and } 0 \leq Y_{rel} \leq 25 \text{ (in.)} \quad \text{in 1 in. increments}$$

(The range of angles and positions correspond to those used in the simulation examples evluated in Section 6.2.2.). A typical map of $-J_{feat}(\underline{X}_{rel})$ is shown in Figure 6-1. The matrix is not evaluated at points where the line is hidden or is out of the field-of-view (OFV). These points are indicated by a "*" on the maps. Under these conditions, the matrix elements are continuous and non-degenerate.

Sensitivity J x10^2

F=5mm
θobj=45°

$\frac{\delta X_{cog}}{\delta X}$ — Y_{rel}

	-4	-3	-2	-1	0	1	2	3	4		-4	-3	-2	-1	0	1	2	3	4	
	-3.13	-3.13	-3.13	-3.13	-3.13	-3.13	-3.13	-3.13	-3.13	25	-0.50	-0.37	-0.25	-0.13	0.00	0.12	0.25	0.37	0.50	
	-3.25	-3.25	-3.25	-3.25	-3.25	-3.26	-3.26	-3.26	-3.26	24	-0.54	-0.41	-0.27	-0.14	0.00	0.13	0.27	0.40	0.54	
	-3.40	-3.40	-3.40	-3.40	-3.40	-3.40	-3.40	-3.40	-3.40	23	-0.59	-0.44	-0.29	-0.15	0.00	0.14	0.29	0.44	0.58	
	-3.55	-3.55	-3.55	-3.55	-3.55	-3.55	-3.55	-3.55	-3.55	22	-0.64	-0.48	-0.32	-0.16	0.00	0.16	0.32	0.48	0.64	
	-3.72	-3.72	-3.72	-3.72	-3.72	-3.72	-3.72	-3.72	-3.72	21	-0.70	-0.53	-0.35	-0.18	0.00	0.17	0.35	0.52	0.70	
	-3.90	-3.90	-3.90	-3.90	-3.90	-3.90	-3.90	-3.90	-3.90	20	-0.78	-0.58	-0.39	-0.20	0.00	0.19	0.38	0.58	0.77	
	-4.10	-4.10	-4.10	-4.10	-4.10	-4.10	-4.10	-4.10	-4.10	19	-0.86	-0.64	-0.43	-0.22	0.00	0.21	0.42	0.64	0.85	
	-4.33	-4.33	-4.33	-4.33	-4.33	-4.33	-4.33	-4.33	-4.33	18	-0.96	-0.72	-0.48	-0.24	0.00	0.23	0.47	0.71	0.95	
	-4.58	-4.58	-4.58	-4.58	-4.58	-4.58	-4.58	-4.58	-4.58	17	-1.07	-0.80	-0.54	-0.27	0.00	0.26	0.53	0.80	1.06	
	-4.86	-4.86	-4.86	-4.86	-4.86	-4.86	-4.86	-4.86	-4.86	16	-1.21	-0.91	-0.61	-0.31	0.00	0.30	0.60	0.90	1.20	
	-5.18	-5.18	-5.18	-5.18	-5.18	-5.18	-5.18	-5.18	-5.18	15	-1.37	-1.03	-0.69	-0.35	-0.01	0.34	0.68	1.02	1.36	
	-5.55	-5.55	-5.55	-5.55	-5.55	-5.55	-5.55	-5.55	-5.55	14	-1.57	-1.18	-0.79	-0.40	-0.01	0.38	0.78	1.17	1.56	
	-5.97	-5.97	-5.97	-5.97	-5.97	-5.97	-5.97	-5.97	-5.97	13	-1.82	-1.37	-0.91	-0.46	-0.01	0.44	0.90	1.35	1.80	
	-6.46	-6.46	-6.46	-6.46	-6.46	-6.46	-6.46	-6.46	-6.46	12	-2.13	-1.60	-1.07	-0.54	-0.01	0.52	1.05	1.58	2.11	
	-7.04	-7.04	-7.04	-7.04	-7.04	-7.04	-7.04	-7.04	-7.04	11	-2.53	-1.90	-1.27	-0.64	-0.01	0.62	1.25	1.88	2.51	
	-7.73	-7.73	-7.73	-7.73	-7.73	-7.73	-7.73	-7.73	-7.73	10	-3.06	-2.30	-1.54	-0.78	-0.02	0.74	1.50	2.26	3.02	
	-8.57	-8.57	-8.57	-8.57	-8.57	-8.57	-8.57	-8.57	-8.57	9	-3.77	-2.83	-1.90	-0.96	-0.03	0.91	1.84	2.78	3.71	
	-9.62	-9.62	-9.62	-9.62	-9.62	-9.62	-9.62	-9.62	-9.62	8	-4.75	-3.57	-2.39	-1.21	-0.04	1.14	2.32	3.50	4.68	
	******	-10.97	-10.97	-10.97	-10.97	-10.97	-10.97	-10.97	-10.97	7	******	-4.65	-3.12	-1.58	-0.05	1.48	3.01	4.54	6.07	
	******	-12.75	-12.75	-12.75	-12.75	-12.75	-12.75	-12.75	******	6	******	-6.30	-4.22	-2.15	-0.08	1.99	4.06	6.13	******	
	******	******	-15.22	-15.22	-15.22	-15.22	-15.22	-15.22	******	5	******	******	-6.05	-3.10	-0.14	2.81	5.77	8.73	******	
	******	******	-18.90	-18.90	-18.90	-18.90	-18.90	******	******	4	******	******	-9.40	-4.84	-0.27	4.30	8.86	******	******	
	******	******	******	-24.94	-24.94	-24.94	******	******	******	3	******	******	******	-8.61	-0.62	7.38	******	******	******	
	******	******	******	******	-36.80	-36.80	******	******	******	2	******	******	******	******	-1.96	15.68	******	******	******	
	******	******	******	******	-72.08	******	******	******	******	1	******	******	******	******	-13.78	******	******	******	******	

$\frac{\delta X_{cog}}{\delta Y}$

$\frac{\delta length}{\delta X}$ — X_{rel}

	-4	-3	-2	-1	0	1	2	3	4		-4	-3	-2	-1	0	1	2	3	4	
	0.09	0.09	0.09	0.09	0.09	0.09	0.09	0.09	0.09	25	0.12	0.11	0.10	0.09	0.09	0.08	0.07	0.07	0.06	
	0.10	0.10	0.10	0.10	0.10	0.10	0.10	0.10	0.10	24	0.13	0.12	0.11	0.10	0.10	0.09	0.08	0.07	0.06	
	0.10	0.10	0.10	0.10	0.10	0.10	0.10	0.10	0.10	23	0.14	0.13	0.12	0.11	0.10	0.09	0.09	0.08	0.07	
	0.11	0.11	0.11	0.11	0.11	0.11	0.11	0.11	0.11	22	0.15	0.14	0.13	0.12	0.11	0.10	0.09	0.08	0.07	
	0.12	0.12	0.12	0.12	0.12	0.12	0.12	0.12	0.12	21	0.17	0.16	0.15	0.14	0.12	0.11	0.10	0.09	0.08	
	0.14	0.14	0.14	0.14	0.14	0.14	0.14	0.14	0.14	20	0.19	0.18	0.16	0.15	0.14	0.12	0.11	0.10	0.08	
	0.15	0.15	0.15	0.15	0.15	0.15	0.15	0.15	0.15	19	0.21	0.20	0.18	0.17	0.15	0.14	0.12	0.10	0.09	
	0.17	0.17	0.17	0.17	0.17	0.17	0.17	0.17	0.17	18	0.24	0.22	0.21	0.19	0.17	0.15	0.13	0.11	0.09	
	0.19	0.19	0.19	0.19	0.19	0.19	0.19	0.19	0.19	17	0.28	0.25	0.23	0.21	0.19	0.17	0.14	0.12	0.10	
	0.21	0.21	0.21	0.21	0.21	0.21	0.21	0.21	0.21	16	0.32	0.29	0.27	0.24	0.21	0.19	0.16	0.13	0.11	
	0.24	0.24	0.24	0.24	0.24	0.24	0.24	0.24	0.24	15	0.37	0.34	0.31	0.27	0.24	0.21	0.18	0.15	0.11	
	0.28	0.28	0.28	0.28	0.28	0.28	0.28	0.28	0.28	14	0.43	0.39	0.35	0.32	0.28	0.24	0.20	0.16	0.12	
	0.32	0.32	0.32	0.32	0.32	0.32	0.32	0.32	0.32	13	0.51	0.47	0.42	0.37	0.32	0.27	0.22	0.17	0.13	
	0.37	0.37	0.37	0.37	0.37	0.37	0.37	0.37	0.37	12	0.62	0.56	0.50	0.44	0.38	0.31	0.25	0.19	0.13	
	0.44	0.44	0.44	0.44	0.44	0.44	0.44	0.44	0.44	11	0.76	0.68	0.60	0.52	0.45	0.37	0.29	0.21	0.13	
	0.54	0.54	0.54	0.54	0.54	0.54	0.54	0.54	0.54	10	0.96	0.85	0.75	0.64	0.54	0.43	0.33	0.22	0.12	
	0.66	0.66	0.66	0.66	0.66	0.66	0.66	0.66	0.66	9	1.24	1.09	0.95	0.80	0.66	0.52	0.37	0.23	0.09	
	0.83	0.83	0.83	0.83	0.83	0.83	0.83	0.83	0.83	8	1.65	1.44	1.24	1.04	0.83	0.63	0.43	0.22	0.02	
	******	1.08	1.08	1.08	1.08	1.08	1.08	1.08	1.08	7	******	1.98	1.68	1.38	1.08	0.78	0.48	0.18	-0.12	
	******	1.45	1.45	1.45	1.45	1.45	1.45	1.45	******	6	******	2.88	2.41	1.94	1.46	0.99	0.52	0.05	******	
	******	******	2.07	2.07	2.07	2.07	2.07	2.07	******	5	******	******	3.69	2.89	2.09	1.29	0.49	-0.31	******	
	******	******	3.18	3.18	3.18	3.18	3.18	******	******	4	******	******	6.29	4.76	3.23	1.70	0.17	******	******	
	******	******	******	6.52	6.52	6.52	******	******	******	3	******	******	******	9.15	5.65	2.16	******	******	******	
	******	******	******	******	11.84	11.84	******	******	******	2	******	******	******	******	12.47	1.40	******	******	******	
	******	******	******	******	42.68	******	******	******	******	1	******	******	******	******	60.73	******	******	******	******	

$\frac{\delta length}{\delta Y}$

Figure 6-1: Sensitivity Map

6.2.1.1. Predicted Path

Evaluation of control performance includes both time and path performance. Path performance is evaluated relative to the predicted path, or trajectory, that would result if the controller could achieve perfect model following. The predicted pathes are calculated in this section. Two approaches are available for deriving these pathes. One method is based on numerical evaluation of the inverse of the sensitivity matrix according to:

$$d\underline{X} = J^{-1}\, d\underline{f}$$

A second approach is to analytically solve the feature-to-Cartesian space mapping (i.e., the interpretation transformation). Since the analytic equations for the Cartesian-to-feature space mapping (i.e., the inverse interpretation transformation) have been derived (in Section 4.5), the later approach is used here. The feature transformation equations (4.30) and (4.31) are rewritten as:

$$X_{rel} = \frac{1}{V}\left\{\frac{ret}{F \bullet SF}\left[V^2 - (0.5 l_o \sin\theta_{rel})^2\right] X_{cog} + \left[(0.5 l_o \sin\theta_{rel})^2 \sin\theta_{rel} \cos\theta_{rel}\right]\right\} \tag{6.3}$$

and

$$V^3 l_{ength} + V^2\left[X_{cog}\sin\theta_{rel} - \frac{F \bullet SF \bullet \cos\theta_{rel}}{ret}\right] - V\left[l_{ength}(0.5 l_o \sin\theta_{rel})^2\right]$$

$$+ \sin\theta_{rel}\left[-\frac{F \bullet SF}{ret}(0.5 l_o)^2 \sin\theta_{rel}\cos\theta_{rel} - X_{cog}(0.5 l_o \sin\theta_{rel})^2\right] = 0 \tag{6.4}$$

where

$$l_o \doteq 1 \text{ (inch) and } V \doteq F_o + Y_{rel}$$

For each sampling period, (6.3) and (6.4) are solved for $X_{rel}(k)$ and $Y_{rel}(k)$, as a function of the feature reference model signals, $X_{cog\text{-}ref}(k)$ and $l_{ength\text{-}ref}(k)$. The cubic equation (6.4) is solved numerically for V, and the resulting Y_{rel} is substituted into (6.3) to obtain X_{rel}. The Cartesian path is then:

$$X(k) = X_{obj} - X_{rel}(k) \text{ and } Y(k) = Y_{obj} - Y_{rel}(k)$$

The relative complexity of this interpretation process for even this 2 DOF system illustrates the potentiality for error and computational complexity which would be required in a position-based system.

The visual servoing tasks evaluated in this section are represented in Figure 6-2. For each

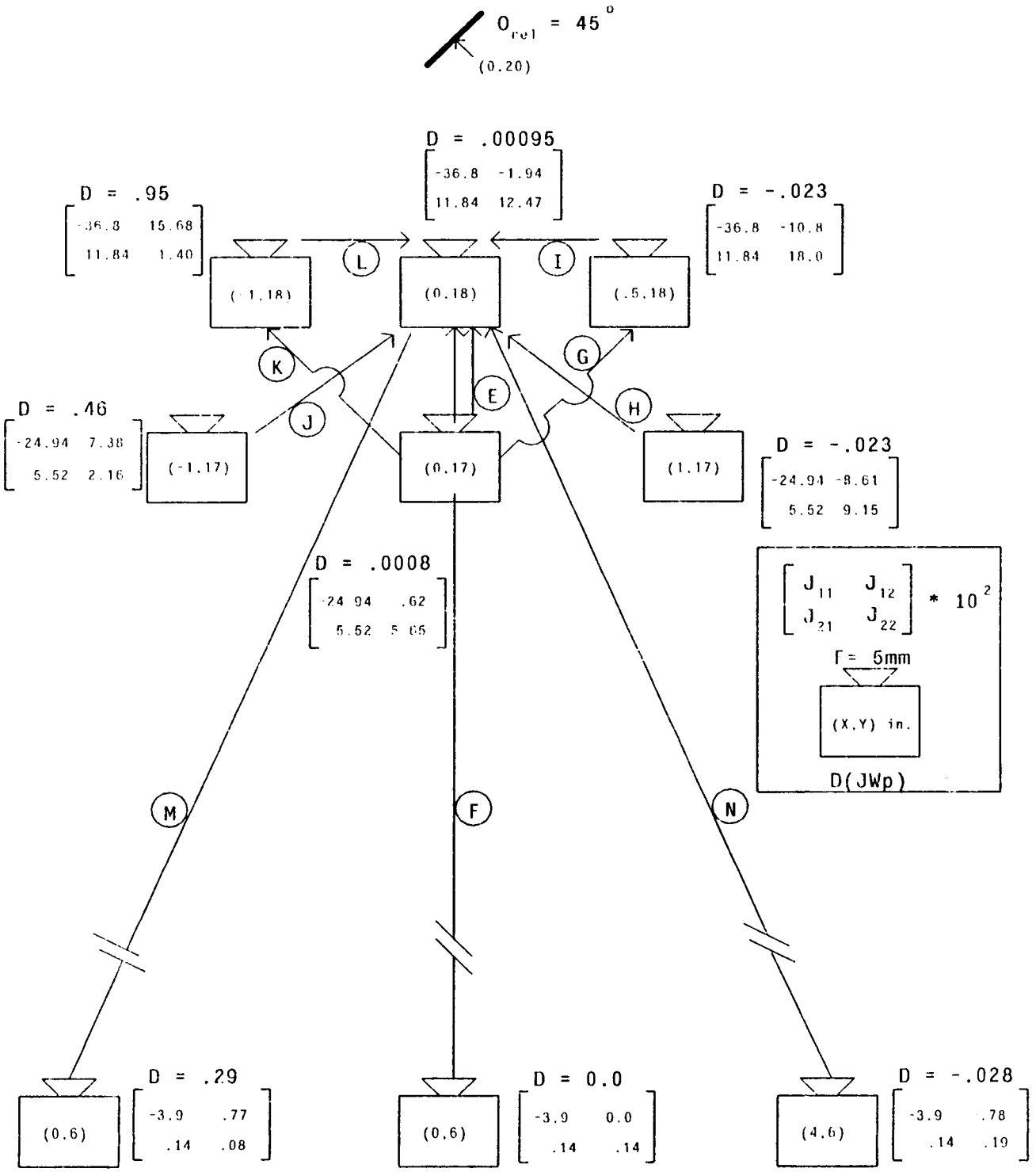

Figure 6-2: 2 DOF Linear Kinematic and Dynamic Tasks

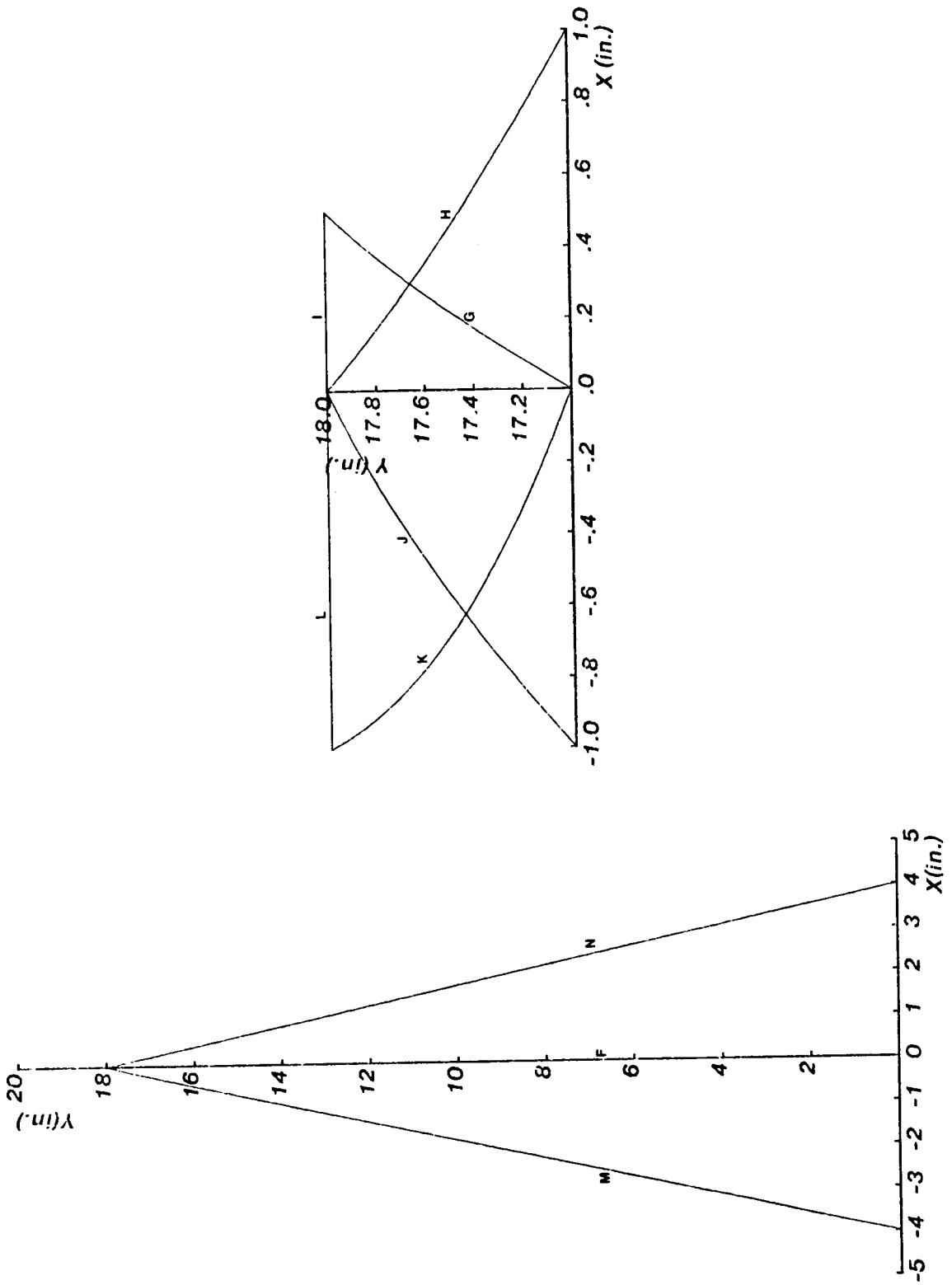

Figure 6-3: Predicted Paths

task, the predicted path (in a forward trajectory) is displayed in Figure 6-3.[8] The analysis demonstrates that, for this limited degree-of-freedom system, the predicted paths are smooth and exhibit nearly straight-line trajectories. Such motion is satisfactory for many applications. Had this 2 DOF system yielded paths with tortuous trajectories, then it would not be very promising to expect better behavior from more general systems.

6.2.1.2. Feature/Joint Assignment

Selection of the feature/joint assignment (Section 2.5.2.1) is based on the column arrangement of the transfer function matrix JW_p which minimizes $D(JW_p)$. The following derivation illustrates this proceedure. The robot transfer function matrix in (6.2) is written as

$$W_p(s) = \begin{bmatrix} K_{11}(s) & 0 \\ 0 & K_{22}(s) \end{bmatrix}$$

and the feature sensitivity in (6.1) is written as

$$J = \begin{bmatrix} j_{11} & j_{12} \\ j_{21} & j_{22} \end{bmatrix}$$

The overall transfer function matrix can be written as either

$$JW_p = \begin{bmatrix} j_{11}K_{11}(s) & j_{12}K_{22}(s) \\ j_{21}K_{11}(s) & j_{22}K_{22}(s) \end{bmatrix} \quad \text{(Case 1)}$$

or

$$JW_p^* = \begin{bmatrix} j_{12}K_{22}(s) & j_{11}K_{11}(s) \\ j_{22}K_{22}(s) & j_{21}K_{11}(s) \end{bmatrix} \text{(Case 2)}$$

The feature changes $\delta\underline{f} = [\delta X_{cog}, \delta l_{ength}]^T$, with respect to the control signal changes $\delta\underline{u} = [\delta u_1, \delta u_2]^T$, become

$$\begin{bmatrix} \delta X_{cog} \\ \delta l_{ength} \end{bmatrix} = \underset{\text{CASE 1}}{JW_p \begin{bmatrix} \delta u_1 \\ \delta u_2 \end{bmatrix}} = \underset{\text{CASE 2}}{JW_p^* \begin{bmatrix} \delta u_2 \\ \delta u_1 \end{bmatrix}}$$

---

[8] In Figure 6-3, predicted paths for Tasks I and L are straight lines, and the paths for Tasks E and F have path deviations from the Y-axis of is 0.002 and 0.026 inches, respectively.

For Case 1, the feature/joint assignment would be $X_{cog} \leftarrow$ X-axis and $l_{ength} \leftarrow$ Y-axis. For Case 2, the assignment would be $X_{cog} \leftarrow$ Y-axis and length $\leftarrow$ X-axis. The assignment decision is based on the column arrangement which minimizes the coupling; i.e.,

$$\text{if } D(\mathbf{J}\mathbf{W}_p) < D(\mathbf{J}\mathbf{W}_p^*) \text{ then select assignment in Case1; else choose Case 2} \tag{6.5}$$

Condition (6.5) leads to

$$|j_{11}j_{22}| \underset{\text{Case 2}}{\overset{\text{Case 1}}{\gtrless}} |j_{12}j_{21}|$$

Maps of feature/joint assignment are derived from sensitivity maps. An assignment map, which corresponds to the sensitivity map of Figure 6-1, is displayed in Figure 6-4.[9] For example, the control structure for the assignment at $\mathbf{X}_{rel} = \{X_{rel}, Y_{rel}\}^T = \{0,3\}^T$ is represented in Figure 6-5. Figure 6-4 indicates that the feature/joint assignment may require switching during a control task. However, upon inspection of these maps, it is observed that the feature/joint assignment remains fixed over large regions of space, and there are no "islands" where the assignment changes, but there is a distinct switching boundary. Further, over most of the soace, X_{cog} is assigned to the X-axis, and l_{ength} to the Y-axis. For θ_{obj} equal to zero, the assignment remains constant over all space. As θ_{obj} increases, the boundary shifts to the left, but X_{cog} remains assigned to the X-axis over most of the region. These observations are in contrast to those for the nonlinear kinematic configuration (in Section 6.3.2.1) for which the assignments do not remain constant over large regions of space.

When the sensitivity matrix is organized in a diagonally dominant fashion, the coupling (or off-diagonal) elements, can change by a larger percentage over space than the main diagonal elements. For example, if the camera were forced to move along a straight line trajectory (represented by Task H in Figure 6-2), then the corresponding percentage change in each of the elements is plotted in Figure 6-6, where

$$\%\text{change} \doteq \frac{|J(-1,3) - J(X_{rel}, Y_{rel})|}{|J(-1,3)|} \times 100\%$$

---

[9] It is noted that the sensitivity matrix did not, in general, satisfy the classic definition of dominance in (2.8). For example, at $\underline{X}_{rel} = \{1,3\}^T$, classical dominance does not hold.

"0" if $X_{cog} \leftarrow X_{axis}$
"1" if $X_{cog} \leftarrow Y_{axis}$ $\Longrightarrow$

									Y_{rel}	
	0	0	0	0	0	0	0	0	0	25
	0	0	0	0	0	0	0	0	0	24
	0	0	0	0	0	0	0	0	0	23
	0	0	0	0	0	0	0	0	0	22
	0	0	0	0	0	0	0	0	0	21
	0	0	0	0	0	0	0	0	0	20
	0	0	0	0	0	0	0	0	0	19
	0	0	0	0	0	0	0	0	0	18
	0	0	0	0	0	0	0	0	0	17
	0	0	0	0	0	0	0	0	0	16
	0	0	0	0	0	0	0	0	0	15
	0	0	0	0	0	0	0	0	0	14
	0	0	0	0	0	0	0	0	0	13
	0	0	0	0	0	0	0	0	0	12
	0	0	0	0	0	0	0	0	1	11
	0	0	0	0	0	0	0	0	1	10
	0	0	0	0	0	0	0	0	1	9
	0	0	0	0	0	0	0	1	1	8
	•	0	0	0	0	0	0	1	1	7
	•	0	0	0	0	0	0	1	•	6
	•	•	0	0	0	0	1	1	•	5
	•	•	0	0	0	0	1	•	•	4
	•	•	•	0	0	0	•	•	•	3
	•	•	•	•	0	1	•	•	•	2
	•	•	•	•	0	•	•	•	•	1
$X_{rel} \rightarrow$	-4	-3	-2	-1	0	1	2	3	4	

Feature/Joint Assignment

Figure 6-4: Feature/Joint Assignment Map

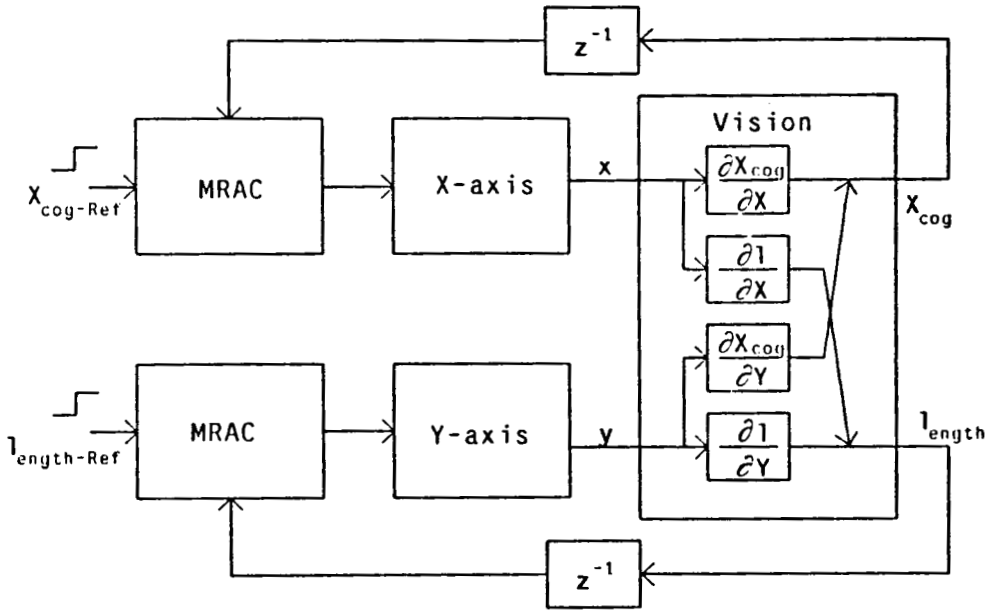

Figure 6-5: Feature/Joint Assignment

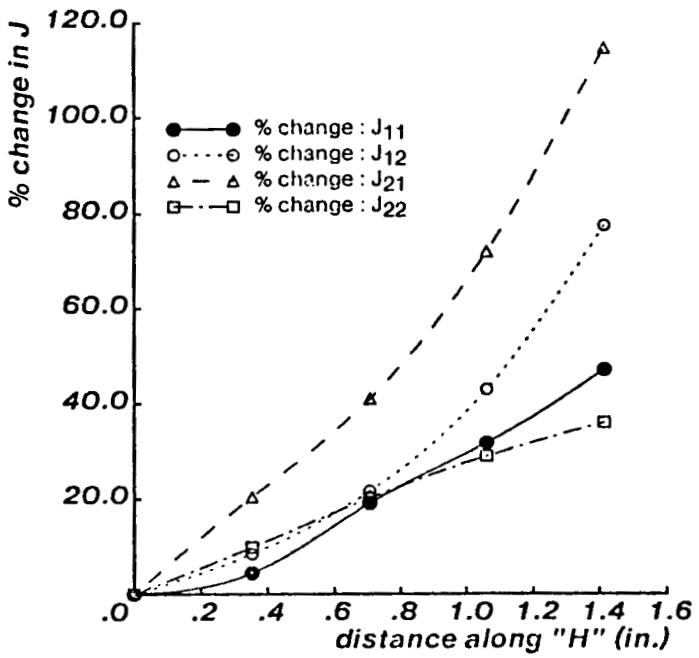

Figure 6-6: Percentage Change In Feature Sensitivity

For other tasks, changes in sensitivity can be even larger (e.g., in Task J, J(2,2) changes by 477% or by a factor of 5.77). The significance of this observation is that it is expected that

even larger sampling-to-bandwidth ratios will be required for identification and control of these coupled image-based systems. When using independent controllers, the coupling elements can be viewed as external disturbances. Thus, the sampling rate must be high enough to reject the apparent rapidly changing disturbances.

In most of the simulations presented in this section, the feature/joint assignment is fixed to $X_{cog} \leftarrow$ X-axis, irrespective of diagonal dominance changes. In some examples, performance is evaluated when the feature/joint assignment is switched at the boundary of diagonal dominance changes. In these examples, control is halted at the boundary and the feature assignment is switched. When the assignment is switched, the identifier parameters must be reset or initialized to the values used for that particular coupling. Control is then restarted with reference model reinitialization. In these examples, D(k) is measured during control using analytic derivations of $J(\underline{X}_{rel})$ and assuming that $\{X_{rel}, Y_{rel}\}$ is known.

6.2.1.3. Path Constraint

A path constraint strategy, for this configuration, would not appear to be required since the predicted paths, in Figure 6-3, approach straight-lines. Such well behaved paths may not result in more general and higher DOF systems. Even for this simple system, perfect model following is not expected because of transient identification errors due to rapidly changing gains, measurement delays, and use of independent controllers. Thus, evaluation of a path constraint strategy is a practical exercise.

A path constraint approach, based on the hierarchical control strategy presented in Chapter 2, is evaluated. The hierarchy is represented in Figure 6-7, where

$$\%\Delta X_{cog} = \frac{|X_{cog\text{-}desired} - X_{cog}(k)|}{\Delta X_{cog\text{-}max}} \times 100\%$$

and the percentage feature error ε is chosen experimentally to be $\varepsilon = 10\%$. The maximum feature change, $\Delta X_{cog\text{-}max}$, is unity, since the image coordinates are normalized to the image boundaries. For these simulations, Y-axis motion is constrained by braking. In the figure, it is assumed that the X_{cog} feature is dominated by movement along the X-axis (i.e., all areas marked with "o" on the feature/joint assignment maps).

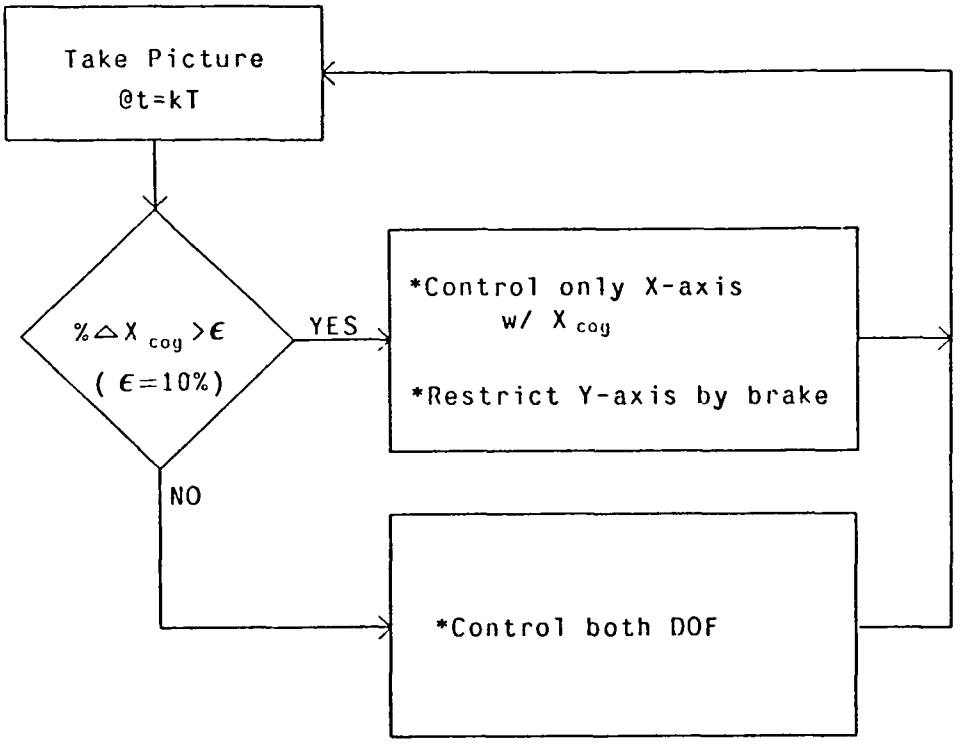

Figure 6-7: Hierarchy for 2 DOF Linear Kinematic System

6.2.2. Control Evaluation

The visual servoing tasks to be evaluated are represented in Figure 6-2. Figure 6-2 also indicates the sensitivity matrices in the initial and desired views, and the associated coupling index[10]. Tasks are simulated for both the forward (or approach) and reverse (or backing-away) directions. The tasks are selected so that, in the desired view, the camera is in close proximity to the object, as if the robot were going to acquire the object. This is a worse case arrangement since **J** changes rapidly as the camera approaches the line.

Each task is simulated at two sampling-to-bandwidth ratios by fixing the bandwidth to $\omega_n = 9.5$ sec^{-1}, and setting the sampling period to either $T = 0.033$ or 0.013 seconds[11], corresponding to

---

[10] For this configuration the magnitude of $\mathbf{W}_p$, used to calculate $D(J\mathbf{W}_p)$, are the translational stage DC gains $K/2\pi p$ (Sections 4.3.3 and 4.4.4). Since the gains are identical for both stages, and $\mathbf{W}_p$ is diagonal, $D(J\mathbf{W}_p) = D(J)$

[11] Due to open-loop reference model time constant round-off, the closed-loop bandwidth is $\omega_n = 9.4$ sec^{-1}, when $T = 0.013$

$f_s/f_{BW} = 20$, when $T = 0.033$ sec.

and

$f_s/f_{BW} = 51$, when $T = 0.013$ sec.

The controller paramters are summarized Appendix C. After each initial adaptive learning trial, a fixed LMFC is implemented using the steady-state estimated plant parameters identified from the initial adaptive trial. The resultant approach trajectories, at the larger sampling-to-bandwidth ratio and with the fixed feature/joint assignment, are shown in Figures 6-8, 6-9, and 6-10. Each plot shows the adaptive control on the second trial, the fixed LMFC, adaptive control with the path constraint hierarchy, and the predicted path. Each plot indicates the rise-time as the maximum of the X-axis and Y-axis position rise-times. Each task is simulated for 3 seconds.

The following observations emerge from the performance evaluation of the adaptive controller:

1. Stability : At the higher sampling-to-bandwidth ratio ($f_s/f_{BW} = 51$) and for the the fixed feature/joint assignment, all simulations are stable, with acceptable transient response, and zero steady-state feature and position errors.

   At the lower ratio ($f_s/f_{BW} = 20$), which was suitable for the 1 DOF configuration, transient response degrades when the tasks are run in the reverse directions, and when crossing boundaries of diagonal dominance changes. Problems associated with independent adaptive control of coupled systems are accentuated, including not switching the feature/joint assignment at boundaries of diagonal dominance changes, and MRAC sign sensitivity. The MRAC sign sensitivity causes momentary changes in the sign of the controller gain, which causes momentary reversals in table directions. Examples of feature/joint reassignment and MRAC sign sensitivity are presented in Section 6.2.3.

2. Parameter Estimation : When the line stays in the field-of-view, steady-state identification errors go to zero. The transient identification-errors approach zero before steady-state positions are reached (i.e., while the camera is still in motion), which indicates that equivalent SISO models of the coupled plant can be identified. Sufficiently large sampling-to-bandwidth ratios are then required to track dynamic changes. Transient identification-errors remained for all examples.

   Type 0 plants were identified in the steady-state, and some of the estimated zero's are non-minimum phase. This demonstrates the need for a control penalty and signal biasing.

   At the higher sampling-to-bandwidth ratio, adaptive performance in the second trial is not significantly improved (relative to the initial trial) due to the higher sampling-to-bandwidth ratio, and better initializations of the parameter vector. Examples of the first trial performances are displayed in Figure 6-11.

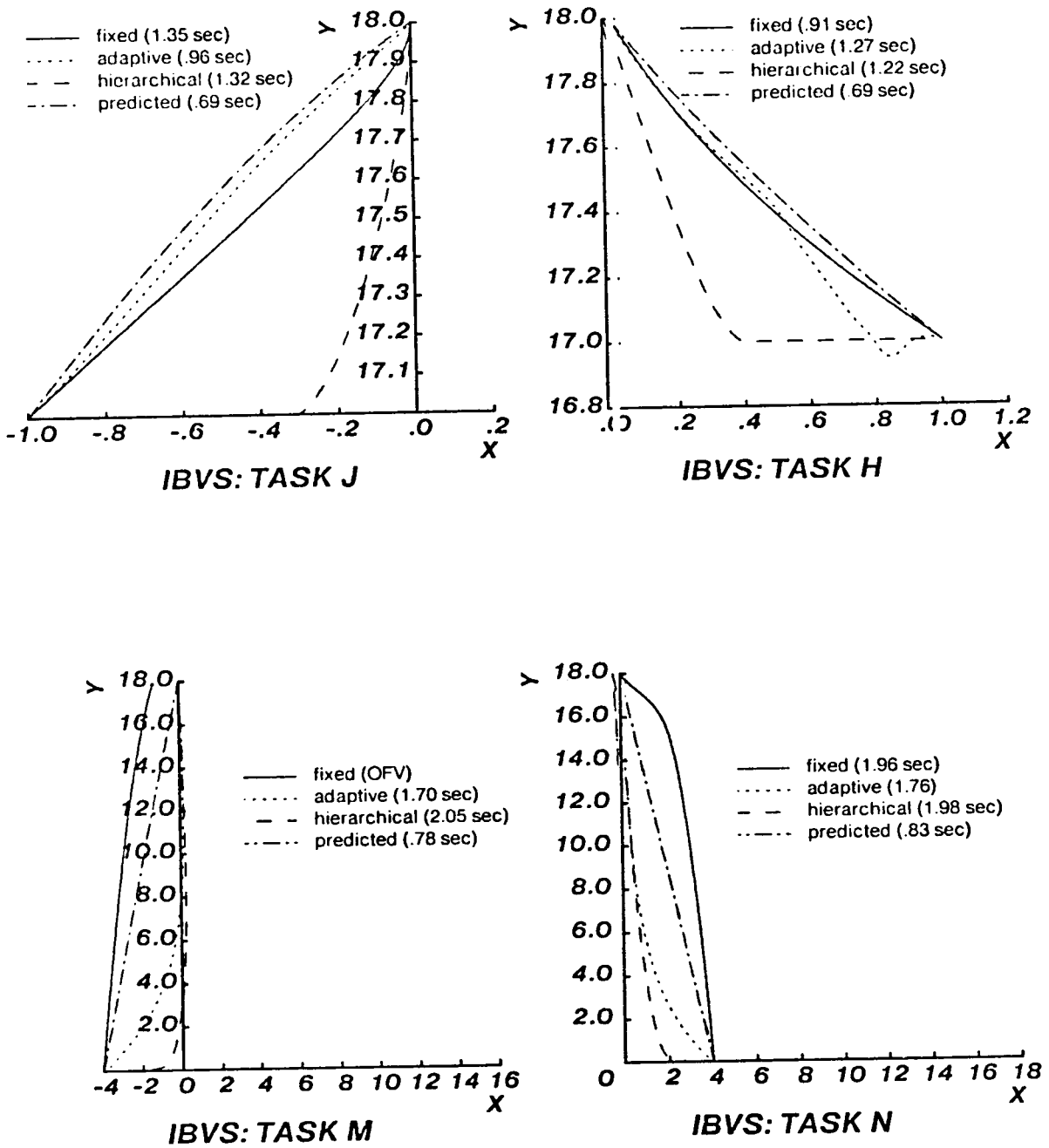

Figure 6-8: Linear Kinematic Trajectories ($f_s/f_{BW} = 51$)

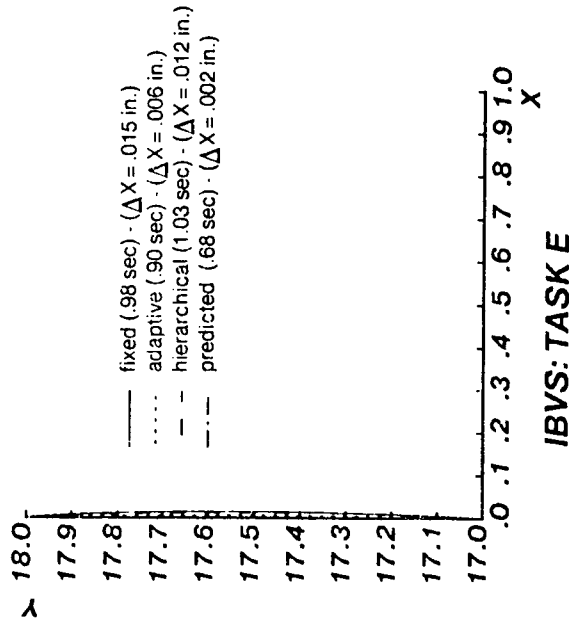

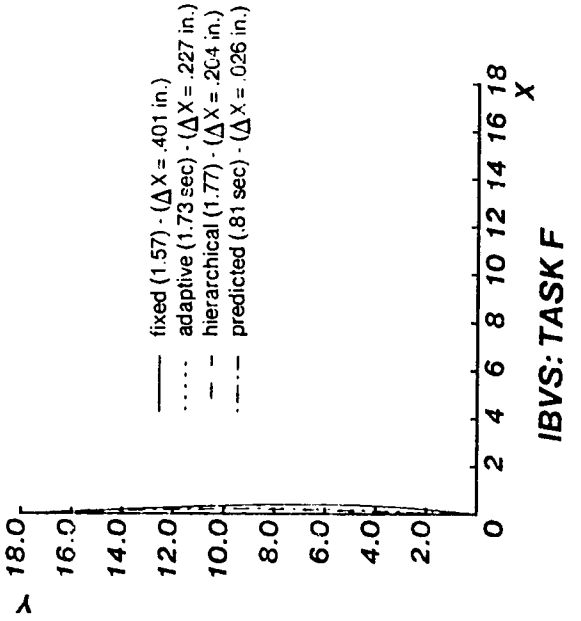

Figure 6-9: Linear Kinematic Trajectories (cont.)

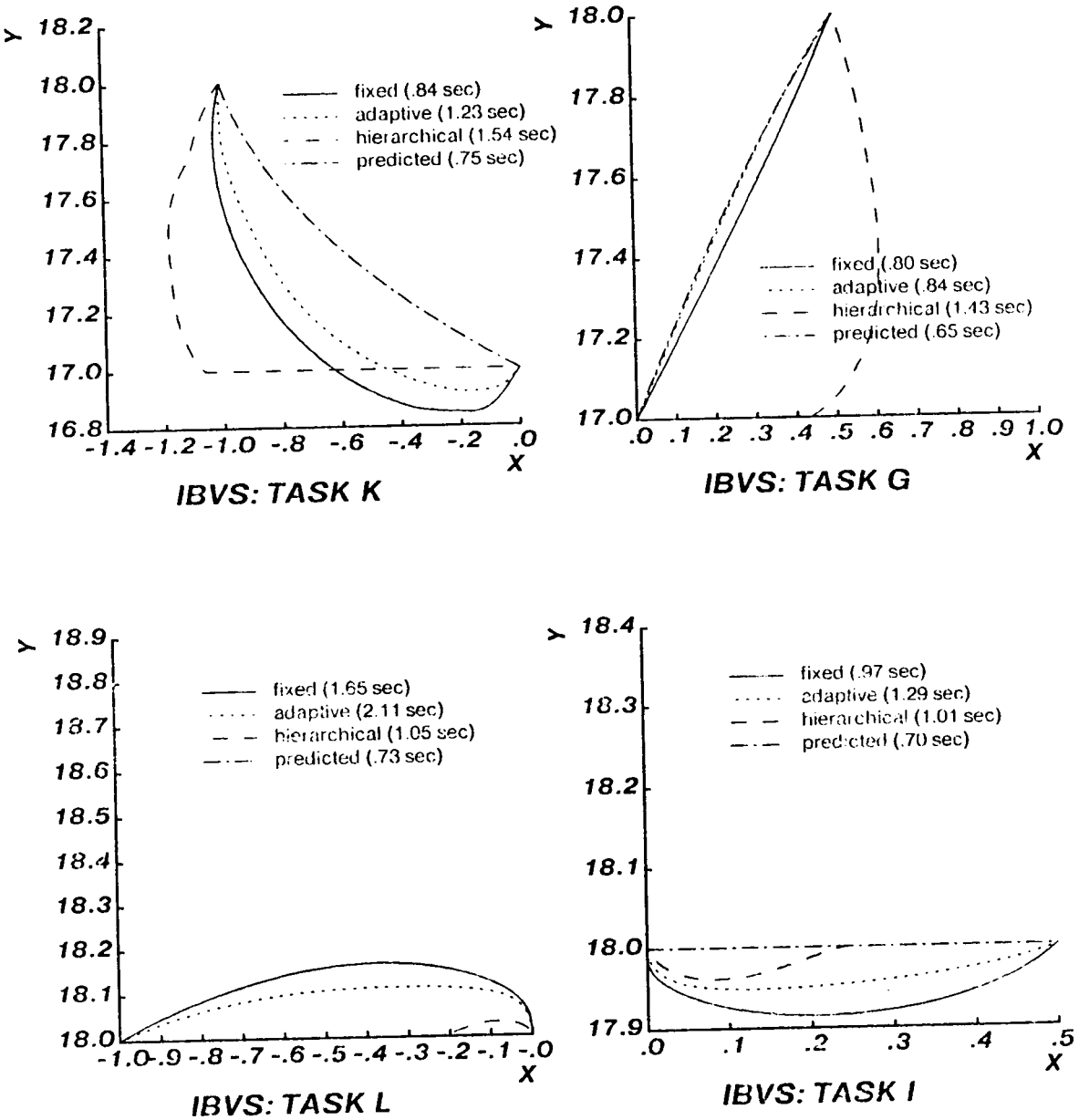

Figure 6-10: Linear Kinematic Trajectories (cont.)

In the second trial trajectories, the object remains in a stationary position between successive trials. If the object is allowed to assume random positions, should the identifier be reset between successive trials? To examine this question, Tasks J, H and I are run successively without resetting the identifier, and with the identifier initialized to the values learned in Task E. This is equivalent to the object being in random positions between successive trials. The results are displayed in Figure 6-12. The responses are not as smooth as if the controller had been reset between trials. This suggests that, for a margin of safety, the controller may be reset between successive trials.

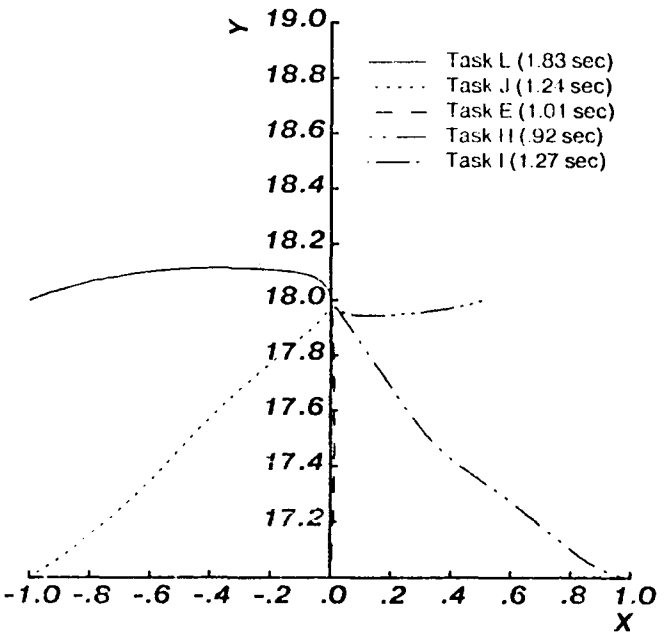

Figure 6-11: Adaptive Trajectories: First Trial

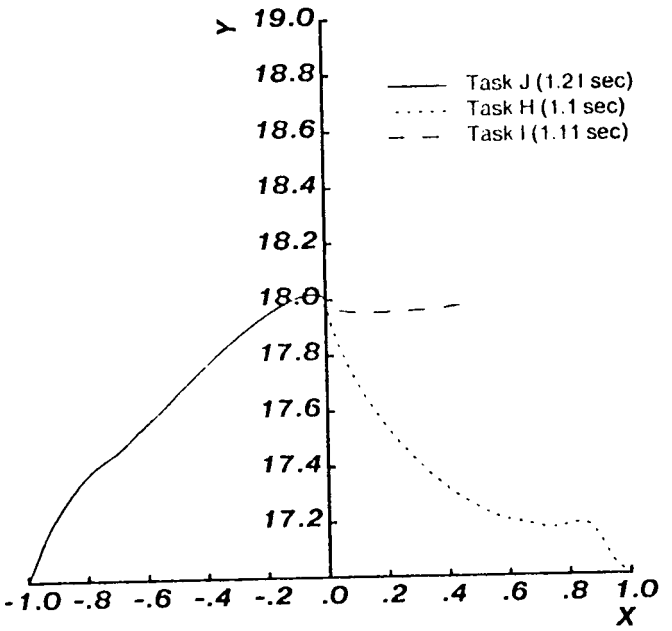

Figure 6-12: Sequential Adaptive Runs

3. Path : Smooth motion trajectories are observed for all cases evaluated at the higher sampling-to-bandwidth ratio ($f_s/f_{BW} = 51$). Such motion is suitable for tasks requiring small corrective motions. Actual paths deviate from the predicted trajectory, and the maximum path deviations are summarized in Table 6-1.

Path Deviation (inches)	TASK G	E	J	H	I	L	K	F	N	M
$\triangle$	≈0.0	0.006	0.03	0.04 .14 (net)	0.05 (after recovery from sign sensitivity)	0.1	0.23	0.23	0.83	0.3

Table 6-1: Maximum Path Deviations

The tasks requiring relatively large distances of travel (e.g., Tasks F, M, and N) show the largest deviations, since control signal saturation and larger identification errors occur in these cases. In most of the smaller motion examples, deviations are relatively small. Tasks L and K exhibit relatively larger deviations, since the sensitivity, J, changes by a relatively large amount, which leads to larger identification errors. In addition, the initial view coupling index (indicated in Figure 6-2) for Tasks L and K are large relative to values for the other cases. (The result observed here is consistent with a systematic study of performance, as a function of the coupling index, in Chapter 7.) In Task H, the initial path oscillation results from sign-sensitivity, and is discussed in Section 6.2.3.1.

Actual position trajectories are not always monotonic. If smooth motion trajectories are acceptable for path performance, then monotonic smooth motion trajectories are desirable. For example, when independent controllers are used, then non-monotonic motions generally result when initial relative displacement is in only one degree-of-freedom. In these cases, there can be initial feature errors for both axes, so that initial motion is forced in both axes (e.g., Tasks E, I, L, and F). Path deviations can be reduced by using larger sampling-to-bandwidth ratios, but typically with only marginal improvement. For example, when Task I is simulated with an extremely large ratio of $f_s/f_{BW} = 213$ ($T = 0.003$ sec and $\omega_n \approx 9.8$ sec^{-1}), the maximum deviation is 0.03 inches, compared with a deviation of 0.05 inches at the lower sampling-to-bandwidth ratio. Thus, SISO control of feature coupled systems tend to have path errors at the start of the trajectory (independent of the sampling-to-bandwidth ratio), which accounts for the observed transient identification errors. An MIMO controller would, in theory, produce superior path performance.

4. Rise-Times: Position rise-times are sluggish relative to the predicted response times. For example, while the predicted rise-time is typically $t_r \simeq 0.7$ sec for the smaller motion tasks, actual times ranged from 0.84 to 1.27 seconds (except for Task L). Saturation, control penalties, and transient identification-errors (which appear to over estimate the gains) produce transient response errors. To illustrate the error due to control penalty, Tasks E and J are simulated without

measurement delay (i.e., $n_d = 0$) so that the controller pole bound can be increased to $\gamma = 0.99$. The rise-times deceased to 0.81 seconds, and the remaining time-domain error arises from transient identification error.

With measurement delay included, a larger control penalty (i.e., smaller pole bound) is required. While no attempt is made to optimize γ for the examples included in the dissertation (i.e., $\gamma = .65$ for all examples and for all f_s/f_{BW}), it is observed, that as f_s/f_{BW} increases, γ can also be increased. For example, if Task J is simulated with $\gamma = 0.75$, and with $n_d = 1$, the rise-time decreases to 0.82 seconds, without degradation of path.

It appears that Task L exhibits exceptionally poor time response (i.e., $t_r = 2.11$ sec for adaptive control, compared with a predicted rise-tme $t_r = .73$ sec) as a result of the relatively large changes in $\partial l_{ength}/\partial Y$ and $\partial X_{cog}/\partial X$ and large value of coupling. For example, in Task L, the initial view coupling index is D = .95, and J(2,2) changes by a factor of 8.9. In Task E, for which the adaptive and predicted rise-times are .9 seconds and .68 seconds, respectively, the initial view coupling is D = .0008, and J(2,2) changes by a factor of 2.2.

Finally, the time response, when moving toward the line, is faster than when moving in the opposite direction. This observation is consistent with the predicted path rise-times.

5. Path Constraint: During hierarchy level transitions, the MRAC controller gains, for each MRAC, are fixed (i.e., run as LMFC) to their current values for 6 sampling periods following the transition. It is observed that this approach could improve the transient response during the transitional interval. It appears that by permitting the additional DOF (i.e., the Y-axis) to accelerate, before identification proceeds, feature changes, and thus gain estimates, are not dominated by the axis already in motion. The number of fixed cycles is determined experimentally.

   The hierarchical strategy minimizes trajectory deviations when initial relative displacement is predominantly in the X direction. At the opposite extreme, there is no effect in cases like Task E where initial displacement is only in the Y direction. In intermediate cases, such as in Tasks M,N,J, and H, the hierarchy degrades the path relative to the predicted path, but at least drives it in a controlled monotonic fashion toward the X-axis. In Task G, where the object is not centered in the image, the hierarchy accentuates the path deviation required to drive the feature center-of-gravity error to zero.

   In general, arbitrary use of the this hierarchy may or may not minimize path non-monotonic trajectory deviations. However, if the object is centered in the image, then a smooth path, biased toward the X-axis, is expected.

Figures 6-8, 6-9, and 6-10 also display the fixed LMFC response. (The fixed controller is only run at the higher sampling-to-bandwidth ratio $f_s/f_{BW} = 51$.) The following observations emerge:

1. Stability: With the exception of Task M, the fixed controllers are stable, with good transient responses, and zero steady-state feature and position errors. In Task M, the line goes OFV, and control stops. In this case, the LMFC is not adequate even with the relatively large bandwidth. This suggests that a fixed control strategy may not be suitable for tasks requiring large motions where the sensitivity, J, changes by large amounts.

2. Path: Each task exhibits smooth path motion. With the exception of Task H, the LMFC produces deviations from the predicted path which are larger than the MRAC path deviations. Task H, which is discussed in Section 6.2.3.1, exhibits an overall LMFC response that is superior to the MRAC, since the fixed controller is not sign-sensitive.

   An additional experiment is conducted in which Tasks L, J, H and I are implemented with the same fixed controller. The fixed controller gains are learned in Task E, and the results are displayed in Figure 6-13.

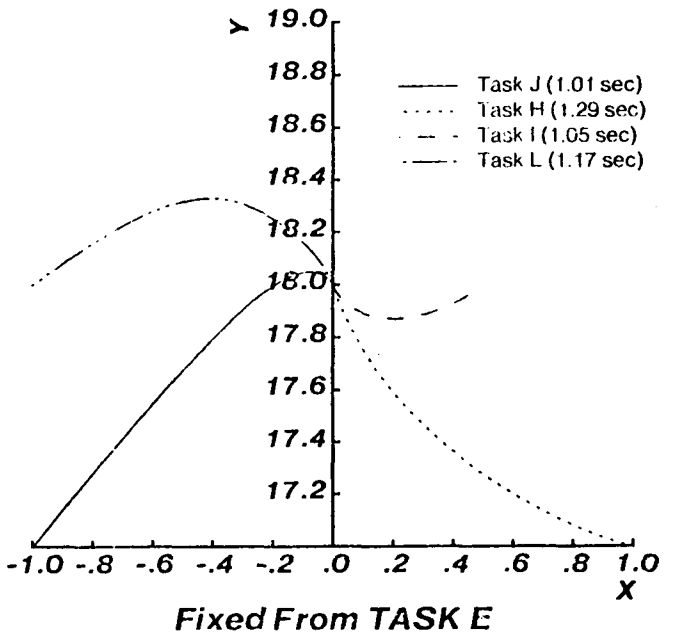

Figure 6-13: Single Fixed Controller for Multiple Tasks

   In these examples, path deviations are larger than those resulting when individually learned LMFCs were used (e.g., in Figure 6-13, the deviation for Task L is 0.35 inches, compared with 0.15 inches for the same task in Figure 6-10 and in). This suggests that a single fixed controller cannot achieve uniform response over a broad range of tasks.

3. Rise-Times: Generalizations cannot made concerning LMFC vs. MRAC rise-times. The LMFC rise-times are faster than the MRAC in seven out of ten trials. The adaptive controller tends to be slower than the fixed controller due to transient identification errors.

6.2.3. Independent Adaptive Control Problems

In the path performance summary in Section 6.2.2, it was explained why transient identification errors will generally occur for SISO control of coupled systems. In this section, other problems associated with independent adaptive control of a feature coupled system are clarified. These problems, which can affect transient response performance, include:

- Adaptive Controller sign-sensitivity; and
- Feature/joint assignment.

A coupled controller would not exhibit similar problems. Algorithms for coupled controllers, and their relative computational complexities, are advanced in Chapter 8 for future research evaluation.

6.2.3.1. Sign-Sensitivity

It is demonstrated, in Section 5.3, that the MRAC controller is sign-sensitive. That is, the identifier sets the sign of the estimated gains to ensure a stable negative feedback system (assuming control of a SISO process). In a coupled system, the SISO identifier sets the gain signs, of estimated equivalent SISO models, to drive each identification-error to zero. It is shown below that, momentary changes in sign can degrade performance by causing an axis to reverse direction and/or decelerate. When the estimated sign switches again, it takes time for the system to recover from the axis reversal due to its momentum in the opposite direction. At the lower sampling-to-bandwidth ratio, it takes a longer time to recover since the axis can travel further and gain more momentum during the longer sampling interval. At the higher ratios, the system recovers faster from subsequent identification-errors.

Sign-sensitivity effects system performance in Task H. In this example, the Y-axis starts out in the correct direction, but then momentarily reverses its motion. The trajectory and the estimated gain for the length feature, $\hat{b}_{1\text{-length}}(k)$, are displayed in Figures 6-14 and 6-15 for the two sampling-to-bandwidth ratios. At the lower sampling-to-bandwidth ratio ($T = 0.033$ sec and $f_s/f_{BW} = 20$), the effects of sign-sensitivity are accentuated. During the initial phase of control, both axis start out in the correct direction (i.e., in such a away as to reduce the feature errors). Over the initial sampling interval, the axes move by

$$\Delta X \simeq -0.025 \text{ inches and } \Delta Y \simeq 0.01 \text{ inches}$$

The change in the length feature, as specified by the sensitivity map in Figure 6-1 becomes:

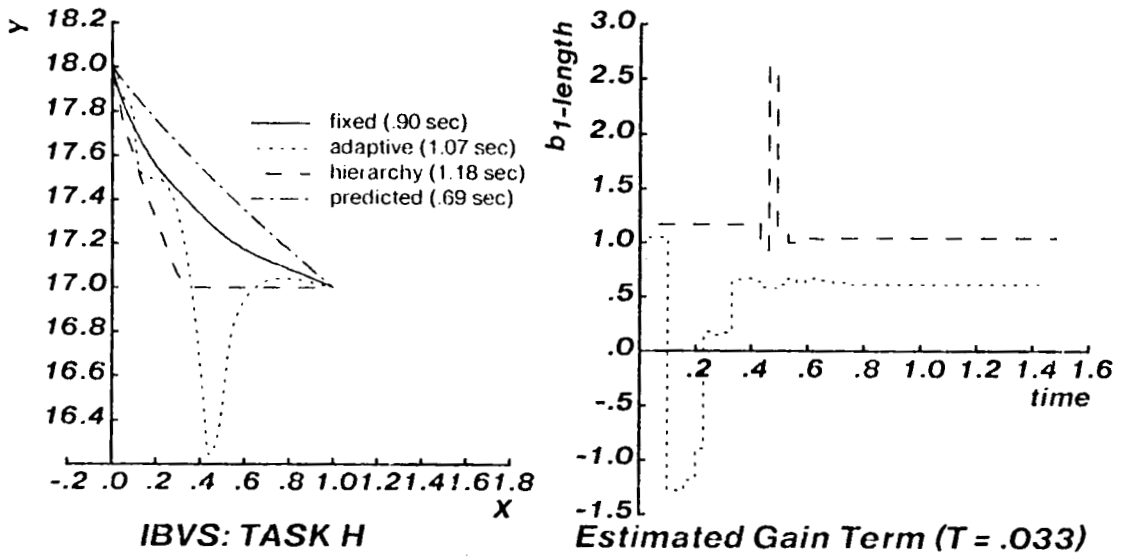

Figure 6-14: Sign-Sensitivity ($T = 0.033$ and $f_s/f_{BW} = 20$)

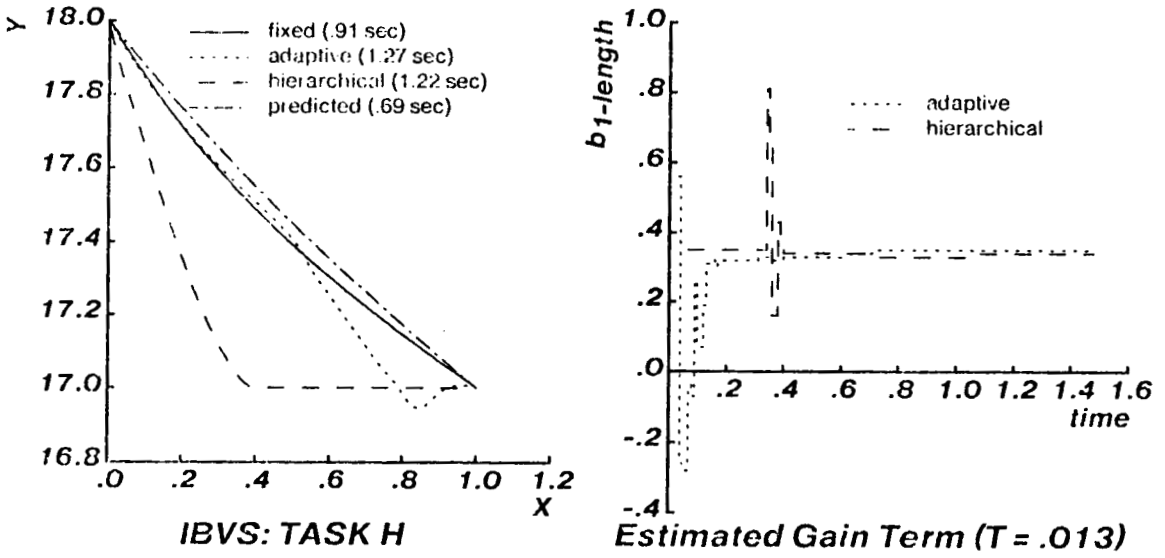

Figure 6-15: Sign Sensitivity ($T = 0.013$ and $f_s/f_{BW} = 51$)

$$\Delta l_{ength} = \left\{ \frac{\partial l_{ength}}{\partial X}\Delta X + \frac{\partial l_{ength}}{\partial Y}\Delta Y \right\} * SF$$

$$\simeq \left\{ (0.05) \times (-0.025) \quad + \quad (0.09) \times (0.01) \right\} 2500.$$

$$= -0.875$$

Since $\Delta Y>0$ and $\Delta l_{ength}<0$, at that instant , $\hat{b}_1$ is forced to be negative, driving the Y-axis in the opposite direction.

Strategies which can be used with the independent MRAC controller to counter these effects, include:

- Clamp sign: experiments are conducted where the sign of the gain term $\hat{b}_1$ is forced to that of the corresponding sign of the diagonal term of the sensitivity matrix. This leads to smooth and stable performance, but the generality of this strategy needs further investigation.

- Higher sampling-to-bandwidth ratios: the higher the ratio, the faster the recovery; and

- Fixed control: sign insensitive.

6.2.3.2. Feature/Joint Reassignment

Trajectories which cross boundaries of change in diagonal-dominance correspond to Tasks K and L. In these cases, a fixed feature joint assignment (i.e., X-axis$\leftarrow X_{cog}$, Y-axis$\leftarrow l_{ength}$) produce stable systems with acceptable transient responses, at the higher sampling-to-bandwidth ratio ($T = 0.013$ sec and $f_s/f_{BW} = 51$). At the lower sampling-to-bandwidth ratio ($T = 0.033$ sec and $f_s/f_{bw} = 51$), poor transient response can cause the line to go OVF. The effects of switching the feature/joint assignment at the boundaries of predicted reassignment are examined in this section. The experiments demonstrate that potential improvements in performance can be gained by assigning features to minimize D(k), and thereby reduce coupling. If a trajectory crosses a boundary of change in diagonal-dominance, without reassignment of features, path performance can degrade and the system can be unstable, especially at lower sampling-to-bandwidth ratios. The effects are more pronounced for systems with nonlinear kineamtics (in Section 6.3), independent of the sampling-to-bandwidth ratio.

The feature/joint reassignment simulations are implemented using the analytic derivations of $J(\underline{X}_{rel})$, and assuming that $\underline{X}_{rel}$ is known. A fixed feature/joint assignment corresponding to X-axis$\leftarrow l_{ength}$, Y-axis$\leftarrow X_{cog}$ is also evaluated.

The response for Task K, at the lower sampling-to-bandwidth ratio ($T = 0.033$ sec and $f_s/f_{BW} = 20$) and with the fixed feature/joint assignment, (corresponding to X-axis$\leftarrow X_{cog}$, Y-axis$\leftarrow l_{ength}$), is shown in Figure 6-16. The system is unstable with the fixed the feature/joint

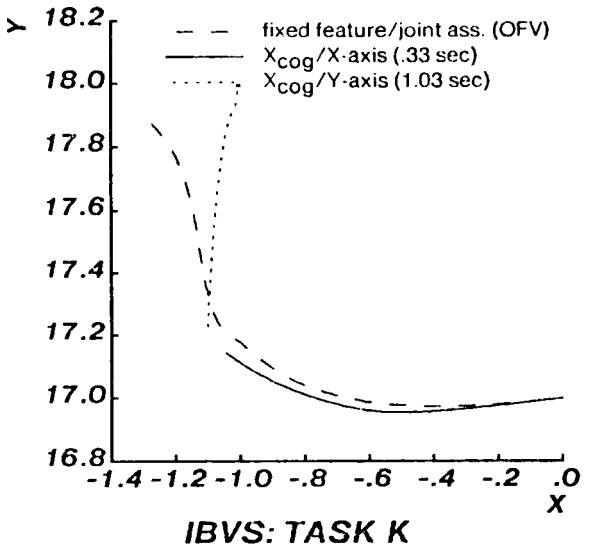

Figure 6-16: Feature/Joint Reassignment ($T = 0.033$ and $f_s/f_{BW} = 20$)

assignment. The line goes OFV in the initial trial, and in second trial (not shown) exhibits even poorer response (i.e., oscillation) before the line goes OVF. Figure 6-16 also includes the response for the second trial of an experiment for which feature/joint reassignment is implemented at the switching boundary. In this experiment, control is halted when the camera reaches the boundary (and it is assumed that control can be stopped instantaneously by manual braking). At this point, the current state of the identifier, including the estimated parameter vector and gain matrix, are held for subsequent use. The feature/joint assignment is then switched, and the identifier is reinitialized, since the dynamics associated with each feature from the first part also switch. Control then proceeds until the completion of the task. At the end of the task, the identifier state is again held for use on subsequent trials in this region. The task is run again, but with the identifier initialized to the previously held states. With this strategy, the line stays in the field-of-view, the system is stable, and the trajectory exhibits acceptable transient performance. By switching the feature/joint assignment, the coupling in the desired view decreases from $D = 0.95$ to $D = 0.39$. The improved stability is a result of the feature/joint reassignment, and not just the stop and then start-up again action. This is verified by stopping the system at the boundary of change of diagonal dominance and then restarting it, without switching the feature/joint assignment. In this example the line still goes OFV. Improved performance is thus achieved by the apparent reduction in coupling gained by the feature/joint reassignment.

The feature/joint reassignment experiment was also implemented at the higher sampling-to-

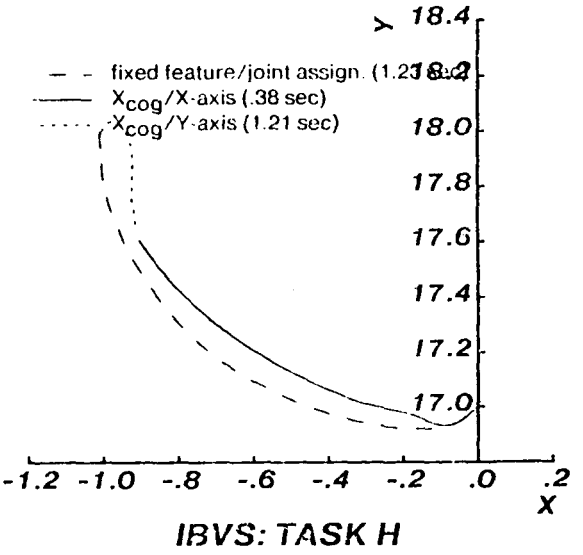

Figure 6-17: Feature/Joint Reassignment ($T = 0.013$ sec and $f_s/f_{BW} = 51$)

bandwidth ratio (see Figure 6-17). There is improvement in path performance, but the rise-time is larger due to model reinitialization at the switching point.

Task K is also evaluated with the opposite fixed feature/joint assignment corresponding to X-axis←l_{ength}, Y-axis→X_{cog}. This assignment forces $D = 1.62$ in the initial view, which is almost two orders of magnitude larger, than for the opposite assignment. This system is unstable, even at the higher sampling-to-bandwidth ratio (f_s/f_{BW}). It could be stabilized by running it at a very high sampling-to-bandwidth ratio, by reducing the sampling period to $T = 0.003$ and $f_s/f_{BW} = 220$, but the transient response is poor (i.e., oscillation).

Task L is also evaluated using the feature/joint reassignment strategy. While the path deviation is slightly larger, the rise-time decreases. A fixed assignment corresponding to X-axis←l, Y-axis←X_{cog} is also implemented. The system is stable, but the transient response is poor (i.e., oscillation).

While the switching strategy used in these experiments is static, in the sense that control is halted at the switching boundary, the potential advantage of reducing coupling by feature/joint reassignment is demonstrated. A method for on-line estimation of J or JW_p is proposed, in Chapter 8, for feature/joint reassignment strategies.

This concludes the evaluation of the 2 DOF linear kinematic and dynamic configuration. The

second part of this chapter extends this evaluation to the nonlinear kinematic and dynamic robot.

6.3. Nonlinear Kinematics and Dynamics

The purpose of this section is to evaluate IBVS control for the nonlinear kinematic and dynamic system of Configuration 2 (Figure 4-2). The articulated robot arm places additional demands on the controller, including nonlinear and coupled kinematics and dynamics. For the control algorithm to be suitable for an image-based system, the controller must be adequate as a joint-level controller. The first part of this section evaluates the enhanced SP MRAC algorithm at the joint-level, and demonstrates its ability to acvhieve stable systems with good transient response.

The image-based control system yields performances which are comparable to the linear kinematic system when tasks are limited to small motions. The performance differs from the linear kinematic system in two key respects:

- For tasks requiring large motions, independent control, of the kinematically coupled system, can produce relatively large path deviations; and
- For the linear kinematic configuration, a fixed feature/joint assignment is adequate. In contrast, the nonlinear kinematic configuration requires a feature/joint reassignment strategy for general implementations, except when the required task motion is small.

6.3.1. Control of Nonlinear Dynamics

Investigations by other researchers (Section 2.3.1.3) have demonstrated the ability of independent adaptive controllers to perform at the joint level. These studies have not payed attention requirements for physical implementation, including computational complexity, controller saturation, noise, and measurement and computational delays. Morris and Neuman [Morris 81] developed the SISO hyperstable SP MRAC taking account of these requirements. They evaluate this algorithm for one DOF linear systems, with slowly varying parameters (without measurment delay), and suggest that this controller can be extended to control a nonlinear and coupled robot [Morris 81]. Before proceeding with the evaluation image-based control, this algorithm is illustrated as a joint level controller (with measurement delay included). Exhaustive testing and evaluation of joint-level control, which is not included in this dissertation, remains a subject for future research.

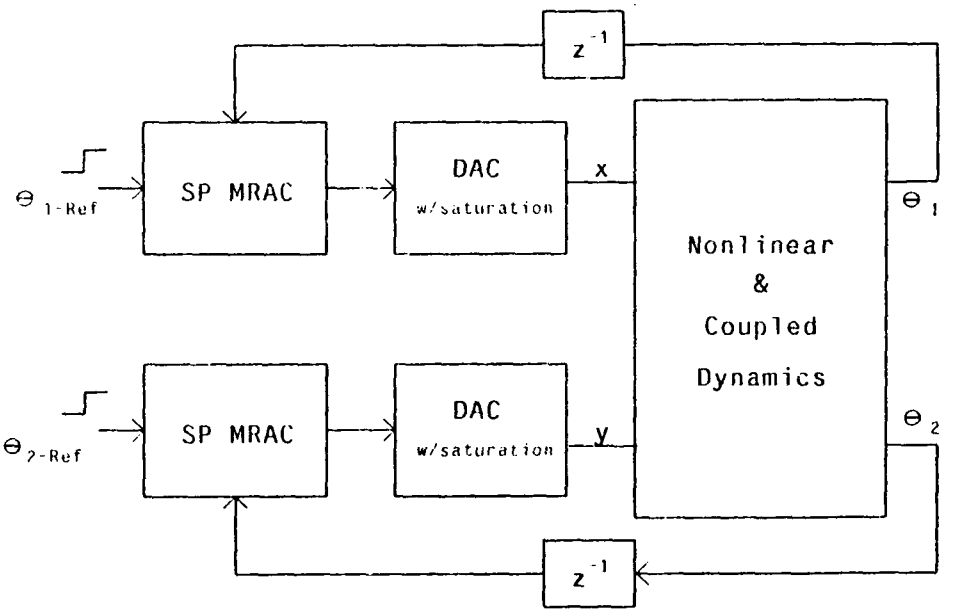

Figure 6-18: Adaptive Control of a 2 DOF Robot Arm

Joint level control of the 2 DOF robot arm is represented in Figure 6-18. With the measurement delay, the independent controller algorithms are implemented according to the outline in Appendix C, with the exception that the scale factors are given by:

$$SF_{T=0.033} = 100$$

and

$$SF_{T=.003} = 1000$$

and, the identifier is initialized according to Table 6-2.

		$P(0)$	P_{Thresh}	$\hat{\underline{\beta}}(0)$
T(sec)	0.033	Diag [10 10 10 10]	1000	$[10\ 10\ 1.1\ 0.1]^T$
	0.003	Diag [.1 .1 .01 .01]	10	$[1\ \ 1\ \ 1.5\ -0.5]^T$

Table 6-2: Identifier Initialization: Joint-Level Control

Some of the experiments are implemented without the measurement delay. For $n_d = 0$, the controller is implemented according to:

- Control Signal: (3.10)

- Identifier: (3.4),(3.5), and (3.6)
- Control Penalty: (A.21) with $\gamma = 0.99$
- SP Reference Model: Appendix A.1

There are simulation errors because of the numerical integrations which comprise the computer simulation of the nonlinear dynamics. The relative magnitudes of error are evaluated by simulating the step-response of each joint, with the other joint locked in a stationary position. In this experiment, each joint acts as a constant linear system, and the estimated parameter vector should equal the actual vector for the linear systems derived in Section 4.4.5.1. This experiment is run at two sampling periods, T = 0.033 sec and T = 0.003 sec. The results are shown in Table 6-3, where the estimated vector is given as its steady-state value after two consecutive learning trials. The percentage error is:

$$\%\text{error} = \left(\frac{\beta - \hat{\beta}_{ss}}{\beta}\right) \times 100\%$$

While the errors are relatively small, the experiments in Chapter 5, for which the dynamics are simulated by analytic equations, produce zero error.

6.3.1.1. Joint-Level Control Examples

While exhaustive testing and evaluation of joint-level control is not performed, initial experimentation, using random arm configurations, produce stable systems with good transient response. An example is presented which demonstrates the ability of the MRAC to achieve satisfactory performance under demanding conditions which include:

1. High joint velocities and accelerations;
2. Control signal saturation; and
3. Measurement delay.

The experiment is set-up as follows:

- Sampling Period: The sample period, T = 0.003 sec, corresponds to the value used in present state-of-art robots.
- Reference Model Bandwidth: A large bandwidth, $\omega_n = 44.5\ \text{sec}^{-1}$, produces high joint speeds (for step-inputs), and produces control signal saturation. This bandwidth corresponds to a sampling-to-bandwidth ratio of $f_s/f_{BW} \approx 47$.
- Task: Run four consecutive adaptive trials (i.e., without reinitialization of the identifier between trials), with step-inputs and varying pay loads according to:

T=0.033 sec
ω_n = 9.5 sec^{-1} (f_s / f_{BW} = 20)

	Θ_1 (Step-input: 0→90° w/Θ_2= 95°)			Θ_2 (0→90°)		
	$\hat{\beta}$	$\hat{\beta}_{actual}$	% error	$\hat{\beta}$	$\hat{\beta}_{actual}$	% error
b_1	4.75918	4.75936	0.003	12.546479	12.546479	0.0
b_2	3.86649	3.86659	0.002	8.47888	8.47911	0.002
a_1	1.53561	1.53524	0.02	1.30493	1.30492	0.0007
a_2	-0.53490	-0.53524	0.06	-0.30493	-0.30492	0.003

T=0.003 sec
ω_n = 44.51 sec^{-1} (f_s / f_{BW} = 47.05)

	Θ_1 (Step-input: 0→90° w/Θ_2= 95°)			Θ_2 (0→90°)		
	$\hat{\beta}$	$\hat{\beta}_{actual}$	% error	$\hat{\beta}$	$\hat{\beta}_{actual}$	% error
b_1	0.47040	0.47042	0.004	1.43257	1.43257	0.0
b_2	0.46156	0.46159	0.006	1.38191	1.381934	0.001
a_1	1.94480	1.94476	0.002	1.89766	1.89765	0.0005
a_2	-0.94473	-0.94476	0.003	-0.89763	-0.89765	0.002

Table 6-3: Nonlinear Dynamic Simulation Error

	Payload (lbs.)	$\theta_{1\text{-ref}}$ (deg)	$\theta_{2\text{-ref}}$ (deg)
Trial 1:	2.5	-21→44	155→90
Trial 2:	5.0	44→-21	90→155
Trail 3:	5.0	-21→44	155→90
Trial 4:	2.5	44→-21	90→155

(6.6)

This particular set of sampling periods, bandwidth, and arm configurations are also useful since they correspond to values which are evaluated, in Section 6.3.3, under imaged-based control.

The position responses are displayed in Figure 6-19, and the control signals and torque components for the second and third trials[12] are displayed in Figures 6-20 and 6-21 respectively. The components of torque are defined in Section 4.4.2 as:

Joint 1

$D_{11}\ddot{\theta}_1$: Inertial

$D_{12}\ddot{\theta}_2$: Inertial Coupling

$D_{112}\dot{\theta}_1\dot{\theta}_2$: Coriolis

$D_{122}\dot{\theta}_2^{\,2}$: Centrifugal

Joint 2

$D_{12}\ddot{\theta}_1$: Inertial Coupling

$D_{22}\ddot{\theta}_2$: Inertial

$D_{211}\dot{\theta}_1^{\,2}$: Centrifugal

The torque plots verify that the dynamics include non-negligible coupling and nonlinear components. Examples for two trials are shown to demonstrate the different contributions which arise from arm configuration dependence. In the second trial, the inertial coupling terms contribute significantly to the net torque during the initial accelerations. As θ_2 increases, D_{12} (Section 4.4.2) decreases with the the cosine of θ_2. Thus, during the final deceleration, there is a smaller contribution of inertial coupling. The opposite effects are then observed in the third trial. The Coriolis and centrigual torques are non-negligible in both cases.

---

[12]Each is run for 3 seconds, but only 0.5 or 1 second of data are shown for clarity and detail.

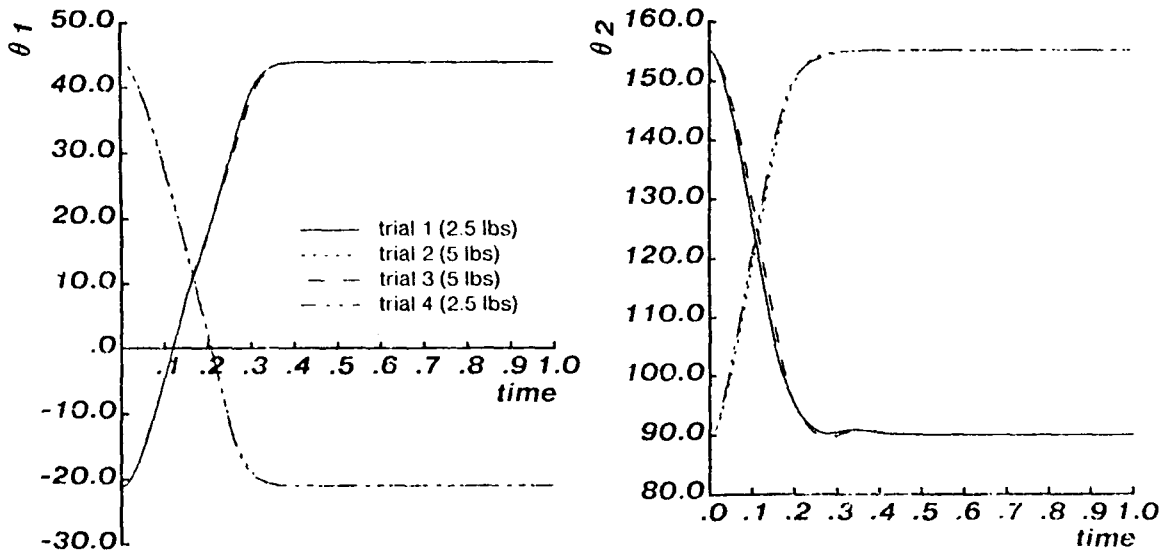

Figure 6-19: Joint Level Nonlinear Dynamic Control

In these examples, the full-parallel errors exhibit large transient tracking errors. The maximum errors are summarized in Table 6-4 for these and similar experiments which are discussed below. In Case 1, the large error is due primarily to saturation and control penalty, since identification errors are relatively small. The experiment is run again (Case 2), but at a smaller bandwidth ($\omega_n = 9.81$ sec^{-1}) to reduce the total time of saturation. The error is reduced by half, and most of the remaining error results from the large control penalty required by the measurement delay. It is observed that larger pole bounds, and thus smaller penalties, could be used for these joint level controllers. The effects of the control penalty are demonstrated by running the experiment without any measurement delay (i.e., $n_d = 0$), and with the pole bound set to $\gamma = 0.99$. In this example (Case 3), there is a dramatic decrease in the full-parallel error. Momentary saturation remains, and small identification errors remain. To reduce further controller saturation, two experiments are run with smaller motions. At the larger bandwidth (Case 4), saturation remains, and at the smaller bandwidth, there is no saturation. The identification errors are thus responsible for the remaining tracking error. The small errors suggest that, for high precision tracking, further compensation (e.g., feedforward control) may still be required.

A fixed LMFC is also simulated for the four consecutive tasks in (6.6). Each task is run with the identifier fixed to the estimated parameter vector learned in Trial 3. The LMFC

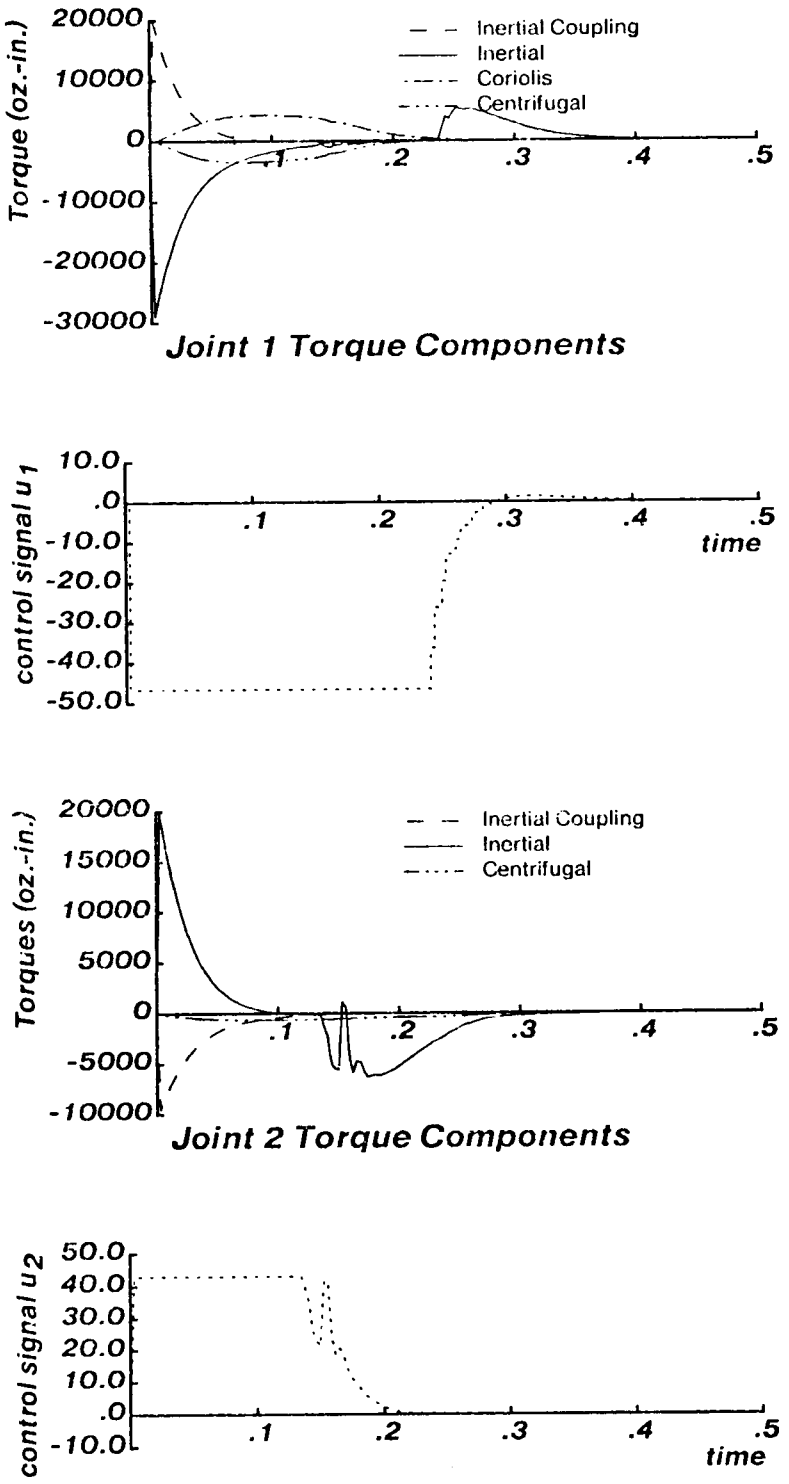

Figure 6-20: Torque Components for Second Trial

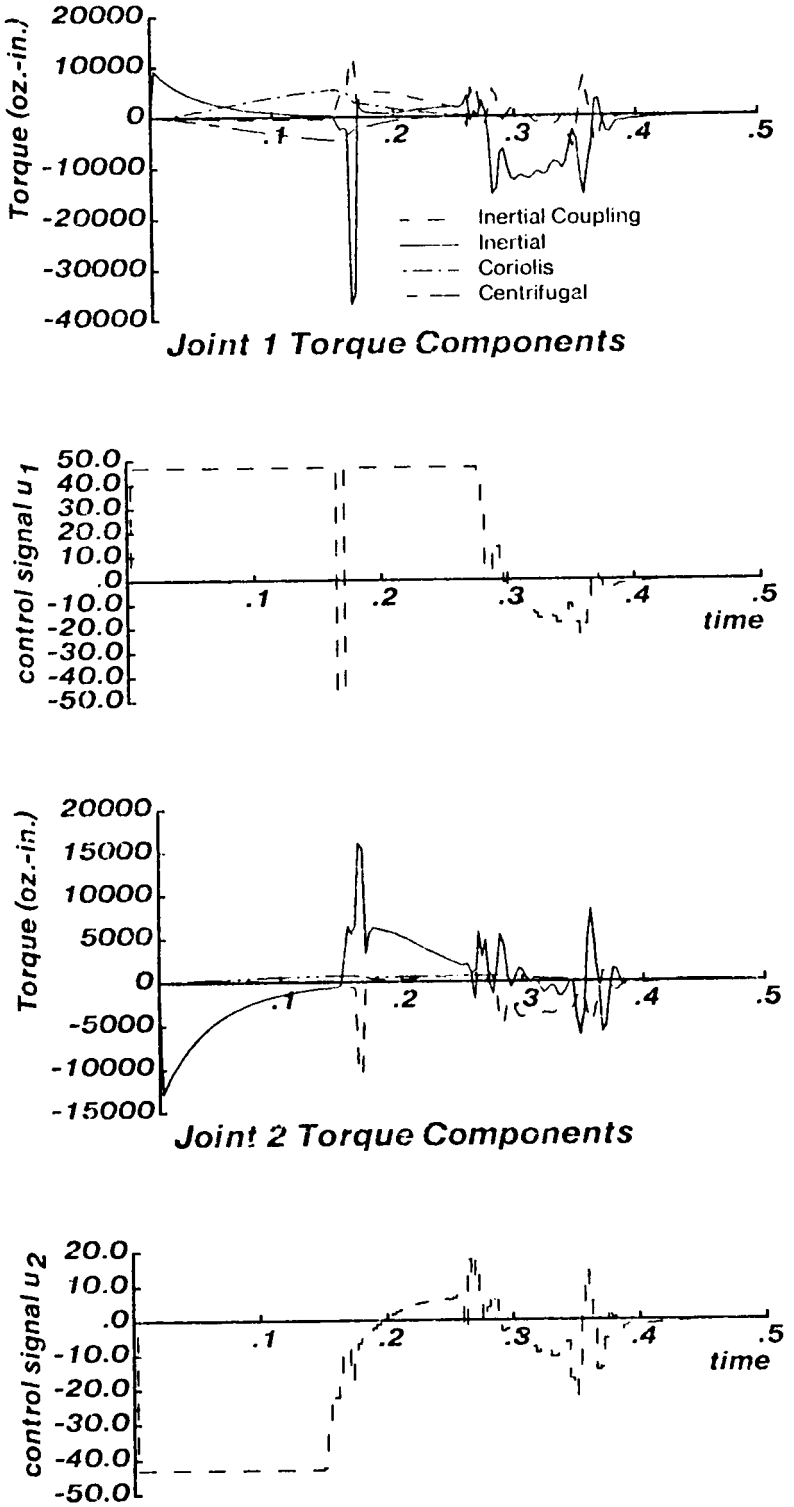

Figure 6-21: Torque Components for Third Trial

	Θ_1 : -21→44° Θ_2 : 155→90°		Θ_1 : 40→45° Θ_2 : 95→90°
ω_n = 44.51 (T=0.003)	Case 1: (n_d = 1) (γ = 0.65) e_{FP-1} 45° e_{FP-2} 35°		Case 4: (n_d = 0) (γ = 0.99) e_{FP-1} 0.09° e_{FP-2} 0.3°
ω_n = 9.81 (T=0.003)	Case 2: (n_d = 1) (γ = 0.65) e_{FP-1} 19.3° e_{FP-2} 19.4°	Case 3: (n_d = 0) (γ = 0.99) e_{FP-1} 0.9° e_{FP-2} 1.4°	Case 5: (n_d = 0) (γ = 0.99) e_{FP-1} 0.01° e_{FP-2} 0.14°

Table 6-4: Joint Level Control: Maximum FP Errors

performance (not displayed) is negligibly different from the MRAC. Performances may be comparable since saturation occurs for a significant percentage of time for both the MRAC and LMFC. Since the control signal is the same for each controller during this period, the position response must also be the same during the saturation interval. To evaluate the contribution of controller saturation, a smaller motion task is simulated (with θ_1: 40→45 deg and θ_2:95→90 deg) to reduce saturation effects. The identifier is fixed to values learned from the first adaptive trial in this configuration. In this case there is only momentary saturation, but both fixed and adaptive performances are still comparable. Another possibility for comparable performance is that, at the high bandwidth, the sensitivity of the fixed controller to apparent external disturbances and parameter variations is small. To evaluate this, the small motion task is run again, at the smaller bandwidth $\omega_n = 9.81$ sec^{-1}. The identifier is fixed to values learned from the first adaptive trial in this configuration, and at the smaller bandwidth. The position responses, displayed in Figure 6-22, show that the MRAC performs better at the lower bandwidth, consistent with the results of Chapter 5. The LMFC still exhibits good transient response and the overall performance is not significantly poorer than that of the MRAC. Another factor accounting for to the satisfactory LMFC response may be attributed to the heavy gearing, which attenuates the changes in torque reflected back to the motor, although it does not change their relative contributions.

While further research is required for conclusive evaluations of adaptive and fixed joint-level control, these limited experiments have the following significance:

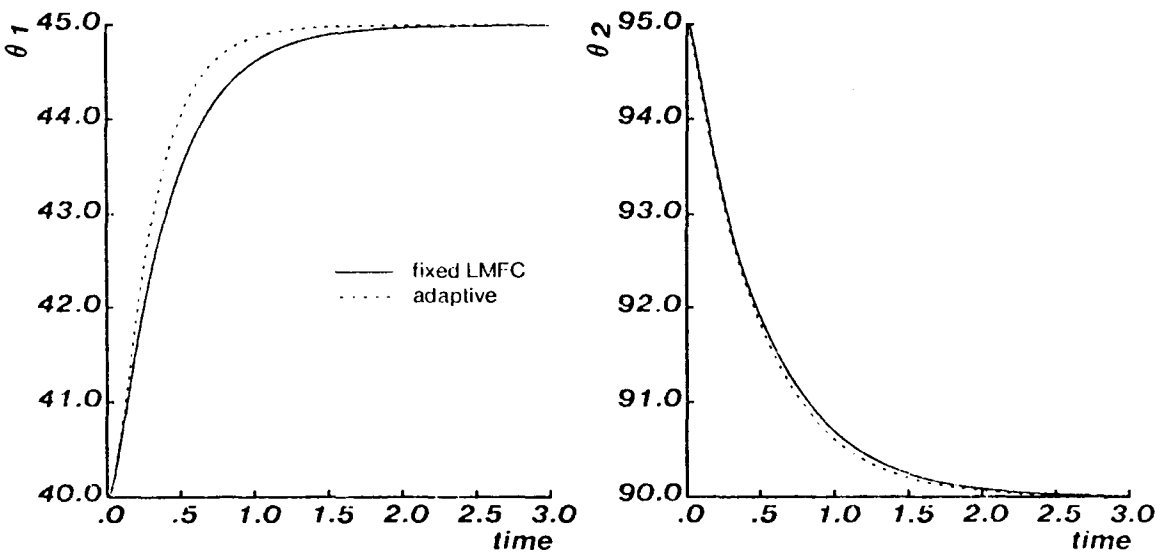

Figure 6-22: Fixed vs. Adaptive Control at Joint level

1. Consistent with work by other researchers, these experiments suggest that independent adaptive controllers can identify equivalent SISO plants and achieve stable systems, with acceptable transient responses, when the plant dynamics contain non-negligible dynamic coupling and nonlinear torque components. While gearing reduces the magnitudes of change of torque components reflected back to the motor, their relative contributions remain the same. To the best of the author's knowledge, this the first demonstration of an enhanced MRAC (i.e., SP MRAC, with control penalty and measurement delay) for robot control.

2. The robot arm is controlled without a'priori knowledge of the physical system (making this an attractive approach for industrial applications). MRAC provides a means to derive a fixed control law which displays good stability. Typically, fixed control law implementations require manual tuning to achieve suitable performance.

3. While the adaptive controller can achieve smooth and fast responses, transient full-parallel tracking error could not be driven to zero. Tasks which require high precision tracking capabilities (e.g., seam welding) will require further control signal augmentation, supplied by a feedforward controller. It remains to determine whether a coupled adaptive control law can achieve superior performance.

6.3.2. Sensitivity Analysis

The sensitivity matrix, in (2.7), for the nonlinear kinematic configuration is

$$J(\underline{\theta}) = -J_{feat}(\underline{X}_{rel})\, J_{arm}(\underline{\theta})$$

and the feature sensitivity matrix, J_{feat}, is defined in (6.1). The arm jacobian, J_{arm} in (2.5), is

$$J_{arm} = \frac{\partial K(\underline{\theta})}{\partial \underline{\theta}} = \begin{bmatrix} \frac{\partial X}{\partial \theta_1} & \frac{\partial X}{\partial \theta_2} \\ \frac{\partial Y}{\partial \theta_1} & \frac{\partial Y}{\partial \theta_2} \end{bmatrix}$$

From (4.13), the direct kinematic solution, $K(\underline{\theta})$ in (2.5) is

$$x = r_2\cos(\theta_1 + \theta_2) + r_1\cos\theta_1$$
$$y = r_2\sin(\theta_1 + \theta_2) + r_1\sin\theta_1$$

and includes the tool or camera mounting transform.

Maps of the sensitivity matrix are made for the visual servoing tasks which are presented in this section. The tasks, represented in Figure 6-23, are equivalent to linear kinematic examples with respect to both the initial and desired relative Cartesian coordinates. The feature sensitivity map for the smaller motion tasks (i.e., all except Tasks V and W) is displayed in Figure 6-24. For this set of tasks, the matrix elements are continuous and nondegenerate. When the arm is in other configurations, which are kinematically degenerate (i.e, $\det[J_{arm}] = 0$), the system is degenerate. For example, when the arm is fully extended (i.e., $\theta_2 = 0$), $\det[J_{arm}] = 0$, which indicates the transition from the "elbow-ups" to "elbows-down" joint configurations. At the joint level, these represent non-unique solutions, but not affect the final Cartesian task coordinates. With respect to effects on dynamic control, such a system cannot (in general) be uncoupled, even when using a coupled controller. Control evaluation of tasks which might traverse such boundaries are not presented in the dissertation

For the smaller motion tasks, sensitivity changes are similar in magnitude to the equivalent linear kinematic examples. Over larger distances (e.g., Tasks W and V), the changes are significantly greater in the nonlinear kinematic configuration, as illustrated in Table 6-5, which compares these changes for Task W and the equivalent linear kinematic Task N. The table indicates the change in sensitivity from the initial to the desired view, and compares it both as a percentage and ratio. By either measure, the nonlinear kinematic configuration exhibits significantly larger changes. It is therefore expected that even higher sampling-to-bandwidth ratios will be required for control of large motion nonlinear kinematic tasks.

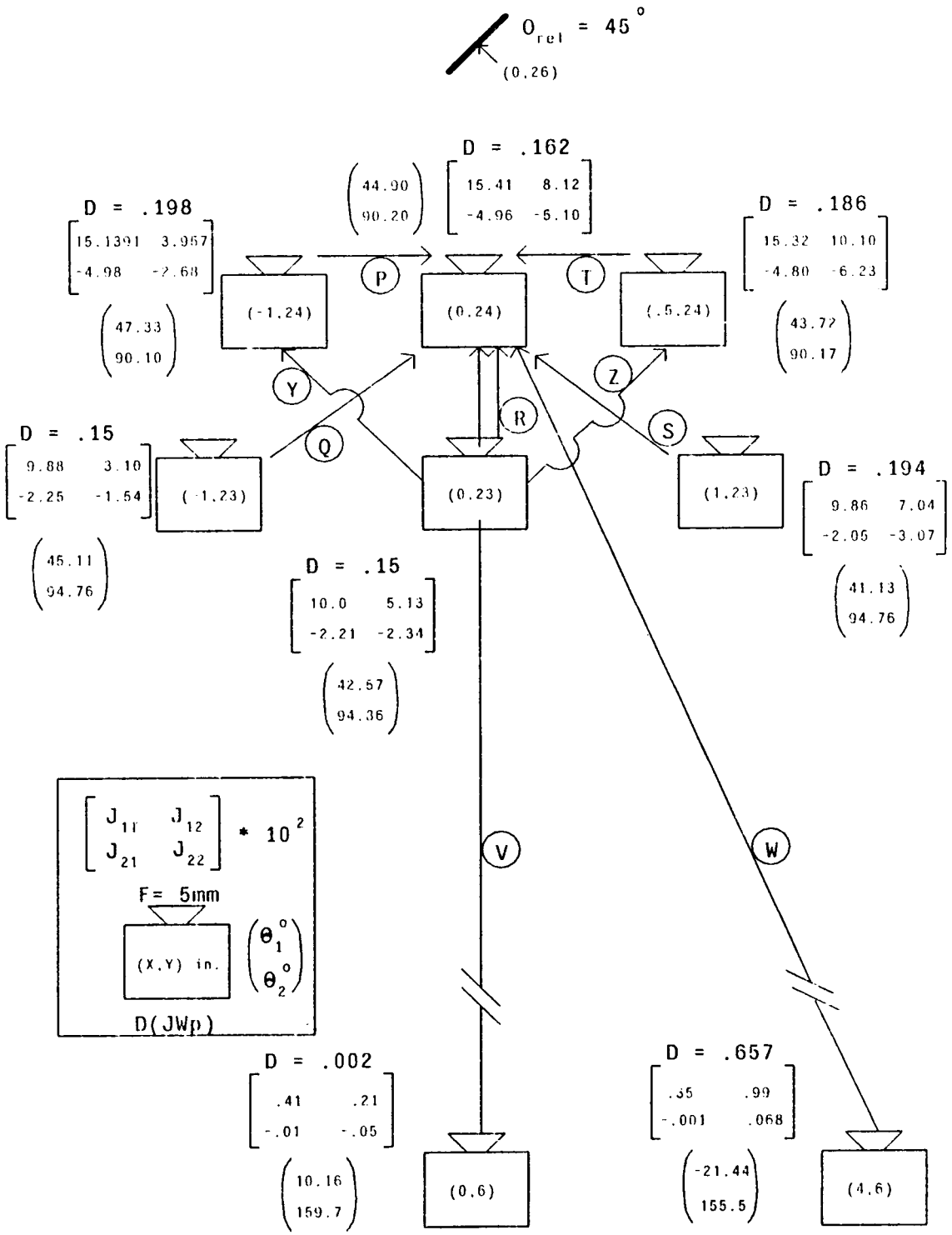

Figure 6-23: 2 DOF Nonlinear Kinematic Tasks

θ_2

$\frac{\delta X_{cog}}{\delta \theta_1}$	40	41	42	43	44	45	46	47	48	$\frac{\delta X_{cog}}{\delta \theta_2}$	40	41	42	43	44	45	46	47	48
	7.92	7.94	7.92	7.86	7.75	7.60	7.42	7.19	******	98	4.58	4.05	3.49	2.92	2.34	1.76	1.18	0.60	******
	8.46	8.51	8.52	8.47	8.37	8.22	8.03	7.80	******	97	5.23	4.65	4.04	3.41	2.77	2.11	1.46	0.82	******
	9.04	9.14	9.17	9.14	9.06	8.97	8.72	8.47	******	96	5.99	5.36	4.69	3.99	3.27	2.54	1.80	1.07	******
	9.68	9.82	9.89	9.90	9.83	9.70	9.50	9.25	******	95	6.89	6.21	5.47	4.69	3.88	3.05	2.22	1.39	******
	10.37	10.57	10.69	10.74	10.70	10.59	10.40	10.13	******	94	7.97	7.22	6.40	5.53	4.62	3.68	2.72	1.77	******
	******	11.39	11.59	11.69	11.70	11.61	11.42	11.15	******	93	******	8.45	7.54	6.56	5.53	4.45	3.35	2.25	******
	******	******	12.58	12.76	12.83	12.78	12.62	12.35	******	92	******	******	8.95	7.85	6.67	5.43	4.15	2.86	******
	******	******	******	13.98	14.14	14.15	14.02	13.75	******	91	******	******	******	9.48	8.12	6.68	5.18	3.65	******
	******	******	******	******	15.65	15.75	15.68	15.44	15.03	90	******	******	******	******	10.01	8.31	6.53	4.69	2.84
$\theta_1 \rightarrow$	40	41	42	43	44	45	46	47	48		40	41	42	43	44	45	46	47	48

$\frac{\delta length}{\delta \theta_1}$	40	41	42	43	44	45	46	47	48	$\frac{\delta length}{\delta \theta_2}$	40	41	42	43	44	45	46	47	48
	-1.41	-1.44	-1.46	-1.46	-1.45	-1.42	-1.38	-1.33	******	98	-1.73	-1.57	-1.39	-1.21	-1.02	-0.83	-0.64	-0.46	******
	-1.58	-1.63	-1.65	-1.66	-1.66	-1.63	-1.58	-1.53	******	97	-2.05	-1.87	-1.66	-1.45	-1.23	-1.00	-0.78	-0.56	******
	-1.77	-1.84	-1.88	-1.90	-1.90	-1.88	-1.83	-1.76	******	96	-2.46	-2.24	-2.01	-1.76	-1.49	-1.22	-0.95	-0.68	******
	-1.98	-2.08	-2.15	-2.19	-2.20	-2.18	-2.13	-2.06	******	95	-2.97	-2.72	-2.44	-2.15	-1.83	-1.50	-1.17	-0.85	******
	-2.23	-2.36	-2.46	-2.52	-2.55	-2.54	-2.50	-2.42	******	94	-3.61	-3.33	-3.01	-2.65	-2.27	-1.87	-1.47	-1.06	******
	******	-2.69	-2.83	-2.93	-2.98	-2.99	-2.95	-2.87	******	93	******	-4.13	-3.75	-3.32	-2.86	-2.37	-1.86	-1.35	******
	******	******	-3.27	-3.42	-3.52	-3.55	-3.52	-3.44	******	92	******	******	-4.73	-4.22	-3.65	-3.04	-2.40	-1.76	******
	******	******	******	-4.03	-4.18	-4.26	-4.26	-4.17	******	91	******	******	******	-5.45	-4.75	-3.97	-3.16	-2.32	******
	******	******	******	******	-5.02	-5.17	-5.21	-5.14	-4.97	90	******	******	******	******	-6.30	-5.31	-4.25	-3.14	-2.04

Sensitivity J x 10^2

	40	41	42	43	44	45	46	47	48	
	0	0	0	0	0	0	0	0	•	98
	0	0	0	0	0	0	0	0	•	97
	0	0	0	0	0	0	0	0	•	96
	0	0	0	0	0	0	0	0	•	95
	0	0	0	0	0	0	0	0	•	94
	•	0	0	0	0	0	0	0	•	93
	•	•	0	0	0	0	0	0	•	92
	•	•	•	0	0	0	0	0	•	91
	•	•	•	•	0	0	0	0	0	90
$\theta_1 \rightarrow$	40	41	42	43	44	45	46	47	48	

Feature/Joint Assignment

$\Leftarrow$ "0" if $X_{cog} \leftarrow \theta_1$
"1" if $X_{cog} \leftarrow \theta_2$.

F-5mm
θobj=45°
Xobj= 0in
Yobj=26in

Figure 6-24: Nonlinear Kinematic Sensitivity and Assignment Map

	TASK N (Linear Kinematics)		TASK W (Nonlinear Kinematics)	
	%	$\frac{J_{desired}}{J_{initial}}$	%	$\frac{J_{desired}}{J_{initial}}$
J_{11}	840	9.4	4300	44
J_{21}	150	2.5	720	8.2
J_{12}	8300	84.0	5.1×10^6	5061
J_{22}	6400	65.0	7300	74.0

Table 6-5: Nonlinear vs. Linear Kinematic Sensitivity Change

6.3.2.1. Feature/Joint Assignment

The nonlinear kinematic configuration is dynamically nonlinear, and a transfer function matrix W_p can be only be obtained by linearizing the dynamics about a nominal trajectory, or by estimating equivalent linear input-output transfer functions. For the purpose of calculating a coupling index, a linear model is generated by neglecting the Coriolis and centrifugal torques, and assuming the inertias are constant for any particular arm configuration. For small motion tasks, the Coriolis and centrifugal torques are shown (in Section 6.3.3.1) to be negligible. For large motion tasks, neglecting these terms is not an issue since the SISO controllers are shown to be not acceptable (in Section 6.3.3.2) even for control of linear dynamic models. The transfer function matrix, from (4.14), (4.15), (4.16), and (4.17), is:

$$JW_p = \frac{s}{\Lambda(s)} \begin{bmatrix} K_{11}(\tau_{11}s+1) & K_{12}(\tau_{12}s+1) \\ K_{21}(\tau_{21}s+1) & K_{22}(\tau_{22}s+1) \end{bmatrix}$$

where

$$K_{11} \doteq \frac{j_{11}A_{22}}{A_{21}} \quad K_{12} \doteq \frac{j_{12}A_{12}}{A_{11}}$$

$$K_{21} \doteq \frac{j_{21}A_{22}}{A_{21}} \quad K_{22} \doteq \frac{j_{22}A_{12}}{A_{11}}$$

$$\tau_{11} \doteq \frac{j_{11}D_{22} + j_{11}A_{23} \cdot j_{12}D_{12}}{j_{11}A_{22}} \quad \tau_{12} \doteq \frac{j_{12}D_{11} + j_{12}A_{13} \cdot j_{11}D_{12}}{j_{12}A_{12}}$$

$$\tau_{21} \doteq \frac{j_{21}D_{22} + j_{21}A_{23} - j_{22}D_{12}}{j_{21}A_{22}} \qquad \tau_{22} \doteq \frac{j_{22}D_{11} + j_{22}A_{13} - j_{21}D_{12}}{j_{22}A_{22}}$$

$$A_{i1} \doteq \frac{K_{ti}\eta_i}{R_{ai}}; \quad A_{i2} \doteq \eta_i^2\left(\frac{K_{ti}K_{bi}}{R_{ai}} + \alpha_i\right); \quad A_{i3} \doteq l_{mi}\eta_i^2$$

and the characteristic polynomial $\Lambda(s)$ is

$$\Lambda(s) = \frac{s^2}{A_{11}A_{21}}\Big[\{(D_{11} + A_{13})(D_{22} + A_{23}) - D_{12}^2\}s^2 + \{A_{22}(D_{11} + A_{13}) + A_{12}(D_{22} + A_{23})\}s + A_{12}A_{22}\Big] \tag{6.7}$$

To calculate the coupling index $D(JW_p)$, the magnitude of JW_p is derived using the DC gains K_{11}, K_{12}, K_{21}, and K_{22}. This is justified since the maximum time constant of the characteristic equation (6.7) for the arm configurations in Figure 6-23 is 51 msec, while the observed position rise-times range from 0.18 to 0.28 seconds. (While the feature rise-times are not recorded, feature rise-times are even larger, according to the analysis in Section 5.4.)

The feature/joint assignment map is also displayed in Figure 6-24. For these examples, the specified assignments are:

$$X_{cog} \leftarrow \theta_1$$

and

$$l_{ength} \leftarrow \theta_2$$

over the entire displayed region, and this assignment also holds for all line angles (θ_{obj}). In contrast to the linear kinematic configuration, this assignment does not hold over large regions. For other arm configurations, the opposite assignment is observed. For example, in the sensitivity and assignment maps displayed in Figure 6-25, there is a boundary where the assignment becomes

$$X_{cog} \leftarrow \theta_2$$

and

$$l_{ength} \leftarrow \theta_1$$

As the line angle decreases, the later assignment holds over the entire displayed space. In contrast to the linear kinematic configuration, a fixed feature/joint assignment is not predicted for large regions of control. The performance when crossing such a boundary, and its effect on implementation using independent adaptive controllers, is discussed in Section 6.3.3.3.

θ_2

$\delta X_{cog}/\delta\theta_1$ \ θ_1	39	40	41	42	43	44	45	46	47	θ_2	39	40	41	42	43	44	45	46	47	$\delta X_{cog}/\delta\theta_2$
	9.50	10.97	12.66	14.61	16.87	******	******	******	******	52	6.71	7.17	7.62	8.06	8.46	******	******	******	******	
	9.04	10.49	12.18	14.15	16.45	******	******	******	******	51	6.69	7.18	7.68	8.19	8.67	******	******	******	******	
	8.54	9.97	11.65	13.62	15.94	18.67	******	******	******	50	6.63	7.16	7.71	8.27	8.83	9.37	******	******	******	
	******	9.41	11.07	13.02	15.34	18.10	******	******	******	49	******	7.10	7.69	8.31	8.94	9.58	******	******	******	
	******	******	10.44	12.36	14.66	17.43	20.78	******	******	48	******	******	7.63	8.30	9.00	9.72	10.44	******	******	
	******	******	******	11.65	13.91	16.66	20.01	******	******	47	******	******	******	8.24	9.00	9.80	10.63	******	******	
	******	******	******	10.90	13.10	15.80	19.12	23.26	******	46	******	******	******	8.13	8.94	9.81	10.74	11.70	******	
	******	******	******	******	12.23	14.86	18.12	22.22	******	45	******	******	******	******	8.83	9.76	10.77	11.86	******	
	******	******	******	******	******	13.85	17.02	21.04	26.22	44	******	******	******	******	******	9.64	10.73	11.92	13.21	

$\delta l_{length}/\delta\theta_1$ \ θ_1	39	40	41	42	43	44	45	46	47	θ_2	39	40	41	42	43	44	45	46	47	$\delta l_{length}/\delta\theta_2$
	0.80	0.72	0.61	0.44	0.20	******	******	******	******	52	-0.53	-0.64	-0.77	-0.91	-1.07	******	******	******	******	
	0.90	0.84	0.75	0.60	0.37	******	******	******	******	51	-0.49	-0.61	-0.74	-0.89	-1.06	******	******	******	******	
	1.00	0.97	0.89	0.76	0.55	0.24	******	******	******	50	-0.45	-0.57	-0.70	-0.85	-1.03	-1.24	******	******	******	
	******	1.09	1.04	0.93	0.75	0.46	******	******	******	49	******	-0.52	-0.65	-0.81	-1.00	-1.22	******	******	******	
	******	******	1.18	1.10	0.96	0.70	0.30	******	******	48	******	******	-0.60	-0.76	-0.95	-1.18	-1.45	******	******	
	******	******	******	1.28	1.17	0.96	0.59	******	******	47	******	******	******	-0.70	-0.89	-1.13	-1.41	******	******	
	******	******	******	1.45	1.38	1.22	0.91	0.37	******	46	******	******	******	-0.63	-0.83	-1.06	-1.36	-1.71	******	
	******	******	******	******	1.59	1.48	1.24	0.77	******	45	******	******	******	******	-0.75	-0.98	-1.28	-1.65	******	
	******	******	******	******	******	1.75	1.57	1.19	0.48	44	******	******	******	******	******	-0.89	-1.19	-1.57	-2.05	

Sensitivity J x 10^2

θ_2

θ_1	39	40	41	42	43	44	45	46	47	θ_2
	1	0	0	0	0	•	•	•	•	52
	1	0	0	0	0	•	•	•	•	51
	1	1	0	0	0	0	•	•	•	50
	•	1	1	0	0	0	•	•	•	49
	•	•	1	0	0	0	0	•	•	48
	•	•	•	1	0	0	0	•	•	47
	•	•	•	1	1	0	0	0	•	46
	•	•	•	•	1	0	0	0	•	45
	•	•	•	•	•	1	0	0	0	44

Feature/Joint Assignment

$\Leftarrow$ "0" if $X_{cog} \leftarrow \theta_1$
"1" if $X_{cog} \leftarrow \theta_2$

F-5mm
θobj=15°
Xobj=12in
Yobj=31in

Figure 6-25: Sensitivity With Diagonal Dominance Changes

6.3.2.2. Path Constraint

Implementation of a path constraint strategy for the nonlinear kinematic configuration requires sensitivity analysis of the arm jacobian according to Section 2.5.3 . This analysis shows which joint level degrees-of-freedom dominate motion in Cartesian space.

The path constraint strategy is analyzed for the tasks represented in Figure 6-23. A map of the arm jacobian and of the Cartesian/joint assignment is displayed in Figure 6-26 for the closer range motions. This assignment map is derived by organizing J_{arm} to minimize D (i.e., in (2.9), JW_p is replaced with J_{arm}). For this particular arm configuration, θ_1 dominates X, and from the feature sensitivity analysis of J_{feat}, X dominates X_{cog}. The hierarchy for this configuration is shown in Figure 6-27.

6.3.3. IBVS Evaluation

The visual servoing tasks evaluated are represented in Figure 6-23. The smaller motion tasks (i.e., all except Tasks V and W) are discussed (in Section 6.3.3.1), seperately from the larger motion examples (in Section 6.3.3.2), since significantly different results are observed in each. Examples of tasks which have trajectories that cross boundaries of diagonal dominance are discussed (in Section 6.3.3.).

Preliminary simulations, which are implemented with a reference model bandwidth of $\omega_n = 9.5$ sec^{-1} and $T = 0.033$ sec (or $f_s/f_{BW} = 20$), are stable, but exhibit poor transient response. In contrast, when the equivalent linear kinematic tasks are implemented with these values, smooth trajectories result (in the forward trajectory and across regions where fixed feature joint assignment is predicted). The problem is isolated to insufficient sampling-to-bandwidth ratio required for suitable identification, and it appears that the added kinematic coupling is responsible. To demonstrate this, the following experiments are simulated for Task S:

1. To verify that the nonlinear dynamics are not the source of the problem, direct joint-level control of the robot arm (in this configuration and with the same bandwidth and sampling period) exhibits accepatble transient response.

2. To assure that the combination of nonlinear dynamics and kinematics do not cause the problem, the visual servoing task is simulated with uncoupled and linear dynamics according to Section 4.4.5.1 . The response exhibits poor transient response.

3. A fixed LMFC, which does not include an on-line identifier, is implemented using

θ_2

$\frac{\partial X_{rel}}{\partial \theta_1}$	40	41	42	43	44	45	46	47	48	θ	40	41	42	43	44	45	46	47	48	$\frac{\partial X_{rel}}{\partial \theta_2}$
	38.93	38.93	38.93	38.91	38.88	38.84	38.78	38.77	••••••	98	19.85	19.47	19.07	18.67	18.27	17.86	17.44	17.02	••••••	
	39.31	39.32	39.32	39.31	39.28	39.25	39.20	39.14	••••••	97	20.24	19.85	19.47	19.07	18.67	18.27	17.86	17.44	••••••	
	39.68	39.70	39.71	39.70	39.68	39.65	39.61	39.56	••••••	96	20.61	20.24	19.85	19.47	19.07	18.67	18.27	17.86	••••••	
	40.05	40.08	40.09	40.09	40.08	40.05	40.02	39.97	••••••	95	20.98	20.61	20.24	19.85	19.47	19.07	18.67	18.27	••••••	
	40.42	40.45	40.46	40.47	40.46	40.45	40.42	40.37	••••••	94	21.34	20.98	20.61	20.24	19.85	19.47	19.07	18.67	••••••	
	••••••	40.81	40.83	40.85	40.85	40.83	40.81	40.77	••••••	93	••••••	21.34	20.98	20.61	20.24	19.85	19.47	19.07	••••••	
	••••••	••••••	41.20	41.22	41.22	41.22	41.20	41.17	••••••	92	••••••	••••••	21.34	20.98	20.61	20.24	19.85	19.47	••••••	
	••••••	••••••	••••••	41.58	41.59	41.59	41.58	41.55	••••••	91	••••••	••••••	••••••	21.34	20.98	20.61	20.24	19.85	••••••	
	••••••	••••••	••••••	••••••	41.95	41.96	41.95	41.94	41.90	90	••••••	••••••	••••••	••••••	21.34	20.98	20.61	20.24	19.85	

$\frac{\partial Y_{rel}}{\partial \theta_1}$	40	41	42	43	44	45	46	47	48	θ	40	41	42	43	44	45	46	47	48	$\frac{\partial Y_{rel}}{\partial \theta_2}$
	-0.68	0.00	0.68	1.36	2.04	2.72	3.39	4.07	••••••	98	22.05	22.39	22.73	23.06	23.38	23.70	24.00	24.30	••••••	
	-1.03	-0.34	0.34	1.03	1.72	2.40	3.09	3.77	••••••	97	21.70	22.05	22.39	22.73	23.06	23.38	23.70	24.00	••••••	
	-1.39	-0.69	0.00	0.69	1.39	2.08	2.77	3.46	••••••	96	21.34	21.70	22.05	22.39	22.73	23.06	23.38	23.70	••••••	
	-1.75	-1.05	-0.35	0.35	1.05	1.75	2.45	3.15	••••••	95	20.98	21.34	21.70	22.05	22.39	22.73	23.06	23.38	••••••	
	-2.12	-1.41	-0.71	0.00	0.71	1.41	2.12	2.82	••••••	94	20.61	20.98	21.34	21.70	22.05	22.39	22.73	23.06	••••••	
	••••••	-1.78	-1.07	-0.36	0.36	1.07	1.78	2.49	••••••	93	••••••	20.61	20.98	21.34	21.70	22.05	22.39	22.73	••••••	
	••••••	••••••	-1.44	-0.72	0.00	0.72	1.44	2.16	••••••	92	••••••	••••••	20.61	20.98	21.34	21.70	22.05	22.39	••••••	
	••••••	••••••	••••••	-1.09	-0.36	0.36	1.09	1.81	••••••	91	••••••	••••••	••••••	20.61	20.98	21.34	21.70	22.05	••••••	
	••••••	••••••	••••••	••••••	-0.73	0.00	0.73	1.46	2.20	90	••••••	••••••	••••••	••••••	20.61	20.98	21.34	21.70	22.05	

Arm Sensitivity $J_{ARM} \times 10^2$

$\theta_1 \rightarrow$	40	41	42	43	44	45	46	47	48	θ
	0	0	0	0	0	0	0	0	•	98
	0	0	0	0	0	0	0	0	•	97
	0	0	0	0	0	0	0	0	•	96
	0	0	0	0	0	0	0	0	•	95
	0	0	0	0	0	0	0	0	•	94
	•	0	0	0	0	0	0	0	•	93
	•	•	0	0	0	0	0	0	•	92
	•	•	•	0	0	0	0	0	•	91
	•	•	•	•	0	0	0	0	0	90

$\Leftarrow \begin{cases} \text{"0" if } X_{rel} \rightarrow \theta_1 \\ \text{"1" if } X_{rel} \rightarrow \theta_2 \end{cases}$

Cartesian Space/Joint Assignment

Figure 6-26: Arm Jacobian Map

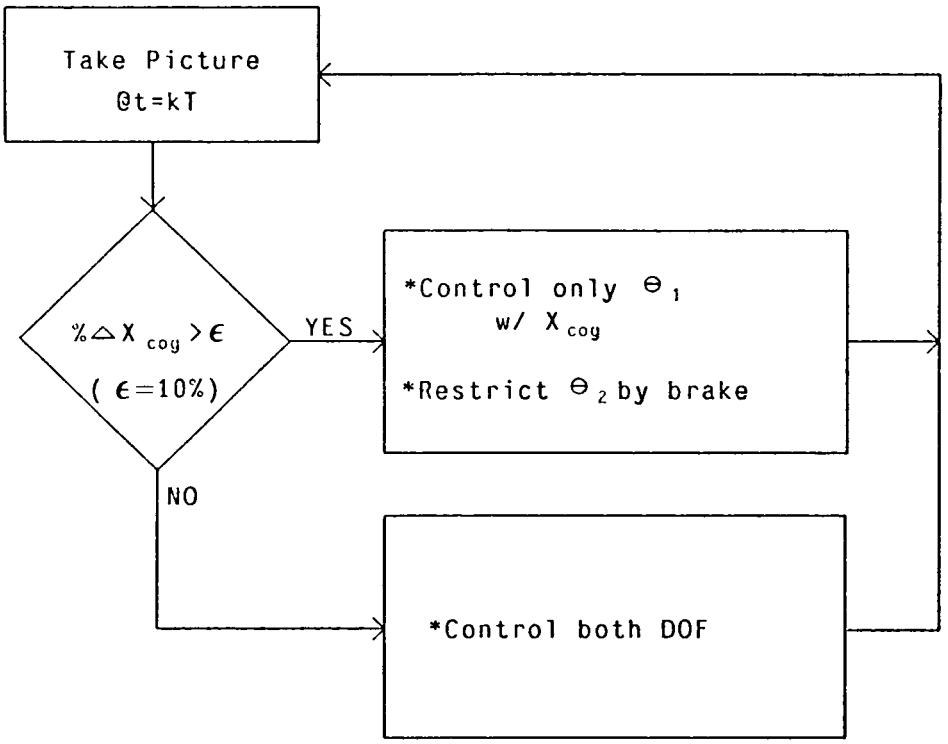

Figure 6-27: Hierarchy for 2 DOF Nonlinear Kinematic Configuration

the steady-state parameter vector learned from an initial adaptive trial. The results are shown in Figure 6-28. While the adaptive system displays a poor transinet response, in both the first and second trials (second trial shown), the LMFC produces a dramatically improved response (i.e., reduced oscillation, and close to monotonic motion).

4. It is verified that the sampling period, T = 0.033 sec, is not too small relative to the robot dynamics (i.e., the time constants associated with the characteristic equation (6.7) are 18.1 msec and 48.9 msec, at $\theta_2 = 90.2$ deg), and that the sampling-to-bandwidth ratio is the important parameter. The task is run with the nonlinear dynamic simulation, and with a smaller bandwidth $\omega_n = 4.39$ sec^{-1}, so that $f_s/f_{BW} = 43$. This results in an acceptable transient response.

The significance of these experiments is that a sampling-to-bandwidth ratio of at least $f_s/f_{BW} \simeq 45$ is required for adaptive control with nonlinear kinematics. In addition, these experiments suggest that a fixed controller is more suitable for control when physical implementation requires smaller f_s/f_{BW} ratios.

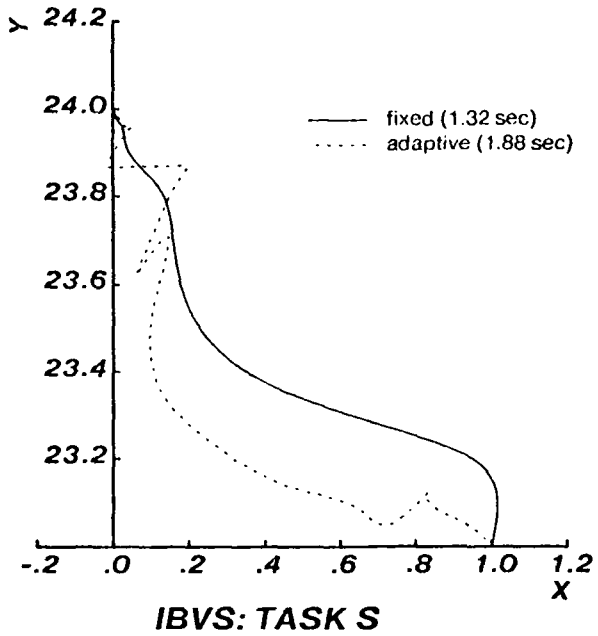

Figure 6-28: Fixed vs. Adaptive: T = 0.033 sec and $f_s/f_{BW} = 20$

6.3.3.1. Small Motion Trajectories

This section includes a summary of the control performance for the small motion trajectories represented in Figure 6-23. The evaluation is based on simulations using T = 0.003 sec and $\omega_n = 44.51$ sec^{-1} ($f_s/f_{BW} = 47$). The smaller sampling period permits a larger banwidth to be specified, which leads to faster speeds and accelerations. This accentuates the magnitudes of the coupled and nonlinear dynamics, testing the MRAC's ability to operate under these demanding conditions. The fixed feature/joint assignment for this configuration is described in the sensitivity analysis in Section 6.3.2.1. The experiments conducted for each task match those for the linear kinematic configuration. That is, after each initial adaptive learning trial, a fixed LMFC is implemented using the steady-state estimated parameter vector. The path constraint strategy is implemented with the controller fixed for 6 sampling periods during the level transitions (Section 6.2.2.). The resultant trajectories are displayed in Figures 6-29 and 6-30.The torque components for the adaptive control of Task P are displayed in Figure 6-31.[13] This representative example demonstrates that there is significant inertial coupling, but the Coriolis and centrifugal torques are negligible for these shorter excursion tasks.

---

[13]While each trial is run for 3 seconds, only 0.4 seconds are shown.

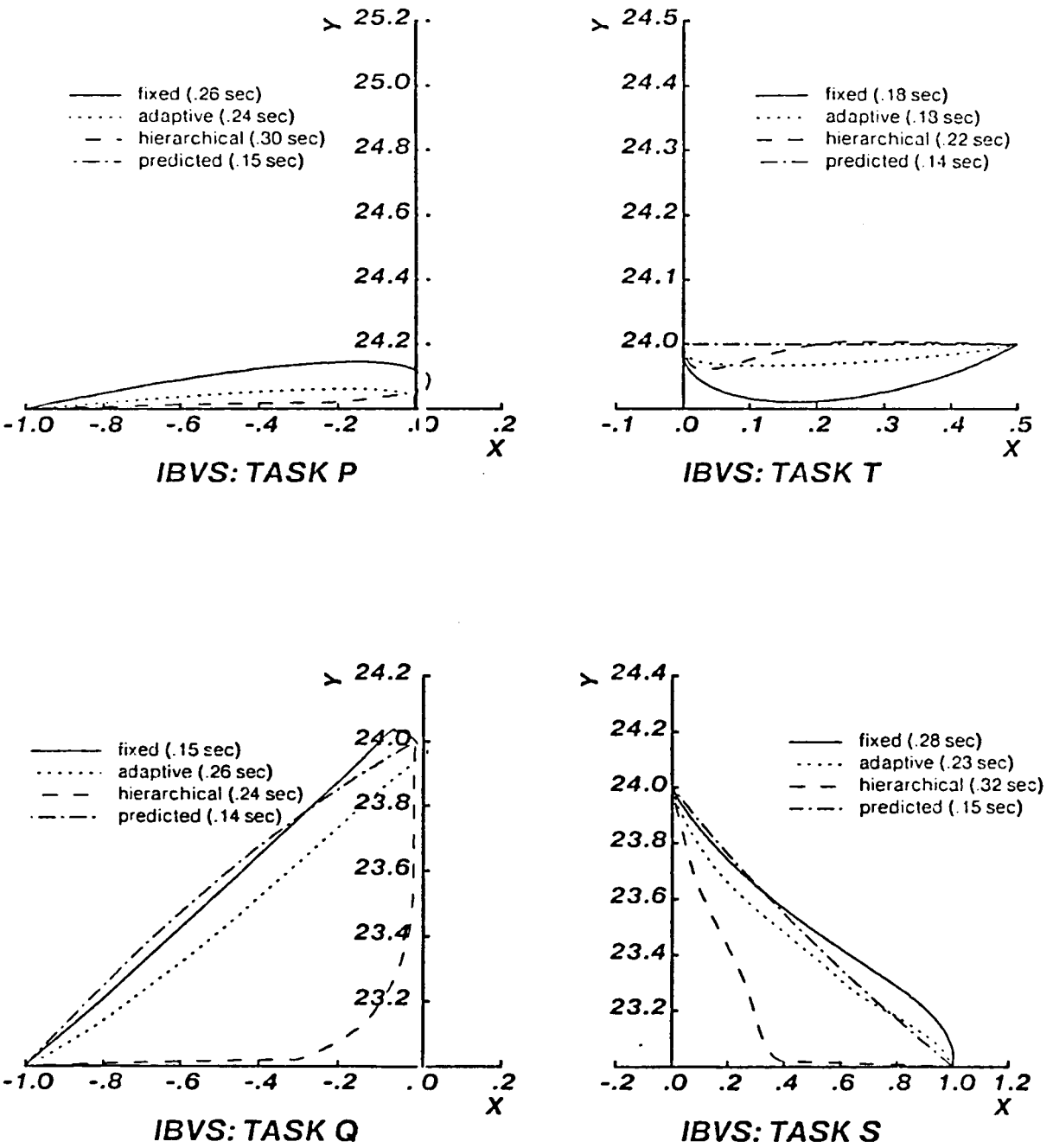

Figure 6-29: Nonlinear Kinematic Trajectories ($T = .003$; $f_s/f_{BW} = 47$)

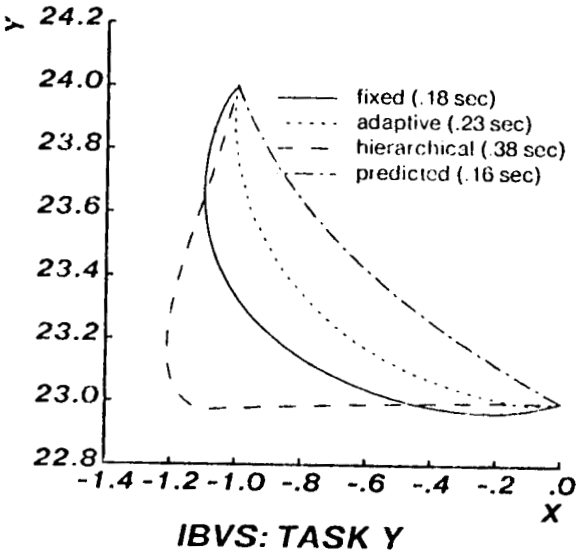

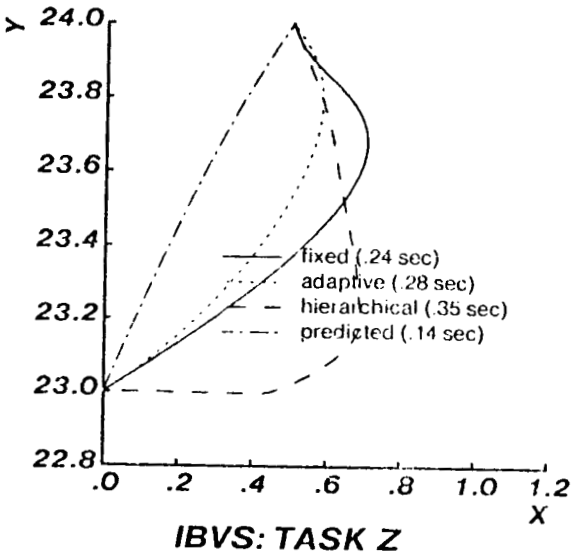

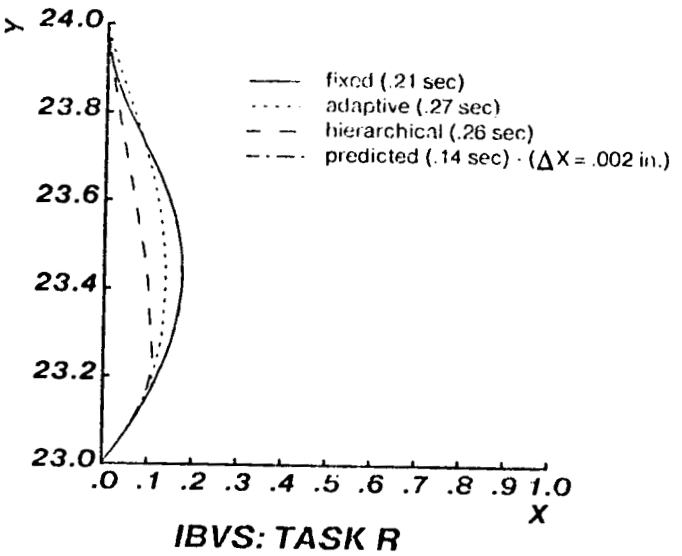

Figure 6-30: Nonlinear Kinematic Trajectories ($f_s/f_{BW} = 47$) (cont.)

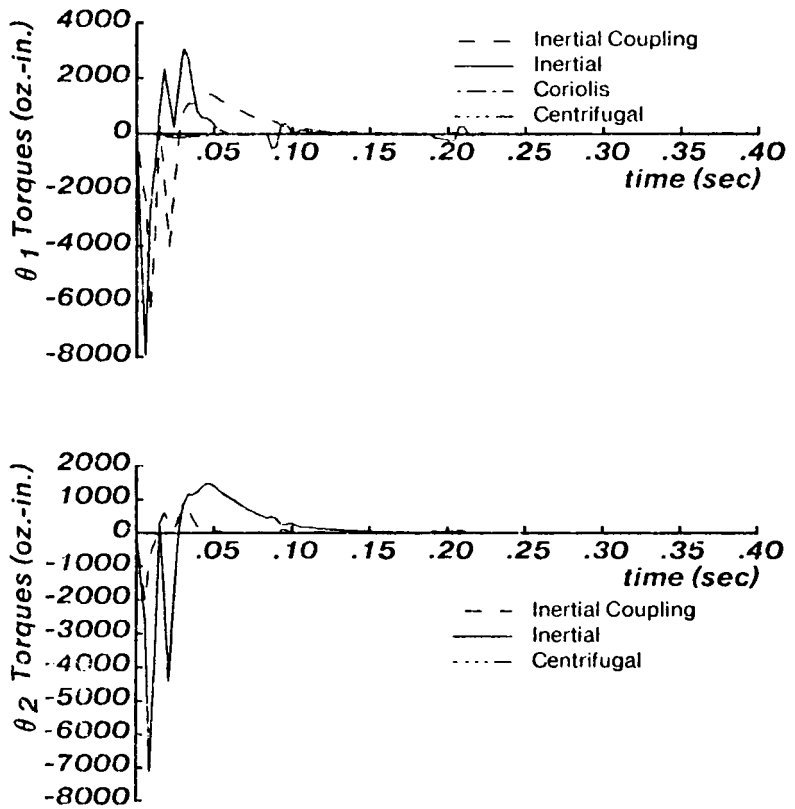

Figure 6-31: Torque Components for TASK Q (MRAC)

Observed performance of the small motion trajectories qualitatively match those of the linear kinematic configuration. In summary, these observations are:

1. Stability: All tasks simulations are stable, with accepatble transient response, and zero steady-state feature and positional errors.

2. Parameter Identification: Steady-state identification errors go to zero. Transient errors approach zero before the steady-state positions are reached.

3. Path: In each case, smooth trajectories are achieved, which deviate from the predicted path. Path deviations are not consistently smaller or larger than for the equivalent linear kinematic configuration.

   Tasks Z and R exhibit relatively large deviations, which result from the nonlinear kinematics (and not the nonlinear dynamics or the combination of nonlinear dynamics and kinematics). To verify this, Task Z is simulated with a linear and uncoupled dynamic plant model according to Section 4.4.5.1 (with $\tau_m = 0.058$ sec and $\tau_m = 0.027$ sec) with similar results.

4. Rise-times: The adaptive rise-times are sluggish, relative to the predicted

response. As noted for the linear kinematic trials, no attempt was made to optimize the controller pole-bound, γ, which is kept constant throughout the experimentation. In practice the control penalty can be reduced as the sampling-to-bandwidth ratio increases, resulting in faster rise-times.

5. Path-Constraint: When the object is centered in the image, the path constraint strategy produce smooth controlled motion toward the X-axis. While this technique is useful for this particular set of arm configurations, more exhaustive testing is required to determine its application in other configurations and geometries. Limitations of this strategy are accentuated in the larger motion studies.

For the fixed LMFC control:

1. Stability: With the exception of Task Q, the LMFC systems are stable, with good transient response, and zero steady-state errors. In Task Q, there is a small oscillation toward the end of the trajectory.

2. Path: Maximum path deviations exceed the adaptive path deviations.

3. Rise-times: No generalizations can be made concerning fixed vs. adaptive rise times. Consistent with the linear kinematic examples, the LMFC tends to be faster that the MRAC in most of the trials.

6.3.3.2. Large Motion Travel

The experiments presented in this section demonstrate that IBVS control of nonlinear kinematic configurations, for tasks requiring large motions, may not be suitable unless coupled controllers and extremely large sampling-to-bandwidth ratios are used.. The evaluations also show that fixed control and the path constraint hierarchy strategies are not suitable for such tasks. With the exception of the fixed controller applicability, these conclusions oppose those for the linear kinematic configuration. What are the possible differences between these configurations which account for these observations? With respect to the linear kinematic configuration, the nonlinear kinematic configuration:

1. Exhibits significantly larger changes in sensitivity over the longer distances (Table 6-5);

2. Has nonlinear and coupled dynamics; and

3. Is kinematically coupled.

Of these differences, it is shown below that the coupled kinematics ultimately limit the use of independent controllers in an IBVS system.

Tasks V and W were simulated with values of f_s/f_{BW} and T used for the small motion studies.

The simulation of Task V produces a smooth stable motion, with a deviation from the predicted path of 1.21 inches on the first trial (and 1.01 inches on the second trial). However, in Task W, the line keeps going OFV due to poor stability. For both examples, the predicted feature/joint assignment is verified to be fixed at $X_{cog} \leftarrow \theta_1$, using analytic measurements along the trajectory. The ability to control Task V may be attributed to

1. Its change in J_{21}, which is two orders of magnitude smaller than in Task W; and

2. Its smaller coupling in the initial view (i.e., $D_{Task\ V} = -0.002$ vs. $D_{Task\ W} = 0.657$. (Chapter 8 includes a systematic study of performance as a function of coupling.)

In neither task would a fixed LMFC keep the line in the field of view.

Further evaluation of Task W isolates kinematic coupling as a source for independent control. It is verified (in Section 6.3.1.1) that the nonlinear dynamics, for this arm configuration, can at least be controlled at the joint level. Next, it is verified that the combination of nonlinear dynamics and kinematics is not a problem. Task W is simulated with linear and uncoupled dynamic plant models (with $\tau_{m\text{-}1} = \tau_{m\text{-}2} = 0.1$ sec in Section 4.4.5.1.), and the line still goes OFV. The sampling-to-bandwidth ratio f_s/f_{BW} is increased to 415 by keeping T = 0.003 sec and decreasing the bandwidth to $\omega_n = 5.03\ sec^{-1}$. The resulting trajectory, on the second trial, is displayed in Figure 6-32.[14] The trajectory exhibits a relatively large deviation from the predicted path. The deviation is due partly to the presence of control signal saturation in the first joint, but not the second. Thus, θ_1, which dominates motion in the X direction, cannot drive the camera toward that axis. However, it is verified that the contribution of saturation to this deviation is minimal, by simulating the task at a lower bandwidths. At the lower bandwidths, saturation does not occur, but the camera's path still exhibits a relatively large deviation from the X-axis of 5.3 inches (compared with 5.8 inches at the higher bandwidth).

The hierarchical approach could not be used to offset these large path deviations. Failure of the hierarchical strategy in the nonlinear kinematic configuration results from the inherently poor trajectory performance. Over the larger distance of travel, the constrained joint (θ_2) tended to be cyclically activated, and then braked, to keep ΔX_{cog} within the error bounds. Frequent switching, back and forth, between levels of the hierarchy results in jerky motion. Such motion cannot be tolerated in a practical robot because of the vibrations and

---

[14]The first trial goes OFV since the parameter vector initialization is too large, and P(0) is increased to Diag[1 1 1 1]. The net time indicated for this trajectory (3 seconds) corresponds to the maximum time that the simulator can run at T = 0.003 sec.

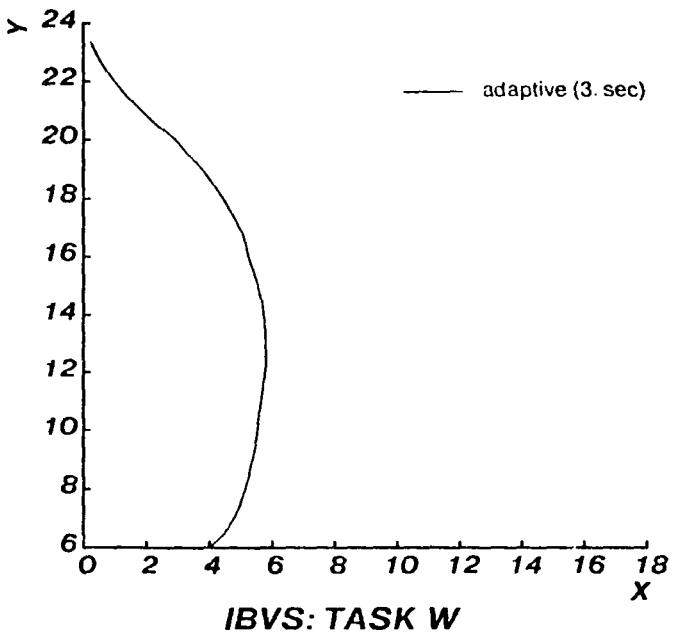

Figure 6-32: Nonlinear Kinematics: Large Motion Travel ($f_s/f_{BW} = 415$)

mechanical resonances which would result. (In the smaller motion tasks, there is only a single transition between levels.) Further, in these large motion examples, it is difficult to select a combination of controller parameters (e.g., P(0), ε, and the number of fixed transition cycles) which would even produce a stable response under these frequent switching conditions.

These experiments demonstrate that, independent IBVS control of nonlinear kinematic configurations, which requirie large motions, can produce large path deviations. While path deviations may be tolerable for for tasks requiring small motions, over larger regions of control there are increased risks of collisions with other obstacles in the region, and it is more difficult to keep the object within the camera's field-of-view. Implementations of IBVS control of nonlinear kinematic robots will require coupled controllers, using relatively large sampling-to-bandwidth ratios. Alternatively, independent controllers may be used if the robot kinematics are first uncoupled by using a dynamic image-based "Look & Move" structure.

6.3.3.3. Feature/Joint Reassignment

Analysis and evaluation of the 2 DOF linear kinematic configuration suggest that a fixed feature/joint assignment is satisfactory for control of such a system. In contrast, the sensitivity analysis in Section 6.3.2, and the example presented in this section demonstrates that, when individual degrees of freedom do not coincide with the camera's frame (e.g. a

nonlinear kinematic configuration), a fixed feature/joint assignment is not generally suitable. The sensitivity analysis shows that the arm jacobian dominance, and therefore overall sensitivity dominance, changes with the arm configuration. This section evaluates motion across a boundary of diagonal dominance change. The experiments suggest that, when crossing such boundaries, a fixed feature/joint assignment can only be used if the required motion is relatively small.

A task which requires crossing a boundary of change in diagonal dominance is represented in Figure 6-33. The task is simulated with three strategies:[15]

1. Fixed feature/joint assignment : $\theta_2 \leftarrow X_{cog}$ (corresponds to assignment predicted in desired view);

2. Feature/joint reassignment: at boundary of diagonal dominance change; and

3. Fixed feature/joint assignment : $\theta_1 \leftarrow X_{cog}$ (corresponds to assignment predicted in initial view).

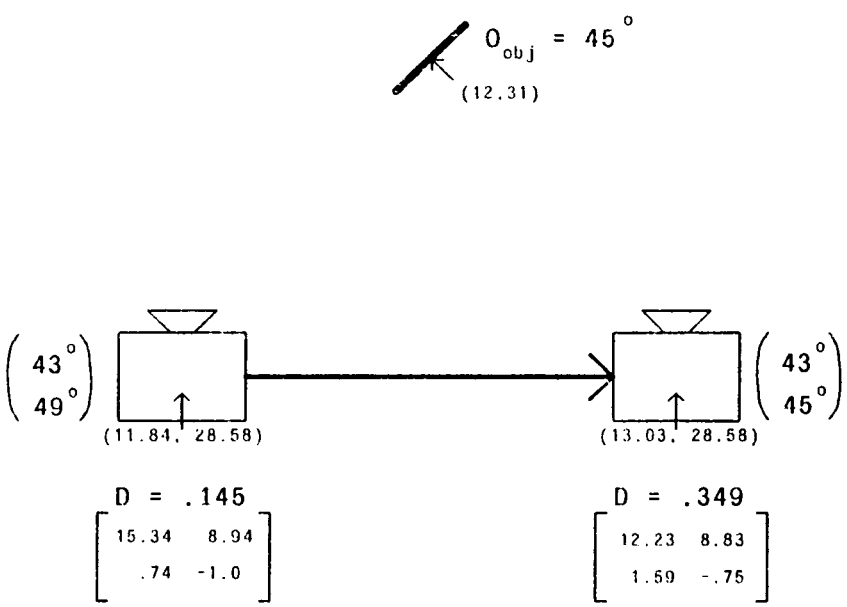

Figure 6-33: Nonlinear Kinematic Feature/Joint Reassignment Task

The resulting trajectories for the first two strategies are displayed in Figure 6-34. The feature/joint reassignment trajectory exhibits a smaller path deviation. In the third strategy (not displayed), which is satisfactory for the configurations evaluated in Section 6.3.3.1, the

[15] These simulations use the controller parameters specified for the small motion tasks in Section 6.3.3.1.

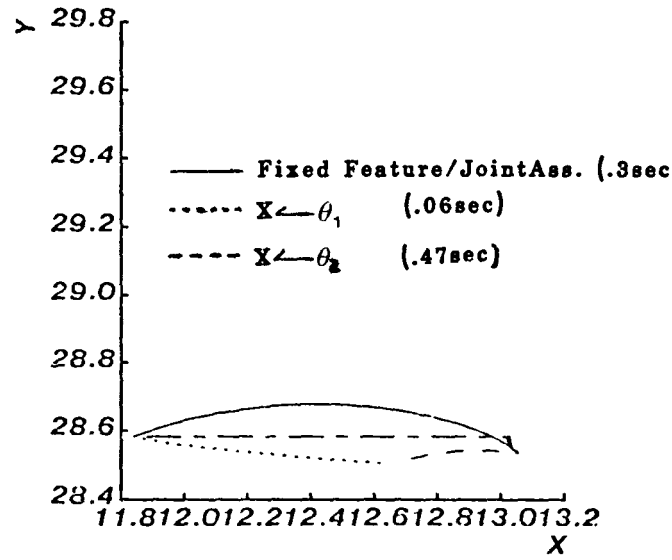

Figure 6-34: Feature/Joint Reassignment (Nonlinear kinematics)

line goes OFV due to large path deviations. For all cases, the fixed LMFC causes the line to go OFV due to large path deviations.

It would not have been suitable to implement this task using a feature/joint assignment based on the sensitivity in the initial view, since the line goes OVF. In practice without an on-line estimation of JW_p, the sensitivity in the initial view is all that can be determined from measurements preceeding the start of control. This issue is discussed in Chapter 7. If the required motion is even smaller (e.g., small corrective tasks), measurement of JW_p preceeding the start of control may be satisfactory. For example, the task in Figure 6-33 is redefined so that the initial and final arm positions are separated by only 0.3 inches (i.e., θ_2 47→46 degrees, and θ_1 is 43 degrees in both initial and final views respectively.) When this task is simulated with $\theta_1 \leftarrow X_{cog}$, the resulting trajectory, which still crosses the diagonal dominance boundary, is stable and displays an approximately straight line motion.

6.4. Summary

The purpose of this two part chapter is to evaluate independent adaptive control of coupled two DOF systems. Visual servoing, of a line in space problem, uses two basic configurations:

1. A linear and uncoupled kinematic and dynamic robot, for which the robot's degrees-of-freedom coincide with the camera's reference frame; and

2. A nonlinear and coupled kinematic and dynamic robot.

While image-based control is emphasized, preliminary evaluation of joint-level control of the nonlinear and coupled plant dynamics is also included. To the best of the author's knowledge, this is the first demonstration of an enhanced MRAC (i.e., SP MRAC, with control penalty and measurement delay) for robot control.

The main conclusion which emerges from this evaluation is that an image-based "teach-by-showing" strategy, using an adaptive control approach, can be used to control robots. Since this approach cannot be used to control path, it appears to be best suited for precision tasks which require small corrective motions (e.g., precision assembly, for parts aquistion and mating alignment). However, predicted postion trajectories, for at least this simple line in space problem, are smooth and approach straight-line. This motivates continuing future research to evaluate more general configurations.

While independent control of the coupled systems achieve stable performance, with acceptable transient response, and zero steady-state error, potential limitations of this approach include:

- Independent controllers produce deviations from the predicted path. While steady-state errors go to zero, deviations arise from transient identification-errors occuring during the intial phases of control. Path deviations are relatively small, with the exception of the large motion nonlinear kinematic tasks. For these tasks, indepenent control is judged not to be suitable due to increased risks of obstacle collison, and the requirement of extremely large sampling-to-bandwith ratios (which may not be suitable for a practical implementations.)

  Independent joint-level control of a dynamically nonlinear and coupled robot, using an enhanced SP MRAC and with measurement delay, is stable with acceptable transient response. The control problem associated with the large motion nonlinear kinematic tasks is then isolated to the nonlinear kinematics (and not to the dynamics).

- Independent control requires a feature/joint reassignment strategy for a general system. While a fixed assignment is adequate for the linear kinemati configuration (using a sufficiently large f_s/f_{BW}), the articulated arm configuration requires a reassignment strategy, unless motion is constrained to small movements. Boundaries of feature/joint reassignment are successfully predicted by minimizing the coupling index D (2.9).

- Since the MRAC is sign-sensitive, independent control of a coupled system can cause momentary large reversals in the axis direction. Large sampling-to-bandwidth ratios can minimize these effects.

These limitations suggest potential performance advantanges which can be gained by using coupled controllers.

Evaluation of a path constraint hierarchy shows that arbitary use of this hierarchy may or may not minimize nonmonotonic path deviations. This strategy produces a smooth controlled path biased toward the X-axis, except for the large motion, nonlinear kinematic tasks. For this configuration, the large path deviations could not be offset because it is difficult to select a combination of controller parameters which would yield a stable system under the frequent switching conditions, and the motion is too jerky for practical systems.

Finally, the MRAC is used to derive fixed LMFC controllers. Relative to the adaptive approach, the fixed controllers exhibit better transient response at lower sampling-to-bandwidth ratios, and tend to have faster rise-times. They produce larger path devaitions; are only suitable for small motion the tasks which have small sensitivity changes; and, a single LMFC is not suitable for a broad range of tasks.

Only two control features were available for the 2 DOF configuration. In Chapter 7, IBVS control is extended to a three DOF system, and control is evaluated for multiple candidate features. Evaluation of a single task, with different control features, provides a consistent and systematic study of performance as a function of the coupling index $D(\mathbf{JW}_p)$.

Chapter 7
Evaluation: Three DOF

7.1. Overview

The purpose of this chapter is to evaluate adaptive image-based SISO control of the 3 DOF configuration described in Section 4.2.3. The simulations described extend adaptive image-based control to a multi-DOF system which models a real configuration. The evaluation focuses on the feature selection process described in Section 2.5.2. The diverse path and time performances, resulting from using different feature subsets, emphasize the importance of feature selection. The coupling index $D(\mathbf{JW}_p)$ is demonstrated to be a suitable discriminant function for selecting among candidate feature subsets. By selecting features which minimize this index, improved system performance (including both path and time response) is achieved as $D(\mathbf{JW}_p)$ decreases. These results are consistent with those observed in Chapter 6 for the related issue of feature/joint assignment, which uses $D(\mathbf{JW}_p)$ to minimize apparent system coupling. The suitabilty of using this index as a measure of coupling becomes an important aspect for implementations of general image-based systems, which will have to select and assign features.

The evaluation also illustrates the hierarchical and fixed control strategies. The hierarchical approach not only constrains path motion, but also facilitates the use of SISO adaptive control by making performance less sensitive to coupling. Adaptive learning trials can be used to synthesize SISO fixed controllers, whose performance begins to degrade as changes in sensitivity become larger.

This chapter is organized as follows. In Section 7.2, the candidate features are defined, and measurement of the system sensitivies is described. The small-signal evaluation, in Section 7.3, uses tasks requiring small motions so that changes in the magnitudes of the feature sensitivity, $\mathbf{J}$, and thus changes in the coupling index, $D(\mathbf{JW}_p)$, are also small over the trajectory. This provides a convenient task for analyzing and evaluating adaptive control

performance as a function of coupling since $D(JW_p)$ remains essentially constant. Larger motion tasks, with significant chages in J, are evaluated in Section 7.4 to investigate the suitabilty of selecting features based on coupling in the initial view, and also to show examples of fixed and hierarchical control. The controller parameters, for the simulations described in this chapter, are summarized in Appendix D.

7.2. Candidate Control Features

The feature selection process (in Section 2.5.2) asks: How should a subset of n control features be selected (n = 3), from a set of m features, where m>n? In Section 2.5.2, it was proposed that the selection may be based on minimization of $D(JW_p)$. In this section, m candidate features (where m = 7) are defined for the control evaluation in Sections 7.3 and 7.4. Measurement of the corresponding sensitivities is then discussed.

The cube (in Figure 4-13) is sitting in a stable position on top of the turntable (i.e., one of the cube's sides is flat), and its image is displayed in Figure 7-1.

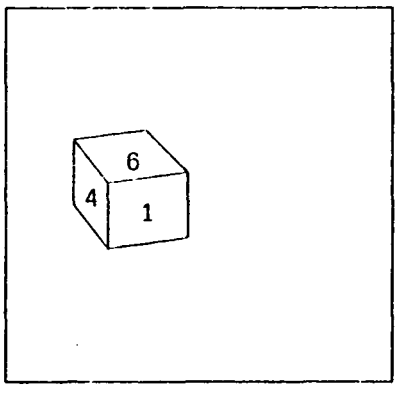

Figure 7-1: Cube Image

In the figure, each plane or node[16], is referenced by the displayed number (e.g. node 6, 4, or 1). It is assumed that the vision system can distinguish the image regions associated with each node (i.e., connected regions [Agin 79]). The vision system can extract the image area, A_i, and centroid, $(X_{cog\text{-}i}, Y_{cog\text{-}i})$, of each ith node. Combinations of these features, such as relative areas:

[16]The origin of *node* is related to a graph structure representation of the image [Sanderson 82]

$$A_{rel\text{-}i,j} \doteq \frac{A_i}{A_i + A_j}$$

and sums of areas:

$$A_{i+j} \doteq A_i + A_j$$

can also be considered for selection. It is initially assumed that the features from only nodes 4 and 1 are available, and the candidate features are:

$$A_1,\ A_2,\ A_{rel\text{-}1,2},\ A_{rel\text{-}2,1},\ A_{1+2},\ X_{cog\text{-}1},\ \text{and}\ X_{cog\text{-}2}$$

There are thus p(7,3) = 210 candidate subsets of ordered features. To limit the number of combinations which are evaluated in the dissertation, feature subsets are selected which include one of each type feature: a center-of-gravity, an area or sum of areas, and a relative area feature. This combination is chosen because the 2 DOF evaluation (in Chapter 6) has already demonstrated that the COG and length of a line, analogous to the centroid and area of a plane, can be used to control depth and position. The relative area feature is added in consideration of the additional orientation DOF. Feature/joint assignment is described (in Section 7.2.2) after the discussion of sensitivity measurements (in Section 7.2.1).

7.2.1. Sensitivity Measurements

Preceding the start of control, it is straightforward to measure the magnitude of JW_p (i.e., $|JW_p|$) in the initial perceived image. With this measurement, the coupling index, $D(JW_p)$, can be calculated for selection and assignment of an initial feature subset. The magnitude of JW_p can be measured by independently evaluating J and $|W_p|$. The robot transfer function matrix is

$$W_p(s) = \begin{bmatrix} \frac{K_m}{s(\tau_{m\text{-}x}s+1)}\frac{1}{2\pi p} & 0 & 0 \\ 0 & \frac{K_m}{s(\tau_{m\text{-}y}s+1)}\frac{1}{2\pi p} & 0 \\ 0 & 0 & \frac{K_m}{s(\tau_{m\text{-}\theta}s+1)}\frac{360}{2\pi\eta} \end{bmatrix} \tag{7.1}$$

The magnitude of W_p is evaluated by assuming that the the open-loop plant time constants,

τ_m, are small relative to the closed-loop time constants. This is justified since the closed-loop position rise-times, observed in the simulation examples, range from 0.16 to 1.4 seconds[17], while the plant time constants range from 0.041 to 0.091 seconds. When, $|W_p|$ is approximated by its low frequency gain characteristics:

$$|W_p(j\omega)| \simeq \omega^{-1} \begin{bmatrix} \frac{K_m}{2\pi p}\left(\frac{in}{volt}\right) & 0 & 0 \\ 0 & \frac{K_m}{2\pi p}\left(\frac{in}{volt}\right) & 0 \\ 0 & 0 & \frac{360K_m}{2\pi\eta}\left(\frac{deg}{volt}\right) \end{bmatrix} \tag{7.2}$$

This assumption simplifies the calculation of $|W_p|$ when the exact dynamic model is not known. In this case, each term in (7.2) can easily be be measured as the magnitude of the impulse response for each joint. For the experiments presented in this chapter, the values used for K_m, p, and η, were derived in Chapter 4. In (7.2), since ω^{-1} is a common factor, the evaluated radian frequency is set to $\omega = 1$. For higher closed-loop bandwidth systems, it would be appropriate to evaluate (7.1) at the closed-loop bandwidth ω_n.

The sensitivity matrix is

$$J = \begin{bmatrix} \frac{\partial X_{cog}}{\partial X} & \frac{\partial X_{cog}}{\partial Y} & \frac{\partial X_{cog}}{\partial \theta} \\ \frac{\partial A}{\partial X} & \frac{\partial A}{\partial Y} & \frac{\partial A}{\partial \theta} \\ \frac{\partial A_{rel}}{\partial X} & \frac{\partial A_{rel}}{\partial Y} & \frac{\partial A_{rel}}{\partial \theta} \end{bmatrix}$$

and is determined by sequentially moving each DOF by a small displacement and then measuring the accompanying feature changes:

[17] The feature control variable rise-times, while not recored, are even larger according to the analysis in Section 5.4

$$J \simeq \begin{bmatrix} \frac{\Delta X_{cog}}{\Delta X}(in^{-1}) & \frac{\Delta X_{cog}}{\Delta Y}(in^{-1}) & \frac{\Delta X_{cog}}{\Delta \theta}(deg^{-1}) \\ \frac{\Delta A}{\Delta X}(in^{-1}) & \frac{\Delta A}{\Delta Y}(in^{-1}) & \frac{\Delta A}{\Delta \theta}(deg^{-1}) \\ \frac{\Delta A_{rel}}{\Delta X}(in^{-1}) & \frac{\Delta A_{rel}}{\Delta Y}(in^{-1}) & \frac{\Delta A_{rel}}{\Delta \theta}(deg^{-1}) \end{bmatrix} \tag{7.3}$$

The magnitude of the joint displacements ($\Delta x, \Delta y, \Delta\theta$) are selected by succesive iterative reduction until successive values of each element of J satisfies

$$\frac{J_i - J_{i-1}}{J_i} X\ 100\% < 0.01\ \%$$

In (7.3), the dimensions of each element are functions of only the joint variable, since the features are normalized to the screen and are dimensionless. Each element of $|JW_p|$ thus has the same units (volt $^{-1}$). This is imperative to be able to compare the relative magnitudes of the sensitivities.

Since the magnitude of the sensitivities can change from the initial to the final image, so can $D(JW_p)$, and the selected feature subset can change along the trajectory. Ideally, it would be convenient if the relative relationships between the coupling index of each subset remained constant along the trajectory. Then, only off-line measurements of the sensitivities, made preceding the start of control, would be sufficient. The 2 DOF evaluation has already demonstrated that feature/joint assignment can change during control for a nonlinear kinematic system. The 3 DOF evaluation shows that the selected features may also change. Thus, in a completely general image-based system, $|JW_p|$ might be estimated on-line. To evaluate the use of $D(JW_p)$ to discriminate among several feature candidates, small motion tasks will be specified so that J and $D(JW_p)$ do not change significantly over the trajectory. Thus, measurement of the intial view couplings are suitable. The use of intial view coupling measurements for larger motion tasks are evaluated in Section 7.4 .

7.2.2. Feature/Joint Assignment

All simulations are implemented using fixed feature/joint assignments corresponding to

$$\begin{aligned} X_{cog} &\leftarrow \text{X-axis} \\ A &\leftarrow \text{Y-axis} \\ A_{rel} &\leftarrow \theta\text{-axis} \end{aligned} \tag{7.4}$$

For each candidate feature subset evaluated, it is verified that these are the assignments predicted according to minimization of $D(JW_p)$. A case where these assignments do not hold will also be discussed.

The evaluation in Chapter 6 demonstrated that minimization of D can provide a suitable feature/joint assignment for a 2 DOF system. For three and higher DOF systems, the question arises: If JW_p is organized to minimize $D(JW_p)$, but partitioned (2x2) matrices of JW_p are not each minimized independently, can control problems arise? For the particular 3 DOF simulations, evaluated in this dissertation, such organizations do not occur. That is, it was verified that the three partitioned matrices, which result by canceling one DOF and the corresponding feature on the diagonal of the $|JW_p|$ matrix, each exhibit a minimum in coupling. The partitioned matrices are:

$$\begin{bmatrix} \frac{\partial X_{cog}}{\partial X}K_x & \frac{\partial X_{cog}}{\partial Y}K_y \\ \frac{\partial A}{\partial X}K_x & \frac{\partial A}{\partial Y}K_y \end{bmatrix} \tag{7.5}$$

$$\begin{bmatrix} \frac{\partial X_{cog}}{\partial X}K_x & \frac{\partial X_{cog}}{\partial \theta}K_\theta \\ \frac{\partial A_{rel}}{\partial X}K_x & \frac{\partial A_{rel}}{\partial \theta}K_\theta \end{bmatrix} \tag{7.6}$$

$$\begin{bmatrix} \frac{\partial A}{\partial Y}K_y & \frac{\partial A}{\partial \theta}K_\theta \\ \frac{\partial A_{rel}}{\partial Y}K_y & \frac{\partial A_{rel}}{\partial \theta}K_\theta \end{bmatrix} \tag{7.7}$$

where

$$K_x = K_y = \frac{K_m}{2\pi p} \text{ (in/volt) and } K_\theta = \frac{360K_m}{2\theta\eta} \text{ (deg/volt)}$$

Future research must verify whether minimization inconsistencies between the entire sensitivity matrix and partitioned (2x2) sections will occur for other configurations. And, if so, will these limit the use of independent controllers?

7.3. Small Signal Evaluation

In this section, a task requiring small motions is specified so that changes in the magnitudes of the sensitivity, J, and thus coupling index, $D(JW_p)$, are also small over the trajectory. The task is specified to have a net displacement of $\Delta X = \Delta Y = 0.1$ inches for the translational stages, and $\Delta\theta = 1$ degree for the rotational stage. In these examples, the coupling index $D(JW_p)$, for each candidate subset, varies from 0.01 to 2 percent from the initial to desired (or final) view. Thus, calculation of $D(JW_p)$, using measurements of $|JW_p|$ in the initial view, can be used to evaluate performance of the different candidate feature subset selections.

The system performance is evaluated by comparing both path performance and time response. It was shown in Section 2.5.2.2, that if J is constant, the predicted path (i.e., that which occurs if perfect model following were achieved) of the translational stages is straight-line motion. For the examples included in this section, changes in sensitivity are typically less than 1 percent. The predicted path can therefore be approximated by a straight-line. As $D(JW_p)$ decreases, we anticipate improved model following capabilities of the SISO controllers, and thus closer to straight-line motion. Path performance will be evaluated by comparing $D(JW_p)$ versus the actual distance traveled, where a straight-line path corresponds to 0.144 inches.[18] Time domain performance is evaluated as a function of largest position rise-time of the three axes.

The task simulations utilize a cube, with its desired image displayed in Figure 7-1, as the control object. The configuration parameters in Table 7-1 are defined in Figure 4-3.

Focal Length F =	35 mm
α =	45 degrees
R =	30 inches
h =	.5 inches
T_{obj} =	[-.5 0 0 (in.), 0 0 0 (Euler-angles)]
Desired X-Y-θ stage positions =	-.5 (in), 0. (in), 30. (deg)
Initial X-Y-θ stage positions =	-.4 (in), .1 (in), 31. (deg)

Table 7-1: Small Motion Task Configuration

The image of the object in the initial view is not displayed since it appears essentially the same as in the desired view.

---

[18] $(\Delta x^2 + \Delta y^2)^{0.5} = 0.144$

A modification of the aforementioned configuration will be used to discuss a case for which the feature/joint assignment specified in (7.4) does not hold. In this example (which is dicussed below), the cube is placed on one of its edges by setting

$$T_{obj} = [-.5, 0, 0, 0, 45, 0]$$

The camera angle and position are modified to $\alpha = 0$ and $h = 0$. The remainder of the parameters remain as in Table 7-1. The image of the cube in this position is displayed in Figure 7-2.

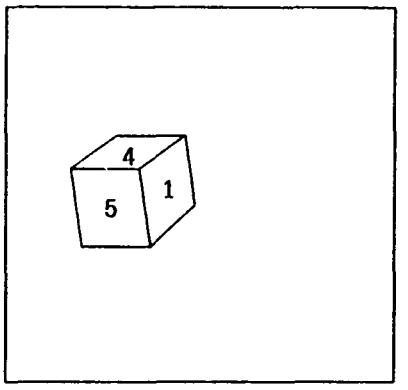

Figure 7-2: Cube on Edge

Results of adaptive control simulations, using a representative set of feature subsets, are summarized in Table 7-2. Discussion of these results will follow explanation of the table entries.The table includes the feature subset and the performance on the second adaptive trial using that subset. It was verified, for each trial, that the actual distance traveled are smooth paths and do not oscillate about a trajectory. The θ-axis trajectories all exhibited smooth motions with negligible overshoots varying between 0.01 to 0.4 percent. Displays of sample trajectories will be included with the discussion. The table indicates the coupling index associated with each feature subset. Additionally, the coupling indices for each of the partitioned (2x2) matricies, (7.5), (7.6) and (7.7), are calculated. The maximum value for each subset is indicated, in the table, by $D_{2x2\text{-}max}$. The significance of this index will follow in the discussion of the results. Except for the final experiment, all examples refer to the image displayed in Figure 7-1. These 17 candidate feature subsets are representative of the 108 possible combinations. Of these, the first 12 correspond to all possible combinations if features from only two nodes (i.e., nodes 1 and 4) were available. The remainder are examples of combinations using features from all three nodes.

Feature Subset				Coupling Index		Performance	
X_{cog-i}	A_{rea}		$A_{rel-i,j}$				
	A_i or A_{i+j}			D	$D_{2x2-max}$	t_r(sec)	distance (in)
i=	i=	i,j=	i,j=				
4	4		4,1	1.69	1.64	0.339	0.353
4	4		1,4	1.69	1.64	0.339	0.353
4	1		4,1	1.04	0.99	0.321	0.194
4	1		1,4	1.04	0.99	0.315	0.194
1	4		4,1	1.69	1.64	0.321	0.374
1	4		1,4	1.69	1.64	0.327	0.373
1	1		4,1	1.04	0.99	0.321	0.218
1	1		1,4	1.04	0.99	0.321	0.218
4		4,1	4,1	0.82	0.76	0.315	0.217
4		4,1	1,4	0.82	0.76	0.315	0.216
1		4,1	4,1	0.81	0.76	0.306	0.221
1		4,1	1,4	0.81	0.76	0.303	0.221
6	6		1,4	-0.38	-0.54	0.165	0.144
6	6		6,4	-0.33	-0.54	0.171	0.144
6	6		6,1	-0.22	-0.53	0.156	0.144
6		6,4	6,4	0.76	0.70	0.267	0.194
6		6,1	6,1	0.46	0.37	0.192	0.147
1	1		4,1	0.61	0.56	0.270	0.163

Table 7-2: Small Motion Task Summary

The last example, which uses the image of the cube on its edge (Figure 7-2), presents a situation for which the feature/joint assignment specified by (7.4) does not hold for all of the image's candidate feature subsets. This example is included to clarify the feature/joint assignment issue. In this case, the feature/joint assignment for the feature subset specified in Table 7-2, $\underline{f} = [X_{cog-1}, A_1, A_{rel-4,1}]$, corresponds to (7.4). However, if the candidate subset had been $\underline{f} = [X_{cog-1}, A_1, A_{rel-4,5}]$, then the sensitivity becomes

$$\begin{bmatrix} \delta X_{cog-1} \\ \delta A_1 \\ \delta A_{rel-4,5} \end{bmatrix} = \begin{bmatrix} 3.97E-3 & 2.91E-5 & -1.78E-4 \\ -1.30E-5 & -3.78E-5 & -1.50E-4 \\ 0. & 1.69E-8 & 0. \end{bmatrix} \begin{bmatrix} \delta u_x \\ \delta u_y \\ \delta u_\theta \end{bmatrix}$$

which shows that the relative area feature, $A_{rel-4,5}$, must be coupled to the Y-axis. The column organization of J, which minimizes $D(JW_p)$, for this case is

$$\begin{bmatrix} \delta X_{cog-1} \\ \delta A_1 \\ \delta A_{rel-4,5} \end{bmatrix} = \begin{bmatrix} 3.97E-3 & -1.78E-4 & 2.91E-5 \\ -1.30E-5 & -1.50E-4 & -3.78E-5 \\ 0. & 0. & 1.69E-8 \end{bmatrix} \begin{bmatrix} \delta u_x \\ \delta u_\theta \\ \delta u_y \end{bmatrix}$$

The important observations which emerge from the small-signal evaluation are:

1. Stability: The simulations provide further verification of the extension of SISO adaptive controllers to achieve stable dynamic control of coupled systems. The systems are stable, with acceptable transient responses, and zero steady-state positional errors. For example, Figure 7-3, shows three representative trajectories. The diverse path and time performances, as a result of using different feature subsets, emphasize the importance of feature selection.

2. Feature Selection: The coupling index, $D,(JW_p)$ is a suitable discriminant function for selecting candidate feature subsets to improve system performance. Plots of coupling index versus path and time performance, for each experiment listed in Table 7-2, are displayed in Figure 7-4. Minimizing $D(JW_p)$ over all potential candidates produces a fast, straight-line response. The feature subset which maximizes $D(JW_p)$ yields the slowest response, with the largest path deviation. As $D(JW_p)$ decreases, both path and time performance improve. Local inconsistencies are observed, with non-significant differences in performance. Order of magnitude decreases in coupling yield substantial performance improvements.

   Further analysis reveals that the coupling index of the overall sensitivity matrix, $D(JW_p)$, reflects the dominant internal couplings. Plots of $D_{2x2\text{-}max}$ are displayed in Figure 7-5. Plots of $D(JW_p)$ and $D_{2x2\text{-}max}$ are similar. Using either coupling measures would have predicted the same selections. The significance of this observation is that for other configurations and tasks, one of these measures may turn out to be a more sensitive discriminant function. Future research investigations should include evaluations based on both measures to determine which is ultimately more significant.

The small-signal simulations and evaluations show the importance of feature selection, and the suitability of the coupling index to accomplish this. The following section, which includes examples requiring larger motions of travel, extends these results to tasks for which variations in J are significantly larger.

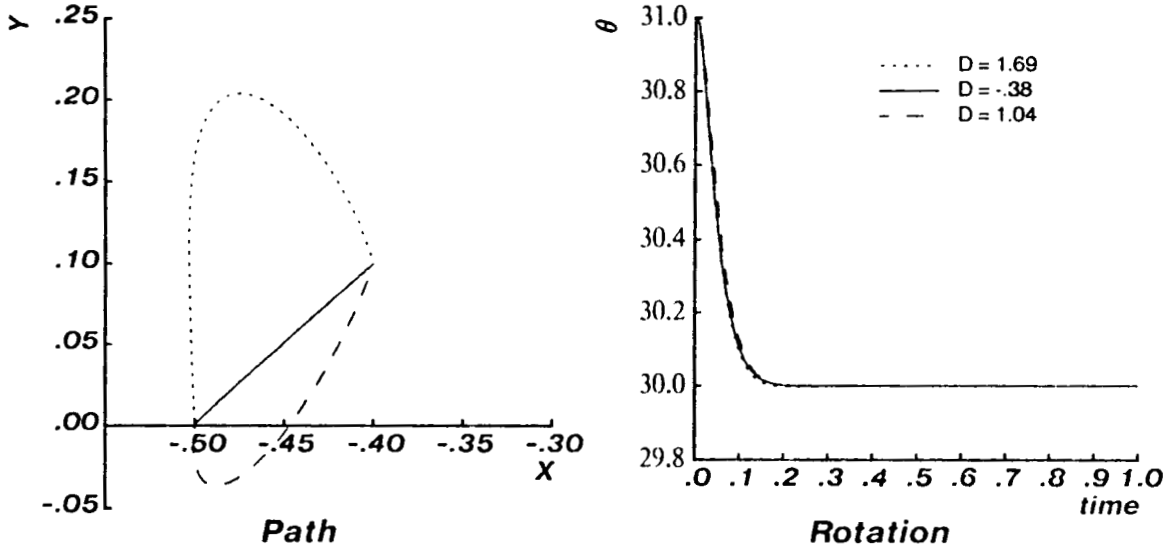

Figure 7-3: Sample Small Motion Task Trajectories

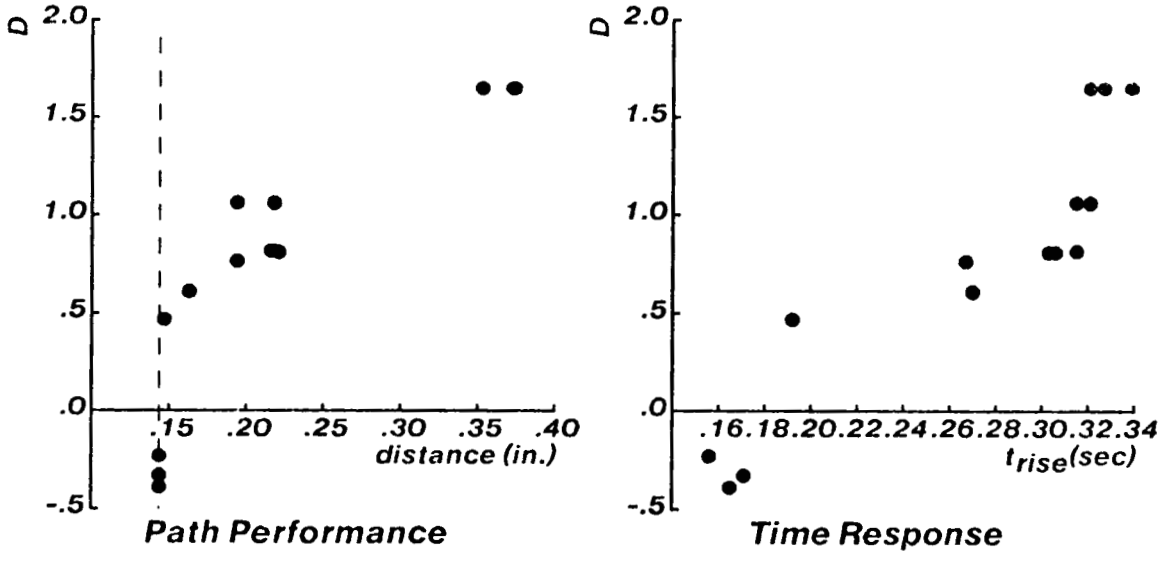

Figure 7-4: Coupling Index vs. Performance

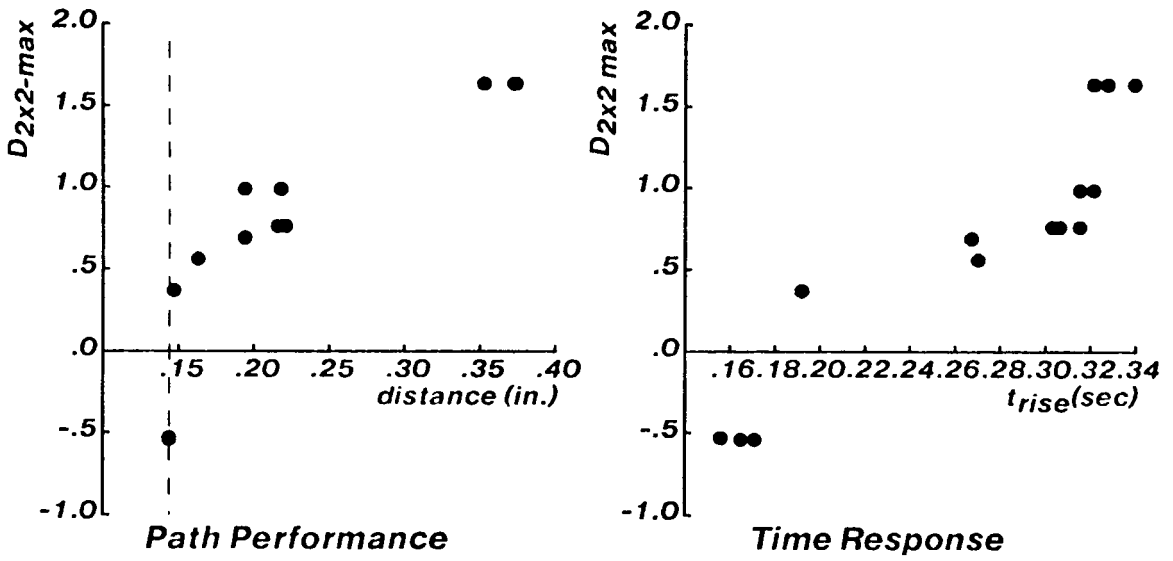

Figure 7-5: Partial Coupling Index vs. Performance

7.4. Large Motion Evaluation

The small-signal simulations provide a convenient means for analysis and evaluation of the suitability of minimizing $D(JW_p)$ to select features. In practice, actual tasks may require larger motions which result in time-varying sensitivities. Significant changes in $D(JW_p)$ can therefore occur, from the initial to the final view. Selecting features based on minimizing $D(JW_p)$ in the initial view may not assure that these are the best selections along the trajectory. The alternative is to estimate $D(JW_p)$ on-line and then implement an on-line feature reselection strategy (i.e., analogous to the feature/joint reassignment procedure in Chapter6). This becomes a more complex strategy. The evaluation included in this section uses examples of large motion tasks to investigate the suitability of selecting features based only on coupling in the *initial* view. This section also includes examples of the fixed and hierarchical control strategies.

The evaluation uses examples based on two task configurations. One configuration, which uses the cube as the control object, is represented by the images displayed in Figure 7-6. This task requires net trajectory displacements of $\Delta X = 2.5$ in., $\Delta Y = 2$ in., and $\Delta\theta = 30$ degrees. These magnitudes are typical of those that observed in the Flexible Assembly Laboratory [Sanderson 83b] when the 3 DOF configuration is used in a static "look and

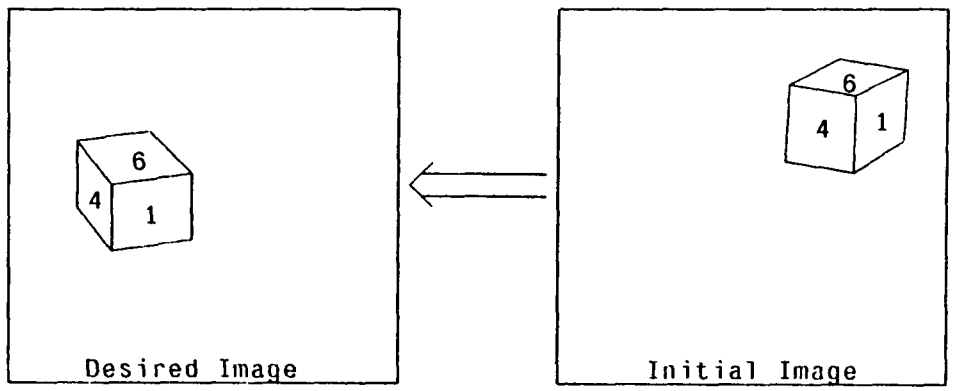

Focal Length F = 35 mm
α = 45 degrees
R = 30 inches
h = 0.5 inches
T_{obj} = [-0.5 0 0 (in.), 0 0 0 (Euler-Angles)]
Desired X-Y-θ stage positions = -0.5 (in), 0 (in), 30 (deg)
Initial X-Y-θ stage positions = 2 (in), 2 (in), 60 (deg)

Figure 7-6: Large Motion Task Images (Cases A, B, C, and D)

move" mode to locate and orient random electronic components. A second task, which uses the pyramid (Figure 4-13) as the object, is represented by the images in Figure 7-7.

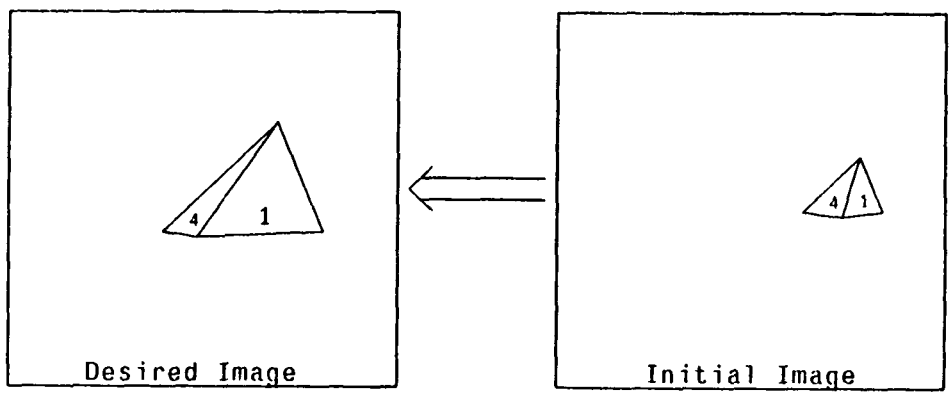

Focal Length F = 35 mm
α = 0 degrees
R = 20 inches
h = 0 inches
T_{obj} = [-0.5 0 0 (in.), 0 0 0 (Euler-angles)]
Desired X-Y-θ stage positions = 0.5 (in), 0 (in), 40 (deg)
Initial X-Y-θ stage positions = 2 (in), 24 (in), 60 (deg)

Figure 7-7: Large Motion Task Images (Cases E and F)

Although such a large trajectory (i.e. $\Delta Y = 20$ in.) is not anticipated for applications with this type of configuration, it is useful to show examples which further accentuate sensitivity and coupling changes.

The evaluation does not include calculation of the predicted path, since compact analytic equations for the feature transformations become complex to derive for higher DOF systems with solid objects. Future investigations could derive predicted paths by numerical integration methods, using estimates of J measured along small increments. For the examples presented, it is anticipated that, as $D(JW_p)$ decreases, there will be relative improvements in time response, and path deviations from a monotonic trajectory will be reduced. That is, if J were diagonal (i.e., $D = -\infty$) and a single valued function of position along the trajectory (i.e., $J_{ii} \neq 0$), then for critically damped features, the path must be monotonic. A summary of system performance for the two tasks is shown in Table 7-3. The table lists performances of both the initial and second (i.e.,subsequent) adaptive trials, and for fixed and hierarchical control. The fixed controller is implemented by fixing the adjustable gains identified in the first adaptive trial. The hierarchical performance is indicated for the second adaptive hierarchical trial. Sample plots for two cases are displayed in Figures 7-8 and 7-9.

		Feature Subset				D Coupling Index in		Path Distance (in)				Rise-time (sec)			
	Case	x_{cog-i}	Area A_i or A_{i+j}		$A_{rel-i,j}$										
		i=	i=	i,j=	i,j=	Desired View	Initial View	1st Adaptive trial	2nd Adaptive trial	Fixed	Hierarchical	1st Adaptive trial	2nd Adaptive trial	Fixed	Hierarchical
Cube	A	4	4		4,1	1.69	0.99	OFV	OFV	OFV	4.57	OFV	OFV	OFV	0.474
	B	1	1		1,4	1.04	1.76	3.64	3.65	3.77	4.55	0.378	0.399	0.405	0.486
	C	4	4	4,1	4,1	0.82	0.84	OFV	3.97	OFV	4.58	OFV	0.315	OFV	0.486
	D	6	6		4,1	-0.39	-0.38	3.31	3.31	3.33	4.57	0.234	0.234	0.225	0.528
Pyramid	E	4	4		4,1	1.51	1.20	29.39	24.89	24.68	25.84	1.416	1.236	1.070	1.30
	F	4		4,1	4,1	0.32	-0.34	24.66	24.61	24.63	25.85	1.188	1.167	1.071	1.326

Table 7-3: Large Motion Task Performance Summary

Comparison of the coupling indices for the first two cases, A and B, reveals that the feature subset, which minimizes the coupling, can change from the initial to the desired views. If the feature selections were limited to these two candidates, then an on-line feature reselection strategy may be useful. A completely generalized image-based system, using SISO controllers, may therefore require this capability. For cases A and B the magnitudes of

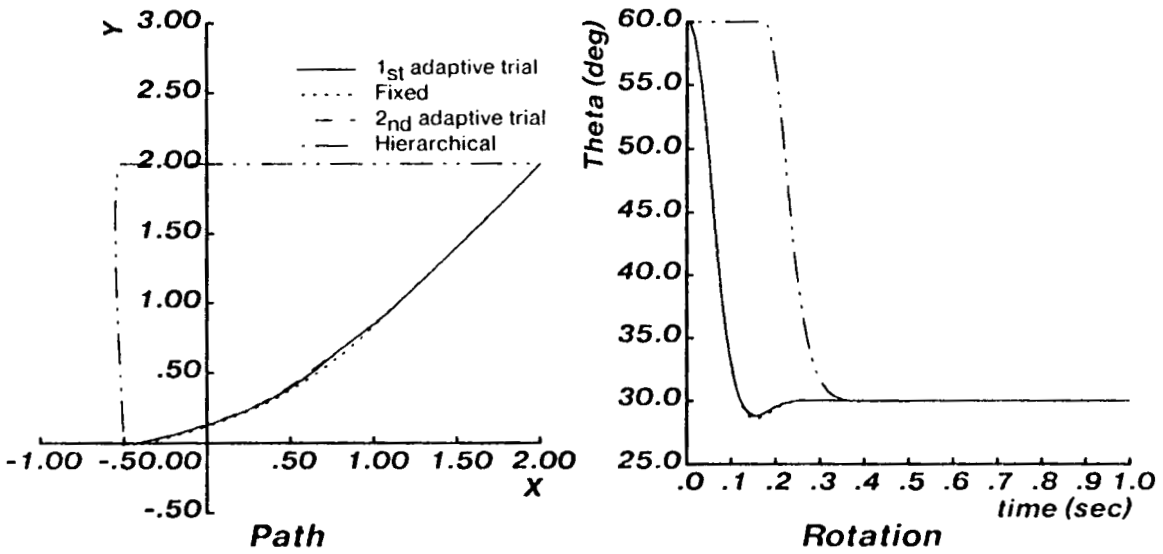

Figure 7-8: 3 DOF Trajectory (Case D)

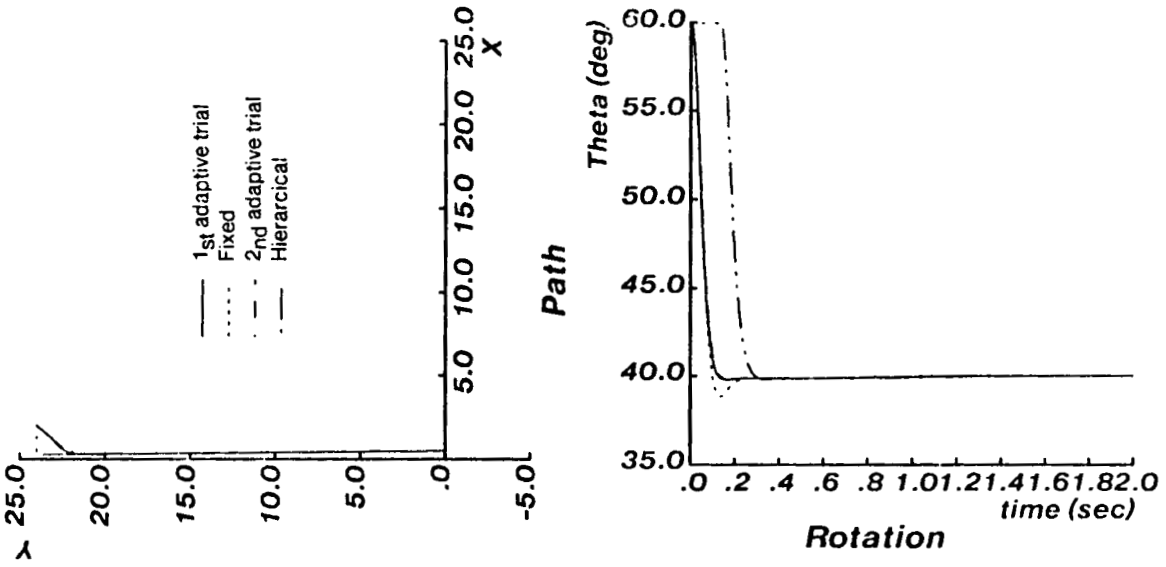

Figure 7-9: 3 DOF Trajectory (Case F)

$D(JW_p)$ are relatively large in all views. If more potential candidates are available, then the possibility of finding a subset with relatively small coupling values, over the trajectory, increases. If $D(JW_p)$ remains small, then reselection strategies may not be crucial. The cases listed do not produce examples with both small couplings and predicted reselections. These

evaluations do suggest that feature subsets, which have initial view couplings that are an order of magnitude smaller than for other candidates, show significant improvements in performance.

The performance features for each control strategy are summarized as:

1. Adaptive Control: Adaptive control yields stable system performance when the object stays in the field of view. The cube goes OVF in both the first and second trials of Case A. This feature subset has relatively large values of coupling. For Case C, where the coupling is smaller, the cube goes OVF only in the first trial, but with improved second trial response.

   The controller which uses the feature subset with the smallest initial view coupling (i.e., Case D for first task, and Case F for second task), produces the best performance for each task. They exhibit the fastest rise-times and the shortest distances of travel. Their trajectories also approach straight-line motions. The deviations from a straight path are on the same order of magnitude observed for the 2 DOF linear kinematic configuration. Further, their first and second adaptive trial performances are virtually identical. The cases with larger coupling show significant changes between these two trials.

   Rise-times associated with the second task (i.e., pyramid examples) are much larger due to control signal saturation in the Y-axis controller. This also affects the initial part of the trajectory and may partly account for the absence of a straighter path there.

   These examples reinforce the suitability for using $D(JW_p)$ as a feature selection discriminant function. These results also suggest that the selection may be based on the initial view coupling, if potential candidates have relatively small coupling values (e.g., $D(JW_p)<0$.)

2. Hierarchical Control: This strategy produces system performances exhibiting two important characteristics. First, the path is constrained, for each case, regardless of the magnitude of $D(JW_p)$. After most of the relative X-axis motion is achieved, the turntable begins the orientation phase. Then, after most of the orienting motion is achieved, the depth control begins. This strategy prevented the object from going OVF.

   Second, both the time and path performances of each case are virtually identical. This characteristic does not result from the trajectories being forced to pass through regions with reduced coupling. It was verified that the coupling values, at the positions where each controller becomes active in the hierarchy, are not significantly smaller than in the initial or desired views. This strategy does however tend to cause changes in any feature to be dominated by only one DOF. That is, as each controller becomes active, the majority of motion for the previously activated controller has already taken place. This facilitates the SISO identification.

3. Fixed Control: Fixed control performance is not significantly different than for the adaptive approach. However, the larger motion task begins to accentuate fixed controller inadequacy for larger gain changes. For example, the rotational stage response for case F exhibits large overshoot (Figure 7-9).

   Fixed control of the smaller motion task is adequate since the sensitivity changes associated with the these cases are relatively small. For example, in Case D, the percentage change of $\partial X_{cog}/\partial X$ is only 4 percent from the initial to the final view, in comparision with the 40 percent change for the 2 DOF example represented in Figure 6-6. The reduced gains for the 3 DOF configuration result from larger focal lengths and larger relative depths between the camera and object. Considering the relatively small gain changes and large closed-loop bandwidths, it is not surprising that the fixed and adaptive responses are similar. For the larger motion pyramid task, for which gain changes are an order of magnitude larger than for the cube task, fixed performance begins to degrade.

7.5. Summary

The 3 DOF evaluation provides further verification of the extension of SISO adaptive control to achieve stablity, with acceptable transient response, of feature coupled systems. The coupling index, $D(JW_p)$, is demonstrated to be a suitable discriminant function for selecting among several candidate feature subsets. The evaluation shows that significant improvements are achieved in both time and path performance as $D(JW_p)$ decreases. For small-signal tasks, the predicted path is straight-line. For larger motion examples, which have time-varying sensitivities, the observed paths approached straight-lines as $D(JW_p)$ decreased. The generality of achieving straight-line paths, for other tasks and configurations, remains to be evaluated in future research.

The hierarchical approach not only constrained the path, but also facilitated the use of SISO controllers for even large coupling values. Thus, the hierarchical approach becomes a conservative and safe strategy for IBVS implementations.

Classical control theory does not provide an effective means to synthesize fixed SISO controllers for coupled and time-varying systems. The adaptive approach provides a means for synthesizing the fixed SISO controllers. Fixed controllers achieved performances similar to the adaptive approach. As gain changes become larger, fixed performance begins to degrade.

Chapter 8
Conclusions

8.1. Overview

In this chapter, the author summarizes the research and contributions of the dissertation. Future directions for research are suggested, including MIMO control, implementation issues (including higher DOF), and comparative evaluation of position versus image based control approaches. Preliminary investigations into some of these areas are described.

8.2. Conclusions

This dissertation provides insight and analytic tools for the analysis, design, and evaluation of vision based dynamic robot control systems. These goals are achieved by:

1. Organizing and categorizing previously implemented and proposed visual servo control systems into well-defined classical control structures; and,

2. Analyzing, designing, and evaluating a control system for the image based approach.

The control requirements for the IBVS "teach-by-showing" strategy (including nonlinearities, coupling, unknown parameters, delay, noise, saturation, path control, and feature selection) are analyzed in Chapter 2. An independent MRAC adaptive controller, a coupling index, and a path constraint hierarchy are proposed to satisfy these requirements.

The SISO enhanced SP MRAC adaptive controller is derived for systems with delay in Chapter 3. Fixed controllers are synthesized by fixing the adjustable gains of the adaptive controller. Guidelines for selection of controller parameters are provided. Fixed versus adaptive control is evaluated (in Chapters 5 through 7), using computer simulations, for systems with increasing complexity to determine the relative contributions (to system performance characteristics) of delay, noise, kinematic and dynamic coupling, and feature coupling.

SISO adaptive control of coupled nonlinear IBVS systems is shown in simulation to be stable, with acceptable transient response, and zero steady-state errors. System performance (including time response and path deviations) improve when features are selected and assigned by minimizing the coupling index D. When the feature sensitivities are constant and coupled, the predicted position trajectories are straight-lines. The predicted trajectories for the 2 DOF configurations are either straight-line or approach straight-lines. For the 3 DOF configuration, the observed trajectories approach straight-line as the coupling index decreases. The generality of such observations must be evaluated in future research. Deviations from the predicted paths are acceptable for both small and large motion tasks, which use a robot with linear uncoupled kinematics. For large motion tasks, with an articulated arm, kinematic coupling leads to unacceptably large path deviations. The hierarchical path constraint strategy is used to guide the robot in a predictable fashion in Cartesian space (i.e., moving first in a centering X direction, then moving in the depth Y direction). The generality of this hierarchical approach remains a topic for future research.

Since path cannot be controlled directly, with the "teach-by-showing" IBVS approach, the author recommends that IBVS can be used for tasks for which exact path is not critical (e.g. in precision assembly, for parts acquisition and mating), and could also be useful to increase the accuracy of position-based approaches.

Fixed LMFC controllers are stable, with acceptable transient response. Comparative evaluation of fixed vs. adaptive control shows:

1. A fixed controller, tuned for one task, may not be suitable for another task. A single adaptive controller is suitable for a range of tasks.

2. Fixed controllers are suitable for tasks with small sensitivity (or gain) changes (e.g., small motion tasks). Adaptive controllers are capable of tracking large sensitivity changes.

3. Fixed control exhibits superior noise performance, and superior stability at lower sampling-to-bandwidth ratios. Fixed control performance becomes sluggish as the specified bandwidth decreases.

The contributions of the dissertation are:

1. Formalization of dynamic visual servo control of robots, by organizing and categorizing them into well-defined classical feedback control structures. These structures are classified as either position-based or image-based, and control either open-loop robots or incremental kinematic robot systems (with internal joint-level compensation, and kinematic decoupling). The formalization facilitates

the control system design by showing the role of computer vision as a feedback transducer (thus affecting closed-loop system dynamics, and requiring a visual servo controller), and stating the static and dynamic characteristics (of the robot and vision) which must be compensated. The categorization, of different visual control approaches, provides a common framework for future comparative evaluations.

2. Introduction and demonstration (by simulation) of a novel "teach-by-showing" image-based approach. In this approach, the visual servoing task is specified by taking a picture of an object in the desired relative position, and extracting the image features in this view. Explicit knowledge of object positions, relationships between features and positions, and robot dynamics are not required. This simplified approach could facilitate the integration of computer vision into factory environments, and increase feedback accuracy (required for precision assembly) by eliminating inaccuracies associated with feature interpretation.

3. To the best of the author's knowledge, the analysis, design, and evaluation of IBVS is the first *in-depth* study of dynamic robot control using visual feedback. Previous studies, appearing in literature, have been limited to ad-hoc control or single DOF systems.

4. The important contributions resulting from the IBVS analysis, design, and evaluation are:

   a. The extension of an enhanced SP MRAC to control of systems with measurement delay and nonlinear gains. For such systems, the delay requires a control penalty enhancement to achieve acceptable stability. The control penalty is also required to assure a locally stable controller, since the hyperstable identifier can identify non-minimum phase zeros resulting from the nonlinear gains. Reference signal biasing is required to drive steady-state full-parallel errors to zero, since the identifier can identify type 0 plants when controlling type I plants with nonlinear gains. Sufficiently large sampling-to-bandwidth ratios are required to track nonlinear gain changes.

   b. To the best of the author's knowledge, the dissertation includes the first demonstration (by simulation) of the enhanced SP MRAC for direct joint-level control of a robot arm. Similar algorithms have appeared in literature to control simulations of nonlinear coupled robot dynamics, but have not utilized the enhancements and stability viewpoints required for implementation issues of saturation, noise, and delay.

   c. Identification of limitations and applicability of SISO control of coupled systems, including:

      - Introduction of an index to measure system coupling. The ability of the SISO controller to track the reference signals degrade (and path deviations and rise-times increase) with increasing values of the index. This index is shown to be a suitable discriminate function for selecting and assigning features for control.

- Identification of a sign-sensitivity (Section 6.2.3.1), which degrades transient response. Large sampling-to-bandwidth ratios are required to minimize this sensitivity.

- Observation that steady-state identification and tracking errors approach zero, but path deviations, for IBVS, and tracking errors, for joint-level robot control, will always occur with SISO control of coupled systems. Transient errors are reduced (but not driven to zero) by increasing the sampling-to-bandwidth ratio.

d. Demonstration of the adaptive approach as a means to synthesize fixed controllers for nonlinear and coupled systems. Fixed controller design is a formidable engineering task, for such systems.

e. Preliminary analysis of the relationships between path trajectory and feature based control. This analysis encourages future evaluation of more general systems by showing that (for critically damped reference feature signals, each with the same time constant):

   - For constant and coupled feature sensitivity (i.e., Jacobian of the features with respect to positions), the predicted paths are straight lines, irrespective of the number of DOF.

   - For the 2 DOF line-in-space configuration tasks (for which the feature sensitivities are not constant and change dramatically over the trajectories), the predicted paths are straight lines or approach straight line motion.

   - For the 3 DOF configuration, the observed path deviations from a straight-line decrease as features are selected to reduce the coupling index.

   Using a path constraint hierarchy, path motion can be constrained along selected DOF, but the generality of this approach remains a topic for future research.

The image-based "teach-by showing" approach is analogous to the basic robot control "teach-mode" operation. In the author's experience, the "teach-mode" strategy for robot task definition has greatly facilitated the incorporation of robots into the industrial environment by providing a simple means for task training. Similarly, the author hopes that the "teach-by showing" approach will have the potential of simplifying applications of visual servoing.

8.3. Suggestions for Future Research

The purpose of this section is to suggest directions for future research, including MIMO control, physical implementation (including higher DOF), and comparative evaluation of the position and image based approaches. Preliminary investigations into some of these issues are also described.

8.3.1. MIMO vs. SISO Adaptive Control

The dissertation isolates problems of SISO control of coupled systems, including sign-sensitivity, feature/joint assignment, and transient tracking errors. An MIMO controller may not exhibit similar problems, and may reduce transient tracking errors. Analysis, design, and evaluation of MIMO control is a fruitful area for future investigations. While the major implementation trade-off between MIMO and SISO control is computational complexity, the author believes that a basic problem of MIMO control will be the additional complexity of selecting and initializing the controller parameters, which must be empirically chosen. In this section, an enhanced MIMO MRAC controller is proposed, and related issues of on-line estimation of J and JW_p (for SISO feature/joint assignment) are described.

The mathematical foundation for an adaptive MIMO controller can be found in [Borison 79], and parallels the development of the SISO controller in Chapter 3. For MIMO control, the model of the plant under control, described by the (m x m) transfer matrix $H(z^{-1})$, with n_d output measurement delays, is

$$\underline{Y}_d(z^{-1}) = z^{-n_d} H(z^{-1}) \underline{U}(z^{-1})$$

The system, $H(z^{-1})$, is identified by applying the hyperstable adjustment mechanism [(3.4), (3.5), and (3.6)] m times to estimate m parameter vectors. For MIMO control, the dimension of the information vector and parameter vectors increases to (2nm x 1). The information vector and each parameter vector are used to predict each ouput [Borison 79]. Calculation of the control signals require matrix inversion operations to invert the vector of identified outputs. And, calculation of the control penalties requires evaluation of the characteristic polynomial of an inverted matrix of estimated gains.

The computational complexity of MIMO versus m independent SISO controllers is summarized in Figure 8-1. The purpose of the comparison is to show that MIMO control requires more computations than the SISO approach. For MIMO control, the computational

complexity of the adjustment mechanism increases by a factor of m^2 as a result of the increased length of the information and parameter vectors. The number of computations indicated in Figure 8-1 for matrix operations is a conservative estimate, and does not account for the possibility of more efficient matrix manipulation algorithms. The salient feature is that complexity of MIMO control is order m^3n^2, versus mn^2 for SISO control. As computer hardware becomes faster and less expensive, the computational differences between these approaches will become less significant. The SISO approach may still remain attractive for factory environments due to its modularity.

Sequence of Operations (SISO Equation References)	m-input m-output n^{th} order identifier MIMO		m independent n^{th} order identifier SISO	
	Multiplications	Additions	Multiplications	Additions
1 SP Identifier (3.7)	$2m^2n$	$2m^2n-m$	$2mn$	$2mn-m$
2 ID Error (3.8)	0	m	0	m
3 m-independent Hyperstable Adjustment Mechanisms: 3.1 A'posteriori Error (3.5)	$4m^3n^2+2m^2n+2m$	$4m^3n^2$	$4mn^2+2mn+2m$	$4mn^2$
3.2 Gain Matrix (3.6)	$16m^3n^2+2m^2n+2m$	$12m^3n^2-2m^2n-m$	$16mn^2-2mn-2m$	$12mn^2-2mn-m$
3.3 Parameter Verctor (3.4)	$4m^3n^2+2m^2n+m$	$4m^3n^2$	$4mn^2+2mn+m$	$4mn^2$
4 Control Penalty (3.12)	$m(n+n_d-1)+1$ Jury Conditions		$m(n+n_d-1)+1$ Jury Conditions	
5 SP Reference Model (A.13)	$2m(n+n_d)$	$2m(n+n_d)-1$	$2m(n+n_d)$	$2m(n+n_d)-1$
6 Control Signal (3.10)	Inverse of a gain matrix is order m^3; Rest of operations require m^3+mn^2	$m^3+m^2n+m(2-n)$	$m(2n+1)$	$m(2n-1)$
Order	m^3n^2	m^3n^2	mn^2	mn^2

Figure 8-1: MIMO vs. SISO Computational Complexity

8.3.1.1. On-Line Sensitivity Estimation

For linear kinematic robot configurations, it appears that off-line measurement of JW_p (prior to the start of control) is sufficient for calculation of the coupling D, to select and assign features. General implementations of SISO control, of coupled systems, will require on-line estimation of JW_p for selecting feature/joint assignment. In the dissertation, a a low-

frequency assumption is made to evaluate $\mathbf{W}_p(j\omega)$ (for the purpose of calculating the coupling index D). Since the low-frequency robot gains can be measured off-line, only J need be estimated on-line.

The author suggests that either J or $\mathbf{JW}_p$ can be measured on-line using the MIMO hyperstable adjustment mechanism, described in Section 8.3.1., with the parameter matrix (i.e., the matrix of the m estimated parameter vectors: $\beta \doteq [\underline{\beta}_1^T | \ldots | \underline{\beta}_m^T]$) replaced with $\beta \leftarrow \mathbf{J}$ or $\beta \leftarrow \mathbf{JW}_p$. For estimation of J, the information vector becomes the robot joint displacement changes $\underline{\Phi} \leftarrow \Delta \underline{q}$ (n x 1), and $\underline{\beta}_i^T$ is (n x 1). For estimation of $\mathbf{JW}_p$, the information and parameter vectors remain (2nm x 1).

8.3.2. Implementation

The evaluation of computer simulated IBVS control (Chapters 5, 6, and 7) demonstrates the feasibility of this approach, and encourages hardware implementations. The 3 DOF configuration (in Chapter 7) can be implemented with hardware currently available in the Robotics Institute Flexible Assembly Laboratory [Sanderson 83b]. The author is currently developing hardware and software to implement an automated PC board insertion task (depicted in Figure 1-2), using IBVS control. To image the lead tip, a specially configured fiber optic sensor [Agrawal 83] is being fabricated (to replace the CCD camera), to achieve high sampling rates, high resolution, and low noise, . This system will use a 3 DOF Cartesian robot.

IBVS implementations, using real robots and sensors, raise control issues relating to robot mechanical structure, sensor resolution, and extension of IBVS control to higher DOF. These issues are discussed below.

8.3.2.1. Robot Mechanical Structure

Physical characteristics of the robot (and actuators), which may place additional constraints on the sampling period selection (Section 3.6.2), include structural resonances, dynamics which are characterized by complex poles, and torque off-sets required to overcome static friction at low velocities.

It has been suggested [Paul 81] that to avoid resonant excitation of non-rigid structures characterized by a structural resonant frequency ω_o, the sampling period should be

$$T<\frac{\pi}{15\omega_o}.$$

If the robot dynamics exhibit complex poles at $\alpha \pm j\omega_{max}$, the sampling period of the MRAC discrete time hyperstable identifier is required, by the Nyquist sampling theorem, to be

$$T<\frac{\pi}{\omega_{max}}.$$

If the vision system cannot extract features at a rate fast enough to satisfy the resonance and Nyquist constraints, the author suggests augmenting the IBVS control with joint-level velocity feedback controllers, which would sample at higher rates (e.g., using tachometer feedback) than the main IBVS feedback loop. The velocity controllers (which could be adaptive) would be tuned to dampen structural resonances and place the poles of the minor loop feedback on the real axis, to satisfy the Nyquist constraints. High-gain velocity feedback overcomes torque off-sets (or equivalently actuator voltage off-set) by amplifying the small velocity errors.

8.3.2.2. Sensor Resolution

Spatial resolution of the sensor (e.g., discrete pixel quantization of a CCD camera) is manifested as measurement noise. Low-pass filtering of the measurement signals can reduce the noise amplitude. The author suggests the following strategy to further reduce these effects. When the spatial resolution of the sensor (denoted by R) is less than the distance traveled during a sampling interval (i.e., $R<V_{rel}T$), then fix the MRAC adjustable gains (at their current value) to create a fixed LMFC controller, since the LMFC is less sensitive to noise.

8.3.2.3. Extension to Higher DOF

The 2 and 3 DOF configurations, evaluated in this dissertation, are practical for specific tasks. Implementation of more general systems (e.g., with other features and 5 or 6 DOF) remain to be analyzed for the relationships of feature control to world coordinate paths, and evaluated for the extension of SISO control to higher DOF.

At the outset of this research, the author conducted preliminary experiments of IBVS control using simulations of a 5 DOF articulated arm. While this system was not investigated in-depth, it served to demonstrate IBVS feasibility, and to gain insight into the control issues which are addressed in this dissertation. The system consisted of:

1. A 5 DOF articulated arm (with kinematic structure similar to the Cincinnati-Milicron T3), modeled with constant linear uncoupled dynamics.

2. A camera (as modeled in Section 4.5) is mounted to the last joint (or end-effector).

3. The task is to position the end-effector relative to polyhedral objects (Section 4.5). Extracted features include both areas and centroids.

4. The controller consists of 5 SISO fixed proportional controllers, which are manually tuned.

5. Feature selection and assignment, and path constraint hierarchies were specified using empirically (i.e., no coupling index was used).

The controllers could be tuned (using empirical gain adjustments and feature selections) to achieve stability, with acceptable transient response and zero steady-state positional errors. The Cartesian paths were not derived (i.e., only the joint motions, and initial and final relative positions were monitored). The proportional gains suitable for one task were not acceptable for another task. It was difficult to tune the system for large motion trajectories (i.e., the response was sluggish for low proportional gains, oscillatory for high gains, and it was difficult to keep the object in the field of view.) Feature/joint assignments and the path constraint hierarchy had to changed with varying robot arm configurations.

8.3.2.4. Position vs. Image Based Control

Approaches to visual servo control are categorized (in Chapter 2) into either position or image based structures. The organization of visual servoing into well defined classical control structures provides a framework for designing and comparing the different control approaches. An analysis, design, and evaluation of position based systems, and their comparative evaluation with image based control, would provide a complete set of design tools for implementation of dynamic visual servo control systems.

Since each approach will have tradeoffs, the author suggests that they may be used to augment one another. For example, position based approaches have the advantage of directly controlling path, while inaccuracies of the required interpretation (i.e., of features to world-space coordinates) decrease closed-loop accuracy. Augmenting position based control with IBVS, by

1. Deriving the control signal by adding both position based and image based control signals; or

2. Initially controlling gross positioning with position-based control; then switching over to IBVS for fast and accurate fine control

seem to be natural combinations.

The author hopes that the proposed research and implementations will enable IBVS control to become a practical system for robot control.

Appendix A
MRAC Without Measurement Delay

The purpose of this appendix is to explain and present a concise derivation of the MRAC controller developed by Neuman and Morris in [Neuman 80].

A block diagram for a SISO process under discrete computer MRAC control is shown in Figure 3-1 [Neuman 80]. An MRAC system comprises three basic components:

1. Analog plant under control;
2. Full-parallel reference model; and
3. Adaptive controller

The reference model transfer function $M(z^{-1})$ specifies the desired closed-loop response of the sampled plant output, y(k), to a reference signal r(k). The adaptive controller is a digital feedback controller. The controller gains are adjusted to drive the closed-loop response of the system to that of the reference model. The controller uses both plant and model input and output information to generate the control signal u(k).

At the heart of the MRAC is the controller adjustment mechanism. If the full-parallel (FP) output error is defined as

$$e_o^{FP}(k) = x(k)-y(k), \tag{A.1}$$

the adjustment mechanism must be designed so that

1. $e_o^{FP}(k)$ asymptotically approaches zero, and
2. The closed-loop system is stable.

Adjustable controller design is based on the identification-error method [Neuman 80]. The plant input-output information generates estimates of the plant parameters and are used by an identifier to predict the plant output. The identification error is

$$e_{ID}(k) = y(k)-t(k) \tag{A.2}$$

where the identifier output t(k) is the predicted plant output. This error drives the adjustment mechanism which updates the estimates of the plant parameters. In turn, these estimates are used to adjust the controller gains. The adjustment mechanism is designed so that $e_{ID}(k)$ is globally asymptotically stable for a SISO linear system. The controller is then designed to guarantee the asymptotic stability of the full-parallel error.

A.1. Reference Model

The discrete time reference model should generate a realizable output, x(k), for an analog process under computer control. Thus, the model can be specified by the cascade of a digital-to-analog converter (DAC), an analog process, and a analog-to-digital converter (ADC) with the desired response characteristics.

If the analog process model is m^{th} order, with m_1 zeros ($m_1<m$), the discrete model transfer function is [Neuman 79a]

$$M(z^{-1}) = \frac{R(z^{-1})}{X(z^{-1})} \doteq \frac{B_m(z^{-1})}{A_m(z^{-1})} \doteq \frac{B_m(z^{-1})}{1-A^{\circ}(z^{-1})} \tag{A.3}$$

$$= \frac{b_1^{\circ}z^{-1} + \ldots + b_m^{\circ}z^{-m}}{1-a_1^{\circ}z^{-1}-\ldots-a_m^{\circ}z^{-m}} \tag{A.4}$$

The sampled data FP model output can thus be characterized by the mth order difference equation

$$x_{FP}(k) = \Big[\sum_{i=1}^{m} b_i^{\circ}q^{-i}\Big]r(k) + \Big[\sum_{i=1}^{m} a_i^{\circ}q^{-i}\Big]x(k) \tag{A.5}$$

where the delay operator q^{-i} is defined by

$$(q^{-i})x(k) \doteq x(k-i).$$

For example,

$$\Big[\sum_{i=1}^{m} b_i q^{-i}\Big]r(k) = b_1 r(k-1) + b_2 r(k-2) + \ldots + b_m r(k-m).$$

The model is a full-parallel model since (A.3) is recursive.

Reference model structures have typically been specified by critically damped, second order systems [Landau 79] for a wide variety of adaptive control tasks. The closed-loop model can be generated by assuming that a type I second-order linear plant, $G_{model}(s)$, is under computer control (Figure A-1), and the proportional gain K_{Pcrit} is tuned to provide critical damping. The open-loop plant transfer function is

$$G_{model}(s) = \frac{K_{model}}{s(\tau_{model}s + 1)} \tag{A.6}$$

where

K_{model} = model gain constant
τ_{model} = model time constant (sec)

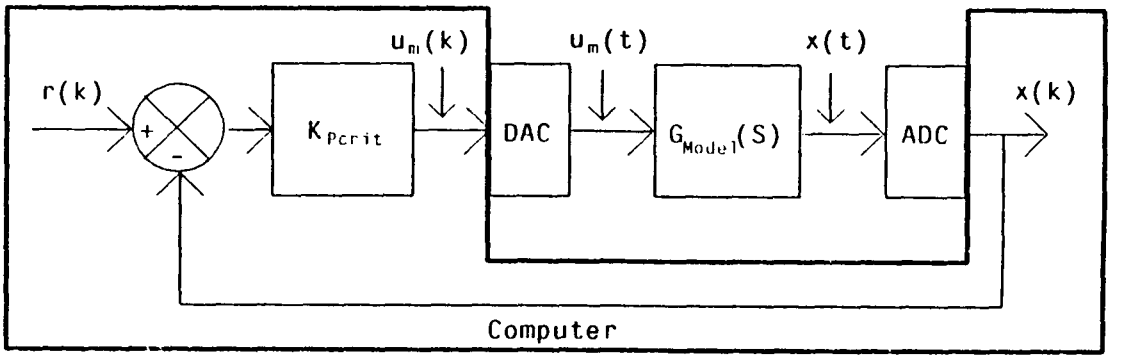

Figure A-1: FP Reference Model

Neuman and Morris specified the reference model in the Z-plane. The derivation presented here differs by first showing an analog plant model in a feedback control structure. This approach facilitates development of a reference model when measurement delays are included (in Chapter 3).

The equivalent z-transform model of Figure A-1 is shown in Figure A-2.

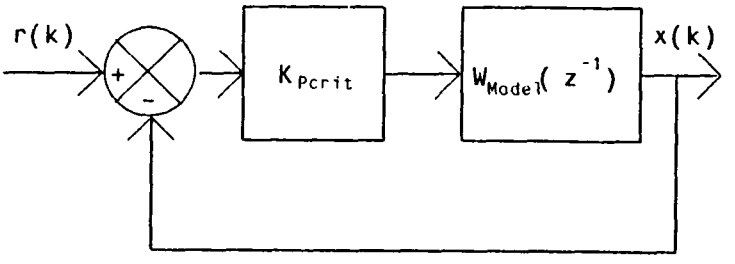

Figure A-2: Discrete Reference Model

In Figure A-2, the digital transfer function

$$W_{model}(z^{-1}) = [1-z^{-1}]\cdot Z\left\{\left[L^{-1}\left(\frac{G_{model}(s)}{s}\right)\right]_{t\leftarrow kT}\right\}$$

models the cascade of the DAC, analog process G(s), and ADC [Neuman 79a]. For the second-order type I analog model in (A.6),

$$W_{model}(z^{-1}) = \frac{b_1 z^{-1} + b_2 z^{-2}}{1-a_1 z^{-1} - a_2 z^{-2}} \tag{A.7}$$

where, for the sampling period T,

$$a_1 = 1 + e^{-T/\tau_{model}}$$

$$a_2 = -e^{-T/\tau_{model}}$$

$$b_1 = -(K\tau_{model})(1-T/\tau_{model}-e^{-rT})$$

$$b_2 = (K\tau_{model})(1-e^{-T/\tau_{model}}-e^{-rT}\,T/\tau_{model})$$

The closed-loop transfer function of Figure A-2 is

$$W_{CL}(z^{-1}) = \frac{K_{Pcrit}[b_1 z^{-1} + b_2 z^{-2}]}{1 + [K_{Pcrit}b_1 - a_1]z^{-1} + [K_{Pcrit}b_2 + a_2]z^{-2}}$$

For critical damping, the gain term K_{Pcrit} must satisfy

$$[K_{Pcrit}b_1 - a_1]^2 = 4[K_{Pcrit}b_2 + a_2]$$

The difference equation of the closed-loop model becomes

$$x_{FP}(k) = K_{Pcrit}b_1 r(k-1) + K_{Pcrit}b_2 r(k-2)$$
$$+ (a_1 - K_{Pcrit}b_1)x(k-1) + (a_2 - K_{Pcrit}b_2)x(k-2)$$

and, the model parameters for (A.5) are

$$b_1^\circ = b_1 K_{Pcrit}$$

$$b_2^\circ = b_2 K_{Pcrit}$$

$$a_1^\circ = a_1 - b_1 K_{Pcrit}$$

$$a_2^\circ = a_1 - b_2 K_{Pcrit}$$

$$m = 2.$$

A.2. Plant Model Structure

For the identifier to track the plant output, the structure of the plant must be defined. If the plant under control is assumed to have an equivalent n^{th} order I/O structure (Section 2.3.1.3), with n_1 zeros ($n_1<n$), then the corresponding discrete-time model is the nth order transfer function

$$W(z^{-1}) = \frac{Y(z^{-1})}{U(z^{-1})} \doteq \frac{B_p(z^{-1})}{A_p(z^{-1})} \tag{A.8}$$

$$= \frac{b_1 z^{-1} + b_2 z^{-2} + \ldots + b_n z^{-n}}{1 - a_1 z^{-1} - a_2 z^{-2} - \ldots\ldots - a_n z^{-n}}$$

where the $\{a_i\}$ and $\{b_i\}$ are unknown parameters. The sampled plant output, y(k), can therefore be modeled by the nth order input-output difference equation

$$y(k) = \left[\sum_{i=1}^{n} b_i q^{-i}\right] u(k) + \left[\sum_{i=1}^{n} a_i q^{-i}\right] y(k). \tag{A.9}$$

In vector notation, (A.9) is

$$y(k) = \underline{\beta}^T \underline{\Phi}(k-1)$$

where

$\underline{\beta}^T \doteq (b_1 \ldots b_n a_1 \ldots a_n)$ is the (2n X 1) parameter vector; and (A.10)

$\underline{\Phi}(k-1) \doteq [u(k-1) \ldots u(k-n) y(k-1) \ldots y(k-n)]^T$ is the (2n X 1) information vector

A.3. Controller

A series-parallel (SP) identifier with adjustable parameters tracks the plant output. The identifier output t(k) is calculated according to

$$t(k) = \left[\sum_{i=1}^{n} \hat{b}_i(k-1) q^{-i}\right] u(k) + \left[\sum_{i=1}^{n} \hat{a}_i(k-1) q^{-i}\right] y(k) \tag{A.11}$$

where $\{\hat{b}_i\}$ and $\{\hat{a}_i\}$ are estimates of the process parameters of an equivalent SISO linear system.

The identifier is series-parallel since it is non-recursive. A full-parallel identifier produces unbiased estimates of the process parameters in the presence of noise (assuming a control signal sufficiently rich in frequency content), but at a slower speed of convergence than for a SP adjustable model. In addition, an FP identifier requires good initial guesses for $\{\hat{b}_i\}$ and

$\{\hat{a}_i\}$. In contrast, the SP identifier produces biased estimates of the plant parameters. In MRAC control, it is shown below, all that is required for FP errors to approach zero asymptotically is an <u>equivalent</u> input/output model which matches the input/output characteristics of the plant.

In vector notation, (A.11) becomes

$$t(k) = \hat{\underline{\beta}}^T(k-1)\underline{\Phi}(k-1)$$

where $\hat{\underline{\beta}}^T(k-1)$ is the estimated parameter vector. The identification error becomes

$$e_{ID}(k) = y(k)-t(k) = \left[\underline{\beta}^T-\hat{\underline{\beta}}^T(k-1)\right]\underline{\Phi}(k-1).$$

In the next section, an adjustment mechanism is presented to guarantee asymptotic stability of $e_{ID}(k)$.

When the identification error converges to zero, the identifier becomes an equivalent input-output model of the plant. The adaptive controller is then constructed by solving for the control signal u(k) required to force the identifier output t(k + 1) to follow the reference signal $X^R(k)$. By inverting (A.11), the control signal becomes

$$u(k) = \frac{1}{\hat{b}_1(k)}\left\{X^R(k)-\left[\sum_{i=2}^{n}\hat{b}_i(k)q^{-(i-1)}\right]u(k)-\left[\sum_{i=1}^{n}\hat{a}_i(k)q^{-(i-1)}\right]y(k)\right\} \tag{A.12}$$

It is now shown that true estimates of the plant parameters are not required to produce an asymptotically stable FP error. True estimates may not occur when:

1. Parameter estimates become biased in the presence of noise;

2. The frequency content of the control signal is poor; and

3. As demonstrated in this dissertation, when the plant being identified is nonlinear, time-varying, or part of a coupled system.

If the reference model signal is chosen to be the output of the one-step ahead FP model,

$$X^R(k) = x(k+1) = \left[\sum_{i=1}^{m}\overset{\circ}{b}_i q^{-(i-1)}\right]r(k) + \left[\sum_{i=1}^{m}\overset{\circ}{a}_i q^{-(i-1)}\right]x(k), \tag{A.13}$$

then, upon convergence of e_{ID}, the identifier becomes

$$t(k+1) = X^R(k) = x(k+1)$$

or,

$$t(k) = x(k),$$

and the FP error is

$$
\begin{aligned}
e_o^{FP} &= x(k)-y(k) \\
&= t(k)-y(k) \\
&= -e_{ID}(k)
\end{aligned}
\tag{A.14}
$$

Thus, the FP output error is asymptotically stable if the adjustment mechanism can assure asymptotic stability of the identification error, regardless of errors in the true parameter estimates!

A.4. Adjustment Mechanism

The adjustment mechanism used for estimating $\hat{\underline{\beta}}$ can be designed from either parametric optimization or stability viewpoints. Optimization techniques, which are based on cost-function minimization, were first applied to adaptive control [Whitaker 61]. These include the gradient descent and least-squares methods. As applied to adaptive control, these methods have drawbacks which require reliable initial estimates of the plant parameters [Price 70] and result in low adaptation speeds to guarantee local stability [Kokotovic 66]. In contrast, the stability viewpoint, which is inherent to the design goals of closed-loop control systems, guarantees asymptotic stability of e_{ID} and thus e_o^{FP}, at higher adaptation speeds, regardless of initial parameter estimates. This approach, which includes Lyapanov's second method [Narendra 74] and Popov's hyperstability theorem [Popov 63], prescribe stability criteria for nonlinear, time-varying , closed-loop systems. The output e_{ID} of the nonlinear, time-varying, closed-loop adjustment mechanism drives the parameter update, and is designed to be asymptotically stable. Landau, who was the first to apply hyperstability to MRAC [Landau 69], claims that with respect to the Lyapanov approach ".... More general results were obtained using the hyperstability approach, perhaps, because it is more systematic." [Landau 74]

The hyperstable adjustment mechanism [Landau 79] specifies the following identifier when the plant is assumed to be linear with <u>slowly</u> varying parameters:

$$\hat{\underline{\beta}}(k) = \hat{\underline{\beta}}(k-1) + \frac{1}{\lambda}P(k-1)\underline{\Phi}(k-1)s(k) \tag{A.15}$$

$$s(k) = \frac{e_{ID}(k)}{1 + (1/\lambda)\underline{\Phi}^T(k-1)P(k-1)\underline{\Phi}(k-1)} \tag{A.16}$$

$$P(k) = \frac{1}{\lambda}P(k-1) - \frac{1}{\lambda^2}\left[\frac{s(k)}{e_{ID}(k)}\right]P(k-1)\underline{\Phi}(k-1)\underline{\Phi}^T(k-1)P(k-1) \tag{A.17}$$

where P(k) is a (2n X 2n) adaptive gain matrix, s(k) is the a'posteriori error (which is the error signal after the parameters are updated at the kth computational cycle), and e_{ID} is the a'priori error signal. The fading factor λ ($0<\lambda\leq 1$) weighs past values of the input/output samples by the progression

$$1, \lambda, \lambda^2, \ldots\ldots \lambda^k.$$

If $\lambda = 1$, new information is averaged with all past data, minimizing overreaction to measurement noise. If $\lambda<1$, old data is weighed less, and the mechanism can track the parameter $\underline{\beta}$ even when the parameters are slowly time-varying.

The adjustment mechanism in (A.15) - (A.17) approximates the optimal recursive weighted least-squares algorithm which is derived from the minimization of the cost function

$$J(k) = (\omega/2)\sum_{i=0}^{k} \lambda^i e_{ID}^2(k-i)$$

This approach is referred to as the hyperstable least-squares adjustment mechanism.

A.5. Enhancements

Performance of the basic MRAC algorithm can be significantly improved by the addition of numerous enhancement strategies [Neuman 79b]. Neuman and Morris present a detailed analysis of enhancement mechanisms [Morris 79], and recommend an enhanced error identification MRAC algorithm. These enhancements include:

1. Control Penalty;
2. Series-Parallel Reference Model Signal;
3. Augmenting Error Filter; and
4. Auxiliary Fixed Control.

The augmenting error filter must be used with caution since it increases the high-frequency gain of the feedback controller, thus amplifying noise and reducing the stability margin. To use the auxiliary fixed controller requires that the system operate around a known and stationary operating point, which in general does not hold for IBVS systems. Thus, only the first two enhancements, which are described below, are used in this dissertation.

Control Penalty

A control signal penalty is obtained by multiplying (A.12) by the positive scaler $\pi(k)$ ($0<\pi\leq 1$). This penalty is introduced to

1. Reduce the magnitude of the control signal and thereby the effect of reduced marginal stability due to control signal saturation;

2. Reduce control signal noise; and

3. Insure a stable and bounded control signal.

Experimental evaluation of MRAC, by Neuman and Morris, demonstrates that control signal saturation in the DAC can occur quite often when controlling low-pass systems, such as robot joint actuators. The feedback path of the FP controller can be characterized as a high-pass filter when the process under control exhibits a low-pass frequency response. Measurement noise is amplified and the control signal quality deteriorates.

Guaranteeing the asymptotic stability of e_{ID} does not insure the asymptotic stability of e_o^{FP} when a control penalty is used.The identification-error becomes

$$e_{ID}(k) = -e_o^{FP}(k) + \frac{\hat{b}_1(k)}{\pi}(1-\pi)u(k-1)$$

If $e_{ID}(k)$ goes to zero, the FP error is related to the control signal according to

$$e_o^{FP} = \frac{\hat{b}_1(k)}{\pi}(1-\pi)u(k-1) \tag{A.18}$$

If the control signal becomes unbounded, the FP error is not asymptotically stable. This can occur if the actual or estimated plant has non-minimum phase zeros lying outside the unit circle. The computations below illustrate that the poles of the adjustable controller are determined by the estimated plant zeros. Thus, when the zeros lie outside of the unit circle, the controller poles become unstable. In addition, the control signal can become quite large if the plant zeros are not accurately estimated. This often occurs in actual implementations when $\hat{b}_1$ is underestimated due to measurement and signal transmision delays through the ADC and DAC converters.

To specify the control penalty, a lower bound b_{LB} is placed on the magnitude of $\hat{b}_1(k)$ used to calculate the controller gain. The value of $\pi(k)$ is specified according to

$$\pi(k) = \begin{cases} \dfrac{\hat{b}_1(k)}{b_{LB}} & \text{if} \quad \hat{b}_1(k) < b_{LB} \\ 1 & \text{if} \quad \hat{b}_1(k) \geq b_{LB}. \end{cases}$$

It remains to choose b_{LB} so that u(k) remains bounded. To accomplish this task, the Jury

stability conditions are applied to test the location of the controller poles $\{p_i\}$ at each computational cycle. When pole magnitudes exceed the design parameter γ, where $0<\gamma<1$, the value of b_{LB} is increased (thus reducing π) until the poles lie within a circle of radius γ in the Z-plane.

The controller characteristic equation is determined by taking the Z-transform of (A.12) with the control penalty enhancement included. The control signal is

$$U(z^{-1}) = \frac{\dfrac{\pi(k)}{\hat{b}_1(k)}\left\{X^R(z^{-1}) - \left[\sum_{i=1}^{n} \hat{a}_i(k)z^{-(i-1)}\right] Y(z^{-1})\right\}}{1 + \dfrac{\pi(k)}{\hat{b}_1(k)}\sum_{i=2}^{n} \hat{b}_i(k)z^{-(i-1)}}$$

and the controller characteristic equation is

$$F(z^{-1}) = 1 + \frac{\pi(k)}{\hat{b}_1(k)}\sum_{i=2}^{n} \hat{b}_i(k)z^{-(i-1)}. \tag{A.19}$$

Thus, the estimated plant zeros determine the controller poles.

The Jury conditions are applied to (A.19) for a second-order system ($n = 2$) by expressing the characteristic equation in positive powers of z as:

$$F(z) = z + \pi(k)\frac{\hat{b}_2(k)}{\hat{b}_1(k)}. \tag{A.20}$$

To test for $|p|<\gamma$, apply the transformation $z = \gamma z^*$ to obtain

$$F(z^*) = \gamma z^* + \pi(k)\frac{\hat{b}_2(k)}{\hat{b}_1(k)}.$$

For this characteristic equation, the Jury condition is:

$$|\pi(k)\hat{b}_2(k)/\hat{b}_1(k)|<\gamma$$

and the control penalty is calculated according to

$$\pi(k) = \begin{cases} 1 & \text{if} \quad |\hat{b}_2/\hat{b}_1|<\gamma \\ (\hat{b}_1/\hat{b}_2)\gamma & \text{if} \quad |\hat{b}_2/\hat{b}_1|\geq\gamma \end{cases} \tag{A.21}$$

Series-Parallel Reference Model Signal

Neuman and Morris have shown that increasing the control penalty of the FP MRAC (to suppress noise and increase the stability margin) can lead to a highly oscillatory closed-loop response. An enhancement which further reduces the high-frequency gain of the feedback path (thus reducing noise amplification and producing a closed-loop system which does not exhibit a highly oscillatory response as the control penalty is increased) is the series-parallel (SP) reference model signal enhancement. The SP reference model signal, which improves performance at the expense of slower tracking of the FP model, is implemented by replacing the recursive component x(k) of (A.13) by a non-recursive filtering of the process output y(k):

$$X_{SP}^{R}(k) = \left[\sum_{i=1}^{m} \overset{\circ}{b}_i q^{-(i-1)}\right] r(k) + \left[\sum_{i=1}^{m} \overset{\circ}{a}_i q^{-(i-1)}\right] y(k). \tag{A.22}$$

In contrast to the control penalty, this enhancement leads to an asymptotically stable FP output error

$$e_o^{FP}(k) = \frac{e_{ID}(k)}{A_m(q^{-1})} \tag{A.23}$$

where

$$A_m(z^{-1}) \doteq Z\left[A_m(q^{-1})\right]$$

If the FP model specifies the stable filter $\left[1/A_m(q^{-1})\right]$, the FP output error is asymptotically stable if $e_{ID}(k)$is asymptotically stable. Transient identification errors produce slower tracking of the reference model due to this filtering effect.

Appendix B
Dynamic Equations for 2 DOF Arm

This appendix presents the derivation of the dynamic equations of motion for the 2 DOF arm described in Section (4.4). The derivation is based on the Lagrange-Euler formulation for rigid body structures [Paul 81]. The Lagrangian function L is first defined as the difference between the kinetic energy K and the potential energy P of the system:

$$L \doteq K - P$$

The dynamic equations are then

$$F_i = \frac{\partial}{\partial t}\frac{\partial L}{\partial \dot{q}_i} - \frac{\partial L}{\partial q_i} \tag{B.1}$$

where q_i and $\dot{q}_i$ are the generalized position and velocity coordinates. F_i is the corresponding force or torque acting on the ith joint. For an articulated robot arm, $q_i \doteq \theta_i$, and F_i corresponds to joint torque. If an n DOF manipulator is described by a set of homogeneous transforms $\{A_i\}$, then (B.1) becomes

$$\begin{aligned} F_i = & \sum_{j=1}^{n}\sum_{k=1}^{j} \mathrm{TRACE}\left(\frac{\partial T_j}{\partial q_k} J_j \frac{\partial T_j^T}{\partial q_i}\right) \ddot{q}_k \\ & + \sum_{j=1}^{n}\sum_{k=1}^{j}\sum_{m=1}^{j} \mathrm{TRACE}\left(\frac{\partial^2 T_j}{\partial q_k \partial q_m} J_j \frac{\partial T_j^T}{\partial q_i}\right) \dot{q}_k \dot{q}_m \\ & + \sum_{i=1}^{n} m_j g^T \frac{\partial T_j}{\partial q_i} {}^j\vec{r}_j \end{aligned} \tag{B.2}$$

where

$$T_k \doteq A_1 A_2 \cdots A_k$$

The pseudo-inertial matrix, J_i, of the ith link is:

$$J_i \doteq \begin{bmatrix} \frac{-I_{ixx}+I_{iyy}+I_{izz}}{2} & I_{ixy} & I_{ixz} & m_i\bar{x}_i \\ I_{ixy} & \frac{I_{ixx}-I_{iyy}+I_{izz}}{2} & I_{iyz} & m_i\bar{y}_i \\ I_{ixz} & I_{iyz} & \frac{I_{ixx}+I_{iyy}-I_{izz}}{2} & m_i\bar{z}_i \\ m_i\bar{x}_i & m_i\bar{y}_i & m_i\bar{z}_i & m_i \end{bmatrix}$$

where the first and second moments are

$$I_{xx} = \int (y^2+z^2)dm \; ; \quad I_{yy} = \int (x^2+z^2)dm \; ; \quad I_{zz} = \int (x^2+y^2)dm \; ;$$

$$I_{xy} = \int xy\, dm \; ; \quad I_{xz} = \int xz\, dm \; ; \quad I_{yz} = \int yz\, dm \; ;$$

$$m\bar{x} = \int x\, dm \; ; \quad m\bar{y} = \int y\, dm \; ; \quad m\bar{z} = \int z\, dm \quad m = \int dm$$

and ${}^{j}\vec{r}_j$ is the homogeneous vector defining the position of the center of mass of link j relative to the jth coordinate frame. $\vec{g}$ defines the gravitational field. And, m_i is the mass of the ith link.

For n = 2, (B.2) is:

$$
\begin{aligned}
F_1 = & \left\{ \mathrm{TRACE}\left(\frac{\partial T_1}{\partial q_1} J_1 \frac{\partial T_1^T}{\partial q_1} \right) + \mathrm{TRACE}\left(\frac{\partial T_2}{\partial q_1} J_2 \frac{\partial T_2^T}{\partial q_1} \right) \right\} \ddot{q}_1 \\
& + \left\{ \mathrm{TRACE}\left(\frac{\partial T_2}{\partial q_2} J_2 \frac{\partial T_2^T}{\partial q_1} \right) \right\} \ddot{q}_2 \\
& + \left\{ \mathrm{TRACE}\left(\frac{\partial^2 T_2}{\partial q_1 \partial q_1} J_1 \frac{\partial T_1^T}{\partial q_1} \right) + \mathrm{TRACE}\left(\frac{\partial^2 T_2}{\partial q_1 \partial q_1} J_2 \frac{\partial T_2^T}{\partial q_1} \right) \right\} \dot{q}_1^{\,2} \\
& + \left\{ \mathrm{TRACE}\left(\frac{\partial^2 T_2}{\partial q_1 \partial q_2} J_2 \frac{\partial T_2^T}{\partial q_1} \right) + \mathrm{TRACE}\left(\frac{\partial^2 T_2}{\partial q_2 \partial q_1} J_2 \frac{\partial T_2^T}{\partial q_1} \right) \right\} \dot{q}_1 \dot{q}_2 \\
& + \left\{ \mathrm{TRACE}\left(\frac{\partial^2 T_2}{\partial q_2 \partial q_2} J_2 \frac{\partial T_2^T}{\partial q_1} \right) \right\} \dot{q}_2^{\,2} \\
& - m_1 \, \mathbf{g}^T \frac{\partial T_1}{\partial q_1} \; {}^1\vec{\mathbf{r}}_1 - m_2 \, \mathbf{g}^T \frac{\partial T_2}{\partial q_1} \; {}^2\vec{\mathbf{r}}_2
\end{aligned}
\tag{B.3}
$$

and,

$$
\begin{aligned}
F_2 = & \left\{ \mathrm{TRACE}\left(\frac{\partial T_2}{\partial q_1} J_2 \frac{\partial T_2^T}{\partial q_2} \right) \ddot{q}_1 \right\} + \left\{ \mathrm{TRACE}\left(\frac{\partial T_2}{\partial q_2} J_2 \frac{\partial T_2^T}{\partial q_2} \right) \right\} \ddot{q}_2 \\
& + \left\{ \mathrm{TRACE}\left(\frac{\partial^2 T_2}{\partial q_1 \partial q_1} J_2 \frac{\partial T_2^T}{\partial q_2} \right) \right\} \dot{q}_1^{\,2} \\
& + \left\{ \mathrm{TRACE}\left(\frac{\partial^2 T_2}{\partial q_1 \partial q_2} J_2 \frac{\partial T_2^T}{\partial q_2} \right) \right\} + \left\{ \mathrm{TRACE}\left(\frac{\partial^2 T_2}{\partial q_2 \partial q_1} J_2 \frac{\partial T_2^T}{\partial q_2} \right) \right\} \dot{q}_1 \dot{q}_2 \\
& + \left\{ \mathrm{TRACE}\left(\frac{\partial^2 T_2}{\partial q_2 \partial q_2} J_2 \frac{\partial T_2^T}{\partial q_2} \right) \right\} \dot{q}_2^{\,2} \\
& - m_2 \, \mathbf{g}^T \frac{\partial T_2}{\partial q_2} \; {}^2\vec{\mathbf{r}}_2
\end{aligned}
\tag{B.4}
$$

For the arm in Figure 4-9, the $\{A_i\}$ matricies are:

$$A_1 = \begin{bmatrix} C_1 & S_1 & 0 & r_1C_1 \\ -S_1 & C_1 & 0 & r_1S_1 \\ 0 & 0 & 1 & 0 \\ 0 & 0 & 0 & 1 \end{bmatrix} \quad ; \quad A_2 = \begin{bmatrix} C_2 & -S_2 & 0 & r_2C_2 \\ S_2 & C_2 & 0 & r_2S_2 \\ 0 & 0 & 1 & 0 \\ 0 & 0 & 0 & 1 \end{bmatrix}$$

where

$$C_i \doteq \cos(\theta_i)$$
$$S_i \doteq \sin(\theta_i)$$

Thus,

$$T_1 = A_1$$

$$T_2 = A_1A_2 = \begin{bmatrix} C_{12} & -S_{12} & 0 & r_2C_{12} + r_1C_1 \\ S_{12} & C_{12} & 0 & r_2S_{12} + r_1S_1 \\ 0 & 0 & 1 & 0 \\ 0 & 0 & 0 & 1 \end{bmatrix}$$

where

$$C_{ij} \doteq \cos(\theta_i + \theta_j)$$
$$S_{ij} \doteq \sin(\theta_i + \theta_j)$$

The partial derivatives of the T transforms are:

$$\frac{\partial T_1}{\partial \theta_1} = \begin{bmatrix} -S_1 & -C_1 & 0 & -r_1S_1 \\ C_1 & -S_1 & 0 & r_1C_1 \\ 0 & 0 & 0 & 0 \\ 0 & 0 & 0 & 0 \end{bmatrix} ; \qquad \frac{\partial T_1}{\partial \theta_2} = \underline{0}$$

$$\frac{\partial T_1^2}{\partial \theta_1 \partial \theta_1} = \begin{bmatrix} -C_1 & S_1 & 0 & -r_1C_1 \\ -S_1 & -C_1 & 0 & -r_1S_1 \\ 0 & 0 & 0 & 0 \\ 0 & 0 & 0 & 0 \end{bmatrix} \quad ; \quad \frac{\partial T_1^2}{\partial \theta_1 \partial \theta_2} = \underline{0}$$

$$\frac{\partial T_2}{\partial \theta_2} = \begin{bmatrix} -S_{12} & -C_{12} & 0 & -r_2S_{12} \\ C_{12} & -S_{12} & 0 & -r_2C_{12} \\ 0 & 0 & 0 & 0 \\ 0 & 0 & 0 & 0 \end{bmatrix} ; \qquad \frac{\partial T_2}{\partial \theta_1} = \begin{bmatrix} -S_{12} & -C_{12} & 0 & -r_2S_{12} - r_1S_1 \\ C_{12} & -S_{12} & 0 & -r_2C_{12} + r_1C_1 \\ 0 & 0 & 0 & 0 \\ 0 & 0 & 0 & 0 \end{bmatrix}$$

$$\frac{\partial T_2^2}{\partial\theta_2\partial\theta_1}=\begin{bmatrix} -C_{12} & S_{12} & 0 & -r_2C_{12} \\ -S_{12} & -C_{12} & 0 & -r_2S_{12} \\ 0 & 0 & 0 & 0 \\ 0 & 0 & 0 & 0 \end{bmatrix};\quad \frac{\partial T_2^2}{\partial\theta_1\partial\theta_2}=\begin{bmatrix} -C_{12} & S_{12} & 0 & -r_2C_{12} \\ -S_{12} & -C_{12} & 0 & -r_2S_{12} \\ 0 & 0 & 0 & 0 \\ 0 & 0 & 0 & 0 \end{bmatrix}$$

$$\frac{\partial T_2^2}{\partial\theta_2\partial\theta_2}=\begin{bmatrix} -C_{12} & S_{12} & 0 & -r_2C_{12} \\ -S_{12} & -C_{12} & 0 & -r_2S_{12} \\ 0 & 0 & 0 & 0 \\ 0 & 0 & 0 & 0 \end{bmatrix};\quad \frac{\partial T_2^2}{\partial\theta_1\partial\theta_1}=\begin{bmatrix} -C_{12} & S_{12} & 0 & -r_2C_{12}-r_1C_1 \\ -S_{12} & -C_{12} & 0 & -r_2S_{12}-r_1S_1 \\ 0 & 0 & 0 & 0 \\ 0 & 0 & 0 & 0 \end{bmatrix}$$

The J_1 and J_2 matricies are calculated for the links in Figure B-2 and Figure B-1.

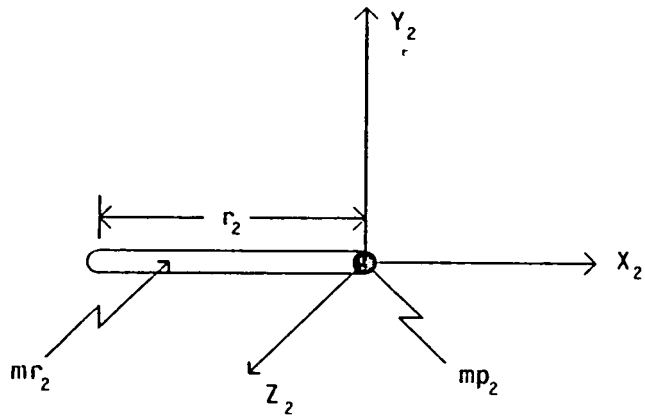

Figure B-1: Link # 2

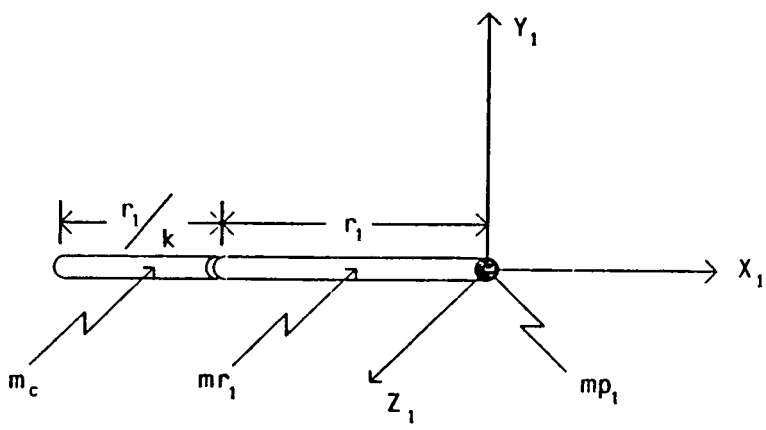

Figure B-2: Link # 1

Since the each link consists of a point mass, located at the orgin of it's coordinate frame, and a thin rod in the X-direction, all of the interial components in the Y and Z directions are zero. Thus,

$$I_{XX} = I_{XY} = I_{XZ} = I_{YZ} = m\bar{y} = m\bar{z} = 0$$

The mass of the portion of the link modeled as a thin rod is

$$m_r = \rho V$$

where ρ is the density and V is the volume. If the rod cross-sectional area is A, then

$$dm_r = \rho A dx$$

Thus,

$$I_{2\text{-}YY} = I_{2\text{-}ZZ} = \int_{-r_2}^{0} x^2\, dm = \int_{-r_2}^{0} \rho A x^2\, dx = \frac{m_{r2} r_2^2}{3}$$

and,

$$m\bar{x} = \int_{-r_2}^{0} x\, dm = \int_{-r_2}^{0} \rho A x\, dx = \frac{-m_{r2} r_2}{2}$$

Thus,

$$J_2 = \begin{bmatrix} \frac{m_{r2} r_2^2}{3} & 0 & 0 & \frac{-m_{r2} R_2}{2} \\ 0 & 0 & 0 & 0 \\ 0 & 0 & 0 & 0 \\ \frac{-m_{r2} R_2}{2} & 0 & 0 & (m_{r2} + m_{p2}) \end{bmatrix}$$

For J_1 (refer to Figure B-2):

$$I_{1\text{-}YY} = I_{1\text{-}ZZ} = \int_{-r_1/k}^{-r_1} x^2 dm + \int_{-r_1}^{0} x^2 dm$$

$$= \left[\frac{m_c}{12}\left(\frac{r_1}{k}\right)^2 + m_c\left(r_1 + \frac{r_1}{2k}\right)^2\right] + \frac{m_{r1} r_1^2}{3}$$

$$= r_1^2\left[\frac{m_{r1}}{3} + m_c\left(1 + \frac{1}{k} + \frac{1}{3k^2}\right)\right]$$

And,

$$m\bar{x} = \int_{-r_1/k}^{-r_1} x\, dm + \int_{-r_1}^{0} x dm = -\left(r_1 + \frac{r_1}{2k}\right) m_c - \frac{m_{r1} r_1}{2}$$

$$= -r_1\left[\frac{m_{r1}}{2} + m_c\left(1 + \frac{1}{2k}\right)\right]$$

Thus,

$$J_1 = \begin{bmatrix} r^2_1\left[\frac{m_{r1}}{3} + m_c\left(1+\frac{1}{k}+\frac{1}{3k^2}\right)\right] & 0 & 0 & -r_1\left[\frac{m_{r1}}{2}+m_c\left(1+\frac{1}{2k}\right)\right] \\ 0 & 0 & 0 & 0 \\ 0 & 0 & 0 & 0 \\ -r_1\left[\frac{m_{r1}}{2}+m_c\left(1+\frac{1}{2k}\right)\right] & 0 & 0 & (m_{r1}+m_{p1}+m_c) \end{bmatrix}$$

The gravitational components are defined next. If gravity acts in the X_o direction, then

$$\vec{g} = [g \;\; 0 \;\; 0 \;\; 0]^T$$

To find the center of mass of the second link, $r_{2\text{-}eq}$, set the first moment, $\int x dm$, equal to the net mass times $r_{2\text{-}eq}$. Thus,

$$-\frac{m_{r2}r_2}{2} = (m_{r2}+m_{p2})r_{2\text{-}eq},$$

$$r_{2\text{-}eq} = -\frac{m_{r2}}{2(m_{r1}+m_{p2})} \cdot r_2$$

and hence

$$^2\vec{r}_2 = [r_{2\text{-}eq} \;\; 0 \;\; 0 \;\; 1]^T.$$

Similarly for link 1

$$r_{1\text{-}eq} = \frac{-r_1\left[\frac{m_{r1}}{2}+m_c\left(1+\frac{1}{2k}\right)\right]}{(m_{r1}+m_{p1}+m_c)r_{1\text{-}eq}}$$

and hence

$$^1\vec{r}_1 = [r_{1\text{-}eq} \;\; 0 \;\; 0 \;\; 1]^T$$

Equations (B.3) and (B.4) become:

$$F_1 = D_{11}\ddot{\theta}_1 + D_{12}\ddot{\theta}_2 + D_{112}\dot{\theta}_1\dot{\theta}_2 + D_{122}\dot{\theta}_2^{\,2} + D_1$$

$$F_2 = D_{12}\ddot{\theta}_1 + D_{22}\ddot{\theta}_2 + D_{211}\dot{\theta}_1^{\,2} + D_2$$

where

$$D_{11} = \left[\frac{m_{r1}}{3} + \frac{m_c}{3k^2} + m_{p1} + m_{r2} + m_{p2}\right] r_1^2 + 2r_1 r_2 C_2 \left[\frac{m_{r2}}{2} + m_{p2}\right] + \left[\frac{m_{r2}}{3} + m_{p2}\right] r_2^2$$

$$D_{12} = \left[m_{p2} + \frac{m_{r2}}{3}\right] r_2^2 + r_1 r_2 C_2 \left[\frac{m_{r2}}{2} + m_{p2}\right]$$

$$D_{112} = -2r_1 r_2 S_2 \left[\frac{m_{r2}}{2} + m_{p2}\right]$$

$$D_{122} = -r_1 r_2 S_2 \left[\frac{m_{r2}}{2} + m_{p2}\right]$$

$$D_1 = g\left\{\left[\frac{m_{r1}}{2} + m_{p1} - \frac{m_c}{2k}\right] r_1 S_1 + \left[\frac{r_2}{2} S_{12} + r_1 S_1\right] m_{r2} + \left[r_2 S_{12} + r_1 S_1\right] m_{p2}\right\}$$

$$D_{22} = \left[m_{p2} + \frac{m_{r2}}{3}\right] r_2^2$$

$$D_{211} = r_1 r_2 S_2 \left[\frac{m_{r2}}{2} + m_{p2}\right]$$

$$D_2 = g r_2 S_{12} \left[m_{p2} + \frac{m_{r2}}{2}\right]$$

Appendix C
2 DOF Controller Parameters

The independent SP MRAC controller, for the 2 DOF configurations, is outlined in this appendix. The same controller parameters are used for both the linear and nonlinear kinematic configurations. All simulations and control structures include a measurement delay (i.e., $n_d = 1$). Independent adaptive and fixed controllers are implemented in Chapter 6 according to:

1. Control signal : (3.10)

2. Identifier : (3.4),(3.5), and (3.6) with $\lambda_\lambda = 0.85$. The identifier is initialized according to Table C-1, and the initial signs of $b_1(0)$ and $b_2(0)$ are selected according to the sign of the corresponding diagonal elements of the sensitivity matrix. The values in Table C-1 are identical to those used in the single degree-of freedom examples (in Table 5-1), with an exception at the sampling period T = 0.003 sec. The gain matrix initilization is increased, to yield acceptable response for the nonlinear robot configuration.

3. Control penalty : (3.12), with $\gamma = .65$

4. SP Reference Model : (A.22). The reference model bandwidth ,ω_n, is specified for each set of examples, while T is varied to evaluate the effects of changing the sampling-to-bandwidth ratio (f_s/f_{BW}). The open-loop reference model time constants are selected according to the methods outlined in section 3.6.1., and the discrete model parameters are generated according to the method outlined in Section 3.3.3. The same closed-loop bandwidth is specified for each independent controller.

5. Scale Factors :

   $SF_{T = .033} = 2500$
   $SF_{T = .013} = 5000$
   $SF_{T = .003} = 10000$

6. LMFC : The fixed controller is implemented by fixing the gains of the adjustable controller to the staedy-state values identified in initial adaptive trials.

T(sec)	P(0)	P_{Thresh}	$\hat{\underline{\beta}}(0)$
0.033	Diag [10 10 80 80]	2500	$[\pm 10 \;\; \pm 10 \;\; 1.1 \;\; -0.1]^T$
0.013	Diag [1 1 1 1]	100	$[\pm 1 \;\; \pm 1 \;\; 1.5 \;\; -0.5]^T$
0.003	x_{cog} Feature Controller Diag [.1 .1 .01 .01] length Feature Controller Diag [1 1 1 1]	10	$[\pm 1 \;\; \pm 1 \;\; 1.5 \;\; -0.5]^T$

Table C-1: Identifier Parameter Initialization (2 DOF)

Appendix D
3 DOF Controller Parameters

The simulations in Chapter 3 are implemented with the sampling period T = 0.003 (sec) and a bandwidth $\omega_n = 44.51$ (sec^{-1}), or $f_s/f_{BW} = 47$, as in the 2 DOF evaluation. The MRAC controller is implemented according to the outline presented in Section 6.2 with the exception of the identifier initialization and scaling factors. The identifier is initialized according to Table D-1.

T(sec)	P(0)	P_{Thresh}	$\hat{\underline{\beta}}(0)$
0.003	X_{cog} & A_{rel} Feature Controllers Diag [.1 .1 .01 .01] Absolute Area Feature Controllers Diag [.5 .5 .1 .1]	10	$[\pm 1 \quad \pm 1 \quad 1.5 \quad -0.5]^T$

Table D-1: 3 DOF Parameter Initialization (T = 0.003 sec)

The initial adaptive gains, P(0), for the absolute area identifiers (i.e., A_i or A_{i+j}) are larger than for the other features. When all feature identifiers were initialized with the lower gains, P(0) = [0.1 0.1 0.01 0.01], the area controller would exhibit poor transient response and result in $sgn[\hat{b}_{1\text{-}ss}] \neq sgn[\hat{b}_{2\text{-}ss}]$. It was observed throughout this research that, when this occurs, improved transient responses can be achieved by increasing the initial adaptive gains for that feature, assuming large enough sampling-to-bandwidth ratios.

The initial parameter vector gain initializations [$\hat{b}_1(0)$ and $\hat{b}_2(0)$] were reduced from the values used for 2 DOF configuration. In the 3 DOF configuration, the camera will be mounted at a relatively long distance from the turntable, which significantly reduces the magnitudes of J, and therefore plant gains.

The scale factors are assigned according to

Feature	SF
X_{cog}	10^3
Area (A_i or A_{i+j})	10^6
A_{rel}	10^4

The path constraint hierarchy, described in Section 2.5.3, is represented in Figure D-1 for the 3 DOF configuration.

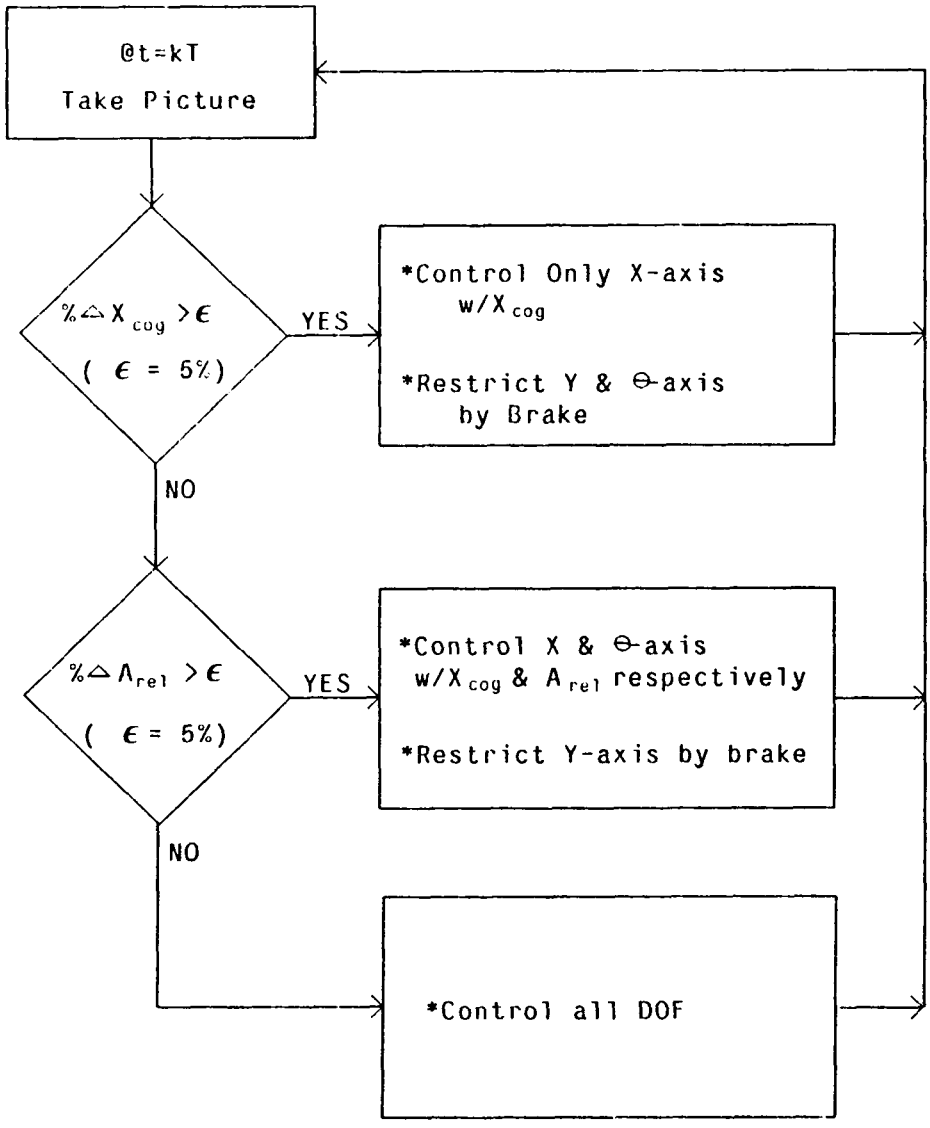

Figure D-1: Hierarchy for 3 DOF Configuration

In Figure D-1, the features which dominate each DOF follow from (7.4). During transitions between levels of the hierarchy, the identifier for each controller is fixed for three sampling periods according to Section 6.2.3.3.

References

[Agin 79] Agin, G.J.
Real Time Control of a Robot with a Mobile Camera.
Technical Report 179, SRI International, Feb., 1979.

[Agrawal 83] Agrawal, A.K., and Jordan, B.W.
Machine Vision Based on Fiber-Optic Imaging.
Electronic Imaging :40-43, Nov., 1983.

[Albus 75] Albus, J.S.
A New Approach to Manipulator Control : The Cerebellar Model Articulation Controller (CMAC).
Trans. ASME, J. Dynamic Systems, Measurement, and Control 97:220-227, Sept., 1975.

[Albus 81] Albus, J. S., et al.
Hierarchical Control for Sensory Interactive Robots.
In *11th International Symposium on Industrial Robots*, pages 497-505. SME and RIA, Oct., 1981.

[Asada 82] Asada, H., Kanade, T., Ichiro, T.
Control of a Direct-Drive Arm.
Technical Report 82-4, Carnegie-Mellon Univ., The Robotics Institute, March, 1982.

[Astrom 77] Astrom, K.J., et al.
Theory and Applications of Self-Tuning Regulators.
Automatica 13(5):457-476, Sept., 1977.

[Bahill 83] Bahill, A. T.
A Simple Adaptive Smith-Predictor for Controlling Time-Delay Systems.
Control Systems Magazine 3(2):16-22, may, 1983.

[Birk 79] Birk, J., et al.
General Methods to Enable Robots with Vision to Aquire, Orient, and Transport Workpieces.
Technical Report 5, Univ. Rhode Island, August, 1979.

[Borison 79] Borison, U.
Self-Tuning Regulators for a Class of Multivariable Systems.
Automatica 15:209-215, 1979.

[Bracho 82] Bracho, R., and Sanderson, A.C.
Design Study of RIP 1: An Image Processor for Robotics.
Technical Report 82-3, Carnegie-Mellon University, The Robotics Institute, May, 1982.

[Chung 82] Chung, M.J., and Lee, C.S.G.
An adaptive Control Strategy for Computer-Based Manipulators.
Technical Report 10-82, The Univ. of Michigan, Ann Arbor, August, 1982.

[Coulon 83] Coulon, P.Y., and Nougaret, M.
Use of a TV Camera System in Closed-Loop Position Control Mechanisms.
In Pugh, A. (editors), *Robot Vision*, . I.F.S. Publications Ltd., 1983.

[Denavit 55] Denavit, J. and Hartenberg, R.S.
A Kinematic Notation for Lower-Pair Mechanisms Based on Matrices.
J. Apllied Mechanics :251-221, June, 1955.

[Dubowsky 79] Dubowsky, S., and DesFOrges, D.T.
The Application of Model-Reference Adaptive Control to Robotic Manipulators.
Trans. ASME, J. Dynamic Systems, Measurement, and Control 101:193-200, Sept., 1979.

[Duda 73] Richard O. Duda and Peter E. Hart.
Pattern Classification and Scene Analysis.
John Wiley and Sons, New York, 1973.

[Electro-Craft 80] D.C. Motors - Speed Controls - Servo Systems
Electro-Craft Corp., 1980.

[Fu 82] Fu, K.S.
Pattern Recognition for Automatic Visual Inspection.
Computer 15(12), Dec., 1982.

[Geschke 82] Geschke, C.
A Robot Task Using Visual Tracking.
Robotics Today :39-43, Winter, 1981-1982.

[Goodwin 84] Goodwin, G.C. and Sin, K.S.
Adaptive Filtering Prediction and Control.
Prentis-Hall, Englewood Cliffs, N.J., 1984.

[Hall 82] Hall, E. L. , et. al.
Maesuring Curved Surfaces for Robot Vision.
Computer 15(12), Dec., 1982.

[Hasegawa 77] Hasegawa, K., et al.
On Visual Siganl Processing for Industrial Robot.
In *7th International Symposium on Industrial Robots*, pages 543-550. SME and RIA, Oct., 1977.

[Hollerbach 80] John M. Hollerbach.
A Recursive Lagrangian Formulation of Manipulator Dynamics and a Comparative Study of Dynamics Formulation Complexity.
IEEE Transactions on Systems, Man, Cybernetics SMC-10(11):730-736, November, 1980.

[Horowitz 80] Horowitz, R., and Tomizuka, M.
An Adaptive Control Scheme for Mechanical Manipulators - Compensation of Nonlinearity and Decoupling Control.
In *Winter Annual Meeting, Dynamics, Systems, and Control Div.*. ASME, Nov., 1980.

[Hunt 82] Hunt, A. E.
Vision-Based Predictive Robotic Tracking of a Moving Target.
Master's thesis, Carnegie-Mellon University, Jan., 1982.

[IMSL 82] *International Mathematical and Statistical Libraries*
IMSL Inc., Houston, Texas, 1982.

[Jarvis 80] Jarvis, J.F.
Visual Inspection Automation.
Computer 13(5), May, 1980.

[Kahn 71] Kahn, M.E., and Roth, B.
THe Near-Minimum-Time Control of Open-Loop Articulated Kinematic Chains.
Trans. ASME, J. Dynamic Systems, Measurement, and Control 93:164-172, Sept, 1971.

[Kanade 83] Kanade, T. and Sommer, T.M.
An Optical Proximity Sensor for Measuring Surface Position and Orientation for Robot Manipulation.
Technical Report CMU-RI-TR-83-15, Carnegie-Mellon University, The Robotics Institute, September, 1983.

[Kashioka 77] Kashioka, S., et al.
An Approach to the Integrated Intelligent Robot with Multiple Sensory Feedback: Visual Recognition Techniques.
In *7th International Symposium on Indutrial Robots*, pages 531-538. SME and RIA, Oct., 1977.

[Kindle 50] Kindle, Joseph H.
Schaum's Outline of Theory and Problems: Analytic Geometry.
McGraw-Hill, 1950.

[Koivo 80] Koivo, A. J., Paul, R. P.
Manipulator with Self-Tuning Control.
In *IEEE Conference on Cybernetics and Society*, pages 1085-1089. IEEE Systems, Man, and Cybernetics Society, 1980.

[Koivo 81] Koivo, A.J., and Guo, T.H.
Control of Robotic Manipulator with Adaptive Controller.
In *Proceedings 20th IEEE Conf. Decision and Control.* Dec., 1981.

[Koivo 83] Koivo, A.J., and Guo, T.H.
Adaptive Linear Controller for Robotic Manipulators.
IEEE Trans. Automatic Control AC-28(2):162-171, Feb., 1983.

[Kokotovic 66] Kokotovic, P.V., et al.
Sensitivity Method in the Experimental Design of Adaptive Control Systems.
In *Proc. 3rd IFAC Congress.* IFAC, 1966.

[Kuo 82] Kuo, Benjamin C.
Automatic Control Systems.
Prentice-Hall, 1982.

[Landau 69] Landau, I.D.
A Hyperstability Criterion for the Model Reference Adaptive Control System.
IEEE Trans. on Automatic Control AC-14(5), Oct, 1969.

[Landau 74] Landau, I.D.
A survey of Model Reference Adaptive Techniques (Theory and Applications).
Automatica 10(4), July, 1974.

[Landau 79] Landau, Y.D.
Control and Systems Theory. Volume 8: *Adaptive Control: The Model Approach.*
Marcel Dekker, Inc., 1979.

[LeBorgne 81] Le Borgne, M., Ibarra, J.M., and Espiau, B.
Adaptive Contro of High Velocity Manipulators.
In *Proceedings of the 11th Intern. Symposium on Industrial Robots*, pages 227-236. Oct., 1981.

[Lee 82a] Lee, George C.S.
Robot Arm Kinematics, Dynamics, and Control.
Computer 15(12), Dec, 1982.

[Lee 82b] Lee, C.S.G.
On the Control of Mechanical Manipulators.
In *Proc. Sixth IFAC Conf. Estimation and Parameter Identification*, pages 1454-1459. IFAC, June, 1982.

[Luh 80] J. Y. S. Luh, M.W. Walker, R. P. C. Paul.
On-Line Computational Scheme for Mechanical Manipulators.
Journal of Dynamic Systems, Measurement, and Control 102:69-76, june, 1980.

[Luh 83] Luh, J.Y.S.
An Anatomy of Industrial Robots and Their Controls.
Automatic Control AC-28(2), Feb., 1983.

[Marks 78] Baumeister, T.
Mark's Standard Handbook for Mechanical Engineers.
Mcgraw-Hill, 1978.

[Merkle 83] Merkle, F.
Hybrid Optical-Digital Image Processing System For Pattern Recognition.
In *10th Internationsl Optical Computing Conference*. April, 1983.

[Morris 79] Morris, R.L.
Design of Microcomputer Adaptive Controllers.
PhD thesis, Carnegie-Mellon University, 1979.

[Morris 81] Morris, R. L. and Neuman, C. P.
Multirate Adaptive Control of a DC Position Servomotor: With Application to Robot Control.
In *Proc. of the 2nd Yale Workshop of Adaptive System Theory*. May, 1981.

[Myers 80] Myers, W.
Industry Begins to Use Visual Pattern Recognition.
Computer 13(5), May, 1980.

[Narendra 74] Narendra, K.S. and Kudva, P.
Stable Adaptive Schemes for System Identification and Control - Parts I and II.
IEEE Trans. on Systems, Man, and Cybernetics SMC-4(6):542-560, Nov, 1974.

[Neuman 79a] Neuman, C.P., Baradello, C.S.
Digital Transfer Functions for Microcomputer Control.
IEEE Trans. on Systems, Man, and Cybernetics Vol. SMC-9(12):856-860, December, 1979.

[Neuman 79b] C.P. Neuman and R.L. Morris.
Microcomputer REquirements for Model Reference Adaptive Controllers.
In *Thirteenth Asilomar Conference on Circuits, Systems and Computers*. Nov., 1979.

[Neuman 80] Neuman, C.P. and Morris, R.L.
Classical Control Interpretation and Design of Microcomputer Adaptive Controllers.
In *Applications of Adaptive Control*, . Academic Press, 1980.

[Neuman 83] Neuman, C.P., and Stone, H.W.
MRAC Control of Robotic Manipulators.
In *Proceedings of the Third Yale Workshop on Applications of Adaptive System Theory*. June, 1983.

[Paul 81] Richard P. Paul.
Robot Manipultors: Mathematics, Programming, and Control.
The MIT Press, Cambridge, Mass., 1981.

[Popov 63] Popov, V.M.
The Solution of a New Stability Problem for Controlled Systems.
Automation and Remote Control 24(1), Jan, 1963.

[Porter 80] Porter, G.B., and Mundy, J.L.
Visula Inspection System Design.
Computer 13(5), May, 1980.

[Price 70] Price, C.F.
An Accelerated Gradient Method for Adaptive Control.
In *Proc. 9th IEEE Symp. Adaptive Processes, Decision, and Control*. IEEE, Dec, 1970.

[Raibert 78] Raibert, M.H., Horn, B.K.P.
Manipulator Control Using the Configuration Space Method.
The Industrial Robot 5:69-73, June, 1978.

[Rosenbrock 74] Rosenbrock, H. H.
Computer-Aided Control System Design.
Academic Press, 1974.

[Sanderson 82] Arthur C. Sanderson and Lee E. Weiss.
Image-Based Visual Servo Control of Robots.
In *26th Annual SPIE Technical Symposium*. SPIE, August, 1982.

[Sanderson 83a] Sanderson, A. C., Weiss, L.
Adaptive Visual Servo Control of Robots.
In Pugh, A. (editor), *Robot Vision*, . I.F.S. Publications Ltd., 1983.

[Sanderson 83b] Sanderson, A.C., and Perry, G.
Sensor-Based Robotic Assembly Systems: Research and Applications in Electronic Manufacturing.
Proceedings of the IEEE 71(7), July, 1983.

[Shah 80] Shah, S. L. and Fisher, D. G.
Algorithmic and Structural Similarities Between Model Reference Adaptive and Self-Tuning Controllers.
In *1980 Joint Automatic Control Conference*. ASME, August, 1980.

[Stermer 83] Stermer, R.L., and Sokoloski, M.
Optical Data Processing for Aerospace Applications.
In *10th International Optical Computing Conference*. April, 1983.

[Stone 84] Stone, H. and Neuman, C.P.
Dynamic Modeling and Adaptive Control of a Three DOF Robotic Manipultor.
IEEE Transactions on Systems, Man, and Cybernetics 14, July, 1984.

[Takegaki 81] Takegaki, M., and Arimoto, S.
An Adaptive Trajectory Control of Manipulators.
Int. J. Control 34(2):219-230, 1981.

[Tani 77] Tani, K., et al.
High Precision Manipualtors with Visual Sense.
In *7th International Symposium on Industrial Robots*, pages 561-568. SME and RIA, Oct., 1977.

[Uicker 67] Uicker, J.J.
Dynamic Force Analysis of Spatial Linkages.
Transactions of the ASME / Journal of Applied Mechanics :418-423, June, 1967.

[Vuylsteke 81] Vuylsteke, P., et al.
Video Rate Recognition of Plane Objects.
Sensor Review 1:132-135, July, 1981.

[Ward 79] Ward, M. R., et al.
Consight: A Practical Vision-Based Robot Guidance System.
In *9th International Symposium on Industrial Robots*, pages 195-211. SME and RIA, March, 1979.

[Whitaker 61] Whitaker, H.P., Osburn, P.V., and Keezer, A.
New Developments in the Design of Adaptive Control Systems.
Inst. Aeronautical Sciences 37(5), 1961.

[Whitney 72] Whitney, D.E.
The Mathematics of Coordinated Control of Prosthetic Arms and Manipulators.
Trans. ASME, J. Dynamic Systems, Measurement, and Control :303-309, Dec., 1972.

[Williams 83] Williams, S.J.
Frequency Response Multivariable Robot Control System Design.
In *Proc. IEE Colloquium on "Control Theory in Robotics"*. IEE, Oct., 1983.

[Wylie 61] Wylie, C. R.
Advanced Engineering Mathematics.
McGraw-Hill, 1961.

[Yuan 77] Yuan, J.C., and Wonham W.M.
Probing Signals for Model Reference Identification.
IEE Trans. on Automatic Control AC-22(4):530-538, August, 1977.